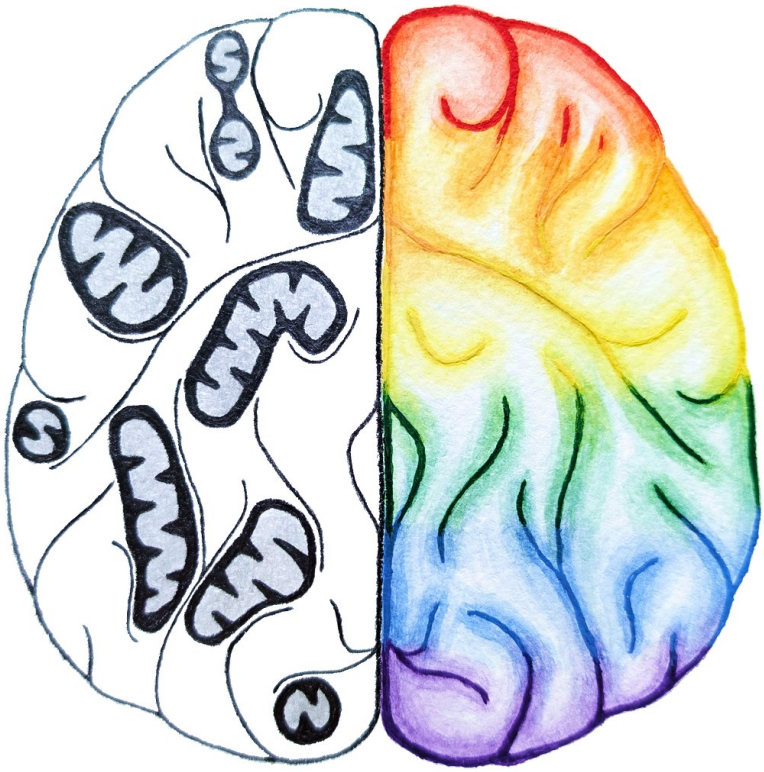

The role of mitochondria in progranulin-related frontotemporal dementia

Javier Sanchez Bautista

March 2024

A thesis submitted for the degree of Doctor of Philosophy

to University College London

Department of Neuromuscular Diseases,

UCL Queen Square Institute of Neurology

Declaration

“I, Javier Sanchez Bautista, confirm that the work presented in my thesis is my own. Where information has been derived from other sources, I confirm that this has been indicated in the thesis.”

Abstract

Mutations in the progranulin (*GRN*) gene are a major cause of frontotemporal dementia (FTD), resulting in haploinsufficiency of the soluble protein progranulin (PGRN). While mitochondrial dysfunction is considered a key mediator in the pathogenesis of several neurological disorders, the impact of PGRN haploinsufficiency on mitochondrial activity remains largely underexplored. The overall aim of this thesis was to characterise the role of mitochondria in *GRN*-related FTD.

Initially, I conducted a comprehensive characterisation of mitochondria in *GRN* knockdown immortalised cell lines, fibroblasts from patients with *GRN* pathogenic mutations and iPSC-derived neurons and astrocytes. This involved biochemical, molecular and genetic approaches. Subsequently, I investigated the role of mitochondria in human post-mortem brains diagnosed with frontotemporal lobar degeneration (FTLD), comparing FTLD-*GRN* cases with sporadic FTLD-TDP cases and controls. Finally, I optimised histopathology techniques and developed semi-automatic quantitative techniques to identify and measure neuropathological changes in FTLD-*GRN* cases.

The experimental work in PGRN-deficient *in vitro* and human post-mortem brains revealed mitochondrial bioenergetic deficits, decreased mitochondrial mass, and mtDNA maintenance defects. These findings collectively establish the presence of mitochondrial dysfunction in *GRN*-related FTD. The data strongly implicate mitochondria as organelles affected by PGRN deficiency, suggesting that mitochondrial dysfunction is involved in *GRN*-related FTD pathogenesis. Consequently, mitochondria emerge as potential therapeutic targets for treating FTLD-*GRN* patients.

Impact Statement

The role of mitochondria has been extensively studied in various forms of FTD associated with genetic mutations such as *C9orf72*, *MAPT* and *CHCHD10*. However, there is a notable gap in the academic literature exploring the molecular mechanisms underlying *GRN*-related FTD pathogenesis, particularly from a mitochondria-centric approach.

From a non-clinical perspective, this is the first study to our knowledge to comprehensively characterise the role of mitochondria in *GRN*-related FTD, especially employing post-mortem brains from FTLD-*GRN* patients. The identification of PGRN haploinsufficiency inducing mitochondrial dysfunction adds a layer of complexity of the disease, implicating mitochondria in the development of *GRN*-related FTD. These findings not only pave the way for further investigation into the causal link between mitochondria, the gene *GRN* and FTD but also contribute foundational knowledge for future research expanding the role of mitochondria in other neurodegenerative diseases.

On the clinical front, there are no current disease-modifying treatments that halt or reverse the progression of FTD. The discovery of mitochondrial dysfunction in PGRN-deficient models opens avenues for developing novel therapeutic strategies to alleviate and potentially one day prevent the progression of clinical syndromes in patients with *GRN*-related FTD. This breakthrough extends our understanding of the broader role of mitochondria in health and disease, offering potential targets for treating other neurodegenerative diseases, including amyotrophic lateral sclerosis, Alzheimer's disease and Parkinson's disease.

Publications arising from this thesis

Bautista, J.S., Falabella, M., Flannery, P.J., Hanna, M.G., Heales, S.J.R., Pope, S.A.S., and Pitceathly, R.D.S. (2022). Advances in Methods to Analyse Cardiolipin and Their Clinical Applications. TrAC Trends in Analytical Chemistry *157*, 116808. 10.1016/j.trac.2022.116808.

Bautista, J.S. (2021). LGBTQ+ STEM @UCL Network: Fostering an inclusive and visible community. Physiology News Magazine: Equity, Diversity and Inclusion Special Issue *123*. 10.36866/pn.123.12.

Bautista, J.S., Lu S., Woodward, C.E., Labrum, R., de Jesus, D.J, Pizzamiglio C., Macken, W.L., Hannah, M.G., Rohrer, J.D., Plun-Favreau, H., Wray, S., Taanman, J.W., Falabella, M, Pitceathly, R.D.S. (In draft stage). Mitochondrial dysfunction is involved in *GRN*-related frontotemporal dementia.

Awards, events and conferences

Presentations at Conferences and Symposiums

- Poster – Euromit 2023 Conference — 11-15th June 2023
- Talk – Annual Meeting - FTD UK Conference — 12th May 2023
- Talk & poster – Alzheimer's Research UK Conference 2023 — 13-15th March 2022
- Poster – Crick 5th Anniversary PhD Student Symposium — 11th July 2022
- Poster – 2022 UCL Neuroscience Symposium — 22nd June 2022
- Poster – UCL LGBTQ+ STEM Conference 2022 — 7th June 2022
- Talk – Faculty of Brain Sciences Conference 2022 — 27th May 2022

Academic awards

- Best Poster – Doctoral School Research Poster Competition — June 2023
- Stuart Pickering-Brown Prize – 10th FTD UK Conference — May 2023
- Best Poster – Alzheimer's Research UK 2023 Conference — March 2023
- 2nd place – Doctoral School Poster Competition (Neuroscience) — August 2022
- Best poster – Crick 5th Anniversary PhD Student Symposium — July 2022
- Best Poster – 2022 UCL Neuroscience Symposium — June 2022
- 3rd place (Special Mention) – 3MT UCL Final — June 2022
- Associate Fellow of the Higher Education Academy (AFHEA) — June 2022
- 3MT People's Choice Award Faculty of Brain Sciences — May 2022
- Student Representative of the Year at the Faculty of Brain Sciences — June 2021
- 2nd place – Institute of Neurology Tutorial Competition — August 2021
- MRC DTP PhD Studentship Award — 2019-2023

Non-academic awards

- Best Poster – MAPS Embedding EDI in Education Poster Competition — July 2023
- Nova 111 List – Top 10 Spanish student in Health and Life sciences — May 2023
- Championing LGBTQ+ Equality Award – UCL Inclusion Awards 2022 — July 2022
- Best Speaker – Kearney Consulting Academy — Feb 2022
- Finalist (Tied 4th place) – BCGxBizsoc Case Study Competition — Jan 2022
- Best Science/Tech Article – SPA Journalism Awards — Oct 2021
- 2nd place – Entrepreneurial Branch of the DECA Case Study Competition — Nov 2020

Acknowledgments

I would like to begin by expressing my gratitude to my supervisors Professor Robert Pitceathly and Dr Micol Falabella for their guidance and support during the development of my research project.

Special thanks to Dr Jan-Willem Taanman and all my research colleagues for their assistance and encouragement. I extend my appreciation to my thesis committee, Professor Selina Wray and Professor Hélène Plun-Favreau, for their input and for being exemplary role models. This work would have not been possible without all the donors of tissue samples from the Queen Square Brain Bank, and the UCL-Birkbeck Medical Research Council Doctoral Training Program for funding my PhD.

This thesis is dedicated to two different collectives. Firstly, the LGBTQ+ STEM community, particularly the LGBTQ+ STEM @UCL Network, for fostering a welcoming environment and promoting the intersectionality between queerness and STEM. Secondly, this thesis is dedicated to all those students with mental health struggles who were unable to complete their studies. This is for all of them.

I would like to extend my thanks to my parents, Maria and Juan Carlos, and my sister, Cristina. Thank you as well to everyone who has listened to me to talk about my PhD, particularly Emily and Marie for their contributions to the artwork in this thesis.

Finally, I am deeply grateful to my beloved partner Chris for his love and support. Throughout the high and lows of my PhD journey, he has always been by my side, ready to listen, encouraging me and helping me overcome any obstacles.

Table of Contents

List of Figures

List of Tables

List of key abbreviations

AD	Alzheimer's disease
ALS	amyotrophic lateral sclerosis
ADP	adenosine diphosphate
ATP	adenosine triphosphate
CBM	cerebellum
CBS	corticobasal syndrome
CSF	cerebrospinal fluid
CI-V	complexes I to V
CL	cardiolipin
CISH	chromogenic *in situ* hybridisation
CNS	central nervous system
COX	cytochrome *c* oxidase
CSF	cerebrospinal fluid
DAB	3,3′-diaminobenzidine
ETC	electron transport chain
FBS	fetal bovine serum
FFPE	formalin-fixed paraffin-embedded
FG	frontal grey
FW	frontal white
FTD	frontotemporal dementia
FTLD	frontotemporal lobar degeneration
GRN	progranulin (gene)
HEK	human embryonic kidney cells
IHC	immunohistochemistry
IMM	inner mitochondrial membrane
IMS	intermembrane space
iPSCs	induced pluripotent stem cells
KD	knockdown
mRNA	messenger RNA
mtDNA	mitochondrial DNA
mtDNAcn	mitochondrial DNA copy number
NGS	next-generation sequencing
OMM	outer mitochondrial membrane
OXPHOS	oxidative phosphorylation
qPCR	quantitative polymerase chain reaction
PD	Parkinson's disease
PGC-1α	proliferator-activated receptor γ coactivator-1α
PGRN	progranulin (protein)
QSBB	Queen Square Brain Bank
ROS	reactive oxygen species
RT-PCR	reverse transcriptase PCR
shRNA	short hairpin RNA
TCA	tricarboxylic acid
TDP	TDP-43, TAR DNA binding protein-43
TG	temporal grey
TW	temporal white

1 General introduction

Life is a powerhouse (collage using newspaper cut-outs) – by Javier S. Bautista

1.1 Frontotemporal dementia

1.1.1 The frontotemporal dementia syndrome

Frontotemporal dementia (FTD) encompasses a spectrum of progressive neurodegenerative disorders characterised by executive, behavioural and language dysfunction[1]. FTD is the second most common cause of young-onset dementia after Alzheimer's disease (AD), with an estimated lifetime risk of 1 in 742[2]. Symptoms manifest between the ages of 40 and 60, when patients experience nerve cell loss due to the atrophy of the frontal and temporal lobes.

Several clinical variants of FTD have been identified (Fig. 1.1). The most common form is the behavioural variant FTD (bvFTD)[3], which is characterised by a plethora of clinical manifestations, such as behavioural inhibition, apathy or inertia, loss of sympathy or empathy, hyperorality, preservative or compulsive behaviours and dysexecutive neuropsychological profile.

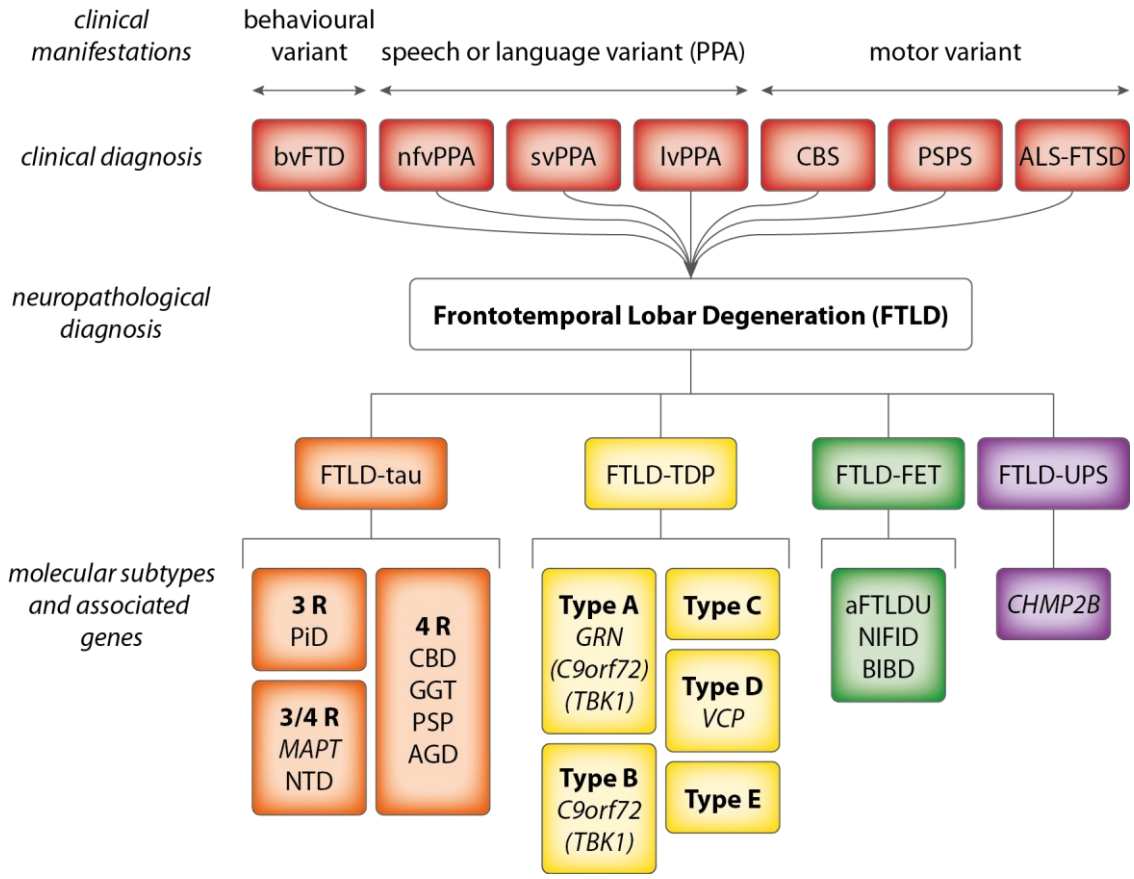

Figure 1.1 Schematic representation of FTD classification. FTD is classified into three different variants depending on the clinical manifestations: behavioural variant (bvFTD); primary progressive aphasia (PPA) affecting speech or language variant (including non-fluent variant, nfvPPA; semantic variant, svPPA; and logopenic variant, lvPPA), and motor variant (including corticobasal syndrome, CBS; progressive supranuclear palsy syndrome, PSPS; and amyotrophic lateral sclerosis-frontotemporal spectrum disorder, ALS-FTSD). FTD leads to the pathological disorder FTLD, which can be divided into four different categories: (1) FTLD-tau divided into 3 R (Pick's disease, PiD), 4 R (corticobasal degeneration, CBD; globular glial tauopathy, GGT; progressive supranuclear palsy, PSP; and argyrophilic grain disease, AGD), and 3/4 R (*MAPT* mutations and neurofibrillary tangle disease, NTD) depending on the most predominant isoform of tau; (2) FTLD-TDP divided into type A (mainly associated with mutations in *GRN* and less often in *C9orf72* and *TBK1*), type B (mainly associated with mutations in *C9orf72* and less often in *TBK1*), type C, type D (*VCP* mutations), and type E; (3) FTLD-FUS including atypical FTLD with ubiquitin inclusions (aFTLDU), neuronal intermediate filament inclusion disease (NIFID) and basophilic inclusion body disease (BIBD); and (4) FTLD-UPS (ubiquitin proteasomal system) caused by *CHMP2B* mutations.

The second type of variant is primary progressive aphasia (PPA) that is divided into three subcategories presenting speech and language impairment. People with non-fluent variant primary progressive aphasia (nfvPPA) present apraxia of speech and agrammatism, together with poor understanding of complex sentences, and spared object knowledge and single-word comprehension[4].

The semantic variant primary progressive aphasia (svPPA) is characterised by poor confrontation naming and single-word comprehension, impaired object knowledge, surface dyslexia, with repetition and speech production generally spared[1]. Lastly, the logopenic variant primary progressive aphasia (lvPPA) is diagnosed by impaired single-word retrieval and repetition of phrases and sentences[4]. In addition, FTD can present a spectrum of motor syndromes, including corticobasal syndrome (CBS) and progressive supranuclear palsy syndrome (PSPS) which involve parkinsonism. A third clinical diagnosis is amyotrophic lateral sclerosis–frontotemporal spectrum disorder (ALS–FTSD), where there is an overlap between FTD and ALS[5].

Currently, there are no disease-modifying treatments that halt or reverse the progression of disease, and clinical management focuses on alleviating the symptoms. This emphasises the need for a better understanding of the pathological mechanism, with the aim to improve treatments and identify potential biomarkers and therapeutic strategies.

1.1.2 Neuropathology of FTLD

Frontotemporal lobar degeneration (FTLD) denotes the neuropathological diagnosis of the heterogeneous FTD clinical syndrome. It is characterised by the progressive degeneration of the frontal and temporal lobes of the brain. A broad range of neuropathological mechanisms and protein accumulations have been identified in FTLD, which has led to the classification in four major subtypes: FTLD-tau, FTLD-TDP, FTLD-FUS and FTLD-UPS (Fig. 1.1)[6–9].

- FTLD-tau (40% of the cases) is characterised by the aggregation of the microtubule-associated protein tau in neurons and/or glia. This can be subclassified depending on the predominant tau isoform in the microtubule binding domain, which can contain 3 or 4 repeats (3R or 4R) of ~32 amino acids. Several conditions associated with tauopathy include Pick's disease[10,11], corticobasal degeneration[12], globular glial tauopathy[13], progressive supranuclear palsy[10] and argyrophilic grain disease[14]. FTLD-tau can also be caused by mutations in the gene microtubule-associated protein tau (*MAPT*)[6], which present clinical and pathological heterogeneity.

- FTLD-TDP (50% of the cases) is defined by the accumulation of the transactive response (TAR) DNA binding protein of 43 kDa (TDP-43), leading to the formation of tau-negative, TDP-43- and ubiquitin-positive inclusion bodies. FTLD-TDP has been further subdivided in five types (type A, B, C, D and E) based on ubiquitin, TDP-43 and phospho-TDP immunohistochemistry (IHC)[15]. FTLD-TDP type A is primarily associated with progranulin (*GRN*) mutations, the gene that encodes for the protein progranulin (PGRN), which plays an important role in lysosomal function and microglial responses in the central nervous system (CNS)[16]. Type B is mainly characterised by mutations in the gene chromosome 9 open reading frame 72

(*C9orf72*), which presents a phenotypical overlap with ALS[5]. Types C and E are not associated with familial mutations but typically with sporadic FTD; and type D is linked to mutations in the gene *VCP*[17].

- FTLD-FUS (5-10% of the cases) is characterised by the co-aggregation of the RNA-binding protein fused in sarcoma (FUS), Ewing sarcoma protein and TATA-binding protein-associated factor 15 (TAF15)[8]. Three rare diseases are associated with FTLD-FUS, including atypical FTLD with ubiquitin inclusions, neuronal intermediate filament inclusion disease and basophilic inclusion body disease.

- FTLD-UPS is defined by the detection of proteins of the ubiquitin-proteasome system (UPS) and the absence of tau, TDP-43 and FUS inclusion bodies. This is caused by truncation mutations in the gene charged multivesicular body protein 2B (*CHMP2B*)[18].

On rare occasions, no inclusion bodies can be detected in patients, which are consequently classified as FTLD-ni (no inclusions).

1.1.3 Genetics of FTD

Familial cases account for 30% of the FLTD cases, with sporadic cases being responsible for the remaining 70% of the cases[1]. However, the heritability of the clinical phenotypes has shown variability from 48% in bvFTD patients to only 12% in PPA patients[19]. Autosomal dominant mutations in *GRN*, *C9orf72* and *MAPT* are responsible for the majority of inherited FTD. Of these, *C9orf72* is the most common genetic cause of FTD being present in 7%-12% of cases, followed up by *GRN* and *MAPT*, each of them causing 5-10% of all FTD[20] (Fig. 1.2). Over the years, other genes have been identified to cause FTD, including presenilin 1 (*PSEN1*), valosin-containing protein (*VCP*), charged multivesicular body protein 2B (*CHMP2B*), TAR DNA binding protein (*TARDBP*), FUS RNA binding protein (*FUS*), ubiquilin 2 (*UBQLN2*), sequestosome 1 (*SQSTM1*), triggering receptor expressed on myeloid cells 2 (*TREM2*), coiled-coil-helix-coiled-coil-helix domain containing protein 10 (*CHCHD10*), TANK-binding kinase 1 (*TBK1*), optineurin (*OPTN*), cyclin F (*CCNF*), and T cell–restricted intracellular antigen 1 (*TIA1*).

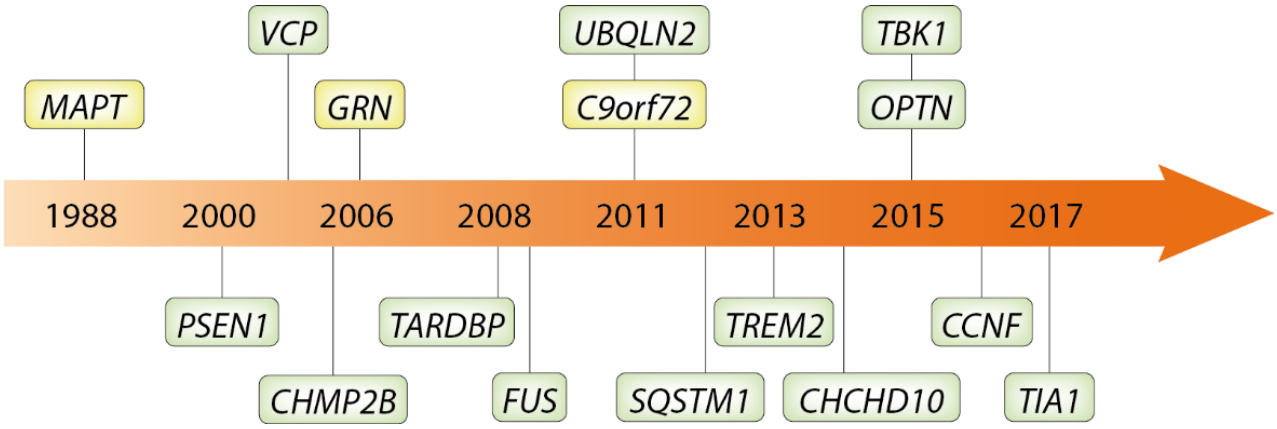

Figure 1.2 Timeline of frontotemporal dementia's gene discovery. *MAPT* (1988), *GRN* (2006) and *C9orf72* (2011) are the three main disease-causing genes (yellow). Other genes that cause FTD at a lower frequency are *PSEN1* (2000), *VCP* (2004), *CHMP2B* (2005), *TARDBP* (2008), *FUS* (2009), *UBQLN2* (2011), *SQSTM1* (2012), *TREM2* (2013), *CHCHD10* (2014), *TBK1* (2015), *OPTN* (2015), *CCNF* (2016), *TIA1* (2017) (green).

Age of onset varies across each genetic form of FTD. Whilst most cases with *MAPT* mutations have complete penetrance, both *GRN* and *C9orf72* mutations display age-related penetrance, with some cases in their 80s and 90s who are yet to develop symptoms[21]. The hexanucleotide G4C2-repeat expansion in *C9orf72* is the most common mutation causing FTD-ALS in Caucasian populations[5,22,23]. In *C9orf72* long expansion carriers, the relationship between the age of onset and the repeat expansion length still remains unclear[24]. However, a study identified that a polymorphism at rs9357140, containing two overlapping genes (*LOC101929163* and *C6orf10*), was associated with a decrease in the age of onset in GG carriers by 6 years in comparison to AA carriers[25].

There are no clear sex-related differences in the clinical diagnosis of FTD, although a recent study suggests that neurodegeneration needs to be more severe in women to produce similar behavioural and executive symptoms to those in men[26]. There is also geographical variability across different genes. For instance, mutations in *GRN* are predominant in the Basque country and Northern Italy[27,28], whereas 8% of the FTD patients in Sardinia are caused by a *TARDBP* mutations[29].

There are two major international collaborative studies: the Genetic FTD Initiative (GENFI) in Europe and Canada (http://www.genfi.org.uk/), and the Advancing Research and Treatment in Frontotemporal Lobar Degeneration (ARTFL) and Longitudinal Evaluation of Familial Frontotemporal Dementia Subjects (LEFFTDS) studies in the United States of America. These studies are playing an important role in elucidating and sharing detailed phenotype of both presymptomatic and symptomatic FTD mutation carriers, developing clinical trials and identifying clinical biomarkers[30].

In the quest to unravel the complexities of FTD and its various subtypes, the study of the gene *GRN* stands out as a critical focus. As highlighted, FTD poses significant challenges,

with limited therapeutic options available to mitigate its progression. Understanding the role of *GRN* mutations in the development of the pathogenesis is of paramount importance in our pursuit of effective treatments and diagnostic biomarkers. The following section will delve deeper into the significance of studying the gene *GRN* and explore its potential implications for the future of FTD research, the typical neuropathological profile and uncovered disease mechanisms.

1.2 Overview of progranulin-related frontotemporal dementia

1.2.1 The gene *GRN* and the identification of pathological mutations

The gene *GRN* is located on chromosome 17 at cytogenetic band 17q21, 1.7 Mb centromeric of the gene *MAPT* (Fig. 1.3)[16]. It consists of 12 protein-coding exons and a 5′ non-coding exon. In humans, the gene encodes for PGRN, a 593 amino acid long protein with a predicted molecular weight of 68.5 kDa.

The protein is composed of multiple tandem repeats of a highly conserved 12-cysteine granulin motif. Human PGRN contains seven and a half granulin domains. The granulin domains are named from the N-terminus of PGRN to the C-terminus: granulins p, G, F, B, A, C, D and E. The “p” domain is called paragranulin and only has the first 6 cysteines of a full domain, whereas the other granulin domains contain 12 cysteines. The structural and functional differences conferred by the cysteine composition are not clearly understood. Each granulin is encoded by two non-identical exons[31] and 11 folds into a prototypic structure consisting of β-hairpins stapled together by six disulphide bonds as revealed by 2-dimension nuclear magnetic resonance spectroscopy[32]. The proteases elastase, proteinase 3 and matrix metalloproteinase can cleave PGRN into the individual granulin peptides. Whether the biological activity is determined by the precursor, cleavage product or both is not clear.

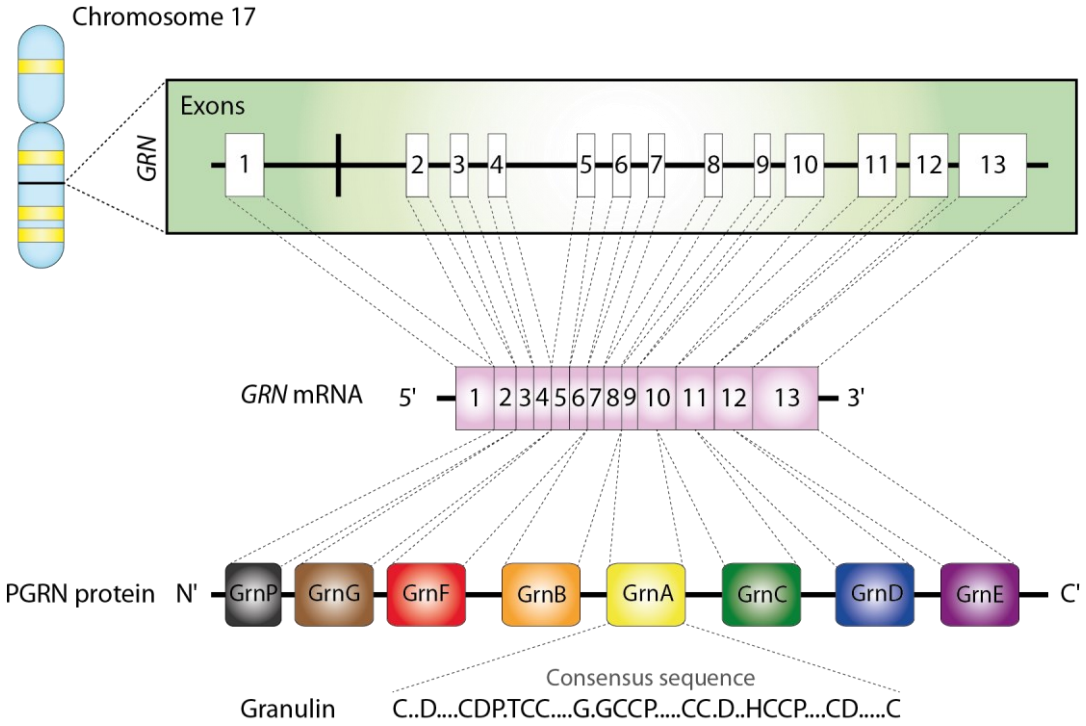

Figure 1.3 The chromosome 17, *GRN* gene, mRNA and PGRN protein structures.

In 2006, the identification of the first human *GRN* mutations linked to FTD marked a significant milestone[16,33]. Since then, over 170 *GRN* mutations have been identified in FTD patients (https://www.ftdtalk.org/what-is-ftd/genetics/grn-mutations/). The majority of these are nonsense and frameshift mutations that introduce premature stop codons, resulting in nuclear degradation of the mutant mRNA[34]. These mutations have led to *GRN*-linked neurodegeneration through a "loss-of-function" mechanism, which induces haploinsufficiency of the PGRN protein expression[35]. Other *GRN* mutations result in gene deletion[36], affecting the initiation of protein translation[37], production and secretion[38].

The clinical phenotypes associated with *GRN* mutations vary greatly among patients. The most common clinical manifestations are bvFTD and nfvPPA. Mild Parkinsonism is also found in some patients, and on certain occasions, clinical manifestations cannot be distinguished from Parkinson's disease (PD) or AD. Rarely, patients with *GRN* mutations can present motor neuron disease, CBS or PSPS.

In 2012, a study found homozygous *GRN* mutations in two siblings who had neuronal ceroid lipofuscinosis, a lysosomal storage disease[39]. Although it is not well understood how neuronal ceroid lipofuscinosis is related to FTD, this highlights the importance of the role of PGRN in lysosomes and its potential role in neuronal proteases.

1.2.2 Neuropathology of *GRN*-related FTD

GENFI and ARTFL/LEFFTDS studies, together with other individual studies, have made significant contributions to the characterisation of the phenotype across the lifespan of *GRN* mutation carriers, identifying potential biomarkers through fluid, imaging and cognitive profiling.

Two main fluid biomarkers have been proposed for *GRN*-related FTD: PGRN and neurofilament light chain (NfL). Low PGRN levels constitute a sensitive and specific marker to detect pathogenic *GRN* mutations[40]. These have been detected in blood, cerebrospinal fluid (CSF) and serum from presymptomatic genetic FTD patients[41]. This decrease has been reported from the earliest timepoint available during adulthood and has remained relatively stable over time. The recovery of the PGRN level to physiological standards can be used as a reference when evaluating disease-modifying clinical trials to treat *GRN*-mutation patients.

Increased NfL levels in blood and CSF are seen in *GRN*-related FTD, indicating axonal damage[42]. Its concentration reflects the intensity and progression of the disease, and longitudinal studies have reported a three-to-four-fold increase in CSF NfL after disease onset[43]. Although an increase in NfL has been observed in other neurological disorders, making an NfL change not exclusive to *GRN*-related FTD, its levels could be explored as a complementary biomarker during clinical trials.

Due to the role of PGRN in inflammation, the identification of neuroinflammatory biomarkers can expand the development of the pathology. For instance, increased levels of the soluble, anti-inflammatory TREM2 protein have been detected in the CSF of *GRN* mutation carriers[44]. Further exploration of other fluid biomarkers and brain morphological changes will contribute to the understanding of the PGRN disease mechanism, progression and survival, as well as monitor the success of clinical trials.

By employing imaging techniques, white matter abnormalities are the earliest change observed in *GRN* mutation carriers, occurring around 15 years prior to onset. This is followed by grey matter abnormalities, and then by white matter hyperintensities. In presymptomatic *GRN* carriers, grey matter atrophy is present about 10 years prior to symptom onset in the frontal, parietal, insular cortex and striatum[45]. Notably, an asymmetrical pattern of brain atrophy can be observed around 5 years prior to onset, but this difference is negligent at advanced stages[30].

Structural neuroimaging studies of genetic FTD have additionally demonstrated an increase in atrophy as the disease worsens, with *GRN* mutation carriers presenting faster rates of atrophy during the symptomatic period, and a more rapid change in volume loss, in comparison with other groups[46]. In addition, novel processing techniques enable the study of subregions within brain structures. A study looking at hippocampal subfield volume showed that the presubiculum and subiculum had the largest volume differences from controls[47]. In contrast to other genetic groups, white matter hyperintensities have been observed in *GRN* mutation carriers, with the frontal and occipital regions being the most affected[48]. This has been suggested to be due to white matter microglial activation and microglial dystrophy[49]. Finally, from a cognitive perspective, cognitive impairment has been observed around disease onset, generally alongside alterations in executive function and verbal fluency, which are characteristic phenotypes of FTD.

1.2.3 Disease-modifiers in *GRN*-related FTD

Potential factors modifying disease onset and disease risk in *GRN* mutations carriers have been identified. In 2010, the first genome-wide association (GWA) study in FTD identified common genetic variability in the gene transmembrane protein 106B (*TMEM106B*) which encodes for the type 2 transmembrane protein TMEM106B[50]. Single-nucleotide polymorphisms (SNPs) in the gene were strongly associated with *GRN* mutation carriers, denoting the gene *TMEM106B* as one of the most significant disease-modifying factors. The GDNF family receptor alpha 2 (*GFRA2*) has also been identified as a disease risk factor in *GRN* carriers[51].

Another GWA study in 2010 also found an association between the chromosome 1p13.3 sortilin locus with plasma PGRN levels, implicating sortilin as an important regulator of *GRN*[52]. Later in 2016, a GWA study discovered a significant association between plasma PGRN levels and SNPs on chromosome 10 at the prosaposin (*PSAP*) and cadherin 23 (*CDH23*) locus[53].

Gene and protein expression are also modified by factors beyond SNPs in genes. For instance, PGRN expression can be regulated by miRNAs, post-transcriptional regulators of gene expression, as observed in brains from patients diagnosed with *GRN*-related FTD[54–56]. In addition, increased methylation of the *GRN* promoter has been reported in peripheral blood mononuclear cells and brains of *GRN* mutation carriers[57,58], suggesting that methylation could also play a disease-modifying role. An increased understanding of the genetic aetiology of FTD will facilitate the characterisation of pathology mechanisms and the identification of potential therapeutic strategies.

1.2.4 *GRN*-related disease mechanisms

PGRN is capable of modulating multiple biological pathways (Fig. 1.4) and its pleiotropic function has led to the protein being given different names across literature, including PC cell-derived growth factor (PCCDF), acrogranin, proepithelin, granulin-epithelin precursor and epithelial transforming growth factor[59–62]. The nomenclature *GRN* for the gene and PGRN for the protein were used in this thesis. Some of the most relevant functions of PGRN are lysosomal homeostasis regulation, neuroinflammation, microglial regulation, nerve regeneration promotion and cell proliferation and death.

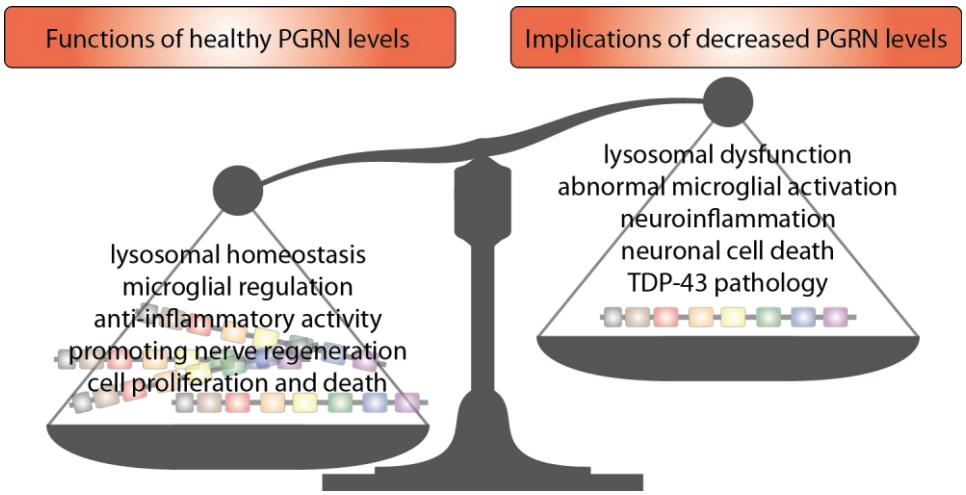

Figure 1.4. Roles of PGRN in the human body.

PGRN has been suggested to play a role in the function and formation of lysosomes. For instance, for unknown reasons, PGRN deficiency leads to an increase in the transcriptional activity of TFEB, which is the master regulator of lysosomal biogenesis[63]. In addition, the promoter of *GRN* contains TFEB binding sites[63]. As a consequence, PGRN impairment can lead to lysosomal defects. TFEB altered transcription has additionally been reported to affect mitochondrial quality control and biogenesis pathways during early lysosome dysfunction as a compensatory mechanism[64], suggesting a potential mechanism linking PGRN, lysosomes and mitochondria.

The involvement of PGRN in inflammation has been largely described. PGRN is involved in wound healing, increasing the accumulation of neutrophils, macrophages, blood vessels, and fibroblasts in the wound[65]. PGRN has also been described as a ligand and antagonist of the inflammatory cytokine tumour necrosis factor (TNF) receptors[66]. Interestingly, full-length PGRN plays an anti-inflammatory role, whereas granulins are pro-inflammatory[67]. At a cellular level, PGRN plays an inhibitory role in excessive microglial activation[49]. Microglia are the immune cells of the CNS, regulating brain inflammation and infections. The loss of PGRN can therefore lead to activated microglia, which consequently releases complement proteins and pro-inflammatory cytokines with downstream consequences, including lysosomal defects, cellular stress and TDP-43 proteinopathy[68].

PGRN is a growth modulating factor involved in the promotion of nerve regeneration and brain development. More specifically, the protein stimulates adult neurogenesis in the dentate gyrus of the hippocampus[69], the proliferation of PC-12 (rat adrenal gland pheochromocytoma)[70] and male-specific brain differentiation[71]. PGRN has also been shown to regulate neurite outgrowth and enhance neuronal survival[72,73]. In a study using primary neuronal culture, the knockout of *GRN* led to a decrease in neurite outgrowth and branching, and the overexpression of PGRN was able to rescue the phenotype, confirming the growth factor role of PGRN[74].

Overall, investigating the pathological phenotype of *GRN* mutations across biological processes, such as the interface with mitochondrial function, is important for understanding the disease and developing therapeutic strategies. Although there is increasing evidence that mitochondrial dysfunction is involved in other genetic types of FTD, especially related to *C9orf72* and *MAPT* mutations, little is known whether PGRN haploinsufficiency affects the role of mitochondria. Therefore, this thesis focused on the gene *GRN* to elucidate whether mitochondrial dysfunction plays a role in *GRN*-related FTD.

1.2.5 *GRN* expression across tissues and cell types

GRN is expressed in many tissues and cell types throughout the body[70]. This includes both the CNS and peripheral tissues, including cell types like fibroblasts which will be used in this thesis. Based on the Human Protein Atlas, *GRN* expression does not majorly differ between the different brain regions. While FTLD-*GRN* primarily affects the frontal and temporal lobes of the brain, the distribution of *GRN* expression across other brain regions explains how the pathological changes can also extend beyond the two main regions and involve other brain areas to varying degrees.

At a single cell level in the CNS, *GRN* is preferentially expressed by neurons and microglia. In murine models, the depletion of PGRN resulted in severe microglial pathology, highlighting the role of the protein in neuroprotection and neuroinflammation[75]. Interestingly, when comparing these two cell types, the expression of *GRN* mRNA is >50-fold enriched in microglia compared to neurons[76]. It is therefore important to note the importance of neuronal-microglial crosstalk when investigating progranulin biology.

1.3 Meet the star of the show: mitochondria

Mitochondria are membrane-bound cell organelles that conduct an orchestra of cellular roles regulating bioenergetics, metabolism and homeostasis. Their well-known role in generating around 90% of the cellular energy has coined mitochondria as the “powerhouse of the cell”[77]. However, the identification of the involvement of mitochondrial dysfunction in disease has expanded the characterisation of mitochondrial biology. This has been reflected in the compendium of literature and how the roles of mitochondria extend to Ca^{2+} homeostasis, haem biosynthesis, antioxidant defence, vitamin and cofactor metabolism, apoptosis defects, inter-organellar interactions, the immune system, stem cell regulation and DNA repair (Fig. 1.5)[78–80]. An introduction to mitochondrial history, biology and functions relevant to this thesis will be described in this section.

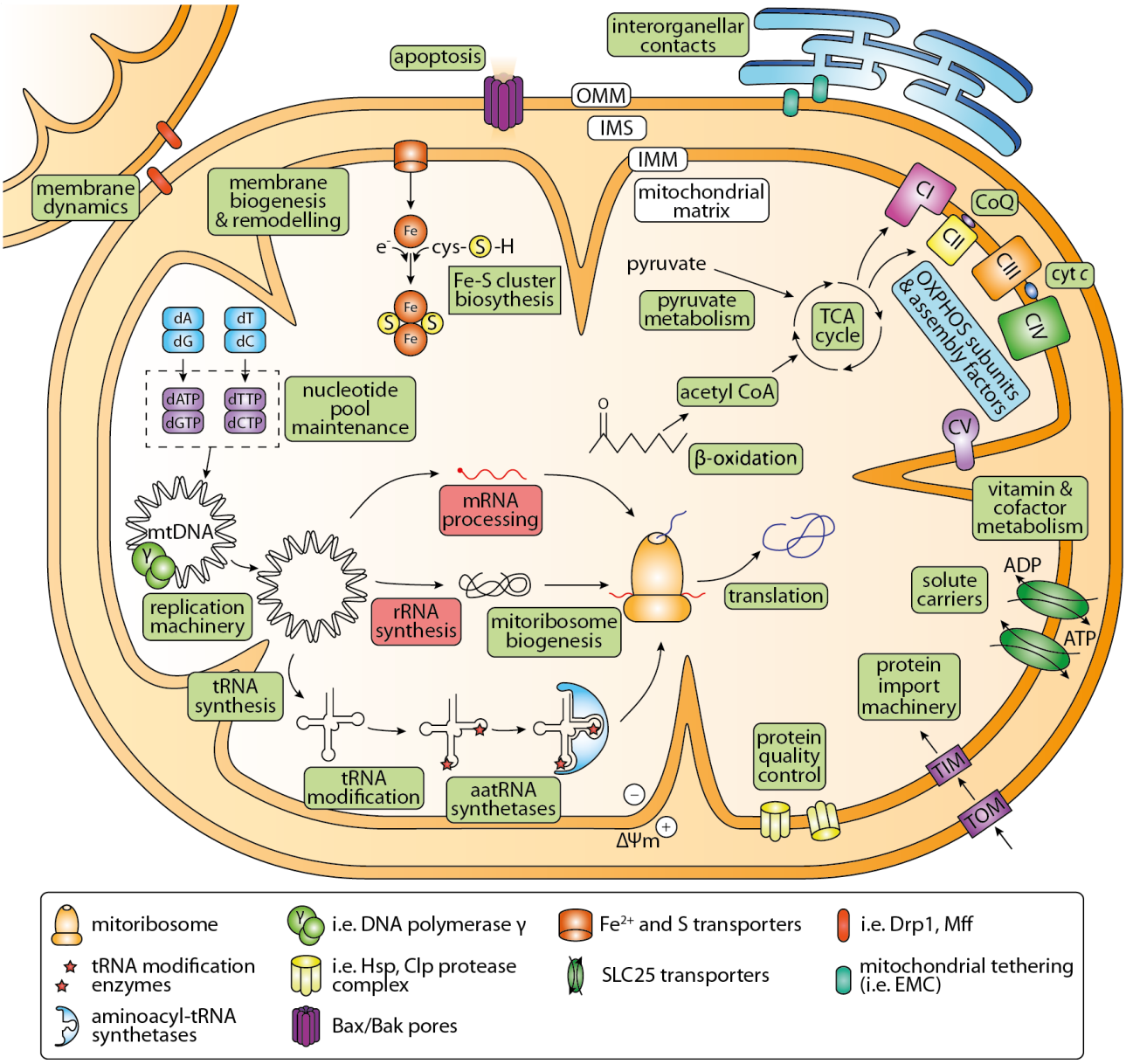

Figure 1.5 Schematic representation of mitochondrial biology. Abbreviations: aatRNA, aminoacyl-tRNA; CoQ, coenzyme Q_{10}; cys, cysteine; Cyt *c*, cytochrome *c*; dATP, deoxyadenosine triphosphate; dCTP, deoxycytidine triphosphate; dGTP, deoxyguanosine triphosphate; dNs (dA, dG, dT and dCTP), deoxynucleosides; dTTP, deoxythymidine triphosphate; Fe, iron; H, hydrogen; IMM, inner mitochondrial membrane; IMS, inner mitochondrial space; mRNA, mature RNA; mtDNA, mitochondrial DNA; OMM, outer mitochondrial membrane; rRNA, ribosomal RNA; S, sulphur; tRNA, transfer RNA; ΔΨm, mitochondrial membrane potential.

1.3.1 The history behind mitochondria

The first observations of intracellular structures representative of mitochondria date back to the 1840s, when physiologist Albert von Kolliker even suggested that these had membranes[81]. In 1890, the pathologist Richard Altmann established them as cell organelles and called them “bioblasts” which appeared ubiquitous throughout the cell[82]. He proposed that bioblasts originated from parasites and had their independent metabolic processes. The microbiologist Carl Benda would later coin the term “mitochondrion” in 1898 derived from the Greek terms μίτος (mitos), meaning "thread", and χονδρίον (chondrion), meaning "granule"[83].

In the first century of mitochondrial discovery, most of the work aimed to understand the bioenergetics role of mitochondria. In 1912, Kingsbury suggested these organelles were involved in cell respiration, although this was exclusively based on morphological observations. It was later in the 1920s when queer-icon physiologist Otto Heinrich Warburg elucidated the nature and mode of action of a so-called “respiratory enzyme” named *Atmungsferment* based on experimental work using extracts of guinea-pig liver[84]. The disentangling of the mitochondrial oxidative phosphorylation (OXPHOS) system culminated as a result of structural and biochemical observations due to advances in fractioning and spectrophotometric methods[85]. Some of the highlights included elucidating the process of cellular respiration using one oxygen molecule to form two adenosine triphosphate (ATP) molecules, Lipmann’s concept of the role of phosphate bonds in cellular conversion[86], and Claude’s structural identification of cytochrome *c* and other OXPHOS enzymes. The outstanding question still remained as to the exact mechanism underpinning the transfer of electrons. The answer laid in 1978 Nobel laureate Peter Michell’s work in chemiosmosis, where an electrochemical gradient was formed in the inner membrane, and protons pumped through the ATP synthase complex synthesised ATP from adenosine diphosphate (ADP)

and inorganic phosphate[87]. The working mechanism of ATP synthase was later further clarified by Boyer and Walker, who won the Nobel Prize in Chemistry in 1997[88,89]. Overall, these discoveries led to the cell biologist Philip Siekevitz coining the popular term “powerhouse of the cell” in 1957, which is still being used in our current times when referring to mitochondria[90].

Up until the 1950s, early scientists had used the redox Janus Green dye to stain mitochondria and foresight conclusions about mitochondrial structure and functions. Early theories, despite later being proven, postulated mitochondria as a reducing site required for respiration and as a “bearer of genes”[91,92]. It was not until 1952 when the first high-resolution micrographs replaced the Janus Green stains, enabling a more detailed analysis of the mitochondrial structure[81]. This confirmed the membrane surrounding the organelle, and additionally the discovery of the inner mitochondrial membrane (IMM) which folds up in ridges and the variation of the mitochondrial size and shape between different cells.

A new era of mitochondrial biology developed with the discovery of the mitochondrial genome in yeast models[93]. The development of methods for mapping the mitochondrial genes enabled the full sequence of the mitochondrial genome in 1981 and the discovery of mitochondrial ribosomes, also known as mitoribosomes[81,94]. This led to the development of theories that the mitochondrial genome was inherited in a bacterial fashion, which would lead to the postulation of the endosymbiotic theory. This stated that mitochondria descend from specialised bacteria that got engulfed by the early ancestors of today’s eukaryotic cells and survived the process of endocytosis[95], partially giving mitochondria its unique morphology.

1.3.2 Mitochondrial membrane and structure

Mitochondria are ubiquitous, double membrane-bound cell organelles, ranging between 0.75 and 3 μm^2 in size[96]. The outer mitochondrial membrane (OMM) contains pore-forming membrane proteins, known as porins, which facilitate the movement of ions and small, uncharged molecules into and out of the mitochondrion. Any larger molecules, especially proteins, are imported by special translocases. On the other hand, the IMM presents a tight diffusion barrier for ions and molecules (e.g., ATP, ADP and small metabolites). This is regulated by highly specific, membrane-embedded transport proteins. The selectivity of ions or molecules in the inner membrane requires an electrochemical membrane potential ($\Delta\Psi m$) of about 180 mV, which is generated by the complexes of the OXPHOS process. The inner and outer membranes are separated by the intermembrane space (IMS), a ~20 nm gap. The space within the inner membrane is known as the matrix, where several biological processes take place including the tricarboxylic (TCA) cycle, fatty acid oxidation and mitochondrial genome maintenance. The pH of the matrix is high at 7.9 to 8, which is needed to maintain the trans-membrane electrochemical gradient that drives ATP gradient[97]. Finally, the inner membrane forms invaginations, called cristae, that extend into the matrix and increase the surface area available to produce energy through the OXPHOS process.

The import of roughly 90% of the nuclear-encoded mitochondrial proteins require the recognition of positively charged mitochondria-targeting sequences (MTS) at the N-terminal signal sequence. The transport of proteins into the mitochondria is regulated by protein translocases of the outer (TOM) and inner (TIM) membrane that can form a TOM/TIM supercomplex spanning the intermembrane space. Briefly, the TOM complex is formed by TOM20, TOM22 and TOM70 receptors, which recognise and bind to the positively charged MTS. The pre-peptide is then channelled through the protein TOM40[98]. If pre-peptides are destined to the IMM or the matrix, the MTS will be recognised by TIM50 and TIM17 and

channelled by TIM23[99]. The TIM complex is supported by the pre-sequence translocase-associated motor which contains HSP60 and other chaperones to translocate pre-proteins into the matrix by ATP hydrolysis and proton gradient[100]. An alternative translocase TIM22 regulates the translocation of multiple domain-containing transmembrane proteins such as OXPHOS proteins[101].

Lipids are fundamental for the structural and functional integrity of mitochondrial membranes. Comprising the mitochondrial bilayers, lipids provide stability, fluidity and flexibility, shaping the intricate network of these essential organelles. Without these lipid components, the structural and functional integrity of mitochondria would be compromised, impacting overall cellular health and vitality.

Mitochondria are capable of synthesising different phospholipids, including phosphatidic acid (PA), phosphatidylglycerol (PG), cardiolipin (CL), and phosphatidylethanolamine (PE). CL is particularly considered to be the signature mitochondrial phospholipid, constituting approximately 15-20% of the total mitochondrial phospholipid content. CL has been associated with a wide range of functions, such as bioenergetics, mitochondrial dynamics, membrane architecture, apoptosis, mitophagy and protein import[100,102,103]. In mammals, the *de novo* CL biosynthesis is a multi-step process that takes place within the IMM and which is illustrated in Fig. 1.6.

Overall, phosphatidic acid is transported from the endoplasmic reticulum into mitochondria, where it is catalysed by several enzymatic reactions which catalyse the formation of premature CL (pCL). This is then remodelled into the transient intermediate phospholipid, monolysocardiolipin (MLCL), which is re-acylated by tafazzin (TAZ) to generate mature CL with its characteristic four acyl chains.

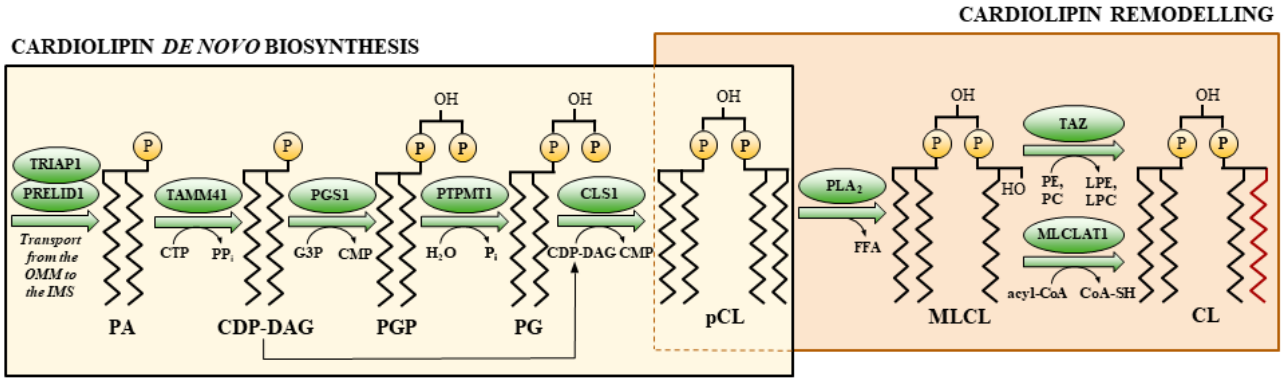

Figure 1.6 Biosynthesis and remodelling pathways of cardiolipin. Abbreviations: Acyl-CoA, acyl-coenzyme A; CDP-DAG, cytidine diphosphate-diacylglycerol; CL, cardiolipin; CLS1, CL synthase; CMP, cytidinemonophosphate; CoA-SH, coenzyme A (unconjugated); CTP, cytidinetriphosphate; FFA, free fatty acid; G3P, glycerol-3-phosphate; H_2O, water; IMS, intermembrane mitochondrial space; LPC, lyso-phosphatidylcholine; LPE, lyso-phosphatidylethanolamine; MLCL, monolysocardiolipin; MLCLAT1, monolysocardiolipin acyltransferase 1; OMM, outer mitochondrial membrane; PA, phosphatidic acid, PC, phosphatidylcholine; pCL, premature CL; PE, phosphatidylethanolamine; PG, phosphatidylglycerol; PGP, phosphatidylglycerol phosphate; PGS1, phosphatidylglycerol phosphate synthase; P_i, inorganic phosphate; PLA_2, phospholipase A2; PP_i, inorganic pyrophosphate; PRELID1, PRELI Domain Containing 1; PTPMT1, protein-tyrosine phosphatase mitochondrial 1; TAMM41, TAM41 mitochondrial translocator assembly and maintenance homolog; TAZ, tafazzin; TRIAP1, TP53 regulated inhibitor of apoptosis 1 (obtained from Bautista, 2023[104]).

CL exists with a diverse array of acyl-chain compositions that exhibit variations in chain length and saturation. Alterations in the molecular conformation of CL can offer valuable insights into issues related to impaired CL synthesis and remodelling[105], shedding light on disease pathophysiology. An increasing body of evidence has linked abnormalities in CL metabolism and content to human diseases, including neurodegeneration[106], cancer[107], and cardiovascular and metabolic disorders[108]. Understanding the full spectrum of tissue-specific CL acyl chains is of utmost importance for advancing analytical assays and interpreting changes in CL composition under pathological circumstances.

1.3.3 The mitochondrial genome

Mitochondria have their own DNA (mtDNA) which contains 16,569 base pairs in length. The human mitochondrial genome is maternally inherited, and it comprises 37 genes that encode for 13 mitochondrial proteins, 2 ribosomal RNAs (rRNAs) and 22 transfer RNAs (tRNAs) (Fig. 1.7)[109]. It has a circular shape with two strands distinguished as the heavy strand and the light strand. The heavy strand contains 28 genes, encoding for 12 proteins, 2 rRNAs and 14 tRNAs; whereas the light strand contains the remaining 9 genes, encoding for the protein MT-ND6 and 8 tRNAs[110,111]. The prevalence of maternally inherited pathogenic mtDNA variants is estimated to be one in every 500 births[112], which are caused by either germline inheritance, intrinsic ageing or external factors, such as foreign chemical products in healthy individuals[113].

In addition to mitochondrial-encoded proteins, the nuclear genome plays an important role in coding mitochondrial-localised proteins. It has been estimated that around 1,500 nuclear and mitochondrial genes are needed for mitochondrial function. An inventory of 1,136 human and 1,140 mouse genes encoding for proteins with strong evidence of mitochondrial localisation has been catalogued in the MitoCarta 3.0 compendium[114]. The dual genomic localisation and the large number of genes responsible for mitochondrial dysfunction mean that they can present multiples modes of inheritance: maternal (related to mtDNA), X-linked, autosomal dominant or recessive, or sporadic (*de novo*).

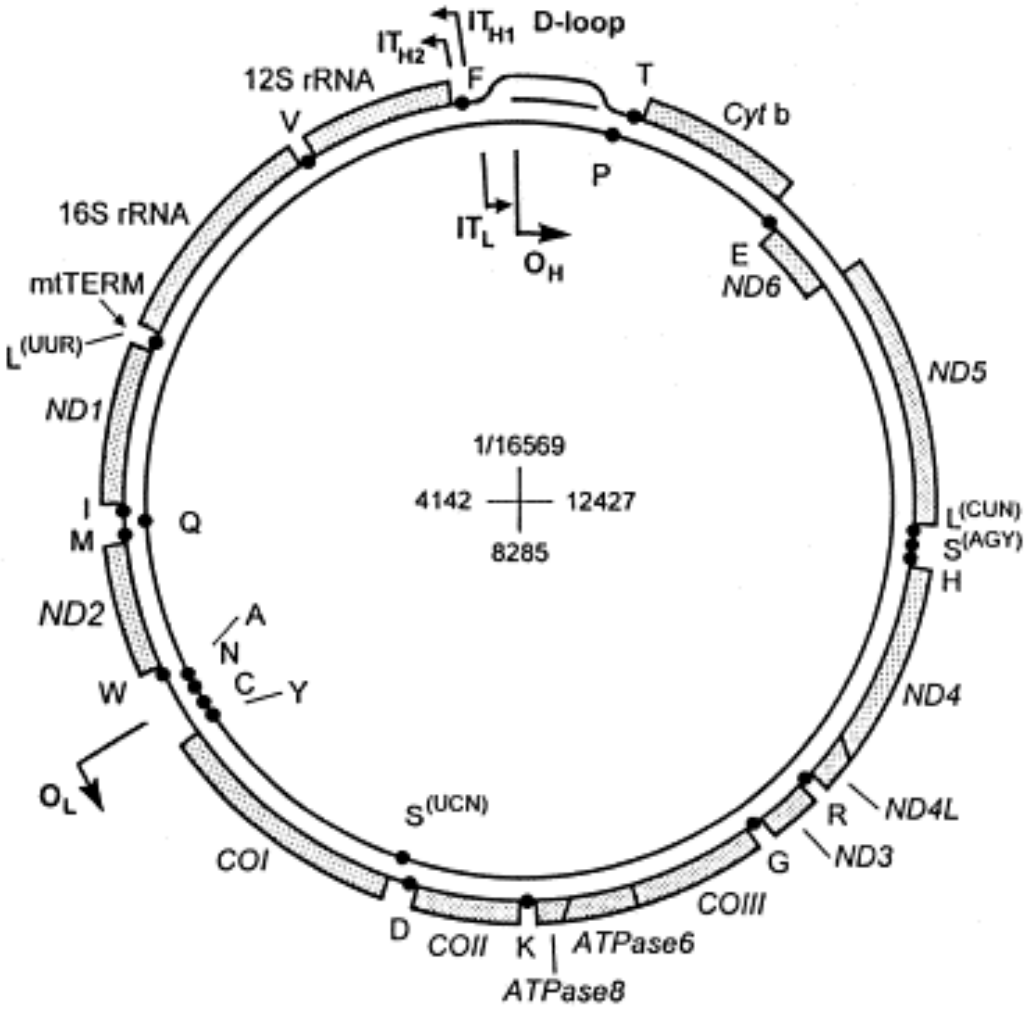

Figure 1.7 Map of the human mitochondrial genome. The outer circle represents the H-strand and the inner circle represents the L-strand. The genes encoding for 13 mitochondrial proteins and 2 rRNAs are depicted by shaded boxes. The 22 tRNA genes are depicted by dots, the single letter code of their amino acids and their codon sequence if carrying serine or leucine (obtained from Taanman, 1999[109]).

The regulation of mitochondrial molecular genetics through mtDNA maintenance, transcription and translation is essential for mitochondrial survival and function.

Mitochondrial DNA maintenance

A balanced pool of the building blocks deoxyribonucleotide triphosphates (dNTP) is necessary for the maintenance of the mtDNA. The supply of the mitochondrial dNTP pool is mostly dependant on the mitochondrial nucleotide salvage pathway. This pathway recovers pre-existing deoxynucleosides during the degradation of DNA and RNA, and converts them into dNTPs in the mitochondrial matrix. The first step in the phosphorylation of pyrimidine deoxyribonucleoside is carried out by the mitochondrial thymidine kinase 2 (*TK2*). The function of this enzyme is to phosphorylate deoxycytidine and thymidine to generate deoxycytidine monophosphate (dCMP) and thymidine monophosphate (TMP), respectively. There are also specific transporters that can import cytosolic nucleosides and nucleotides into the mitochondrial matrix, contributing to the available pool of dNTPs.

The maintenance of mtDNA depends on a series nuclear-encoded proteins that have a role in the mtDNA replication machinery and the nucleotide pool maintenance. The mtDNA machinery, also known as the replisome, is formed by a series of enzymes including the DNA polymerase ɣ (*POLG* and *POLG2*), the TWINKLE helicase (*TWNK*), mitochondrial topoisomerase I, mitochondrial RNA polymerase, RNase H1 (*RNASEH1*) and the mitochondrial genome maintenance exonuclease 1 (*MGEM1*).

Mitochondrial DNA transcription and translation

The transcription of mtDNA originates in the heavy strand and light strand promoters. As a summary, transcription initiation is driven by a DNA-dependant RNA polymerase called POLRMT in association with mitochondrial transcription factor A (TFAM) and mitochondrial transcription factor B2 (TFB2M). TFAM also plays a role in packing mtDNA into supramolecular assemblies called nucleoids, of which there are about 1000 per cell[115,116]. Nucleoids are roughly spherical, have a diameter of around 100 nm, which each containing a copy of mtDNA[117]. Transcription initiation is followed by transcription elongation in coordination with the transcription elongation factor (TEFM), and finally by transcription termination that is majorly regulated by a mitochondrial termination factor 1 (MTERF1)[118].

The process of mitochondrial translation involves mitochondrial tRNAs, aminoacyl-tRNA synthetases (ARSs), tRNA modification enzymes, mRNA processing and mitoribosomes. Mitochondrial tRNAs help to decode mRNA sequences from the mtDNA into a protein, which are necessary to encode the 13 essential subunits of the OXPHOS complex. ARSs are enzymes that catalyse the attachment of the appropriate amino acid onto its cognate tRNA, and any further tRNA modulation may be carried out by tRNA modification enzymes.

The last step of protein translation occurs in the mitoribosomes. These are attached to the inner membrane in humans to facilitate the co-translational integration of highly hydrophobic nascent polypeptides. Mitochondrial rRNAs (*MT-RNR1* and *MT-RNR2*) and nuclear-encoded genes are required to synthesise the mitoribosomal protein subunits, assembly and recycling factors, and translation initiation, elongation and termination factors.

1.3.4 Oxidative phosphorylation and other bioenergetic pathways

Bioenergetics is considered the main function of mitochondria, leading to the generation of ATP through the process of OXPHOS. Other bioenergetic pathways taking place in the mitochondria include the TCA cycle, fatty acid oxidation and antioxidant biosynthesis.

The OXPHOS system

The OXPHOS complex in humans, which is highly preserved during evolution, is located in the IMM. It consists of five enzyme complexes alongside the mobile electron carriers Coenzyme Q_{10} (CoQ_{10}) and cytochrome *c*. As proposed in Mitchell's chemiosmotic hypothesis, a proton-motive force is generated by the transfer of electrons from complexes I to IV, also known as the electron transport chain (ETC). This enables the complex V, an ATP synthase enzyme, to catalyse the phosphorylation of ADP to ATP in a process known as chemiosmosis. A visual representation of the OXPHOS system can be found in Figure 1.8.

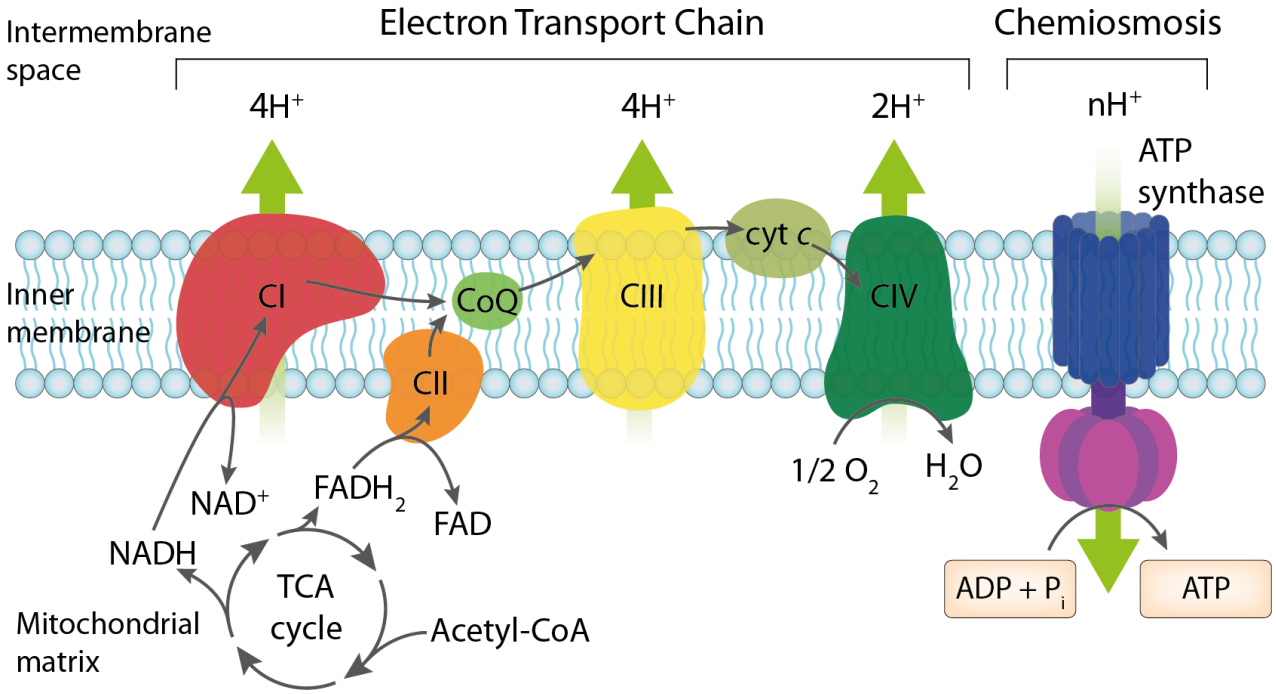

Figure 1.8 Mitochondrial oxidative phosphorylation process. Abbreviations: ADP, adenosine diphosphate; ATP, adenosine triphosphate; CI, complex I; CII, complex II; CIII, complex III; CIV, complex; CoQ, coenzyme Q_{10}; cyt c, cytochrome *c*; FAD(H_2), flavin adenine dinucleotide (hydrogen); H^+, proton; H_2O, water; n, number; NAD(H), nicotinamide adenine dinucleotide (hydrogen); P_i, phosphate; TCA, tricarboxylic acid cycle.

Complex I (CI), also known as NADH:ubiquinone oxidoreductase, consists of 45 subunits and is approximately 1 MDa. The essential energy transduction involves fourteen “core” subunits, divided into two domains. Seven subunits, referred to as ND subunits, are encoded by the mitochondrial genome and comprise the hydrophobic Q-module. The other seven core subunits are nuclear-encoded and constitute the hydrophilic matrix-facing N-module. A third module known as the P-module pumps protons across the IMM[119]. The remaining 31 subunits are nuclear-encoded, with 26 of them being crucial for maintaining CI stability[120]. Assembly of the complex follows a sequential process, commencing with the assembly of the Q-module, followed by the P-module, and concluding with the incorporation of the N-module. CI operates by oxidizing reduced nicotinamide adenine dinucleotide (NADH), a reducing by-product of the TCA cycle. NADH is the main donor of electrons in the mitochondria and the oxidation/reduction process of $NADH/NAD^+$ is as follows:

$$NADH + H^+ + CoQ + 4\ H^+_{(in)} \rightleftharpoons NAD^+ + CoQH^{2+} + 4\ H^+_{(out)}$$

The flavin group of NADH binds to the tip of the N-module and undergoes oxidation. Subsequently, two electrons are transported through a series of iron-sulphur clusters[121], reducing ubiquinone to ubiquinol and facilitating the pumping of four protons across the IMM per molecule of NADH[122]. CI exhibits reversible activity, allowing it to utilize the proton-motive force to convert NAD^+ back to NADH, a crucial process for regulating the cellular NAD^+/NADH ratio. CI is also the main generator of reactive oxygen species (ROS) by reducing molecular oxygen to the superoxide radical, which affects not only mitochondrial disorders but also a wide spectrum of health and disease areas, including neurodegenerative disorders[123], ischemia/reperfusion injury[124] and ageing[125].

Complex II (CII), known as Succinate-CoQ oxidoreductase, consists of four nuclear-encoded subunits. The first two subunits are a flavoprotein (SDHA) and an iron-sulphur protein (SDHB), which form a hydrophilic head; and the two others are hydrophobic membrane anchor subunits, SDHC and SDHD. SDHB contains three iron-sulphur clusters, whereas SDHC and SDHD contain one haem b group and a ubiquinone-binding site. CII operates by oxidising reduced succinate, another reducing agent formed during the TCA cycle. The oxidation/reduction process of succinate/fumarate is as follows:

$$Succinate + CoQ \rightleftharpoons Fumarate + CoQH_2$$

CII oxidizes succinate to fumarate using flavin adenine dinucleotide (FAD) as a cofactor within the SDHA subunit, which houses the enzyme's active site. The flavin group accepts two electrons, which then migrate along the iron-sulphur clusters in the SDHB subunit to reduce ubiquinone to ubiquinol. Due to the lower energy of electrons from $FADH_2$, CII does not contribute to proton pumping across the IMM. Metabolic alterations to CII subunits have

wider implications on cellular processes, ranging from mitochondrial diseases to neurodegenerative diseases and tumours[126–128].

Both CI and CII donate their electrons to CoQ_{10} which transfers the electrons to CIII. Other roles of CoQ_{10} include acting as an antioxidant to remove free radicals, inhibiting lipid peroxidation, and aiding in the generation of the antioxidant α-tocopherol, a type of vitamin E[129].

Complex III (CIII), also known as coenzyme Q:cytochrome *c* oxidoreductase, encompasses 11 subunits, including the respiratory subunits cytochrome *b*, cytochrome *c1*, and an iron-sulphur cluster known as the Rieske iron-sulphur protein (RISP). The mitochondrial gene *MT-CYB* encodes cytochrome *b*, which contains two haem groups crucial for electron transfer within the complex. Upon assembly, CIII promptly forms dimers, which are considered the functional units of the enzyme. Electron transfer through CIII occurs via the Q cycle, involving the oxidation of two ubiquinol molecules from CI and CII in divergent electron transfer steps. Overall, CIII oxidizes CoQ_{10} and reduces cytochrome *c*, releasing a total of four protons into the IMS.

$$CoQH_2 + 2\ \text{cyt}\ c\ (Fe^{3+}) + 2\ H^+_{(in)} \rightleftharpoons CoQ + 2\ \text{cyt}\ c\ (Fe^{2+}) + 4\ H^+_{(out)}$$

Additionally, CIII has dual roles as an electron transducer and as a regulator and producer of ROS. Crucially, CIII can form and release superoxides into the cytosol, which is thought to play a role in ageing as part of the free radical theory of ageing[130]. Mutations in CIII-related genes have been associated with exercise intolerance[131], septo-optic dysplasia[132] and multisystem disorders[133].

Cytochrome *c* is another mobile electron carrier that transfers electrons between CIII and complex IV. The haemprotein is capable of undergoing oxidation and reduction, conferring

it antioxidant properties[134]. Cytochrome *c* also plays a role in apoptosis when released from the mitochondrial to the cytosol[135].

Complex IV (CIV), known as cytochrome *c* oxidase (COX), belongs to the haem-copper oxidase superfamily, a group of proton-pumping enzymes. CIV consists of 14 subunits, with three core catalytic subunits encoded by mtDNA (*MT-CO1*, *MT-CO2*, and *MT-CO3*). The complex contains two haem groups, called haem *a* and haem a_3, and two copper centres[136]. The catalytic subunits facilitate the oxidation of cytochrome *c* to reduce molecular oxygen, leading to the recruitment of two protons from the matrix to form a water molecule:

$$2 \text{ cyt } c \ (Fe^{2+}) + 2\ H^+ + ½\ O_2 + 2\ H^+_{(in)} \rightleftharpoons 2 \text{ cyt } c \ (Fe^{3+}) + H_2O + 2\ H^+_{(out)}$$

Due to the high amount of potential energy in the CIV, dysfunctional COX has been linked to mitochondrial disease[137], neurodegenerative disease[138], and ageing[139].

Finally, the proton-motive force generated across the ETC enables the generation of ATP in complex V (CV), known as F_1F_0 ATP-synthase. CV consists of two subcomplexes that synthesize ATP through rotary catalysis. The F_0 subcomplex serves as a proton pore, generating torque that allows the catalytic F_1 subcomplex to synthesize ATP. CV catalyses the conversion of ADP to ATP, the primary energy currency of the cell, as follows:

$$ADP + P_i + 3H^+_{(out)} \rightleftharpoons ATP + H_2O + 3\ H^+_{(in)}$$

While two components of the peripheral stalk are mitochondrial-encoded, the remaining subunits and assembly factors are nuclear-encoded. CV defects have been associated with ATP deficiency and pathogenic events, including cardiovascular[140], neurodegenerative[141,142] and neurocognitive diseases[143].

Mitochondrial supercomplexes theory

Although the complexes were individually described, mitochondrial complexes assemble in larger, supramolecular structures known as supercomplexes or respirasomes that do not follow a canonical structure. A traditional fluid model was originally considered where individual complexes were dispersed across the IMM. Then in 1955, the first theory of supercomplexes was stated[144], which was later supported by independent experiments isolating supercomplexes from bacteria and yeast[145,146].

The most reported supercomplexes are Complex I/III, Complex I/III/IV, and Complex III/IV. The trigger leading to respiratory enzymes appearing in their free-floating form or as part of supercomplexes remains unclear. One of the main hypotheses for respirasome formation involved the lipid composition of the membranes, especially the presence of the mitochondrial lipid CL[147]. Another hypothesis states that the mitochondrial membrane potential mediates the assembly or disassembly of supercomplexes[148].

Their physiological role is still being characterised, with several studies suggesting that their organised structures reduce oxidative damage and increase metabolism efficiency. For instance, Schäfer and colleagues demonstrated that CI and CIII presented a higher activity in the supercomplex I/III/IV than in the supercomplex I/III due to the presence of CIV[149]. In addition, supercomplexes enable the stabilisation of CI as observed by the destabilising effect on CI due to mutations in either CIII or CIV[148].

The TCA cycle feeding OXPHOS

The TCA cycle is comprised by a series of chemical reactions that release stored energy. This metabolic pathway requires fuel sources to maintain the TCA cycle, such as acetyl-CoA, pyruvate and fatty acids. This leads to a chain of enzymatic reactions creating by-products like citrate and succinate. Two of the main metabolic coenzymes are reduced nicotinamide adenine dinucleotide (NADH) and flavin adenine dinucleotide ($FADH_2$), which are transported to the ETC for the donation of electrons to the complexes and proton pumping out of the matrix.

Downstream effects of impaired TCA cycle metabolites can cause defects in chromatin modification, DNA methylation and post-translational protein modification[150]. This has been reflected on alterations of the cell function and fate, which have linked mitochondria to the immune system and oncogenesis[151]. Although this mechanism is not fully understood, it is hypothesised that metabolic impairments may be sensed as hypoxia, which would trigger the activation of growth-promoting transcriptional pathways.

1.3.5 Mitochondrial quality control

Whilst mitochondria are essential for cell survival and metabolic regulation, mitochondrial dysfunction causes respiratory defects, ROS accumulation, pro-apoptotic molecules, and eventually death. Mitochondria have therefore developed intricate quality control mechanisms to counteract mitochondrial defects and maintain cellular homeostasis. These mechanisms encompass mitochondrial biogenesis, proteostasis, dynamics and mitophagy.

Mitochondrial biogenesis

The process of mitochondrial biogenesis is important to generate a new pool of mitochondria and regulate OXPHOS, maintaining a delicate equilibrium to replace defective ones. The pathway of mitochondrial biogenesis is coordinated by the peroxisome proliferator-activated receptor γ coactivator-1α (PGC-1α) and nuclear receptors[152]. PGC-1α induces the nuclear respiratory factor 1 and 2 (NRF1 and NRF2), and subsequently the activation of TFAM, which is involved in the replication and transcription process of mtDNA as previously described[153]. Hence, PGC-1α is commonly referred to as the master regulator of mitochondrial biogenesis and the mitochondrial biogenesis pathway is synthesised as PGC-1α-NRF-TFAM which is essential for the synthesis of mtDNA, proteins and new mitochondria.

Other upstream factors regulate PGC-1α and biogenesis, including NAD-dependent deacetylase sirtuin 1 (SIRT1), AMP-activated kinase (AMPK), and the transcription factor cAMP-response element-binding protein (CREB)[154–156]. Interestingly, AMPK may activate PGC-1α by direct phosphorylation or by indirect stimulation of SIRT1[157]. Therefore, the AMPK–SIRT1–PGC-1α axis is considered pivotal to maintain a healthy pool of mitochondria under stressful conditions.

Mitochondrial proteostasis

In humans, only 13 proteins are encoded by the mitochondrial genome. Therefore, most of the mitochondrial proteins (around 99% of them) are encoded by the nuclear DNA, synthesised as precursors in the cytosol and imported into the mitochondria through the protein import machinery for posttranslational assembly. Dysfunction of mitochondria may lead to increased accumulation of ROS, which can cause protein unfolding and DNA mutations, leading to further organellar damage. To counteract this, mitochondria have developed a sophisticated protein quality control system aiming at restoring the mitochondrial function.

The mitochondria unfolded protein response (UPR^{mt}) is a major process that senses defective mitochondrial proteins, communicates with the nuclear genome and cascades a series of reactions that correctly translate, fold and degrade proteins within the organelles in response to stress[158]. The UPR^{mt} is comprised by chaperones (e.g., heat shock proteins) that fold and assemble proteins, and by proteases (e.g., the i-AAA protease, the m-AAA protease, LON, and ClpXP) that eliminate damaged proteins[159]. Another process involves the ubiquitin–proteasome system in which proteins of the OMM are tagged with a lysine 48-linked polyubiquitin chain for degradation.

Mitochondrial dynamics

Mitochondria engage in several dynamic behaviours including fusion, fission and transport that are critical for mitochondrial health and normal functioning. The dynamics machinery is required for buffering intracellular molecules such as calcium, efficient trafficking, OXPHOS and homogenisation of the mitochondrial population.

Mitochondrial fusion is the process of overcoming the energetic barrier to bring two mitochondria together and allowing them to fuse. This allows two mitochondria to share components, such as DNA and proteins, and repair each other. The fusion of the OMM is regulated by mitofusins, especially Mfn1 and Mfn2, whereas the fusion of the IMM is mediated by optic atrophy 1 (OPA1). On the other hand, mitochondrial fission relies on the GTPase dynamin-related protein 1 (DRP1), which is encoded by the gene *DNM1L*, and it pinches off the membrane stalk between the two mitochondria daughters. *DNM1L* is also involved in peroxisomal fission, highlighting the crosstalk between the two organelles[160]. Several DRP1 binding proteins have been established, including the mitochondrial fission factors MFF and MIEF2.

Beyond mitochondrial fusion and fission, mitochondrial transport ensures the trafficking and distribution of mitochondria based on changes in metabolic activity and demand, as well as the physiological or pathological stress. This process is mostly coordinated by the KIF5–Milton–MIRO complex and is involved in synaptic homeostasis and neurodegeneration[161].

Finally, it is important to note the role of mitochondrial autophagy, also known as mitophagy, in degrading and recycling defective mitochondria[162]. During mitophagy, defective mitochondria are engulfed by phagophores, forming autophagosomes, which then fuse with lysosomes for the removal of their contents.

1.4 Mitochondrial dysfunction as a cause of FTD

1.4.1 Mitochondria in health and disease

Over the last decades, a better understanding of the roles of mitochondria have highlighted the involvement of organelle in health and disease. Mitochondrial dysfunction has been associated with multiple pathologies, beyond mitochondrial disorders, providing insights into novel mechanisms and offering a new pharmacological target for the treatment of a wide range of diseases. At this stage, it is important to indicate that the term “mitochondrial dysfunction” refers to the mitochondria potentially still working, but not to the full extent of its capacity in comparison to healthy, normal conditions. Therefore, the observation of mitochondrial dysfunction across diseases may play an important role in the development of the pathogenicity.

A strong clinical, radiological or histological suspicion of metabolic impairments can suggest a potential defect in mitochondria, and an understanding of common genotype-phenotype correlations may instigate the correct prognosis and treatment of the syndrome[163]. The concept of mitochondrial diseases or disorders encompass a group of heterogeneous disorders generally characterised by defective cellular energy production[164]. These could be subdivided into primary mitochondrial disorders (PMDs) generally due to pathogenic mtDNA or nuclear DNA mutations encoding for OXPHOS or function, or into secondary mitochondrial dysfunction (SMD) due to either environmental factors or germline mutations in genes not directly encoding for OXPHOS or mitochondrial function[164]. Throughout this thesis, I consistently referred to both groups as mitochondrial disorders, delving into the mechanisms by which mitochondrial dysfunction can emerge and contribute to disease, with a primary focus on *GRN*-related FTD.

Mitochondrial dysfunction may arise as a result of genetic mutations, ageing, infections or insufficient physical activity. Hence, the clinical, genetic and biochemical complexities of mitochondrial disorders lead to diagnostic odysseys for affected patients. There are no universally accepted robust diagnostic criteria to diagnose mitochondrial disorders, which emphasises the need for wide genetic screening to identify the responsible genetic variants in individual patients. Phenotypic clinical manifestations can be used to identify mitochondrial disorders and their associated genetic variants. However, clinical manifestations from PMDs can be linked to diverse genetic variations that complicates the diagnosis and treatment of patients. For instance, Leigh syndrome, a progressive neurodegenerative disorder, has been associated with nearly 100 disease genes encoded by either mtDNA or nuclear DNA[165].

Conversely, the same genetic variant may lead to different clinical phenotypes across individuals and tissues. For mtDNA disorders, this may be partly explained by a difference in heteroplasmy, which depends on the proportion of mutant mtDNA and tissue segregation. In that case, a biochemical threshold has been hypothesised for the amount of mutated mtDNA that determines the degree of mitochondrial manifestations. This threshold could be related to genetic modifiers which affect either mtDNA or nuclear DNA, environmental modifiers such as metabolic stress and stress, or even effects mediated via mitochondrial biogenesis and/or mitophagy[166].

The development of revolutionary techniques to analyse and identify variants in our genome in the last decade has been reflected in an exponential increase in the identification of novel genes associated, directly or indirectly, with mitochondrial function and dysfunction. This has facilitated a further characterisation of the cellular roles of mitochondria in health and disease, and the genetic mechanisms leading to mitochondrial disorder.

Indeed, pathological mutations in all 37 open reading frames in mtDNA have been identified, with multiple mtDNA mutations associated with mitochondrial disease and other disorders (www.mitomap.org). Thus, mtDNA integrity is essential for a correct mitochondrial function and genomic variants can lead to mitochondrial pathologies. Pathogenic variants in these nuclear genes can cause a group of diseases known as mtDNA maintenance defects (MDMD). These conditions are characterised by mtDNA synthesis defects that can occur either by mtDNA depletion or mtDNA multiple deletions. This leads to impaired mtDNA-encoded protein synthesis, leading to downstream energy production dysfunction and affecting energy-dependent organs.

The interest in investigating the role of mtDNA deletions and depletions have increased over the last decade as diseases have been associated with impaired mtDNA integrity. Deletions are caused by qualitative downstream mitochondrial genomic effects that come from the loss of mtDNA molecule fragments[167], whereas depletion is characterised by a quantitative reduction in mtDNA content[168]. There are two suggested pathomechanisms that aim to explain how pathogenic mutations in the replication machinery can cause mtDNA deletions. On one hand, the stalling of the replication fork can lead to the formation of secondary structures which may be bypassed by the replication slippage mechanism. On the other hand, upon the stalling of the replication fork, single- and double-stranded breaks may be formed causing rearrangements in the mtDNA. The effect in mtDNA integrity is additionally age- and tissue-dependent, and its impairment commonly present in PMDs, as well as neuromuscular disorders, cancer and neurodegenerative diseases[169].

Pathogenic mutations in both mtDNA and nuclear DNA have been linked to defects in the OXPHOS subunits, as well as the activity and assembly of the OXPHOS complexes and supercomplexes. Since mitochondria orchestrate the production of most of the ATP found in cells, the dysfunction of the organelle and OXPHOS primarily affects those organs with a

high ATP demand, such as the brain, skeletal muscle or heart, although virtually any organ or tissue may be affected[170]. Consequently, mitochondrial dysfunction has been associated with multiple human diseases, commonly reporting a defect in mitochondrial respiratory capacity or energy production. Some of the most explored diseases in which mitochondrial dysfunction plays a role in the pathological mechanism include type 2 diabetes[171], cancer[172], cardiovascular diseases[173] and neurodegenerative diseases[174]. Over the next subsection, I will be discussing the studies reporting how mitochondrial dysfunction may affect FTD.

1.4.2 Evidence of mitochondrial dysfunction as an origin for FTD

Given the essential role of mitochondria in neuronal viability, defects in these organelles can result in neuronal dysfunction and death. The presence of mitochondrial dysfunction has been consistently observed in various neurodegenerative disorders, including AD and PD. In the last decade, studies have increasingly characterised the role of mitochondria in both FTD and FTD/ALS syndrome, employing a wide range of models such as immortalised cells, drosophila, rodents and human samples. This section provides an overview of key findings that link mitochondrial dysfunction with FTD, with the exception of the gene *GRN*, which will be discussed in the following subsection.

There are two closely related approaches to study the state of mitochondria in FTD, one based on FTD-related genes (e.g. *GRN*, *c9orf72* and *MAPT*) and the other one being the effect by FTD-linked proteinophaties (e.g. TDP-43, FUS and tau). Increasing evidence has suggested strong associations between mitochondrial dysfunction and cases of FTLD with mutations in the genes *C9orf72*, *MAPT* and *CHCHD10*[175–177].

The GGGGCC repeat expansion in the *C9orf72* gene is the most common genetic cause of ALS and FTD[178]. One of the main suggested pathological theories linked to *C9orf72* repeat expansions involves the formation and accumulation of RNA foci and dipeptide repeat (DPR) proteins, including poly(GP), poly(GR), and poly(GA). Notably several studies have reported different mechanistic links between *C9orf72*, DPR proteins and mitochondrial function by investigating immortalised cell lines, animal and human models. For example, by studying primary cortical excitatory neurons in an inducible mouse model of poly(GR) toxicity, a study in 2019 demonstrated that *C9orf72*-associated poly(GR) preferentially bound to CV component ATP5A1, increasing its ubiquitination and degradation[142]. This induced mitochondrial defects, such as impaired mitochondrial trafficking and decreased complexes

activity. In another study, Metha et al. showed dysfunctional bioenergetics and axonal homeostasis, as well as reduced mitochondrial-encoded transcript expression in *C9orf72* ALS/FTD motor neurons[175]. Boosting mitochondrial bioenergetics though PGC-1α overexpression restored dysfunctional homeostasis, suggesting a potential underlying mechanism and therapeutic strategy. Across literature, other proposed mechanisms linking mitochondria and *C9orf72* involved a disruption of the ER-mitochondria tethering and signalling[179] and UPR^{mt} activation[180]. Taken together, these representatives studies suggest that mitochondrial function may be comprised by *C9orf72* genetic impairment.

Both *c9orf72* and *GRN* genes have been classified within the subtype FTLD-TDP, which is characterised by TDP-43 proteinopathy. The interaction between TDP-43 and mitochondria was first reported in 2016 by Wang and colleagues who demonstrated that TDP-43 enters mitochondria[181], later reporting that the increase in TDP-43 expression induced mitochondrial damage and activated the UPR^{mt} [182]. Several lines of evidence have proven that TDP-43 plays a role in mitochondrial function by interacting with the mtDNA or nuclear DNA[183,184], mitochondrial Ca^{2+} buffering[185], cellular homeostasis and protein quality control[186]. Multiple mechanisms have been suggested, with TDP-43 triggering mtDNA release to activate the inflammatory cGAS/STING pathway as one of the most supported hypotheses[183]. The relevance of the protein as a pathogenic factor in FTD and ALS has coined TDP-43 as a target for emerging therapies[187].

The *MAPT* gene is the second most common genetic cause of FTD, together with the *GRN* gene. Mutations in *MAPT* are characterized by the aggregation of the microtubule-associated protein tau, to which mitochondrial proteins have been reported to bind to[188]. A study showed that induced pluripotent stem cells (iPSC)-derived neurons with FTD tau mutations led to a decrease in mitochondrial bioenergetics[188], strengthening the mechanistic link. Mitochondrial hyperpolarization was also observed in iPSC-derived neurons from

patients with frontotemporal dementia and parkinsonism linked to chromosome 17, leading to oxidative stress and neurodegeneration[176]. Further work in these iPSC-derived neurons with the FTD-related 10+16 *MAPT* mutation also demonstrated that the overproduction of mitochondrial ROS affects neuronal excitability and cell fate, and this can be restored by mitochondrial antioxidants[189].

In contrast to the previously discussed FTD-related genes, *CHCHD10* encodes for a protein directly involved in mitochondrial function. This protein is located in the IMS, forming part of the mitochondrial contact site and cristae organizing system (MICOS) complex[190]. *CHCHD10* mutations cause MICOS complex disassembly, mitochondrial cristae loss and decreased mtDNA nucleoid number and organisation. As a consequence, there is an observed accumulation of mtDNA deletions in skeletal muscle[177]. Interestingly, a recent report has proposed a new mechanistic hypothesis by which CHCHD10 normally suppresses the activity of the fusion enzyme OMA1, and *CHCHD10* mutations trigger mitochondrial integrated response stress and affect mitochondrial dynamics[191].

Beyond the conventional gene- or proteinopathy-specific strategies to identify FTD mechanisms related to mitochondrial dysfunction, another research approach consists of characterising overarching FTD mechanisms without distinguishing between molecular subtypes or associated genes. This may be due to the hypothesis that there are shared pathological hallmarks, such as TDP-43 pathology, or due to studies not having enough biological samples with the same mutated gene to have sufficient statistical significance, and therefore grouping all the FTD cases together. As an example of studies not differentiating between FTD cases when characterising mitochondria, Wei and colleagues assessed the mitochondrial genome in 236 FTLD brain tissues and 351 controls[192]. They observed an increase in heteroplasmic mtDNA variants, but no changes in the mtDNA copy number (mtDNAcn). Only 13% of those cases were diagnosed with *GRN*-related FTD, and

it would be interesting to identify whether PGRN deficiency is specifically leading to the abnormalities in mtDNA.

Finally, in the human brain, lipids make up over 50% of the dry weight, and they sustain the structure and function of the CNS. Therefore, there has also been an interest in employing lipidomic techniques to characterise mitochondrial lipids. For instance, by using HPLC-MS, Phan and colleagues reported a decrease in CL total levels in the serum of sporadic FTLD cases[193], suggesting the existence of a causal link between CL metabolism, mitochondrial dysfunction and FTD pathogenesis. While impaired mitochondrial function and altered CL content represent molecular hallmarks of FTD, their direct contribution to disease pathogenesis remains unclear.

Overall, there is an umbrella of mitochondrial defects occurring across different FTD syndromes. However, it is still uncertain whether mitochondrial dysfunction is involved in *GRN*-related FTD pathogenesis.

1.4.3 Suggested involvement of mitochondrial dysfunction in *GRN*-related FTD

Most of what it is known about the role of PGRN on mitochondrial function has been studied in non-FTD models, including diabetic nephropathy[194], lung cancer[195], cholangiocarcinoma[196] and hepatocellular carcinoma[197]. In summary, these studies suggest that PGRN acts as a regulator of mitochondrial homeostasis, affecting mitochondrial biogenesis and mitophagy. In addition, PGRN has been shown to regulate cell proliferation and apoptosis across several models, including ischemic mice and human thyroid cancer cell lines[198,199].

Exploring the compendium of literature on FTD over the last few years, a few studies have attempted to characterise a link between PGRN deficiency and mitochondrial dysfunction. One of the earliest attempts to characterise the state of mitochondria in a PGRN-deficient model was carried out in 2012 using iPSC-neurons derived from *GRN* mutation carriers[200]. They observed that iPSC-derived neurons did not show any PGRN-dependent mitochondrial dysfunction under different doses of rotenone and hydrogen peroxidase, two mitochondrial stressors. Although they discussed that mitochondrial dysfunction was not present in *GRN*-related FTD, they also raised concerns whether this was due to cultured neurons not reflecting the real human model. Furthermore, they questioned whether mitochondrial dysfunction might develop at a later stage in the progression of FTD in patients.

One year later in 2013, an Australian team investigated cerebral glucose metabolism changes in presymptomatic FTLD patients with *GRN* mutations and non-carriers from five families by using [18F]-fluorodeoxyglucose-PET[201]. They reported anterior brain glucose hypometabolism in FTLD-*GRN* patients, providing evidence for the first time of metabolic alterations in patients with *GRN* mutations, although mitochondria *per se* were not explored.

After nearly a decade, in 2021, a Polish lab observed parkin downregulation in fibroblasts derived from patients with *GRN* mutations[202]. Whilst parkin partners MFN2 and VDAC1 were decreased in fibroblasts with a transient *GRN* knockdown (KD), these proteins were unaltered in fibroblasts from patients with *GRN* mutations. This could be due to compensatory responses to lifelong PGRN deficiency that are absent in the transient KD.

Several studies have performed lipidomic assays shedding light into the presence of mitochondrial dysfunction in *GRN*-related FTD. In 2022, an American study carried out HPLC-mass spectrometry in human post-mortem brains, with the aim of investigating gangliosidosis, and observed a decrease in CL abundance in the frontal lobe of patients diagnosed with *GRN*-related FTD in comparison to controls[203]. The CL levels in sporadic FTLD-TDP patients was also decreased, but not significantly, suggesting *GRN* mutations specifically induce a more striking mitochondrial dysfunction phenotype. A year later in 2023, an Australian team reported increased levels of long chain (C16-C20) acylcarnitines in the frontal grey matter of FTD patients with *GRN* mutations[204]. Bearing in mind that acylcarnitines serve as carriers to import fatty acids into mitochondria for subsequent β-oxidation, their accumulation is associated with defective fatty acid β-oxidation[205]. This could indirectly suggest the presence in mitochondrial dysfunction in *GRN*-related FTD.

Finally, also in 2023, a Spanish lab reported impaired mitophagy and increased mitochondrial mass in a transient *GRN*-KD SH-SY5Y neuroblastoma model, largely attributed to TDP-43 accumulation[206]. They also noted a decrease in mitochondrial membrane potential and ATP levels in patient-derived lymphoblasts. Notably, the inhibition of TDP-43 restored the mitochondrial membrane potential in *GRN* KD SH-SY5Y cells.

Overall, these preliminary studies hint at mitochondrial dysfunction in PGRN-deficient models, yet a comprehensive characterisation, especially in human post-mortem brain tissue, is lacking. Therefore, the investigation of the effect of PGRN deficiency on mitochondrial function could shed light on the development of *GRN*-related FTD pathogenesis.

In this PhD thesis, the role of mitochondria was characterised by using *in vitro* PGRN-deficient models, encompassing stable *GRN* KD immortalised cell lines, skin fibroblasts from patients with *GRN* pathogenic mutations and iPSC-derived neurons and astrocytes. Human post-mortem brains from FTLD-*GRN* cases were additionally assessed in comparison with sporadic FTLD-TDP cases and controls. By employing bioenergetic, biochemical and molecular approaches, mitochondrial dysfunction was identified across PGRN-deficient *in vitro* models and human tissues. Specifically, PGRN haploinsufficiency induced bioenergetic deficit due to defective mitochondrial respiration, accompanied by a decrease in mitochondrial mass, biogenesis and content, along with an impairment in mtDNA with increased deletions. Additionally, histopathological techniques were optimised and developed, observing brain region-specific increases in phosphorylated TDP-43 (pTDP-43) accumulation in FTLD-*GRN* patients. In summary, this PhD project identified mitochondrial dysfunction as a pathological hallmark associated with *GRN*-related FTD, which presents a promising therapeutic target for FTD patients.

1.5 Hypothesis and Objectives

The hypothesis of this thesis proposed that mitochondrial dysfunction plays a role in *GRN*-related FTD. The overarching aim focused on a comprehensive characterisation of the mitochondrial phenotype across PGRN-deficient *in vitro* and human models to investigate the presence of mitochondrial pathology in FTLD-*GRN* patients. Additionally, the long-term objectives of this PhD thesis encompassed gaining a deeper understanding of the development of FTLD pathology, enhancing overall diagnosis and prognosis, and facilitating the identification of novel therapeutic strategies.

The specific aims of this thesis as discussed across chapters were:

1) To characterise the state of mitochondria in shGRN KD immortalised cell lines from a genetic, biochemical and molecular approach (Chapter 3);

2) To validate and explore the *in vitro* results in skin fibroblasts derived from presymptomatic patients with *GRN* pathogenic mutations and in iPSC-derived neurons and astrocytes, particularly assessing mitochondrial genomics (Chapter 3);

3) To investigate the presence of mitochondrial function or dysfunction in human post-mortem brains from FTLD-*GRN* patients (Chapter 4);

4) To optimise and develop novel histopathological techniques to characterise human post-mortem brain sections from FTLD patients (Chapter 5).

2 Materials and methods

Methods under the sea of madness (watercolours) – by Dr Marie Sion

2.1 H4 and SH-SY5Y cell culture

Human neuroglioma H4 cells were generously provided by Professor Hélène Plun-Favreau (UCL). They were cultured in Dulbecco's modified Eagle Medium (DMEM, Thermo Fisher Scientific) supplemented with high glucose and 10% (v/v) heat-inactivated fetal bovine serum (FBS).

SH-SY5Y cells were purchased from ATCC. They were cultured in DMEM F-12 and GlutaMAX (Thermo Fisher Scientific) containing 10% FBS, 100 U/mL penicillin and 100 mg/mL streptomycin.

All the cell lines were grown at 37°C under standard conditions (5% CO_2, ambient O_2, 95% relative humidity) and regularly tested for mycoplasma. Upon reaching ~80% confluency, cells were trypsinised, pelleted at 200 x g for 5 min, and washed with Phosphate Buffered Saline (PBS). For passaging, the cell pellet was then resuspended in its corresponding fresh DMEM media containing all the supplements and transferred to a cell culture flask for expansion. Experiments were conducted on H4 and SH-SY5Y cells with the same passage number between 6 and 16.

2.2 Fibroblasts from presymptomatic patients with *GRN* mutations

Fibroblasts from five presymptomatic patients harbouring *GRN* pathogenic mutations were kindly donated by Professor Jonathan Rohrer (UCL). The fibroblasts from the presymptomatic cases were compared to fibroblasts from six control individuals to assess the effects of PGRN deficiency on mitochondrial function. Case demographics for control and patient fibroblasts were described in Table 2.1.

Case ID	Clinical diagnosis	Sex (F/M)	Genetic mutation
1	Control	F	-
2	Control	M	-
3	Control	M	-
4	Control	F	-
5	Control	F	-
6	Control	F	-
7	FTLD-*GRN*	F	*GRN* C31fs
8	FTLD-*GRN*	M	*GRN* C31fs
9	FTLD-*GRN*	F	*GRN* R493X
10	FTLD-*GRN*	F	*GRN* C31fs
11	FTLD-*GRN*	M	*GRN* V141fs

Table 2.1 Case demographics for human fibroblasts with *GRN* mutations. Abbreviations: F, female; M, male.

Fibroblasts were grown in DMEM (Thermo Fisher Scientific) containing high glucose, 10% (v/v) FBS, 100 U/mL penicillin and 100 mg/mL streptomycin, and 1% sodium pyruvate (Thermo Fisher Scientific). Fibroblasts were grown at 37°C under standard conditions (5% CO_2, ambient O_2, 95% relative humidity) and regularly tested for mycoplasma. Upon reaching ~80% confluency, cells were trypsinised, pelleted at 200 x g for 5 min, and washed with PBS. For passaging, the cell pellet was then resuspended in fresh DMEM media containing all the supplements and transferred to a cell culture flask for expansion. Experiments were conducted with the passage numbers between 6 and 16.

2.1 RNA from iPSC-derived neurons and astrocytes

Professor Selina Wray's lab (UCL) generated and kindly gave us RNA extracted from iPSC-derived cortical neurons and astrocytes from three FTD patients carrying *GRN* mutations, and from control lines. For the iPSC lines derived from patients with *GRN* mutations, Wray's lab used the same skin fibroblasts employed in this PhD project, with two patients having the *GRN* R493X mutation and the third patient having a *GRN* C31fs mutation.

Additionally, from Wray's lab, RNA was obtained from a CRISPR series of neurons and astrocytes from the human iPSC Neurodegenerative Disease Initiative (iNDI)[207] with an isogenic control, heterozygous and homozygous R493X mutation lines.

Limited extracted RNA was available, and one to three biological replicates were employed for each genetic condition, which restricted the statistical power and the capability to carry out statistical analysis.

The work at Wray's lab on these iPSC-derived neurons and astrocytes remains unpublished as of the submission of this thesis, and consequently the derivation process was not included.

2.2 Cohort of brains from FTLD patients

Brains from twenty-seven cases (17 FTLD and 10 controls) were selected from the Queen Square Brain Bank (QSBB). The Materials Transfer Agreement (MTA) included ethical approval to work with the samples for research purposes (UCLMTA-6-21). Case demographics can be found in Table 2.2. The final cohort consisted of 17 different FLTD cases, including seven with *GRN* mutations (FTLD-*GRN*; three C31fs, two R493X, one Q130fs and one IVS3-7T>G; all FTLD-TDPA) and ten with sporadic FTLD-TDP cases without *GRN* mutations (sporadic FTLD-TDP; three FTLD-TDPA, three FTLD-TDPB and four FTLD-TDPC). White the underlying pathologies may differ between FTLD-*GRN* cases and sporadic FTLD-TDP subtypes, including these cases facilitated a preliminary yet comprehensive exploration of FTLD heterogeneity, common pathways, and potential therapeutic targets.

Controls were requested to be “age- and sex-matched” with the FTLD cases. For the *GRN* pathogenic variants, there were no restrictions on gene variants. Individuals with a higher Braak and Braak stage have been reported to exhibit less mitochondrial activity[208], and variations in the Braak and Braak stage could impact mitochondrial comparisons between groups. Therefore, the criteria for the requested controls excluded cases with age-related TDP-43 and tau proteinopathies, and with Braak and Braak stage above 2.

Snap-frozen brains were obtained from all twenty-seven cases. However, formalin-fixed paraffin-embedded (FFPE) brain sections were obtained only from eighteen out of all the cases, as indicated in Table 2.2. The lower number of cases for FFPE sections is due to the histopathology experiments (Chapter 5) being considered a pilot research project explored in this PhD. Depending on the findings from this thesis, there may be an expansion and request for additional FFPE sections from the remaining cases.

Case ID	Sex (M/F)	Familial history (Y/N)	TDP-43 type	Genetic Mutation	Age at onset (years)	Age at death (years)	Disease duration (years)	PMD (hours)	Braak stage	FFPE sections?
Controls (*n*=10)										
1	F	-	-	-	-	71	-	76.2	III	X
2	M	-	-	-	-	101	-	60.6	I	X
3	F	-	-	-	-	96	-	60.0	II	X
4	F	-	-	-	-	86	-	120.0	I	X
5	M	-	-	-	-	69	-	168.0	I	
6	F	-	-	-	-	71	-	79.0	*na*	
7	M	-	-	-	-	71	-	38.8	*na*	
8	M	-	-	-	-	76	-	39.1	*na*	
9	F	-	-	-	-	78	-	30.8	II	
10	F	-	-	-	-	84	-	53.6	II	
	4M / 6F					80.3±3.6		72.6±13.4		
FTLD-*GRN* (*n*=7)										
11	M	Y	A	*GRN* C31fs	53	61	8	72.6	*na*	X
12	M	Y	A	*GRN* C31fs	50	55	5	29.3	I	X
13	M	Y	A	*GRN* R493X	59	70	11	44.1	*na*	X
14	F	Y	A	*GRN* Q130fs	62	68	6	96.0	*na*	X
15*	F	Y	A	*GRN* C31fs	59	66	7	115.0	II	
16	F	Y	A	*GRN* IVS3-7T>G	57	72	15	42.3	*na*	
17	M	Y	A	*GRN* R493X	60	71	11	90.1	*na*	
	4M / 3F				57.1±1.6	66.1±2.3	9.0±1.3	69.9±12.1		

Sporadic FTLD-TDP (*n*=10)										
18	M	N	A	-	51	60	9	40.4	II	X
19	M	Y	A	-	47	72	25	29.5	II	X
20	M	*na*	A	-	46	53	7	33.1	I	X
21	M	N	B	-	67	69	2	69.1	*na*	X
22	F	Y	B	-	62	83	21	30.1	II	X
23	F	N	B	-	63	67	4	48.0	*na*	X
24	M	N	C	-	64	74	10	38.4	II	X
25	F	N	C	-	53	65	12	57.7	*na*	X
26	M	N	C	-	58	71	13	54.1	*na*	X
27	M	N	C	-	70	83	13	59.8	V	X
	7M / 3F				58.1±2.7	69.7±3.0	11.6±2.2	46.0±4.4		

Table 2.2 Clinical meta-data of all human post-mortem brains. Post-mortem delay refers to the time interval between death and tissue processing, serving as an indicator of tissue preservation quality. The male/female distribution and the mean ± standard error of the mean (SEM) can be found at the bottom of each group for the different parameters. Abbreviations: F, female; M, male; N, no; *n,* number of cases; na, not available; PMD*,* post-mortem delay; Y, yes. *Case with *C9orf72* mutation

The following brain regions were obtained: superior frontal gyrus (white and grey matter), tip of the temporal pole (white and grey matter), and cerebellum (Fig. 2.1). These regions were selected to identify potential brain region-specific changes in mitochondrial function. The frontal and temporal lobes were chosen due to their known pathological involvement in *GRN*-related FTD. The cerebellum was included as a "control" region expected to be free from proteinaceous inclusions compared to the frontal and temporal lobes.

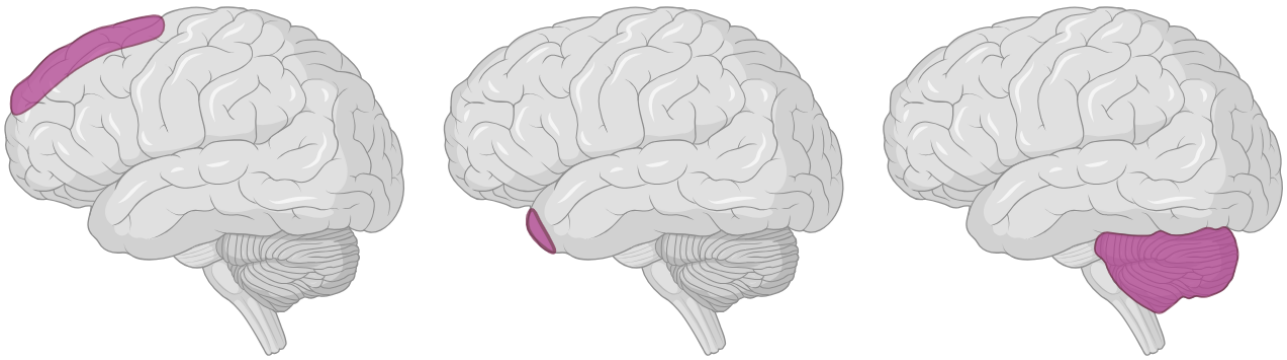

Figure 2.1 Visualisation of the brain regions explored in this PhD thesis. Brain regions denote the superior frontal lobe, tip of the temporal pole and cerebellum (left to right).

In addition, both white and grey matter were explored to identify any neuropathological differences. Albeit mitochondria are present and active in both brain matters, their functions and distribution can vary within these regions. On one hand, the grey matter primarily consists of neuronal cell bodies, dendrites, and synapses which require a high energy demand supplied by mitochondria to support the neuronal signalling and the synthesis of neurotransmitters. On the other hand, the white matter is comprised by nerve fibres, also known as axons, that required mitochondrial energy to enable axonal transport and maintain myelin sheaths. Remarkably, the difference between both brain matters is reflected in the metabolic rate which is approximately 25–50% higher in the grey matter than in the white matter[209,210]. Therefore, it would be insightful to identify grey or white matter-specific changes in the mitochondrial phenotype.

In this thesis, the following abbreviations were used when comparing between the different brain regions: frontal grey (FG), frontal white (FW), temporal grey (TG), temporal white (TW) and cerebellum (CBM).

2.3 Lentiviral shRNA transduction

Human embryonic kidney 293 cells expressing the SV40 large T antigen (HEK293T) were seeded in T25 flasks at 70% confluence in DMEM containing high glucose, 10% (v/v) heat-inactivated FBS, 100 U/mL penicillin and 100 mg/mL streptomycin at 37°C with 5% CO_2 in a humidified incubator. The following day, HEK293T cells were reverse transduced with pGIPZ lentiviral short hairpin RNAs against *GRN* (shGRN). Control transduction was performed using non-targeting shRNA (shCTR). Lentiviral shRNA transduction was carried out in 5mL DMEM high glucose final volume containing 750µL Optimem, 13 µL p3000™, 18 µL p3000 Reagent, 6 µg DNA, 7.5 µg psPAX, and 6 µg VSV-G. On day 2, the virus was filtered using acetate filter 0.45 and added to H4 and/or SH-SY5Y cells at 60% confluence. On day 5, the virus was discarded and the H4 and/or SH-SY5Y cells were incubated in their own media. The next day, cells were selected for three days using 2 µg/mL puromycin. Non-transduced cells were used as a control to test antibiotic resistance.

Three different shGRN pGIPZ vectors from Dharmacon were tested to induce a *GRN* KD in SH-SY5Y and H4 (V2LHS_266570, V3LHS_327101 and V3LHS_351385). Reverse transcription-quantitative polymerase chain reaction (RT-qPCR) was used to measure the transcript expression of the *GRN* gene (Fig. 2.2). Vector V2LHS_266570 showed the strongest *GRN* mRNA KD in both SH-SY5Y and H4 cells, and it was therefore chosen for the experimental work reported in this thesis. *GRN* mRNA levels were routinely monitored across passages using RT-qPCR to confirm the stable KD was still present in the transduced cell lines. If the transduced cell lines reached passage number 16 or if *GRN* mRNA levels were no longer decreased, a new line of H4 or SH-SY5Y cells was transduced.

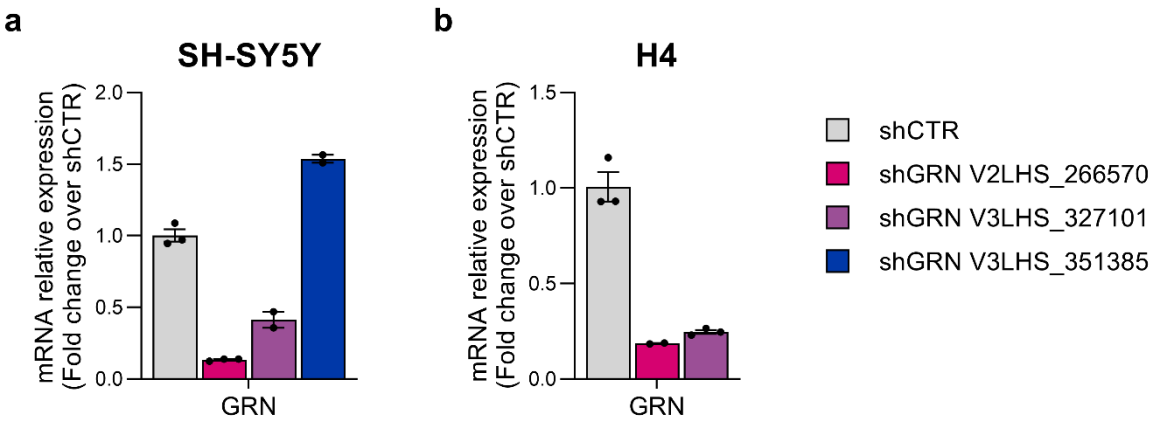

Figure 2.2 *GRN* transcription expression in a) SH-SY5Y neuroblastoma and b) H4 neuroglioma cells transduced with different shGRN lentiviral vectors. Data are expressed as mean±SEM, where each data point represents a technical replicate.

2.4 Cell proliferation assay

Cellular proliferation was assessed using an Agilent xCELLigence Real-Time Cell Analysis instrument. 20,000 H4 cells per well were seeded in a glass E-Plate 16, recording cell index (electrical impedance) every 30 min for 96h under standard conditions (5% CO_2, ambient O_2, 95% relative humidity). Data were baseline corrected to medium-only-containing wells. The cell proliferation assay was performed by our collaborator Dr Daniel De Jesus (Queen Mary University).

2.5 Trypan blue cell viability

Cell viability was determined using 0.4% Trypan Blue Solution (Thermo Fisher Scientific). This method was based on the principle that live cells possessed intact cell membranes that did not take up the dye Trypan Blue, whereas dead cells are permeable and can take up the dye. Therefore, dead (non-viable) cells would be blue and live (viable) cells would remain unstained. Trypsinized cells were centrifuged and the pellet was resuspended in PBS. A 1:1 mix dilution of the cell suspension and 0.4% Trypan Blue dye were incubated at room temperature for 3 min. A sample was added to a haemocytometer, where both dead stained and live unstained cells were counted by eye under a light microscope as illustrated in Figure 2.3. The percentage of viable cells was calculated by diving the total number of viable cells per mL by the total number of cells per mL.

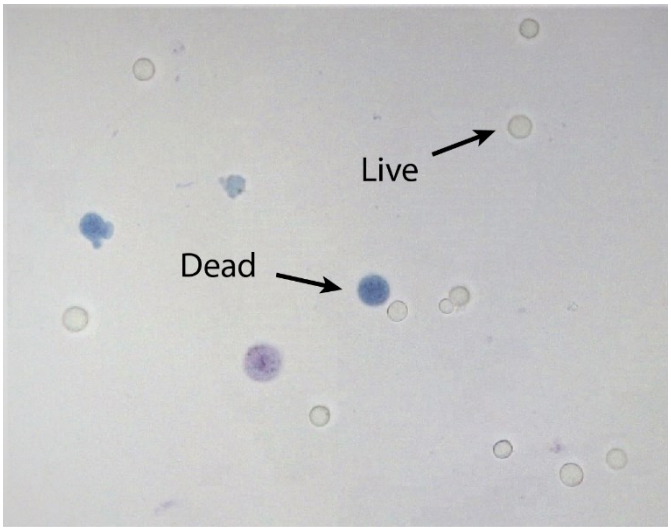

Figure 2.3 Representative image of Trypan Blue staining on H4 neuroglioma cells under a light microscope. Arrows indicate dead cells stained blue and live cells that are unstained.

2.6 Assessment of the mtDNA copy number

Proteinase K digestion buffer was previously prepared using 100 mM Tris-HCl (pH 8.5), 5 mM EDTA, 0.2% SDS, and 200 mM NaCl. Proteinase K (ITW Reagents) was resuspended in 1 mM CaCl2, 50% glycerol and 20 mM Tris-HCl (pH 7.4).

For H4, SH-SY5Y and fibroblast cell lines, the premix including 240.5 µL Proteinase K digestion buffer, 7.5 µl Proteinase K and 2 µL 1:100 β-mercaptoethanol (BME) was added. The point of the pipet tip was used to loosen the cell pellet at the bottom of the tube. The tubes were flicked or inverted to ensure the even distribution of buffer to cells, and digested overnight at 55°C. The following day, 250 µL of Proteinase K digestion buffer and 170 µl 5 M NaCl were added, followed by inversions for 5 min, and centrifuged at high speed (>25,000g) for 15 min at 4°C. The supernatant was transferred to a fresh tube, mixed by inversion in 800 µL 100% EtOH and 1 µL GlycoBlue (Thermo Fisher Scientific), and centrifuged again at high speed (>25,000 g) for 15 min at 4°C. The supernatant was discarded and the pellet was washed with 500 µL 70% EtOH, inverted and centrifuged at maximum speed for 5 min at 4°C. The ethanol was removed and the pellet was left to air-dry overnight, protected from light. Finally, the DNA was resuspended in 30 µL Tris-EDTA (TE) buffer and 1 µL RNAse A, mixed by flicking and incubated for 1 hour at 55°C.

A similar protocol was employed for the DNA extraction from human post-mortem brains. Briefly, ~27 mg of the frozen human brain sample were resuspended in 490.5 µL Proteinase K digestion buffer, 7.5 µl Proteinase K and 2 µL 1:100 BME, homogenised and incubated for overnight digestion at 55°C. The following day, 10 µL Proteinase K were added and digested for an additional hour at 55°C. Then, 250 µL of Proteinase K digestion buffer and 170 µl 5 M NaCl were mixed in, followed by inversions for 5 min, and centrifuged at high speed (>25,000g) for 15 min at 4°C. The supernatant was transferred to a fresh tube and

800 µL 100% EtOH and 1 µL GlycoBlue were added, mixed by inversion and centrifuged at high speed (>25,000 g) for 15 min at 4°C. The supernatant was discarded and the pellet was washed with 500 µL 70% EtOH, inverted and centrifuged at maximum speed for 5 min at 4°C. The ethanol was removed and the pellet was left to air-dry overnight, protected from light. Finally, the DNA was then resuspended in 98 µL TE buffer and 2 µL RNAse A, mixed by flicking and incubated for 1h30 at 55°C to obtain the DNA. The Agilent 4200 TapeStation system was used to quantify the DNA concentration and ensure a high DNA integrity number, indicating a highly intact DNA.

The mtDNAcn was determined using TaqMan Fast Advance Master Mix (Thermo Fisher Scientific), according to manufacturer's protocol, and qPCR reactions were undertaken using a QuantStudio 5 thermal cycler (Thermo Fisher Scientific). The fast Taqman cycling program was one cycle at 95°C for 20 sec (polymerase activation), and 40 cycles at 95°C for 1 sec (denaturation) and at 60°C for 20 sec (annealing/extension). Two sets of probes quantified mitochondrial fragments in the mitochondrial genome (*MT-CYB* and *MT-ND1*) relative to a single copy region of a nuclear gene (*GUSB* and *B2M*, respectively) using the ΔΔCq method[211]. All experiments were run in triplicate and details on the probes (Integrated DNA Technologies) are shown in Table 2.3.

Gene target	Probe and primer sequences (5' to 3')
MT-CYB (VIC-labelled)	Probe: /5HEX/ATCATCCGC/ZEN/TACCTTCACGCAAT/3IABkFQ/ Primer 1: GATGTGTAGGAAGAGGCAGATAAA Primer 2: CCACATCACTCGAGACGTAAAT
GUSB (FAM-labelled)	Probe: /56-FAM/AAGAGTGGT/ZEN/GCTGAGGATTGGCA/3IABkFQ/ Primer 1: ACGATGGCATAGGAATGGG Primer 2: TGGTACGAACGGGAGGT
MT-ND1 (VIC-labelled)	Probe: /5HEX/CCATCACCC/ZEN/TCTACATCACCGCCC/3IABkFQ/ Primer 1: CCCTAAAACCCGCCACATCT Primer 2: GAGCGATGGTGAGAGCTAAGGT
B2M (FAM-labelled)	Probe: /56-FAM/ATGTGTCTG/ZEN/GGTTTCATCCATCCGACA/3IABkFQ/ Primer 1: CCAGCAGAGAATGGAAAGTCAA Primer 2: TCTCTCTCCATTCTTCAGTAAGTCAACT

Table 2.3 List of human TaqMan assays probes for mtDNAcn measurement from Integrated DNA Technologies.

Validating *MT-CYB*/*GUSB* and *MT-ND1*/*B2M* probes for multiplex assay

Two pairs of probes *MT-CYB*/*GUSB* and *MT-ND1*/*B2M* were validated for multiplex assay to interrogate a potential interaction between the probes when measuring mtDNAcn in human brains. This validation process what carried out based on Belmonte and colleagues' paper[212]. Using a series of dilutions of human brain DNA in triplicate replicates, the average fluorescence signal curve (ΔRn) for each dilution of the human brain DNA showed a proportional shift in both probes (Fig. 2.4a, 2.4d). After calculating the linear regression analysis of the average C_q values plotted as a function of DNA concentration, the slopes of the probes in each pair in the multiplex assay were in close agreement (Fig. 2.4b, 2.4e). When the delta Cq (ΔC_q) values were plotted as a function of DNA, the slope of the multiplexed reaction (0.178 for *MT-CYB*/*GUSB* and 0.122 for *MT-ND1*/*B2M*) revealed a modest effect of DNA concentration on the ΔC_q values (Fig. 2.4c, 2.4f). These results validated the use of both pairs of probes for multiplex assays to quantify relative mtDNAcn abundance.

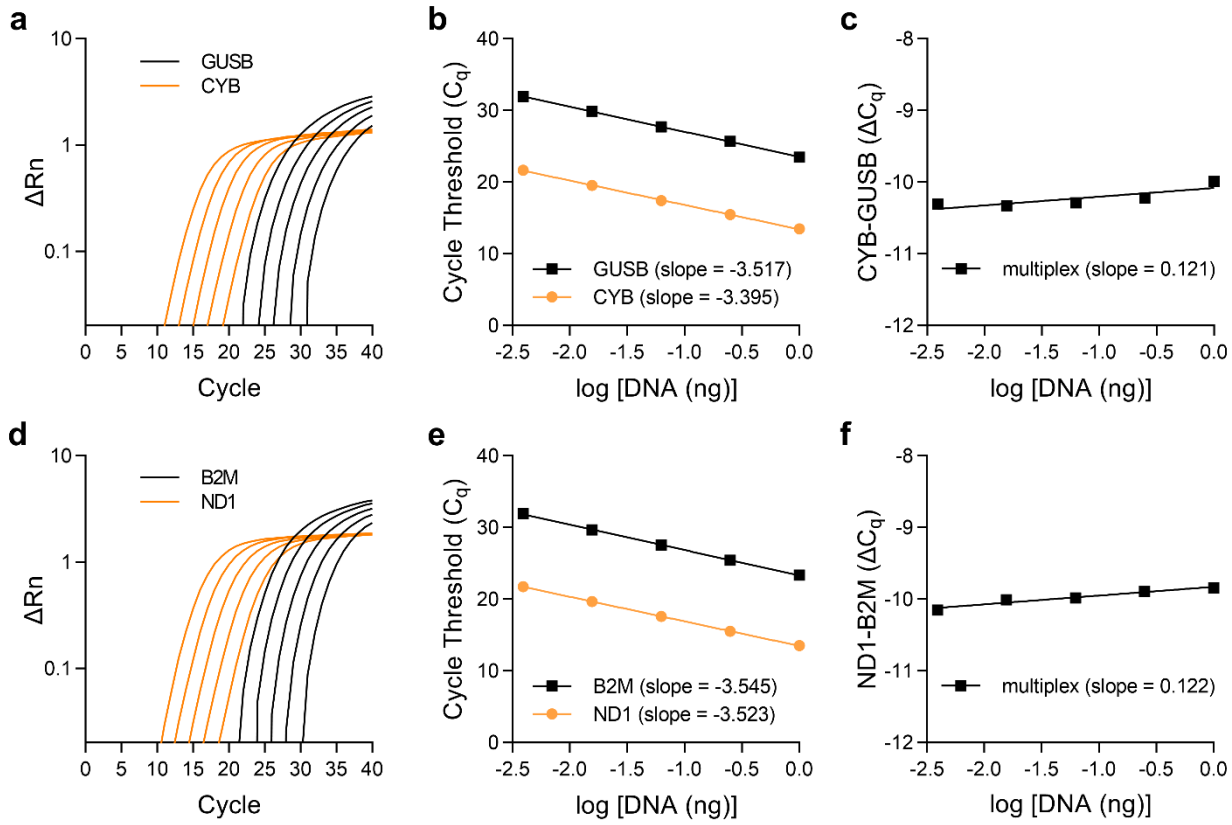

Figure 2.4 Validation of the multiplex mtDNAcn assay using Taqman *MT-CYB*/*GUSB* and *MT-ND1*/*B2M* probes. a Log plots of the fluorescence signal (ΔRn) for *MT-CYB* (Hex) and *GUSB* (FAM) Taqman probes in a dilution series of human brain total DNA preparation in multiplex assays. Each dilution was performed in triplicate replicates and shown in the figure is an average curve for each dilution. **b** Average C_q values of *MT-CYB*/*GUSB* plotted as a function of DNA concentration. Slopes were determined by linear regression (both are $R^2 \geq 0.99$). **c** Delta Cq values of *MT-CYB*/*GUSB* were plotted as a function of DNA in the multiplex assay. **d** Log plots of the fluorescence signal (ΔRn) for *MT-ND1* (Hex) and *B2M* (FAM) Taqman probes in a dilution series of human brain total DNA preparation in multiplex assays. Each dilution was performed in triplicate replicates and shown in the figure is an average curve for each dilution. **e** Average C_q values of *MT-ND1*/*B2M* plotted as a function of DNA concentration. Slopes were determined by linear regression (both are $R^2 \geq 0.99$). **f** Delta Cq values of *MT-ND1*/*B2M* were plotted as a function of DNA in the multiplex assay.

2.7 Next-Generation Sequencing

Prior to next-generation sequencing (NGS) of the mtDNA of human post-mortem brains, long PCR was performed using GoTaq® Long PCR Master Mix to amplify the mtDNA. The following primers were employed:

mt16426F (L16426) F5'-CCGCACAAGAGTGCTACTCTCCTC-3'

mt16425R (H16425) 5'-GATATTGATTTCACGGAGGATGGTG-3'.

For the long PCR assay, 1.5 µL human genomic DNA (200 ng) were mixed with 25ul GoTaq® Long PCR Master Mix (Promega) and 1 µL long PCR control primer pair. The long PCR cycling program was one cycle at 95°C for 2 min (initial denaturation), 30 cycles at 92°C for 30 sec (denaturation) and at 55°C-69°C for 14:30 min (annealing/extension), and one last cycle at 72°C for 10 min (final extension). The PCR products were analysed by 0.8% gel electrophoresis (Fig. 2.5) and made visible at ~16.6 kb by UV illumination following ethidium-bromide staining, confirming the amplification of the mtDNA. Shanti Lu and Micol Falabella amplified the mtDNA, and Cathy Woodward processed the NGS data using eKLIPse analysis.

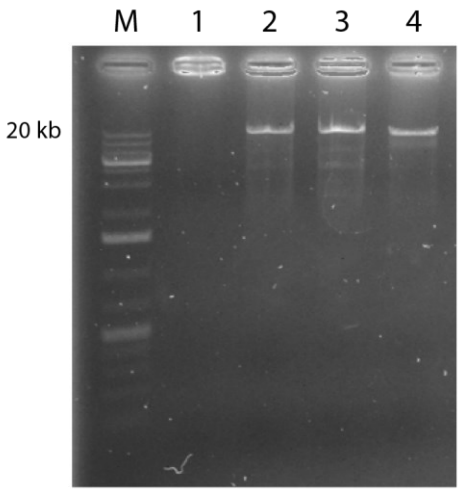

Figure 2.5 Amplification of ~16.6 kb mtDNA from human brain genomic DNA using GoTaq® Long PCR Master Mix. Lane M contains Lambda DNA/HindIII Markers. Lane 1 is empty and does not show any product. Lanes 2 to 4 contain mtDNA PCR products from three different patients. Each lane contains 10 µl of the amplification reaction.

2.8 RNA extraction

RNA was extracted using the RNeasy Micro Kit (QIAGEN) and DNA was removed using the DNA-free™ Kit (Thermo Fisher Scientific). Quality of the extracted RNA was assessed by the A260nm/A280nm absorbance ratio (Nanodrop One, Thermo Fisher Scientific). The cDNA synthesis was carried out using High-Capacity cDNA Kit (Thermo Fisher Scientific). The experimental work was performed according to manufacturers' protocols. All experiments were run in triplicate and the gene expression levels were normalised to the *B2M* results using the ΔΔCq method[211].

2.9 Reverse transcription-quantitative PCR

RT-qPCR was used to detect and quantify RNA. First RNA was transcribed into complementary DNA (cDNA), which was then used as a template for PCR. This technique used a fluorescent probe to measure the amount of amplification product after each PCR cycle. The Taqman assay was employed to detect and amplify cDNA, enabling the measurement of one (singleplex) or more than one (multiplex) simultaneous probes in the same cDNA sample. The Taqman assay uses a hydrolysis-based probe that detects the amplification by degradation of the probe by Taq polymerase and release of the fluorophore.

Taqman assays for gene expression analysis

For singleplex TaqMan RT-qPCR assays, 2.5 µL cDNA (diluted 1:5-1:10) were mixed with 5 µL TaqMan Fast Universal PCR Master Mix (2x) (Thermo Fisher Scientific), 0.5 µL TaqMan assays probe (20x) and 2 µL of H_2O. For multiplex TaqMan RT-qPCR assays, 2.5 µL cDNA (diluted 1:5-1:10) were mixed with 5 µL TaqMan Fast Universal PCR Master Mix (2x) (Thermo Fisher Scientific), 0.5 µL of each TaqMan assays probe (20x) and 1.5 µL of H_2O. The fast Taqman cycling program was one cycle at 95°C for 20 sec (polymerase activation), and 40 cycles at 95°C for 1 sec (denaturation) and at 60°C for 20 sec (annealing/extension). All reactions were set up in technical triplicates, and RT-qPCR was performed in an Applied Biosystems QuantStudio 5 Real-Time PCR System. Details on the TaqMan primer/probe assays are shown in Table 2.4 and Table 2.5.

Gene Target	Assay ID	Details Company
ATP5A1	Hs00900735_m1	FAM-labelled MGB probe
CLS1	Hs00219512_m1	FAM-labelled MGB probe
COX5A	Hs00362067_m1	FAM-labelled MGB probe
GRN	Hs00963707_g1	FAM-labelled MGB probe
MT-ATP6	Hs02596862_g1	FAM-labelled MGB probe
MT-CO1	Hs02596864_g1	FAM-labelled MGB probe
MT-CO3	Hs02596866_g1	FAM-labelled MGB probe
MT-CYB	Hs02596867_s1	FAM-labelled MGB probe
MT-ND1	Hs02596873_s1	FAM-labelled MGB probe
MT-ND6	Hs02596879_g1	FAM-labelled MGB probe
MT-RNR1	Hs02596859_g1	FAM-labelled MGB probe
NDUFB8	Hs00428204_m1	FAM-labelled MGB probe
PRELID1	Hs02638995_g1	FAM-labelled MGB probe
SDHB	Hs01042481_m1	FAM-labelled MGB probe
TRIAP1	Hs00429934_g1	FAM-labelled MGB probe
UQCRC2	Hs00996395_m1	FAM-labelled MGB probe
B2M	Hs00187842_m1	VIC-labelled MGB probe
GAPDH	Hs02786624_g1	FAM-labelled MGB probe

Table 2.4 List of human TaqMan assays probes for transcripts measurement from Thermo Fisher Scientific.

Gene Target	Probe and primers sequences (5' to 3')
TAMM41 (FAM-labelled)	Probe:/56-FAM/TAGACGAAA/ZEN/GCCAGACTCAGCTCCT/3IABkFQ/ Primer 1: GCAAGATCCTGTCTCACTTCC Primer 2: GAACACAAAGTCCAGCATAGC
PGS1 (FAM-labelled)	Probe: /56-FAM/TTGGAACAG/ZEN/GAGCTGGTGGACTG/3IABkFQ/ Primer 1: GCAGATAAGAGTAGCCAAGAGG' Primer 2: GGAAACTTTGCTTGGAGTGAC
PTPMT1 (FAM-labelled)	Probe:/56-FAM/ACCATGAAC/ZEN/GAGGAGTACGAGACGA/3IABkFQ/ Primer 1: AGCTGGTACAGGACGAGAA Primer 2: GTCATGTCTACTGTGCTGAGC
TAZ (FAM-labelled)	Probe: /56-FAM/AGGTTCCAG/ZEN/ATGTGGCGGAGTTTC/3IABkFQ/ Primer 1: CCAATCACCAGTCCTGCAT Primer 2: TCCTTGGTGAAGCAGATGTC

Table 2.5 List of human TaqMan assays probes for transcripts measurement from Integrated DNA Technologies.

2.10 Western Blot

H4 and fibroblast cell pellets for sodium dodecyl sulphate (SDS)-polyacrylamide gel electrophoresis (PAGE) were lysed in RIPA buffer (50 mM Tris-HCl, pH 7.4, 150 mM NaCl, 0.25% sodium deoxycholate, 1 mM EDTA, 1% NP-40; Sigma-Aldrich), supplemented with 1X complete protease inhibitor cocktail (Roche Molecular Diagnostics). Lysates were incubated on ice for 30 min and centrifuged at 13,000 x g for 15 min at 4°C after which the supernatant was obtained. The protein concentration was estimated using the Coomassie protein assay reagent (Thermo Fisher Scientific) and the absorbance was measured at 595 nm in a Tecan Spark plate reader.

Then, 20-50 ug protein were mixed with dH_2O and x1 NuPAGE LDS sample buffer (Invitrogen) containing 2.5% (v/v) beta-mercaptoethanol, and denatured for 5 min at 95°C. Equal amounts of the protein and Precision Plus Protein Dual Xtra Standards (Bio-Rad) were separated on NuPAGE 4-12% Bis-Tris gels (Invitrogen) using x1 NuPAGE MOPS SDS Running Buffer (Life Technologies) for 2 hours at 80-120 V. Proteins were then transferred to a Trans-Blot Turbo 0.2 µm nitrocellulose membrane (Bio-Rad) using the Trans-Blot Turbo Transfer System. Membranes were blocked with blocking solution (LI-COR) for 1 hour with agitation on a plate shaker. Primary antibodies were diluted in the blocking solution and applied overnight at 4°C with agitation on a plate shaker. The primary antibody was removed, and the membranes were washed three times in TBST (x1 TBS and 0.1% (v/v) Tween-20) for 15 min each time with agitation on a plate shaker. Membranes were incubated with the secondary antibodies in a dilution in the blocking solution for 1 hour at room temperature with agitation on a plate shaker. The secondary solution was removed and the membranes were washed three times in TBST, 15 min each time with agitation in a plate shaker. Table 2.6 shows the list of the primary and secondary antibodies that were used in this PhD project. Signal intensity was detected with the LI-COR Odyssey infrared Imager at

680 and 800 nm, and image analysis was carried out using ImageJ v.2.0.0 software (NIH, USA).

Human post-mortem brains for SDS-PAGE were extracted using x1 protein solubilising solution (PSS, 1 M 6-aminocaproic, 50 mM bistris at pH 7.0), supplemented with 0.5% (v/v) n-Dodecyl-B-D-Maltoside and 0.1% (v/v) protease inhibitors (1M PMSF, 1 µg/mL Leupeptin and 1 µg/mL Pepstatin A) and incubated on ice for 15 min, with vortex every 5 min to ensure resuspension. Cells were centrifuged at 13,000 g for 15 min at 4°C and the supernatant was collected. The protein concentration was estimated using the Pierce™ BCA Protein Assay Kit (Thermo Fisher Scientific) and the absorbance was measured in a BioTek Cytation1 imaging reader at 562 nm wavelength, according to manufacturer's protocol. Total protein extracts were resolved on 4-20% Criterion TGX protein gels (Bio-Rad) and then transferred to a Trans-Blot Turbo nitrocellulose membrane (Bio-Rad). Signal intensity was detected by chemiluminescence using Clarity Western ECL Substrate (Bio-Rad) in the Bio-Rad ChemiDoc Imaging and image analysis was carried out using ImageJ v.2.0.0 software (NIH, USA).

The following antibodies were used in this PhD project:

Antibody	Species	Dilution	Incubation	Company	Product Code
Primary antibodies for SDS-PAGE					
GAPDH	Rb	1:10000	overnight	Proteintech	60004-1-Ig
HSP60	Rb	1:1000	overnight	Cell Signalling	4870
MIC60	Rb	1:1000	overnight	Proteintech	10179-1-AP
MT-ATP8	Ms	1:6000	overnight	Abcam	ab243667
MT-CO1	Ms	1:1000	overnight	Abcam	ab14705
MT-CYB	Ms	1:3000	overnight	Abcam	ab219823
MT-ND1	Rb	1:1000	overnight	Proteintech	19703-1-AP
OXPHOS cocktail	Ms	1:500	overnight	Abcam	ab110411
PGC-1α	Rb	1:500	overnight	Novus	NBP1-04676
PGRN	Gt	1:200	overnight	R&D	AF2420
TFAM	Rb	1:500	overnight	Sigma	SAB1401383
TOMM20	Rb	1:3,000	overnight	St. Cruz Biotec.	C0614
VDAC	Rb	1:1000	overnight	Cell Signalling	D73D12
β-Actin	Rb	1:10000	overnight	Proteintech	60008-1-Ig
β-tubulin	Rb	1:6,000	overnight	Abcam	ab6046
GAPDH	Rb	1:10000	overnight	Proteintech	60004-1-Ig
Primary antibodies for BN-PAGE and CN-PAGE					
NDUFB6	Ms	1:1,000	overnight	Abcam	ab110244
SDHA	Ms	1:1,500	overnight	Abcam	ab14715
UQCRC2	Ms	1:1,000	overnight	Abcam	ab14745
MT-CO2	Ms	1:6,000	overnight	Abcam	ab110258
ATP5A	Ms	1:6000	overnight	Abcam	ab14748
Secondary antibodies for fluorescence					
IRDye® 680LT	Gt anti-Ms	1:10000	1h at RT	LI-COR	926-68020
IRDye® 800CW	Gt anti-Rb	1:10000	1h at RT	LI-COR	926-32211
IRDye® 800CW	Dk anti-Gt	1:10000	1h at RT	LI-COR	926-32214
Secondary antibodies for chemiluminescence					
Gt anti-Ms		1:4,000	1h at RT	Dako	P0447
Gt anti-Rb		1:4,000	1h at RT	Dako	P0448
Rb anti-Gt		1:4,000	1h at RT	Dako	P0449

Table 2.6 List of primary and secondary antibodies used for western blot SDS-PAGE, BN-PAGE and CN-PAGE. Overnight incubation occurs at 4°C. Abbreviations: BN, blue native; CN, clear native; Dk, donkey; Gt, goat; Ms, mouse; PAGE, polyacrylamide gel electrophoresis; Rb, rabbit; RT, room temperature; SDS, sodium dodecyl sulphate.

Identifying the best loading control for western blot SDS-PAGE quantification of human post-mortem brains

Quantification of the western blot SDS-PAGE experiments required the identification of the best loading control. Three different housekeeping proteins (β-tubulin, β-actin and GAPDH) and one mitochondrial marker (TOM20) were assessed.

Equal protein amounts from human post-mortem brains, including 10 controls and 7 patients with *GRN* mutations, were ran in western blot SDS-PAGE (Fig. 2.6). GAPDH displayed the most stable signal across the different samples, followed closely by ACTB, whereas β-tubulin and TOM20 were not as consistent across brain samples. Hence, GAPDH was employed as the loading control for human brains when running WB SDS-PAGE.

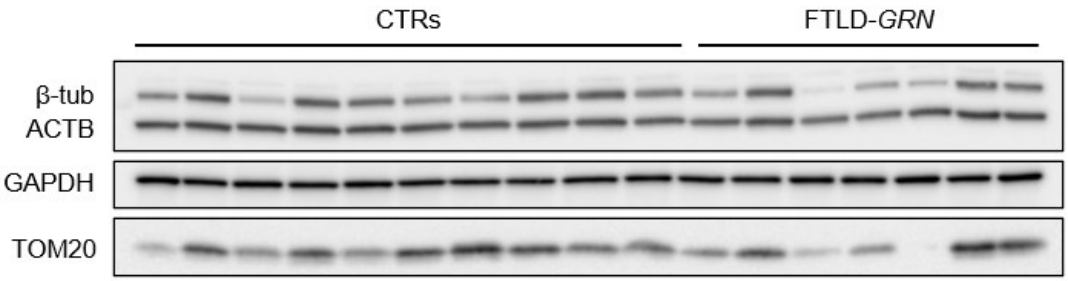

Figure 2.6 Identification of the best loading control for western blot SDS-PAGE quantification of human post-mortem brains. Western blot showing the protein expression of β-tubulin, β-actin, GAPDH and TOM20.

2.11 Seahorse assay

Cellular oxygen consumption rate (OCR) was quantified using the Seahorse XF96 Extracellular Flux Analyzer (Seahorse Bioscience). 15,000 H4 cells per well were seeded one day before in a Seahorse XF96 Cell Culture Plate. Prior to the experiment day, the XF sensor cartridge was hydrated with 200 µL of Seahorse XF Calibrant Solution, incubated overnight at 37°C in a CO_2-free incubator. The next day, adherent cells were washed with XF Assay Medium (comprising 1 gL^{-1} Seahorse XF Glucose, 1 mM Seahorse XF Pyruvate, 2 mM Seahorse XF L-Glutamine, all in Seahorse XF DMEM Medium) and incubated for one hour at 37°C in a CO_2-free incubator.

Compounds from Sigma that selectively target the OXPHOS system were introduced to assess the mitochondrial bioenergetics. These drugs included rotenone to inhibit CI, antimycin A to inhibit CIII, oligomycin to inhibit CV, and FCCP as an uncoupler of OXPHOS by transporting protons across the IMM (Fig. 2.7a). OCR measurements were recorded before and after the addition of 25 µL of each corresponding compound through injection ports labelled A to D in the following order: (A) 5 µM oligomycin, (B) 1 µM FCCP, (C) 2 µM FCCP, and (D) 0.5 µM/0.5 µM Antimycin A/Rotenone. These compounds facilitated the assessment of five distinct OCR parameters: basal respiration, proton leak, ATP-linked respiration, maximal respiration, and non-mitochondrial oxygen consumption. The non-mitochondrial oxygen consumption value was subtracted from all other parameters to obtain accurate mitochondria-specific values (Fig. 2.7b).

After measurements, H4 cells were stained with 5 µM Hoechst 33342 (Thermo Fisher Scientific) for 30 min. The number of cell nuclei, which served as a proxy for cell count, was quantified in each well using ImageXpress. This count was then used to normalise the Seahorse OCR experimental readings.

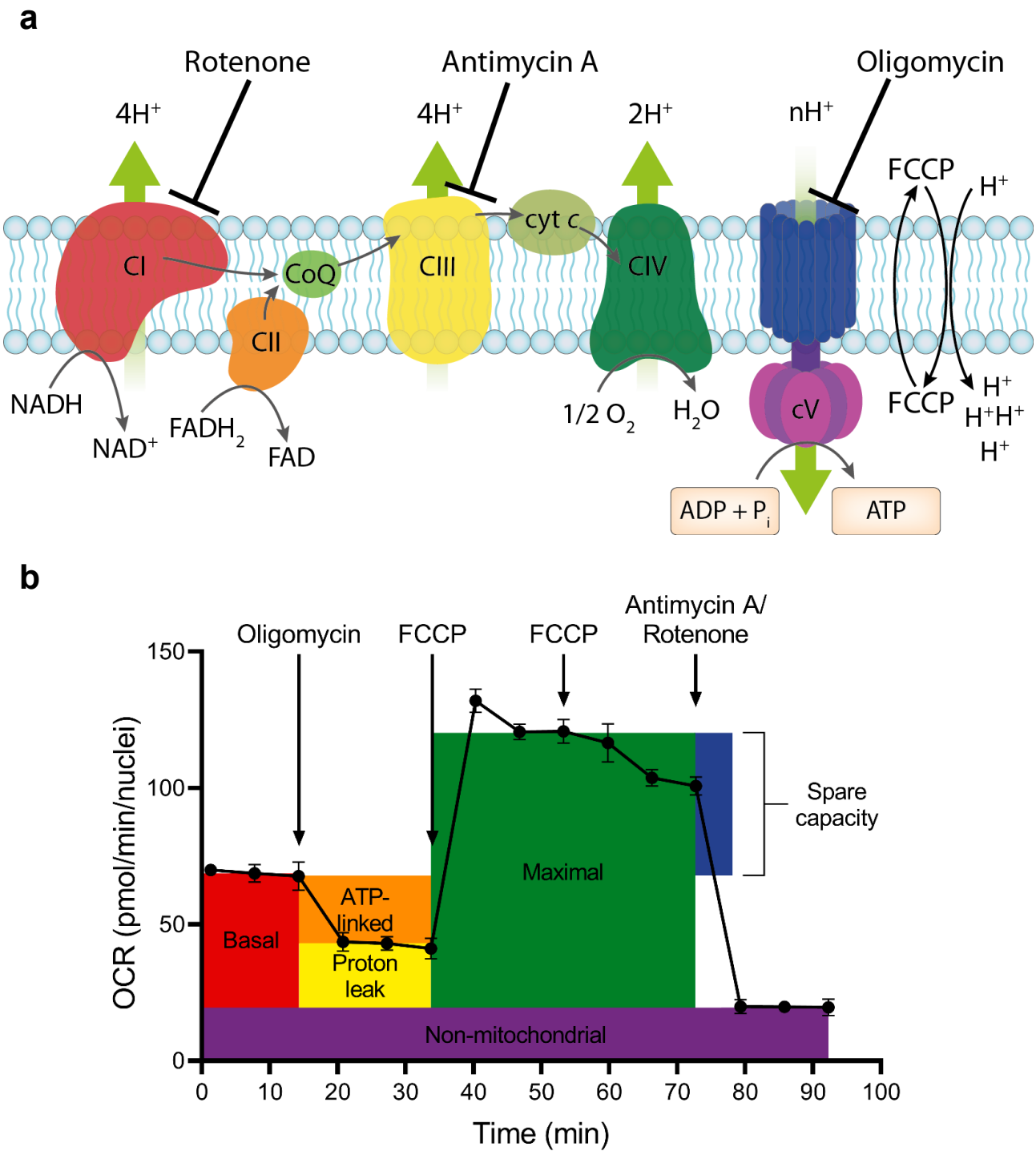

Figure 2.7 Seahorse XF Analyser experimental design and theoretical trace. a Experimental design utilised oligomycin, FCCP and Rotenone/Antimycin A, consecutively. **b** Theoretical trace depicting basal respiration, OCR associated with ATP turnover, proton leak, maximal respiration, spare reserve capacity, and non-mitochondrial oxygen consumption.

2.12 Blue Native- and Clear Native-Polyacrylamide Gel Electrophoresis

Native protein extraction and quantification

In order to isolate the intact protein complexes, cell pellets were lysed in x1 protein solubilising solution (PSS, 1 M 6-aminocaproic, 50 mM bistris at 7.0 pH), supplemented with 0.5% (v/v) n-Dodecyl-B-D-Maltoside (DDM) and 0.1% (v/v) protease inhibitors (1M PMSF, 1 mg/mL Leupeptin and 1 mg/mL Pepstatin A) and incubated on ice for 15 min, with vortex every 5 min to ensure resuspension. Cells were centrifuged at 13,000 g for 15 min at 4°C and the supernatant was collected. The protein concentration was estimated using the Pierce™ BCA Protein Assay Kit and the absorbance was measured in a BioTek Cytation1 imaging reader at 562 nm wavelength following the manufacturer's protocol.

Gel pouring protocol

The following components were prepared as follows: Acrylamide-bis (48% acrylamide, 1.5% bis-acrylamide (49.5%T 3%C) at 4°C), 3x gel buffer (1.5 M 6-aminocaproic acid, 150 mM bis-tris at 4°C), 10% ammonium persulphate (APS) at 4°C, and water-saturated butanol (1:1 volumes of ddH_2O and butan-2-ol).

Gradient 3-12% gels were prepared using a gradient gel pouring apparatus and a pump. 200 µL H_2O-saturated butanol were added after the 3-12% gradient solutions had been poured. After polymerisation, the butanol was rinsed and the 3% stacking gel solution was added together with the comb.

The 3%, 12% and stack gel solutions were mixed as follows:

	3% solution	12% solution	3% stack solution
Acrylamide-bis	0.744 mL	2.44 mL	0.38 mL
3x gel buffer	3.96 mL	3.3 mL	2.0 mL
ddH_2O	3.55 mL	2.51 mL	3.12 mL
APS	70 µL	35 µL	50 µL
TEMED	10 µL	5 µL	5 µL
Glycerol	-	1.98 g	-

Table 2.7 Preparation of 3% solution, 12% solution and 3% stack solution used for gel pouring. Abbreviations: APS, 10% Amonium persulphate; TEMED, Tetramethylethylenediamine.

Running of BN-PAGE and CN-PAGE

BN-PAGE and CN-PAGE were run to either quantify the mitochondrial complexes assembly expression or the mitochondrial complexes activity. Regardless of the objective, BN-PAGE and CN-PAGE were run relatively the same way, except for the cathode buffer being used. The following buffers were prepared in advance and stored at 4°C:

Buffer	Measurement	Components
AB	BN-PAGE and CN-PAGE	50 mM bistris at pH 7.0
CBa	BN-PAGE CI-V	50 mM tricine, 15 mM bistris, 0.02% Serva blue G at pH 7.0
CBb	BN-PAGE CI activity	50 mM tricine, 15 mM bistris at pH 7.0
CBc	CN-PAGE, CV assembly and activity	50 mM tricine, 15 mM bistris, 0.05% Triton X-100, 0.05% DOC
CBd	CN-PAGE, CII activity	50 mM tricine, 15 mM bistris, 0.02% DDM, 0.05% DOC
TB	For transfer of BN-PAGE and CN-PAGE	25 mM tris-base, 192 mM glycine, 20% methanol

Table 2.8 Preparation of buffers for BN-PAGE and CN-PAGE. CI activity and CV assembly were used using both BN-PAGE and CN-PAGE as part of the optimisation protocol. Abbreviations: AB, anode buffer; BN, blue-native; CI-V, complexes I to V; CBa, cathode buffer A; CBb, cathode buffer B; CBc, cathode buffer C; CBd, cathode buffer D; CN, clear-native; DDM, n-Dodecyl-B-D-Maltoside; DOC, sodium deoxycholate; TB, Towbin's buffer.

For BN-PAGE, equal protein amounts were mixed in x1 PSS buffer, supplemented with 0.5% (v/v) DDM, and loading buffer (1 M 6-aminocaproic acid, 5% Serva blue G). For CN-

PAGE, equal amounts of the protein were mixed in x1 PSS buffer, supplemented with 0.5% (v/v) DDM, 5% glycerol and x1 Ponceau S solution.

Gels were assembled in a Mini-PROTEAN Tetra Cell and the inner chamber was filled with cathode buffer A (CBa), cathode buffer B (CBc) or cathode buffer D (CBd) depending on the experiment as specified on Table 2.8, and anode buffer (AB) was added into the tank to cover the anode. For BN-PAGE detection of CI-V assembly, gels were run at 100 V for 15 min, and then run at 4 mA fixed current per gel – or 8 mA for two gels – until the front ran off. For BN-PAGE in-gel activity staining of CI, gels were run at 100 V for 15 min using CBa, followed up by a change of cathode buffer to cathode buffer B (CBb) at 4 mA fixed current per gel until the front ran off. For CN-PAGE in-gel activity staining of CII and CV, gels were run in their corresponding cathode buffers at 100 V for 15 min, and then run at 4 mA fixed current per gel until the front runs off.

Transfer of BN-PAGE and CN-PAGE

The Immobilon®-P PVDF transfer membrane was briefly submerged in methanol, following equilibration in Towbin's buffer (TB). The gel holder cassette was assembled in the following order: sponge, 1 Whatman 3MM paper, gel with samples, wet transfer membrane, 1 Whatman 3MM paper and sponge. The Mini Trans-Blot cell was inserted in the Bio-Rad Mini-PROTEAN electrophoresis system and submerged in TB. The blot was transferred at 100 V for 1.25 h. Once the protein was transferred, the membranes were wet in methanol three times and washed in PBS-T (phosphate-buffered saline 0.3% TWEEN 20). Membranes were blocked with 10% (v/v) milk powder in PBS for 1 hour with agitation on a plate shaker, followed by two rinses in PBS-T.

Primary antibodies were diluted in PBS-T and applied overnight at 4°C with agitation on a roller mixer. The primary antibody was removed, and the membranes were washed three

times in PBS-T for 10 min each time with agitation on a roller mixer. Membranes were incubated with the secondary antibodies in a dilution in PBS-T for 1 hour at room temperature with agitation on a roller mixer. The secondary solution was removed and the membranes were washed three times in PBS-T, 10 min each time with agitation in a roller mixer. Table 2.6 shows the list of the primary and secondary antibodies that were used with BN-PAGE and CN-PAGE. The membrane was incubated with 1:1 Peroxide Solution:Luminol/Enhancer Reagent Clarity Western ECL Substrate (BioRAD) for 5 min, signal intensity was detected with ChemiDoc^{TM} Imaging System and image analysis was carried out using ImageJ.

BN-PAGE and CN-PAGE in-gel activity staining

BN-PAGE and CN-PAGE were also run for in-gel activity staining of the mitochondrial CI, CII and CV. Gels were briefly rinsed with dH_2O after transfer, and followed up by the staining which varies between the different complexes:

- NADH dehydrogenase (CI) stain: 30 ml 2 mM Tris·HCl (pH 7.4), 3 mg NADH and 75 mg of nitroblue tetrazolium (NBT).
- Succinate dehydrogenase (CII) staining: 30 ml 2 mM Tris-HCl (pH 7.4), 84 mM Na+ succinate, 0.2 mM N-methylphenazonium methylsulphate and 2.5 mg/ml of NBT.
- ATPase (CV) staining: 50 ml 34 mM Tris, 270 mM glycine, 14 mM $MgSO_4$, 0.2% $Pb(NO_3)_2$, 8 mM ATP (pH 7.8) were added to the gel and incubated for 1-2 hours at 37°C with agitation. After dH_2O washes, the gel was briefly incubated with 1% ammonium sulphide ($S(NH_4)_2$) solution. This converts the white $Pb_3(PO_4)_2$ precipitate into a black/brown PbS precipitate.

Once the signal desired has been achieved, colour images were captured using a mobile phone for illustration purposes. Black-and-white images were acquired with ChemiDoc™ Imaging System and bands were quantitatively analysed using ImageJ.

Identifying the best relative measurement for BN-PAGE and CN-PAGE quantification of H4 cells

Quantification of the BN-PAGE and CN-PAGE experiments required the identification of the best relative measurement. Four different markers were assessed: stain-free gel, stain-free blot, β-tubulin and TOMM20. CI and CII signal obtained from BN-PAGE were used in this optimisation protocol.

The samples used for BN-PAGE and CN-PAGE were mixed with x1 Laemmli sample buffer (Bio-Rad). Equal amounts of the protein and protein marker were separated on 4-12% Mini-PROTEAN TGX Stain-Free Precast Gels (Bio-Rad) using x1 Tris/Glycine/SDS Running Buffer (Bio-Rad). Visualisation of the protein separation was captured using a stain-free imager in the pre-transferred gel (Fig. 2.8). The proteins were transferred to a Trans-Blot Turbo 0.2 µm PVDF membrane (Bio-Rad) using the Trans-Blot Turbo 29 Transfer System, and the protein was visualised by capturing a stain-free image of the blot (Fig. 2.8). Blocking, primary antibodies, secondary antibodies and read-outs were performed as previously mentioned. β-tubulin was employed as a standard protein marker and TOM20 as a mitochondrial mass marker (Fig. 2.8). Table 2.8 contains information on these two antibodies.

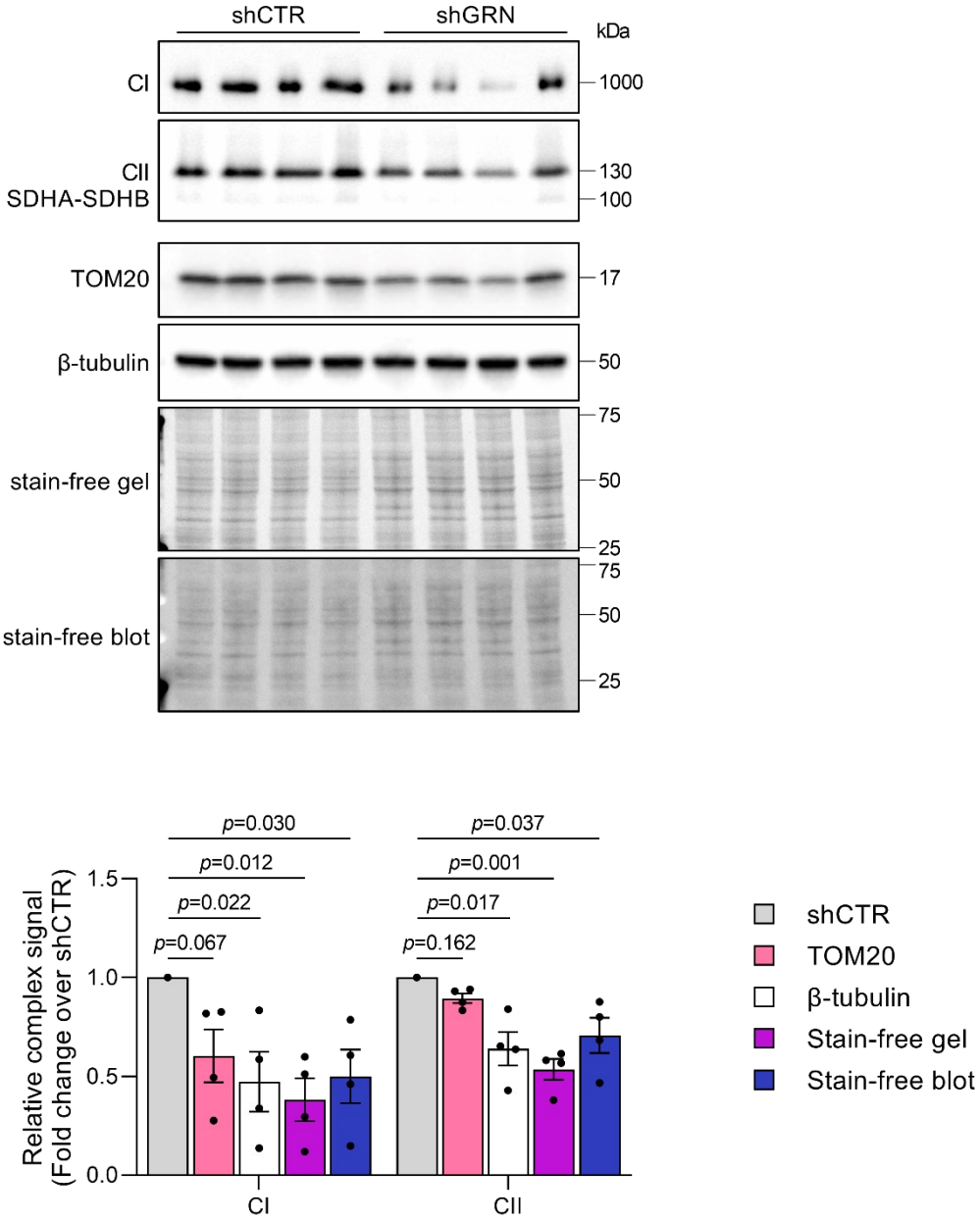

Figure 2.8 Identification of the best relative measurement for BN-PAGE and CN-PAGE quantification of H4 cells. Western blot and summary bar showing the shGRN H4 complexes signal relative to stain-free gel, stain-free blot, β-tubulin and TOMM20. Data are expressed as mean±SEM, where each data point represents a technical replicate; one-way ANOVA with Tukey's multiple comparison test.

The relative complex signal over the stain-free gel displayed the most statistically significant decrease in complexes assembly, while both the stain-free blot and β-tubulin presented a similar trend with a modest decrease. Finally, the relative signal over TOM20 was the only not significant decrease, implying that mitochondrial mass may affect the observed OXPHOS assembly changes, a topic that will be discussed in this thesis. In summary, β-

tubulin was selected as the preferred relative measurement due to its status as a well-established housekeeping protein and its relative complex assembly signal falling within the range between the stain-free gel and the stain-free blot.

Optimising the assessment of CV assembly

The signal from the different complexes was initially assessed using BN-PAGE. However, CV did not maintain a stable native form when using BN-PAGE, and the split signal originated from the CV, the F_1 subcomplex of CV and the ATP5A protein (Fig. 2.9a). This limitation made the quantification of CV inaccessible. As an optimisation step, CV signal was measured in CN-PAGE, in which the native form was better preserved with no F_1 subcomplex or ATP5A signal (Fig. 2.9b). The scientific rationale was that the cathode buffer used in the CN-PAGE employed Triton X-100 and 0.05% sodium deoxycholate, which are milder non-ionic detergents that preserved better the CV structure[213,214]. Therefore, CN-PAGE was employed to measure and quantify CV signal.

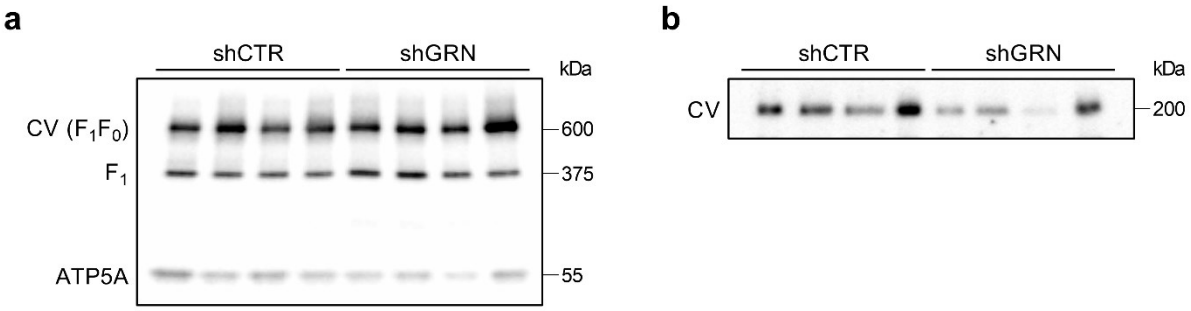

Figure 2.9 Comparison of CV signal using a) BN-PAGE and b) CN-PAGE in H4 cells.

2.13 Citrate synthase activity assay

Citrate synthase is a nuclear-encoded mitochondrial matrix enzyme involved in the TCA cycle. Citrate synthase activity can be used as a mitochondrial enzyme marker to quantify the presence of mitochondrial content in a sample. Overall, citrate synthase catalyses the following reaction:

$$\text{Acetyl-CoA} + \text{oxaloacetate}^{2-} + H_2O \rightarrow \text{citrate}^{3-} + \text{CoA-SH} + H^+$$

where the presence of the free sulfhydryl (SH) groups of the released CoA-SH represents citrate synthase activity.

The citrate synthase activity assay was based on Srere's method[215], in which free SH can be measured by using 5,5'-dithiobis-(2-nitrobenzoate), also known as DTNB or Ellman's reagent. The reaction of DTNB with the -SH group on CoA resulted in a colorimetric increase at 412 nm due to mercaptide ion's strong absorption (ε = 14,150 M^{-1} cm^{-1}), which was measured at pH 7.4-9.0. Protein extraction was performed using Triton-X. The assay solution was prepared at a final concentration of 100 mM Tris-HCl (pH 8.0), 200 µM Acetyl-Coenzyme A (Sigma-Aldrich), 100 µM oxalacetic acid (Sigma-Aldrich) and 200 µM DNTB (Sigma-Aldrich). 10 µL of each sample were added to 990 µL of the assay solution, and 200 µL of each sample mixture were added in triplicates to a 96-well plate. An additional water blank was used. Absorption was measured against time using BioTek Gen5 Data Analysis Software in a BioTek Cytation 1 imaging plate reader at 412 nm, pre-warmed at 30°C.

Citrate synthase activity was calculated as follows:

$$\text{citrate synthase activity} = (\text{mean } V_{max_{sample}} - \text{mean } V_{max_{water}}) / (\varepsilon * p) * DF / PC$$

where mean Vmax was the mean of the maximum rate of the triplicates, ε was the absorption molar (14,150 M^{-1} cm^{-1}), p was the path length in centimetres (0.85 cm), D was the dilution factor (1000/volume of sample), and PC was the protein concentration for each sample (mg/mL, previously calculated). The final activity was calculated based on the average of the different biological examples, expressed as µmol min^{-1} mg^{-1}.

2.14 Cytochrome *c* oxidase activity assay

The COX activity assay measured the rate of oxidation of reduced cytochrome *c*, a haem protein that transfers electrons between CIII and CIV of the respiratory chain. This method was carried out based on Wharton and Tzagoloff's paper[216], which provides a read-out of mitochondrial activity employing a spectrophotometric approach.

Ferrocytochrome *c* was prepared by the reduction of 1 g of horse heart ferricytochrome *c* (Sigma-Aldrich) with 13 mg of L-ascorbic acid in 100 mL of 100 mM KP_i at pH 7.0, followed by extensive dialysis in 10 mM K^+ phosphate buffer at pH 7.0 at 4°C, and was stored at −80°C. This protocol used a Hitachi spectrometer pre-warmed at 30°C. Samples were measured at a wavelength of 550 nm. 750 µL of ddH_2O and 100 µL of 0.1 M K^+ phosphate buffer were added to a cuvette, which was warmed at 30°C in a water bath. 140 µL of reduced ferrocytochrome *c* were added to the mix in two cuvettes, and once the absorbance stabilised after 30-40 sec, 10 µL of K^+ ferricyanide were added to the reference cuvette. The difference in the content of reduced cytochrome *c* between the reference and blank cuvettes represented the maximum absorbance.

For the H4 samples, 5 µL of the protein suspension (dilution 1:200) were added to the mix instead of K^+ ferricyanide, and the absorbance was measured over 5 min. For the brain samples, 10 µL of the protein suspension (1:100) were mixed instead. Each sample was measured in three or four technical replicates to ensure high precision. The COX activity was measured using the absorbance values for four time points t = 0, 1, 2 & 3 (where t = 0 represents the start of the reaction rate) and the following formulae:

$$\text{cyt } c \text{ activity} = \sum(\ln A\ t=0 - \ln A\ (t=n)) * DF / PC$$

where ∑ was the average of different technical replicates, ln was the natural logarithm, A was the absorption, n was the time points (min), DF was the dilution factor (1000/volume of sample), and PC was the protein concentration (mg/mL, previously calculated). The final activity was calculated based on the average of the different biological examples, expressed as k min^{-1} mg^{-1}.

2.15 IHC staining of pTDP-43 in human FFPE brains

For pTDP-43 staining, FFPE brain sections were baked for 1 hour at 60°C. IHC staining was performed in the BenchMark ULTRA IHC System according to the validated protocol at the National Hospital for Neurology and Neurosurgery (NHNN), Queen Square, the UK's largest dedicated neurological and neurosurgical hospital. The protocol included deparaffinisation at 72°C, followed by three washes with EZ Prep (mild detergent), antigen retrieval with CC1 (tris-based buffer) for 32 min at 91°C, washes with reaction buffer (tris-based buffer), and OptiView Peroxidase Inhibitor for 4 min at 36°C. After washes with reaction buffer, the sections were incubated with the primary antibody pTDP-43 (phosphorylated Ser409/410, 1:2,000, CosmoBio, CAC-TIP-PTD-P01) for 44 min at 36°C, followed by washes with reaction buffer. Then, the slides were incubated with the reagents in the OptiView DAB IHC Detection Kit: OptiView HQ Universal Linker for 8 min at 36°C, OptiView HRP Multimer for 8 min at 36°C, OptiView H_2O_2 and OptiView DAB simultaneously for 8 min at 36°C, and OptiView Copper for 4 min at 36°C; all with washes in between. This detection kit is an indirect, biotin-free system for detecting primary antibodies by producing a visible brown precipitate. Tissues were counterstained with haematoxylin for 12 min and then bluing reagent for 4 min to create a brown-blue contrast that facilitates the detection of pTDP-43 staining. Finally, the slides were placed in the HistoCore SPECTRA Workstation (Leica Biosystems), where they underwent dehydration through graded alcohols, were cleared in xylene and then coverslipped.

The specificity of the pTDP-43 antibody was validated by using a slide with cortical region of a patient brain with confirmed pTDP-43 proteinopathy from the NHNN (Fig. 2.10). It is important to note that pTDP-43 staining is known to vary between cases and may extend beyond pathological TDP-43. These considerations will be taken into account when interpreting the quantification results.

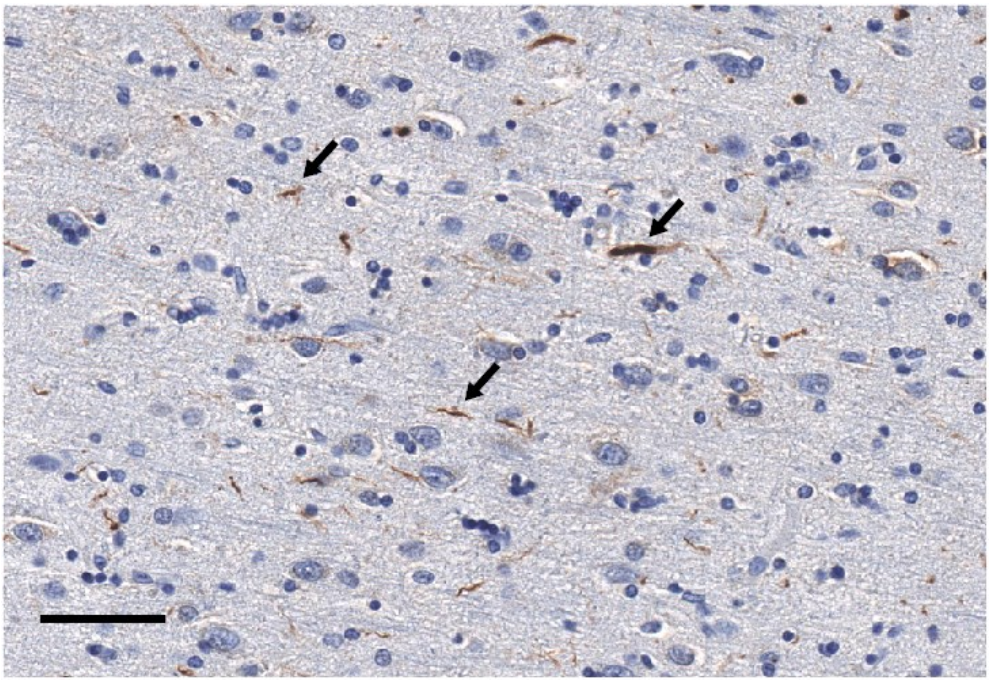

Figure 2.10 Positive control validating the pTDP-43 antibody. Arrows indicate some of the pTDP-43 aggregates. Scale bar = 50 μm.

Developing a quantification method to assess pTDP-43 signal in FFPE brains

The pTDP-43-stained sections were digitally scanned on the Hamamatsu NanoZoomer S60 scanner. Images were loaded into QuPath software for the quantification of pTDP-43 burden in the human post-mortem brains of FTLD-*GRN* patients in comparison to controls and sporadic FTLD-TDP patients.

A semi-automatic method was developed to accurately detect and quantify pTDP-43 burden. A combination of scripts and manual inputs were used and the workflow was as follows:

1st STEP: Ten random squares, each 500x500 μm, were drawn and analysed in the area of interest within each region for each case.

2nd STEP: The following scripts shown in Figure 2.11 were developed and ran on QuPath. The values for the Stain 1 (Haematoxylin) and Stain 2 (3,3′-diaminobenzidine, DAB) were initially calculated as an average of the value across different regions and cases.

Subsequently, the parameters were manually adjusted to optimise the detection of DAB signal, based on visual observations.

```
1  //setting image to Brightfield with DAB staining
2  setImageType('BRIGHTFIELD_H_DAB');
3
4  //setting stain parameters
5  setColorDeconvolutionStains('{"Name" : "H-DAB modified",
6                               "Stain 1" : "Hematoxylin", "Values 1" : "0.618 0.619 0.486",
7                               "Stain 2" : "DAB", "Values 2" : "0.376 0.570 0.718",
8                               "Background" : " 255 255 255"}');
9
10 //defining annotations
11 annotations = getAnnotationObjects()
12 for (anno in annotations){
13 def cell = PathObjects.createCellObject(anno.getROI(), null, null, null)
14 getCurrentHierarchy().addObject(cell)
15 }
16
17 //Quantify pTDP-43 signal in all the objects
18 selectAllObjects()
19 runPlugin('qupath.imagej.detect.cells.SubcellularDetection', '{"detection[DAB]":0.25,
20           "doSmoothing":true,"splitByIntensity":false,"splitByShape":false,
21           "spotSizeMicrons":1,"minSpotSizeMicrons":0.3,"maxSpotSizeMicrons":10.0,
22           "includeClusters":true}')
23
24 print 'Done!'
```

Figure 2.11 QuPath scripts to quantify pTDP-43 burden. Note that the function setColorDeconvolutionStains (lanes 5-8) and the function *runPlugin* (lanes 19-22) were distributed as columns for easier visualisation for the thesis, but these functions should be continuous lanes when running on QuPath. Comments can be found explaining the scripts.

3rd STEP: The following key parameters were obtained after running the script: pTDP-43 DAB area, number of single pTDP-43 DAB spots, number of pTDP-43 DAB clusters (i.e., several single spots closely neighbouring each other), and estimated number of pTDP-43 DAB spots (i.e., including single spots and individual spots forming the clusters). A representation of pTDP-43 differentiating between clusters (dark brown) and single spots (orange) can be found in Figure 2.12.

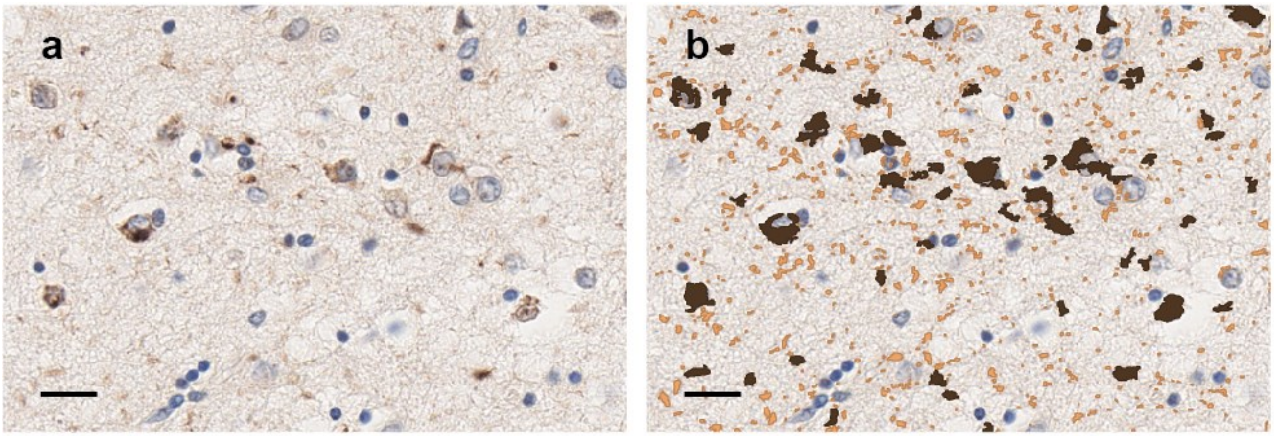

Figure 2.12 Single spots and clusters of pTDP-43 in human brain sections. a pTDP-43 antibody in human post-mortem brain. **b** After running the scripts, QuPath distinguishes between single spots (orange) and clusters (brown). Scale bar = 20 μm.

4th STEP: Since there is not an agreement on the best quantification method of pTDP-43 burden, three different quantitative approaches were explored and compared to select the best one(s):

1) Percentage of pTDP-43-stained area: based on the surface area that is pTDP-43-stained over the total area.

$$\text{pTDP-43 burden (\% stained/mm}^2) = \sum \frac{\text{pTDP-43-stained area}}{\text{Total area}}$$

The remaining two approaches focused on the QuPath software's classification of pTDP-43-stained inclusions in stained sections. One approach quantified the number of clusters, the characteristic hallmark of pTDP-43 aggregations. The other approach identified individual spots of pTDP-43, encompassing both multiple spots forming clusters and single spots, the latter of which may not necessarily be considered pathologically relevant. In summary, these two approaches were:

2) Number of pTDP-43 clusters: counting the number of pTDP-43 clusters over the total area.

$$\text{pTDP-43 burden (\# clusters/mm}^2) = \sum \frac{\text{Number of pTDP-43 clusters}}{\text{Total area}}$$

3) Total number of pTDP-43 spots: accounting for individual pTDP-43 spots that may be gathered in clusters or single spots.

$$\text{pTDP-43 burden (\# spots/mm}^2) = \sum \frac{\text{Number pTDP-43 spots}}{\text{Total area}}$$

2.16 IHC staining of MT-CO1 in human FFPE brain samples

Figure 2.13 presents an overview of IHC staining for MT-CO1 in FFPE brain sections. The process involves a biotinylated secondary antibody, a streptavidin conjugated HRP (Horseradish Peroxidase) and DAB for protein localisation.

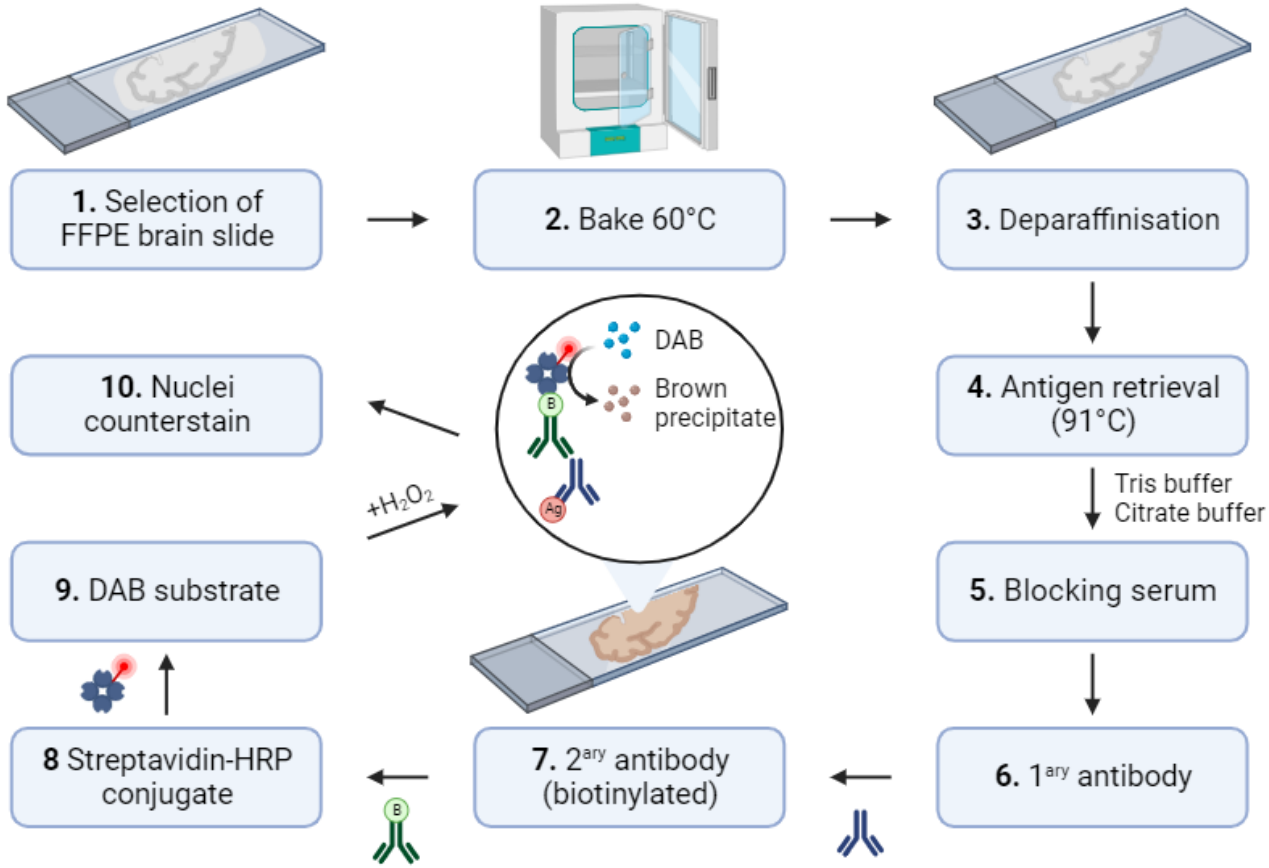

Figure 2.13 Overview of workflow for peroxidase-streptavidin IHC staining. Abbreviations: Ag, antigen; B, biotin; DAB, diaminobenzidine; FFPE, formalin-fixed paraffin-embedded; HRP, horseradish peroxidase.

Brain sections were baked for 1 hour at 60°C. Deparaffinisation and antigen retrieval were performed in the DISCOVERY ULTRA Research Staining System (Roche Diagnostics). The sections were deparaffinated, washed three times with EZ Prep (mild detergent) at 69°C, followed by antigen retrieval with CC1 (tris-based buffer) for 16 min at 91°C and then CC2 (citrate-based buffer) for 16 min at 91°C.

Manual staining was performed for the remaining steps due to its superior results compared to machine staining for the antibody MT-CO1. After washing with EZ Prep, sections were circled with a hydrophobic liquid blocker pen and blocked with 5% sheep serum (Sigma-Aldrich) in PBS + 0.5% bovine albumin serum (BSA, Sigma) for 1 hour at room temperature (RT). The primary antibody MT-CO1 (1:200, Abcam, ab14705) was diluted in PBS + 0.5% BSA, and the sections were incubated with the primary antibody solution for 1h at RT, followed by five washes of 3 min with PBS + 0.1% BSA.

To develop biotin-streptavidin amplification, slides were incubated with IgG biotinylated anti-mouse secondary antibody (1:200, Cytiva, RPN1004), diluted in PBS + 0.5% BSA, for 1 hour at RT and then washed with PBS + 0.1% BSA. The sections were then incubated in streptavidin-HRP conjugate (1:100, Cytiva, RPN1231) for 1 hour at RT and washed with PBS + 0.1% BSA. Hydrogen peroxide and DAB tablets (Sigma-Aldrich, D4168) were dissolved separately in a ratio of 1 tablet:500 µL distilled water and added to the sections, which were incubated for 15 min at RT. After distilled water washes, nuclei were counterstained using Harris' Haematoxylin (VWR, 1:15) for 45 sec, followed by tap water rinses. Finally, slides were placed in the HistoCore SPECTRA Workstation (Leica Biosystems) for dehydration through graded alcohols, clearing in xylene, and coverslipping.

The IHC staining of MT-CO1 followed the standard operating protocol within the Department of Neuropathology, Queen Square. However, the original protocol did not include a blocking step, leading to a high background signal in the negative control staining (Fig. 2.14a), which compromised the reproducibility and validity of MT-CO1 staining. To address this issue, an additional blocking step using sheep serum successfully eliminated the background signal in the negative control (Fig. 2.14b).

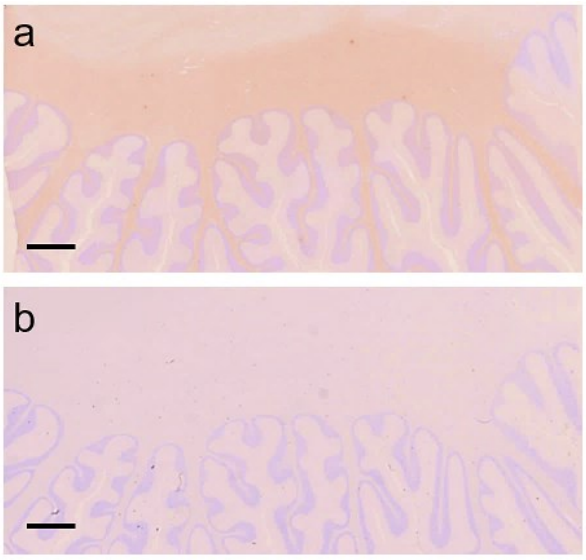

Figure 2.14 Optimisation of the peroxidase-streptavidin staining adding a blocking serum. a Negative control staining without blocking step. **b** Negative control staining using sheep blocking serum. Scale bar = 2.5 mm

2.17 *MT-ND5* RNAscope ISH assay

RNAscope *in situ* hybridisation (ISH) is a molecular biology technique used to detect and localise DNA and/or RNA molecules, enabling visualisation of the spatial distribution and abundance of specific gene patterns within cells and tissues.

A simplification of the RNAscope ISH protocol involves 1) permeabilization to allow probes access to DNA/RNA, 2) hybridisation of ~20 double Z probe pairs to the complementary sequence, 3) amplification (typically based on chromogenic or fluorescent detection methods), 4) spatial signal visualisation, and 5) data analysis and quantification (Fig. 2.15).

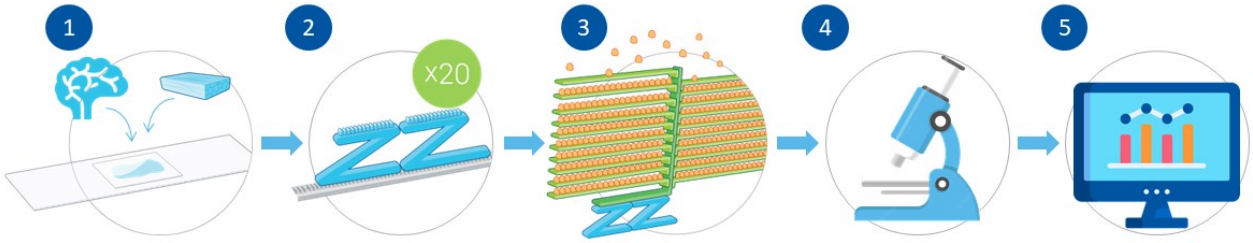

Figure 2.15 Schematic representation of the RNAscope ISH workflow. The protocol consists of five main steps: 1) permeabilisation of the tissue, 2) probe hybridisation, 3) signal amplification (the yellow beads represent the probe and the green objects are amplifiers), 4) visualisation, and 5) data analysis and quantification (Adapted from ACDBio website).

With the aim of targeting mtDNA, an innovative aspect of this experimental work involves the utilisation of a sense strand *MT-ND5* probe (Hs-MT-ND5-sense, ACDBio). Specifically designed for the RNAscope assay, this custom-designed mitochondrial 20ZZ probe targets the reverse complement sequence of 238-1527 of NCBI Reference Sequence: NC_012920.1 (mitochondrial genome coordinates 12337-14148), binding exclusively to the negative strand of mtDNA and not RNA

Optimising the *MT-ND5* CISH RNAscope assay in skeletal muscle

Previously, *MT-ND5* staining had only been carried out in fresh-frozen skeletal muscle using fluorescence techniques. Leveraging the optimised RNAscope Multiplex Fluorescent V2 Assay (ACDBio), this technique was used to detect the *MT-ND5* probe in skeletal muscle as a proof-of-concept of the results typically obtained from RNAscope (Fig. 2.16). This showcased the characteristic punctate signal indicative of successful hybridisation and amplification of the probe to the mtDNA target. While this project predominantly focused on RNAscope chromogenic *in situ* hybridisation (CISH), the protocol for fluorescent RNAscope was not described, but can be found in [217] or on the manufacturer's ACDBio website.

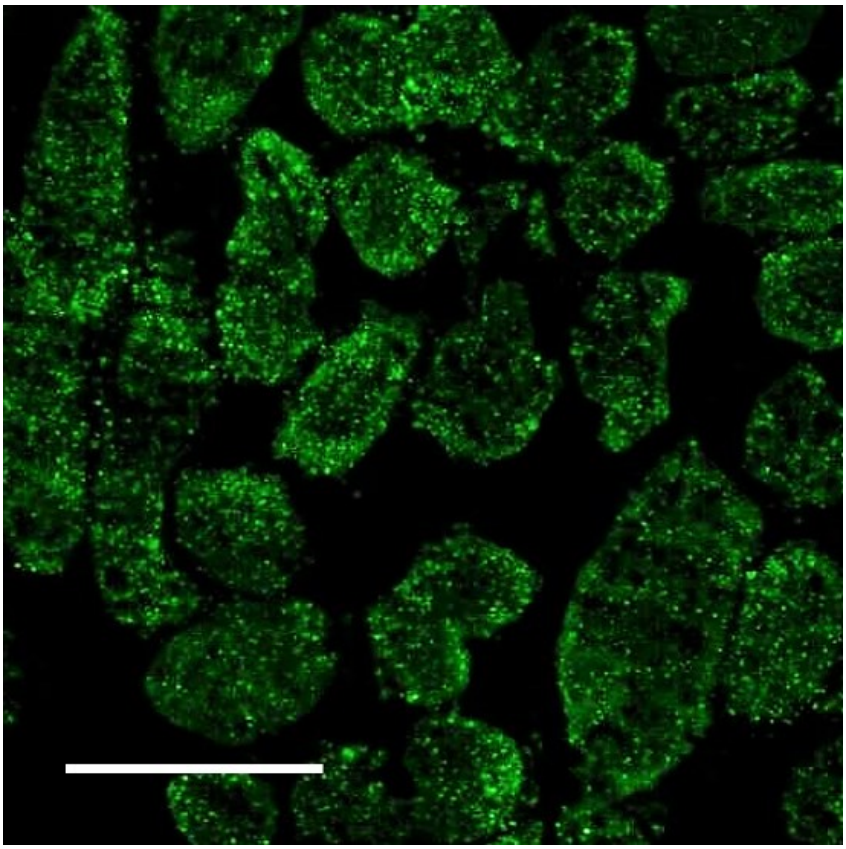

Figure 2.16 MT-ND5 signal using RNAscope fluorescence in fresh-frozen skeletal muscle. Scale bar = 250 µm.

To minimise autofluorescence in FFPE brain sections, the experimental work required the optimisation of the *MT-ND5* probe using RNAscope CISH staining. As part of the optimisation pipeline, I interrogated whether the use of formalin fixation and antigen target

retrieval could disrupt the binding sites of the probe in the epitopes, and consequently the specificity of the mtDNA probe. 7 µm serial sections of fresh-frozen skeletal muscle were prepared by Darren Chambers using the CM1860 UV Cryostat (Leica Biosystems). I then used for hybridisation of the *MT-ND5* probe using the RNAscope 2.5 HD Reagent Kit-RED assay (ACDBio). This technique will be described in more detail later in the next subsection as part of the brain experimental optimisation. Half of the sections were preserved as fresh frozen, while the other half underwent formalin fixation with 10% neutral buffered formalin (NBF) for 2 hours, followed by antigen retrieval. Three different RNAscope probes from ACDBio were applied to fresh-frozen and formalin-fixed sections: *MT-ND5*, ubiquitin as positive control, and a negative control probe (Fig. 2.17).

MT-ND5 demonstrated successful performance in both fresh-frozen and formalin-fixed skeletal muscle sections, displaying a ubiquitous-like signal distribution with variations in mtDNA levels among different fibres. Positive and negative controls were effective, producing abundant ubiquitous signal and an absence of signal, respectively. Surprisingly, *MT-ND5* signal was stronger in formalin-fixed skeletal muscle sections compared to fresh-frozen sections. This result may be attributed to the formalin fixation better preserving tissue integrity during the pretreatment process. In addition, the antigen retrieval step may be exposing epitopes more effectively in formalin-fixed sections than in fresh-frozen sections which did not undergo antigen retrieval. Hence, it is evident that the *MT-ND5* probe performs well with RNAscope CISH staining of formalin-fixed skeletal muscle within the specified duration of fixation. However, it should be noted that tissue type and duration of fixation may affect staining outcomes, and this conclusion may not directly apply to the FFPE brain sections.

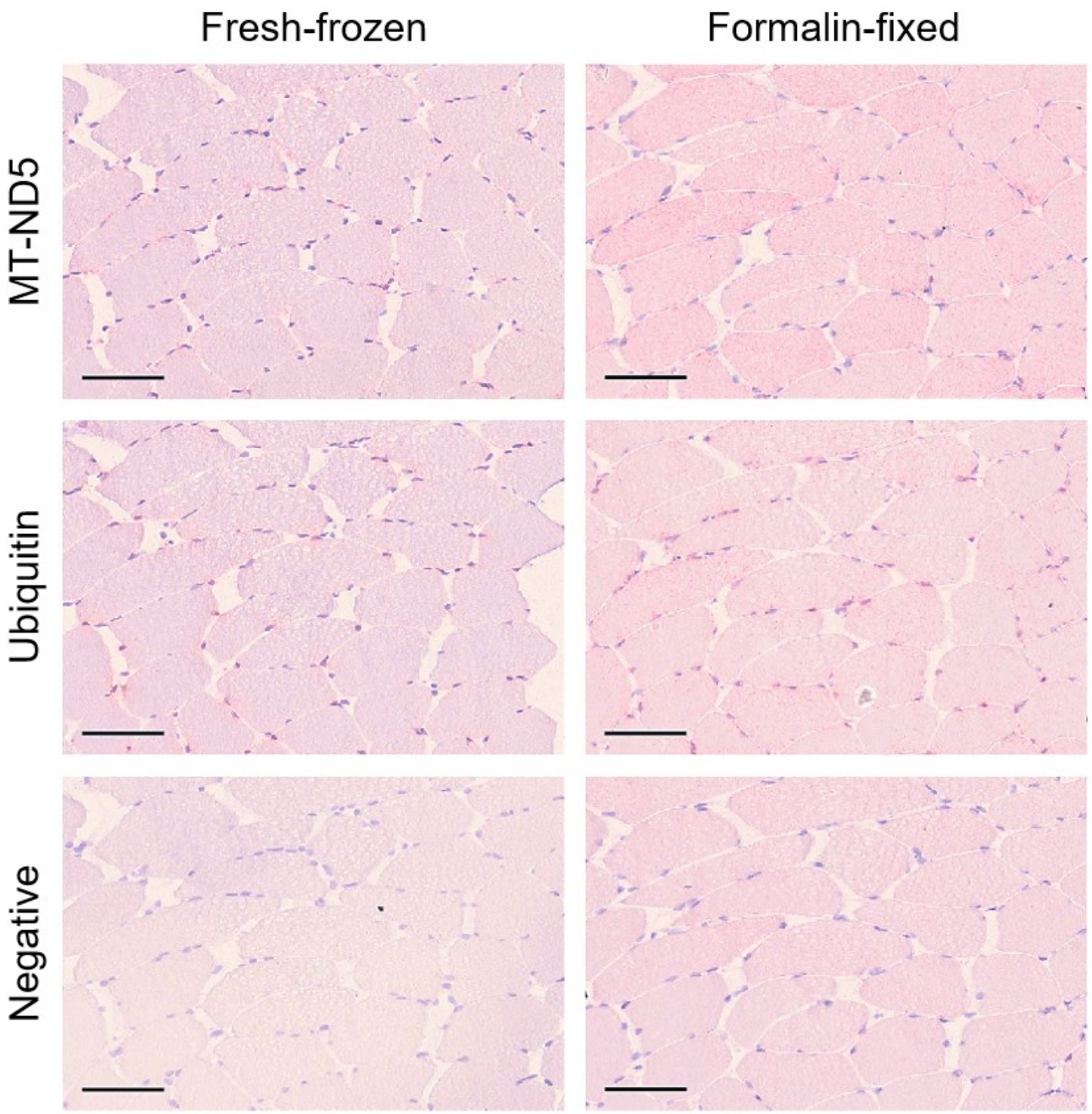

Figure 2.17 Validating RNAscope mtDNA probes in fresh-frozen and formalin-fixed skeletal muscles. Scale bar = 50 μm.

Optimising the *MT-ND5* CISH RNAscope assay in brain samples

Once the mtDNA probes had been validated in formalin-fixed skeletal muscles, RNAscope CISH was carried out in FFPE brains. An overview of the RNAscope 2.5 HD Reagent Kit-RED assay is represented in Figure 2.18.

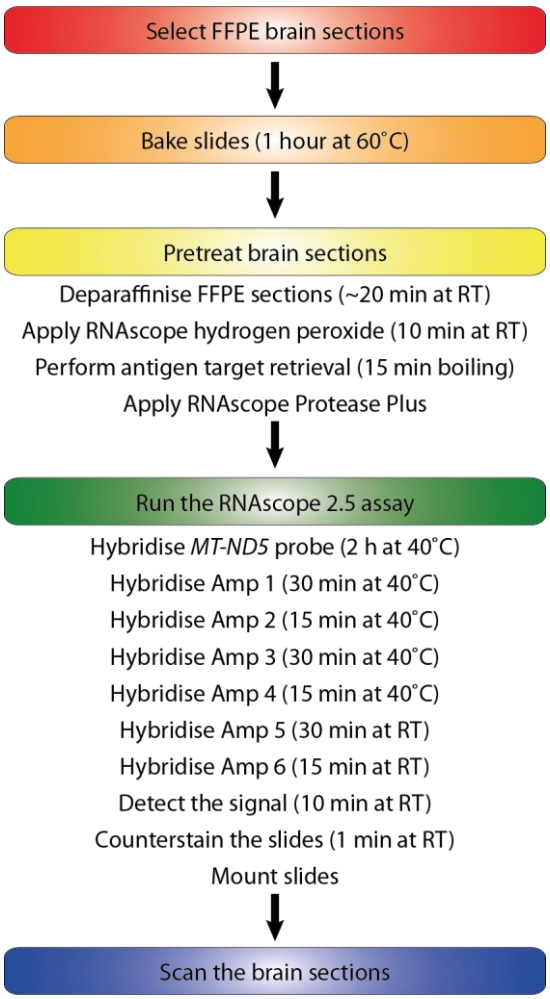

Figure 2.18 Overview of workflow for the RNAscope 2.5 assay. Abbreviation: FFPE, formalin-fixed paraffin-embedded; RT, room temperature.

FFPE brain sections were selected and baked for 1 hour at 60°C. They were then deparaffinised by incubation in xylene for 5 min at RT, fresh xylene for 5 min at RT, 100% ethanol for 2 min at RT and fresh 100% ethanol for 2 min at RT . After completely drying the slides in an oven for 5 min at 60°C, sections were incubated with hydrogen peroxide for 10 min at RT and washed in distilled water. Antigen retrieval was performed in boiling

RNAscope 1X target retrieval reagent for 15 min followed by a brief rinse in distilled water and transfer to 100% ethanol for 3 min at RT. The slides were left to dry overnight at RT.

The following day, a barrier was created around each sample using a hydrophobic liquid blocker pen. Brain sections were incubated with RNAscope Protease Plus for 30 min at 40°C, followed by washes in distilled water. For the RNAscope 2.5 assay, the following steps were followed: *MT-ND5* probe hybridisation for 2 hour at 40°C, Amp 1 hybridisation for 30 min at 40°C, Amp 2 hybridisation for 15 min at 40˚C, Amp 3 hybridisation for 30 min at 40˚C, Amp 4 hybridisation for 15 min at 40˚C, Amp 5 hybridisation for 30 min at RT and Amp 6 hybridisation for 15 min at 40˚C, all of them followed by washes in x1 wash buffer. Fast RED-B and Fast RED-A were mixed in a 1:60 ratio and added to the sections for 10 min at RT. The slides were then counterstained in Haematoxylin, washed with tap water, dried for at least 15 min at 60˚C, briefly submerged in xylene and coverslipped. Finally, the stained sections were digitally scanned using a Hammatsu NanoZoomer S60 scanner.

The specificity of the *MT-ND5* probe was validated by adding 200 U/mL DNase I (QIAGEN) or 50µg/mL RNase A (Thermo Fisher Scientific) for 30 min at 40˚C to brain sections. This step took place between the antigen target retrieval and the RNAscope Protease Plus steps. DNase I treatment results in the elimination of the *MT-ND5* probe expression (Fig. 2.19a), whilst RNase A treatment did not cause any effects (Fig. 2.19b), confirming that the probe specifically binds to DNA and not RNA.

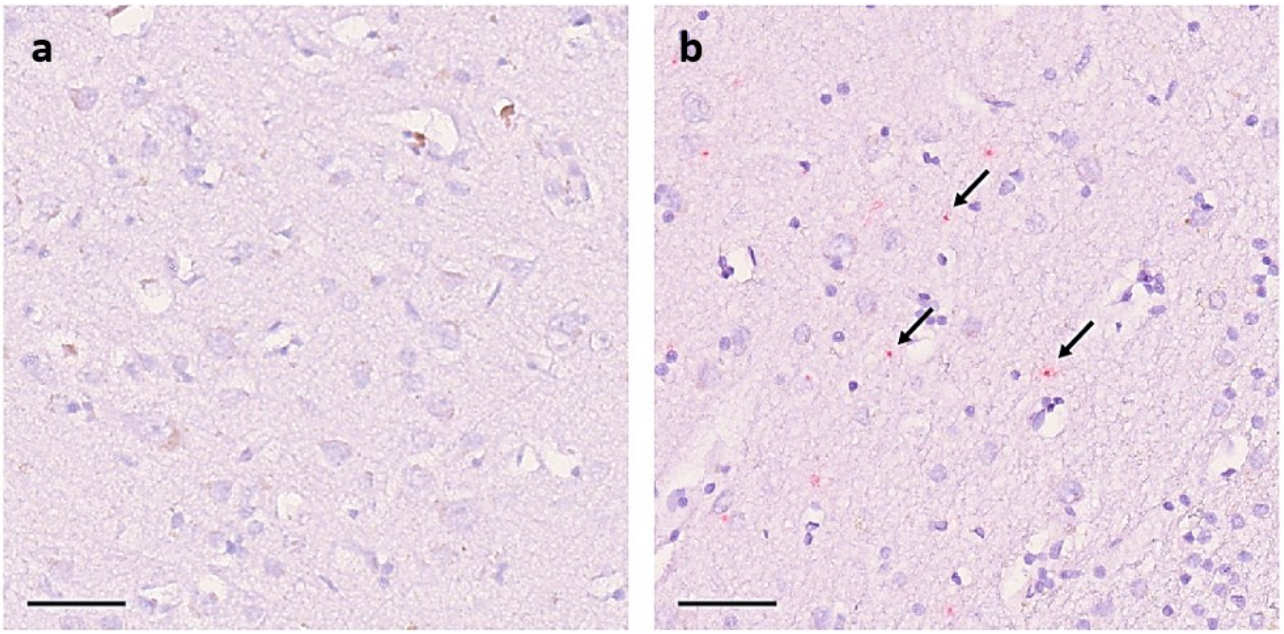

Figure 2.19 Validation of the *MT-ND5* RNAscope probe in brain sections. a DNase I and (**b**) RNase A treatment of brain tissues. Arrows indicate *MT-ND5* signal. Scale bar = 50 μm.

Developing a quantification method to assess *MT-ND5* signal in FFPE brains

Based on the validation and optimisation of the *MT-ND5* probe in skeletal muscles and brains, RNAscope CISH was carried out in FTD sections as previously described. After scanning, stained images were loaded into QuPath software to quantify the *MT-ND5* spots in the FG and FW regions across FTLD-*GRN* cases, sporadic FTLD-TDP cases and controls. A semi-automatic method was designed for the quantification of *MT-ND5* spots, which required a combination of coding scripts and minimal manual inputs. A summary of the workflow is described as follows:

1st STEP: Ten random squares, each 500x500 µm, were drawn and analysed in the area of interest within each region for each case.

2nd STEP: The following scripts shown in Figure 2.20 were developed and ran on QuPath. Stain vectors for haematoxylin and the *MT-ND5* probe were initially estimated based on the average of tissue expression across different biological cases (Fig. 2.20a). Subsequently, the parameters were adjusted to optimise the detection of *MT-ND5* spots, ensuring the quantification of specific probe signal while minimising non-specific signal, based on visual observations. The annotation was then manually selected and loaded on the scripts (Fig. 2.20b) to detect the nuclei from the haematoxylin stain, generating an object from the annotation. Finally, the object from the annotation was manually selected and the scripts on Fig. 2.20c were ran to quantify the number of *MT-ND5* spots.

a

```
//Set image type
setImageType('BRIGHTFIELD_OTHER');

//Set stains settings
setColorDeconvolutionStains('{"Name" : "H-DAB modified", "Stain 1" :
                            "Hematoxylin", "Values 1" : "0.52907 0.7531 0.39105",
                            "Stain 2" : "DAB", "Values 2" : "0.24807 0.83025 0.49915",
                            "Stain 3" : "Residual", "Values 3" : "0.46916 0.68023 0.56319",
                            "Background" : " 255 255 255"}');
```

b

```
//Detects nuclei in the selected annotation
runPlugin('qupath.imagej.detect.cells.WatershedCellDetection',
          '{"detectionImageBrightfield":"Hematoxylin OD","requestedPixelSizeMicrons":0.5,
          "backgroundRadiusMicrons":8.0,"backgroundByReconstruction":true,
          "medianRadiusMicrons":0.0,"sigmaMicrons":1.5,"minAreaMicrons":10.0,
          "maxAreaMicrons":400.0,"threshold":0.13,"maxBackground":2.0,
          "watershedPostProcess":true,"excludeDAB":false,"cellExpansionMicrons":5.0,
          "includeNuclei":true,"smoothBoundaries":true,"makeMeasurements":true}')

//Unlocks the annotation
getSelectedObjects().each {
   it.setLocked(false)
}
fireHierarchyUpdate()

//Creates an object out of the whole annotation
def selected = getSelectedObject()
def cell = PathObjects.createCellObject(selected.getROI(), null, null, null)
getCurrentHierarchy().addObject(cell)

print 'Done!'
```

c

```
//Counts DAB spots and clusters
runPlugin('qupath.imagej.detect.cells.SubcellularDetection',
          '{"detection[DAB]":0.20,"detection[Residual]":-1.0,"doSmoothing":true,
          "splitByIntensity":false,"splitByShape":false,"spotSizeMicrons":0.5,
          "minSpotSizeMicrons":0.3,"maxSpotSizeMicrons":16.0,"includeClusters":true}')

print 'Done!'
```

Figure 2.20 QuPath scripts to quantify *MT-ND5* spots using RNAscope assay. Note that the function setColorDeconvolutionStains on (**a**) (lanes 5-8) and the functions *runPlugin* on (**b**) (lanes 2-8) and on (**c**) (lanes 2-5) were distributed as columns for easier visualisation for the thesis, but these functions should be continuous lanes when running on QuPath. Comments can be found explaining the scripts.

A visual explanation of the scripts can be found in Figure 2.21. Overall, the scripts were run on the scanned brain section (Fig. 2.21a), enabling the identification and quantification of the haematoxylin-stained nuclei (Fig. 2.21b) and the *MT-ND5* spots generated by the probe (Fig. 2.21c). An overlap of both detections can be found in Figure 2.21d.

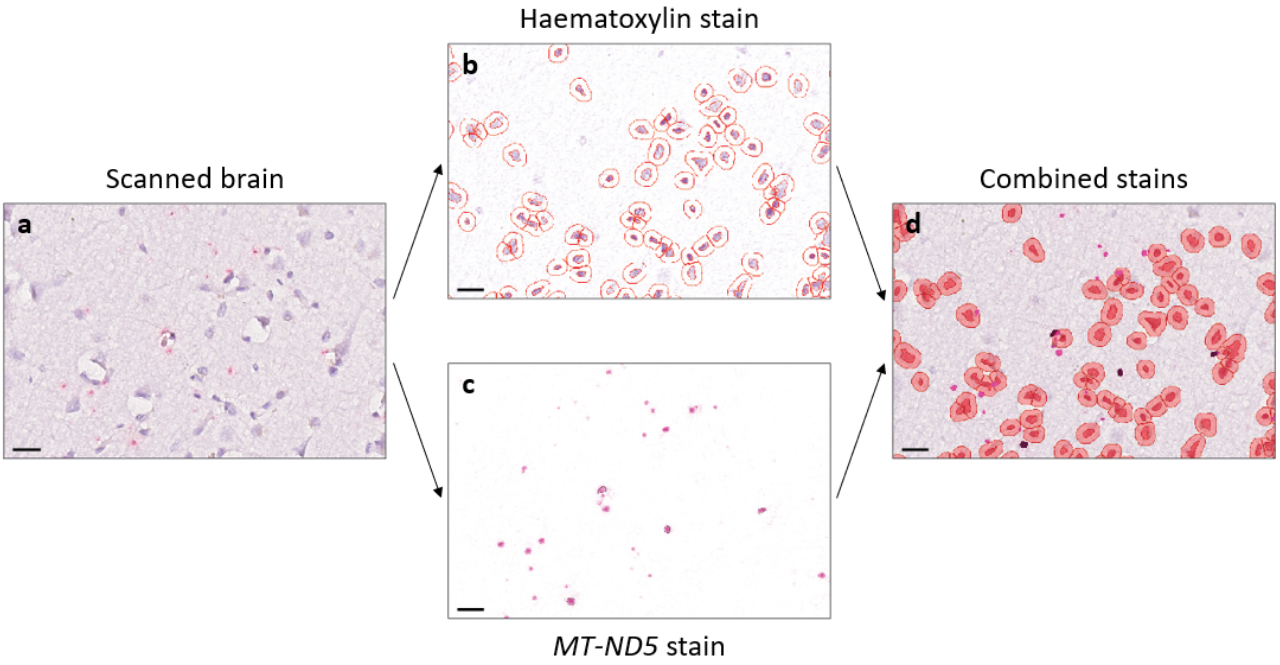

Figure 2.21 Visual workflow of *MT-ND5* spots quantification. a Original scanned brain. **b** Scripts detecting haematoxylin-stained nuclei. **c** Scripts detecting *MT-ND5* spots. **d** Combination of both *MT-ND5* (pink) and haematoxylin (red) stains. Scale bar = 20 µm.

3rd STEP: The following key parameters were obtained after running the script: number of nuclei and number of *MT-ND5* spots. The number of *MT-ND5* spots were then normalised to the area of the annotation and averaged across the ten annotations to give mean values in each region.

Finally, a validation of this new semi-automatic quantitative method was performed by comparison of the results to a manual counting of the *MT-ND5* spots. Measurements were taken in annotations across the FG and FW regions in various FTD cases and controls. The validation was assessed through a Pearson's correlation test (Fig. 2.22), demonstrating a robust correlation in both regions (R^2 = 0.975, p < 0.0001 for FG and R^2 = 0.965, p < 0.0001 for FW). These results confirmed the development of a fast and consistent quantitative method.

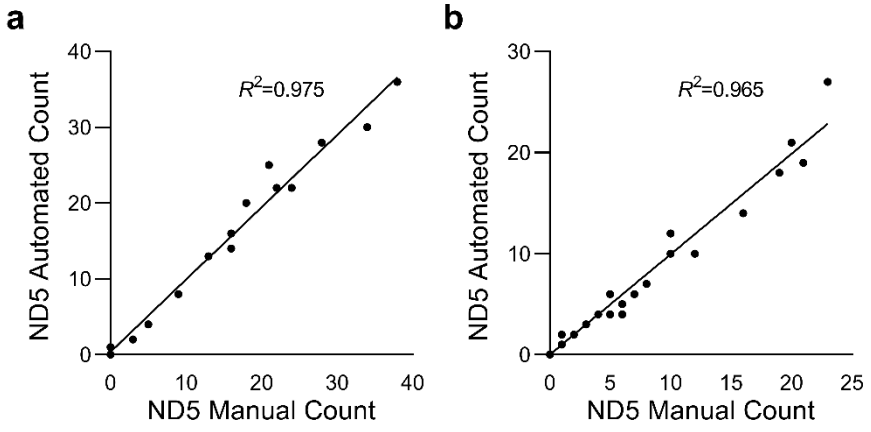

Figure 2.22 Comparison of the semi-automatic quantitative method and manual count for *MT-ND5* spots measurement. Strong Pearson's correlation in the (**a**) FG and (**b**) FW. Each dot represents an annotation measured in the brain section. Pearson's correlation test.

2.18 Statistical analysis

GraphPad Prism 9 was employed for statistical analysis and graph representation. Data are reported as mean ± standard error of the mean (SEM) of at least three biological replicates. Significance was determined using Student's *t*-test or one-way analysis of variance (ANOVA) with Tukey's multiple comparison test. Correlation was determined using Pearson's chi-squared test. Outliers analysis was conducted using Grubbs' test.

3 Investigating mitochondria in PGRN-deficient *in vitro* models

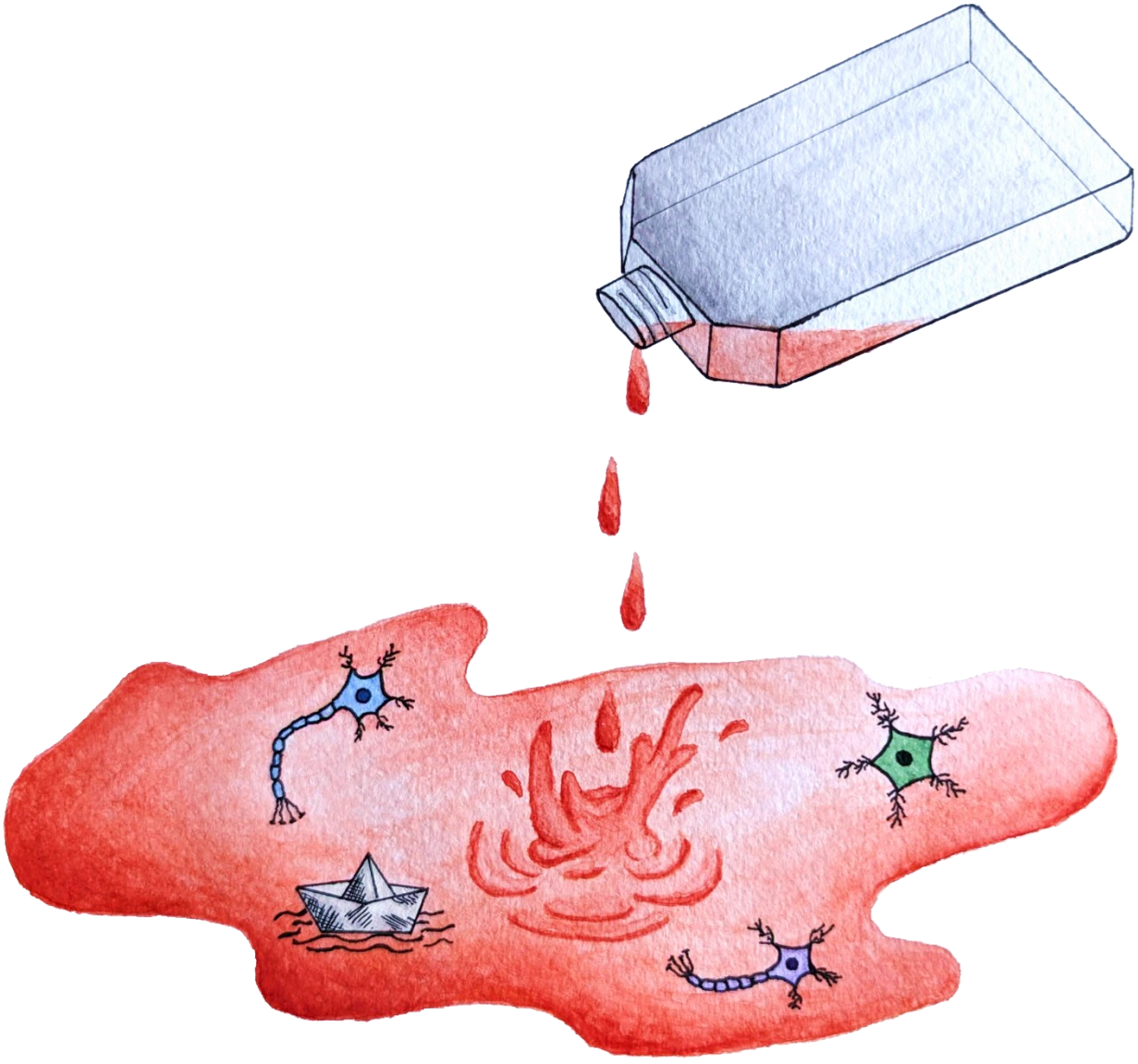

Neuronal ocean (watercolours) – by Javier S. Bautista

3.1 Introduction

The use of *in vitro* models for neurodegenerative studies

The nature of neurodegenerative diseases is characterised by the progressive loss of structure or function of neurons, primarily affecting the CNS. The limited availability of effective drugs for the treatment of neurodegenerative diseases reflects the complexity in aetiology and pathogenesis. In the timeline of drug development, basic research represents the initial milestone, usually carried out by a combination of *in vitro* models, animal models and human tissues. This is then followed up by drug discovery, pre-clinical studies, clinical trials and the review of the drug by Medicines and Healthcare products Regulatory Agency (MHRA) in the United Kingdom (UK) and the Food and Drug Administration (FDA) in the United States of America (USA). However, the recent failure of several clinical trials targeting neurodegenerative diseases highlights the need of better models to understand the pathomechanisms and to identify suitable therapeutic targets[218,219]. Therefore, during the basic research phase, the selection of optimal *in vitro* models with a high physiological relevance is essential to bridge the gap between the experimental results to pre-clinical animal models and humans.

In vitro models, derived from the Latin term “in glass”, refer to experiments conducted in a controlled environment outside a living organism, typically in a laboratory setting. These offer numerous advantages, including cost-effectiveness, ethical considerations, and the ability to control variables. Traditionally, *in vitro* models involved 2D-layer immortalised cell lines in cell culture flasks or plates that were derived from various tissues and organs, such as Henrieta Lacks (HeLa) cells, SH-SY5Y cells and H4 cells. These immortalised cell lines have been modified or selected to continue proliferating indefinitely, effectively bypassing the normal cellular aging and senescence that occurs in most primary cells. This removes

the need to use tissue, although they may present genetic abnormalities in comparison to normal human cells[220]. Immortalized cell lines have become indispensable tools, enabling the exploration of various aspects of cell biology, disease mechanisms and drug development.

Patient-derived human fibroblasts, which are common connective tissue cells, offer unique advantages for investigating the pathophysiology of neurodegenerative diseases. One of the key advantages of using this model is their ease of accessibility through minimally invasive skin biopsies. By culturing patient-derived fibroblasts, specific genetic mutations or pathological features can be investigating which provide a valuable platform for modelling the progression and physiology of neurodegenerative diseases. However, they may become senescent and grow slowly, especially in older individuals. While challenges remain, the use of fibroblasts as a cellular model for the study of neurodegenerative diseases offers a promising avenue of research, which can additionally be used to derive iPSCs.

By reprogramming fibroblasts into iPSCs and subsequently differentiating them into various cell types such as neurons, researchers can create patient-specific neuronal models for the study of neurodegenerative diseases. This methodology enables the investigation of disease mechanisms in a cellular context, assessing specific genetic mutations, environmental factors, or other variables impacting neuronal function and survival. This approach is particularly advantageous when studying diseases with complex aetiologies, such as AD and PD, providing a powerful tool for personalized medicine and drug discovery. Finally, although not used in this thesis, organoids represent another type of *in vitro* model with more sophisticated 3D structures that maintain key structural and functional aspects of real organs, closely mimicking the behaviour of neurons and brain tissues[221].

These *in vitro* cellular tools have expanded our understanding of the pathophysiology of conditions like AD, PD, Huntington's, ALS and FTD. Collectively, immortalised cell lines, patient-derived fibroblasts and iPSCs are enabling the exploration of disease mechanisms, the conduction of drug screenings and the development of potential therapies. The continued advancements in these models promise to unlock new insights and therapeutic breakthroughs in the pursuit to mitigate and control neurodegenerative diseases.

Characterising mitochondria in *GRN*-related FTD using *in vitro* models

The characterisation of mitochondria in neurodegenerative diseases has traditionally relied on the use of *in vitro* models due to the limited access to brain samples from FTD patients. Therefore, several culture models have been developed to study the pathogenicity of mitochondria in FTD, identifying potential pathomechanisms and drug targets. These are easy to genetically manipulate, providing with preliminary insights into the state of mitochondria.

In contrast to brain biopsies, human skin fibroblasts biopsies are not as invasive, providing patient-derived human cultures that possess the same genetic variance related to pathogenicity. Notably, fibroblasts reproduce metabolic changes observed in neurons, and reported mitochondrial dysfunction in fibroblasts can correlate with features observed in patients with neurodegenerative diseases[222,223].

Nowadays, cross-validation of the results in different experimental models is necessary to ensure the findings hold true across various approaches or systems, confirming their robustness and generalisability. This helps ensure that the observed effects or outcomes are not specific to a single model but are consistent and reproducible in different experimental setups or contexts. As an example, the 2014 study reporting a link between the FTD-related *CHCHD10* gene and mitochondrial function employed patients' fibroblasts to demonstrate respiratory chain deficiency and abnormal mitochondrial structure[177]. In addition, they used HeLa cells to confirm the previous results, genetically overexpressing mutant CHCHD10 and demonstrating an increase in mitochondrial network fragmentation and defective cristae maintenance.

The generation of iPSC-derived cells (e.g., neurons, microglia and astrocytes) have additionally enabled the characterisation of mitochondrial pathology in specific cell types

relevant to FTD. For instance, a study generated *c9orf72* iPSC-derived motor neurons from patients' fibroblasts and observed mitochondrial bioenergetic deficit and dysfunctional axonal homeostasis, which phenotype was later confirmed in human post-mortem samples[175]. Another study generated iPSC-derived neurons from patients of FTDP-17 with 10+16 MAPT mutation and observed oxidative stress and neurodegeneration[176].

This PhD project initially sought to determine whether mitochondrial dysfunction was involved in *GRN*-related FTD by using three *in vitro* models. These cell culture models included immortalised cell lines (specifically H4 neuroglioma cells and SH-SY5Y neuroblastoma cells), primary human skin fibroblasts and iPSC-derived neurons and astrocytes. Regarding the immortalised cell lines, H4 cells are derived from the brain of a 37-year-old white male with neuroglioma, and SH-SY5Y cells are derived from a bone marrow biopsy of a 4-year-old girl with metastatic neuroblastoma. Although SH-SY5Y cells are widely used in FTD research, their low expression of PGRN protein in comparison to H4 cells draws a significant limitation in their use to study *GRN*-related FTD[224]. Thus, due to the higher PGRN expression levels in H4 cells, the neuroglioma cell line was mostly used for the characterisation of mitochondria.

Fibroblasts from presymptomatic patients with *GRN* pathogenic mutations were used to validate the results obtained from the experimental work in H4 cells, exploring the mitochondrial molecular biology and any correlations between PGRN expression and mitochondrial function.

The final PGRN-deficient model in this thesis employed RNA extracted from iPSC-derived neurons and astrocytes. The deficiency of PGRN in neurons and astrocytes has been identified as key player in the development of *GRN*-related FTD, promoting synaptic

degeneration, neuronal stress, and TDP-43 proteinopathy[225–227]. Therefore, these two cell types represent an optimal model for the study of the neurodegenerative disease.

The iPSC lines were derived from four controls, three FTD patients with *GRN* mutations and an isogenic CRISPR series with control, heterozygous and homozygous *R493X* mutation lines. Heterozygous *GRN* mutations closely resemble the FTLD-*GRN* phenotype with PGRN haploinsufficiency, whereas homozygous mutations recapitulate neuronal ceroid lipofuscinosis-like phenotypes. Therefore, the two different degrees in *GRN* expression levels between heterozygous and homozygous mutations may indicate a *GRN* expression-dependent effect on mitochondrial function.

Overall, by employing these three different PGRN-deficient models, this chapter will characterise the state of mitochondria and provide new insights into the pathological hallmarks of *GRN*-related FTD.

3.2 Aims

The overall aim of this chapter was to characterise the state of mitochondria in three different *in vitro* models of *GRN*-related FTD from a biochemical, molecular and genetic approach.

The specific aims were:

- To generate a shGRN H4 cell model to characterise mitochondrial activity, function and genome in a PGRN-deficient model;

- To develop a shGRN SH-SY5Y cell model to briefly characterise mitochondria and compare its results to H4 cells;

- To investigate the molecular biology of mitochondria in skin fibroblasts derived from presymptomatic patients with *GRN* pathogenic mutations by exploring the mtDNA, transcripts and protein levels;

- To characterise the effect of *GRN* mutations in mitochondrial-encoded mRNA transcripts using iPSC-derived neurons and astrocytes, including a CRISPR series with an isogenic control, heterozygous and homozygous *GRN* mutation lines.

3.3 Materials and methods

Mitochondrial characterisation was carried out across various PGRN-deficient *in vitro* models, including immortalised cell lines (H4 neuroglioma and SH-SY5Y neuroblastoma cells), fibroblast from patients with pathogenic *GRN* mutations (a summary of the demographics is presented in Table 2.1), and iPSC-derived neurons and astrocytes. Mitochondria were predominantly investigated in the shGRN H4 cells based on to the robustness of the *GRN* KD model, the fast growth rate of the cell line facilitating the acquisition of material for all the experiments, and the physiological relevance of PGRN in microglia and consequently the closely related neuroglioma model.

A wide range of biochemical and molecular genetic techniques were carried out to investigate mitochondria in the *in vitro* models. The *GRN* KD validation was validated and characterised in the H4 cells by RT-qPCR, western blotting, cell proliferation assay and trypan blue cell proliferation, and in the SH-SY5Y cells by RT-qPCR. PGRN deficiency was also interrogated in the fibroblasts by RT-qPCR and western blotting. Mitochondrial bioenergetics in the shGRN H4 cells were measured by Seahorse assay, BN-PAGE, CN-PAGE and COX activity assay. Mitochondrial mass, biogenesis and content in the shGRN H4 cells were assessed by western blotting and citrate synthase activity assay. Mitochondrial genomics were investigated in the H4 cells by qPCR, RT-qPCR and western blotting, in the SH-SY5Y cells and the fibroblasts by qPCR and RT-qPCR, and in the iPSC-derived neurons and astrocytes by RT-qPCR. Finally, mitochondrial- and nuclear-encoded proteins were quantified in the H4 cells and the fibroblasts by western blotting. Detailed materials and methods can be found in chapter 2.

3.4 Results

Validation and characterisation of the shGRN H4 cell model

A stable *GRN* KD was generated in H4 neuroglioma cells using a lentiviral shRNA vector. The efficiency of gene KD was validated using RT-qPCR and western blotting (Fig. 3.1a, 3.1b), which confirmed a decrease in *GRN* transcription expression and PGRN deficiency. The shGRN H4 cell model was consequently employed to characterise the role of PGRN deficiency in mitochondrial function.

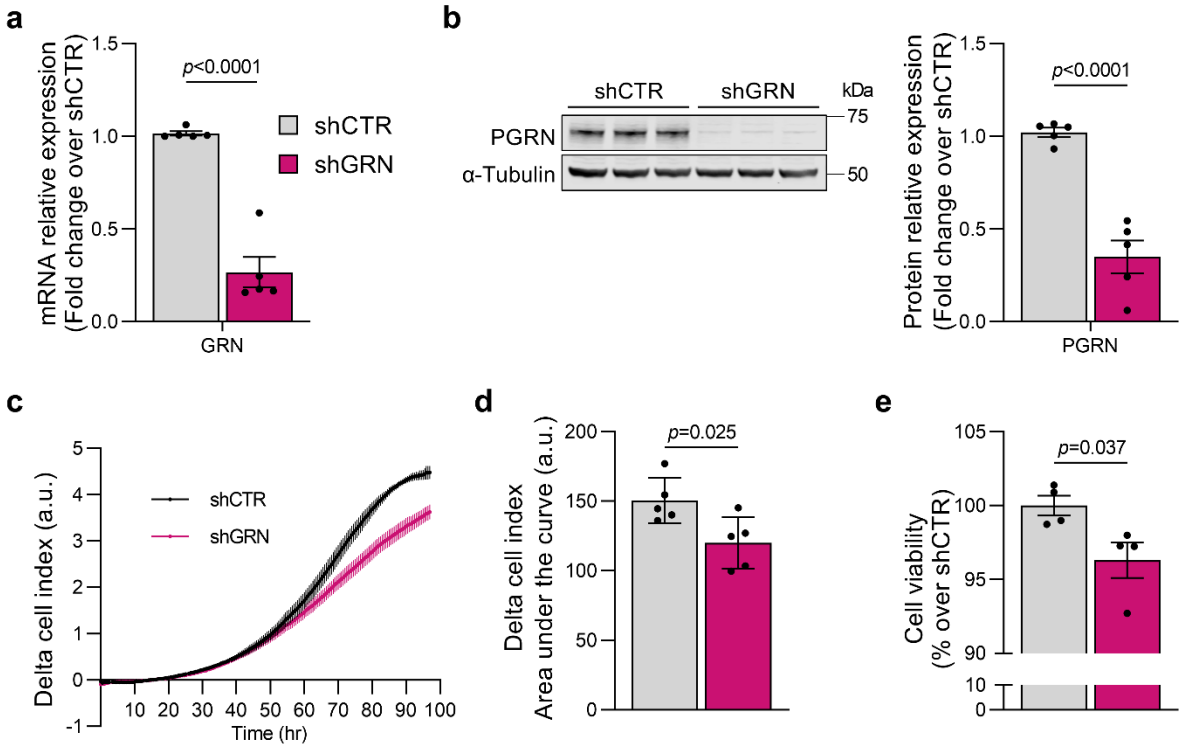

Figure 3.1 Validation and characterisation of the shGRN H4 cell model. a Relative expression of *GRN* mRNA in H4 cells analysed by RT-qPCR (*n=5*). **b** Representative western blot and summary graph bar showing significant decrease in PGRN protein (*n*=5). **c** Real-time cell proliferation of shCTR and shGRN H4 cells over 100 h using xCELLigence (*n*=5). **d** Comparison of delta cell index area under the curve between shCTR and shGRN cells (*n*=5). **e** Cell viability comparing shCTR and shGRN H4 cells (*n*=4). Data are expressed as mean±SEM, where each data point represents an independent passage, and it is the average of at least three technical replicates; unpaired *t*-test.

Real-time proliferation measurements of shGRN H4 cells showed a significant decrease in comparison to control cells over 100 h (Fig. 3.1c, 3.1d). Additionally, shGRN H4 cells exhibited a 5% decrease in cell viability (Fig. 3.1e). These findings suggested that PGRN deficiency leads to less healthy cells, which may be partially attributed to a slight increase in cell death, consistent with previous studies[199,228].

PGRN deficiency induces mitochondrial bioenergetic deficit in shGRN H4 cells

Energy generation represents the core function of the organelle and any changes may indicate mitochondrial dysfunction. Therefore, bioenergetics were initially assessed by measuring the oxygen consumption rate using the SeahorseFlux Analyser. A decrease in basal respiration, proton leak, ATP-linked respiration and maximal respiration was observed in shGRN H4 cells (Fig. 3.2a, 3.2b). These findings suggested an impairment in the ETC and/or mitochondrial substrate provision, necessary for electron flow maintenance.

Since the ETC is comprised by five different mitochondrial complexes, I proceeded to investigate whether the impairment in the assembly of a specific complex was involved in the mitochondrial bioenergetic deficits. The assembly of the mitochondrial complexes was interrogated using BN-PAGE (CI-IV) and CN-PAGE (CV). The assembly of (CI-IV) was found impaired, whereas CV assembly remained intact (Fig. 3.2c).

To assess the impact of impaired complexes assembly on their activity, this parameter was measured using BN-PAGE (CI) and CN-PAGE (CII and CV) in-gel activity assay following established methods[214]. CI activity was significantly decreased, whilst CII and CV showed a trend towards a decrease (Fig. 3.2d). COX activity as a proxy for CIV was spectrophotometrically measured, showing a reduction that further localised the impairment in mitochondrial activity and bioenergetic deficits (Fig. 3.2e). Overall, these observations suggested mitochondrial dysfunction as a pathological manifestation in *GRN*-related FTD.

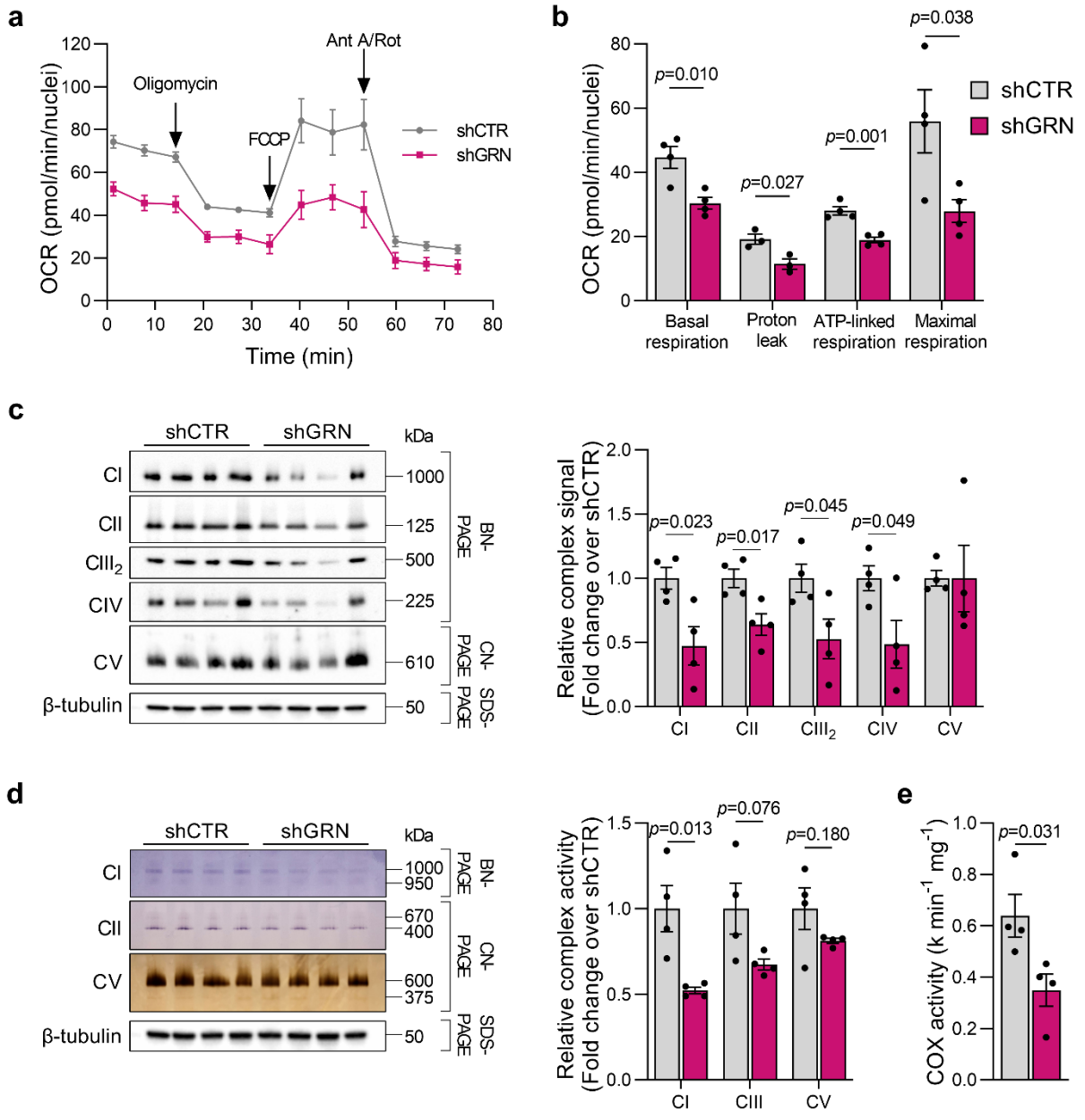

Figure 3.2 PGRN deficiency causes impaired mitochondrial bioenergetics in H4 cells. a Representative oxygen consumption rate curves as measured by the Seahorse Analyser, normalised to the total count of nuclei. **b** Summary bar graph of basal respiration, proton leak, ATP-linked respiration and maximal respiration (*n*=4). **c** Representative BN-PAGE (CI-IV) and CN-PAGE (CV) and summary bar graph showing the signal of the native complexes, relative to the SDS-PAGE membrane (*n*=4). **d** Representative BN-PAGE (CI) and CN-PAGE (CII and CV) and summary bar graph showing the complexes in-gel activity, relative to the SDS-PAGE membrane (*n*=4). **e** COX activity measurement in shGRN H4 cells (*n*=4). Data are expressed as mean±SEM, where each data point represents an independent passage, and it is the average of at least three technical replicates; unpaired *t*-test.

PGRN insufficiency decreases mitochondrial mass and biogenesis in shGRN H4 cells

Following the observation of an impairment in mitochondrial bioenergetics, I investigated whether this was due to a change in mitochondrial mass. By measuring different protein markers, it was determined that TOM20 protein levels, and consequently mitochondrial mass, were decreased, whilst VDAC and HSP60 showed no changes (Fig. 3.3a, 3.3b). A decrease in mitochondrial mass could be due to a downregulation of PGC-1α, the mitochondrial master regulator of biogenesis and function which has been associated with neurodegenerative disorders[229,230]. PGC-1α protein levels were indeed significantly reduced in shGRN H4 cells (Fig. 3.3c), which may account for the decrease in mitochondrial mass and bioenergetics in *GRN*-related FTD. Finally, the decrease in mitochondrial content was additionally confirmed by a decreased in citrate synthase activity in shGRN H4 cells (Fig. 3.3d).

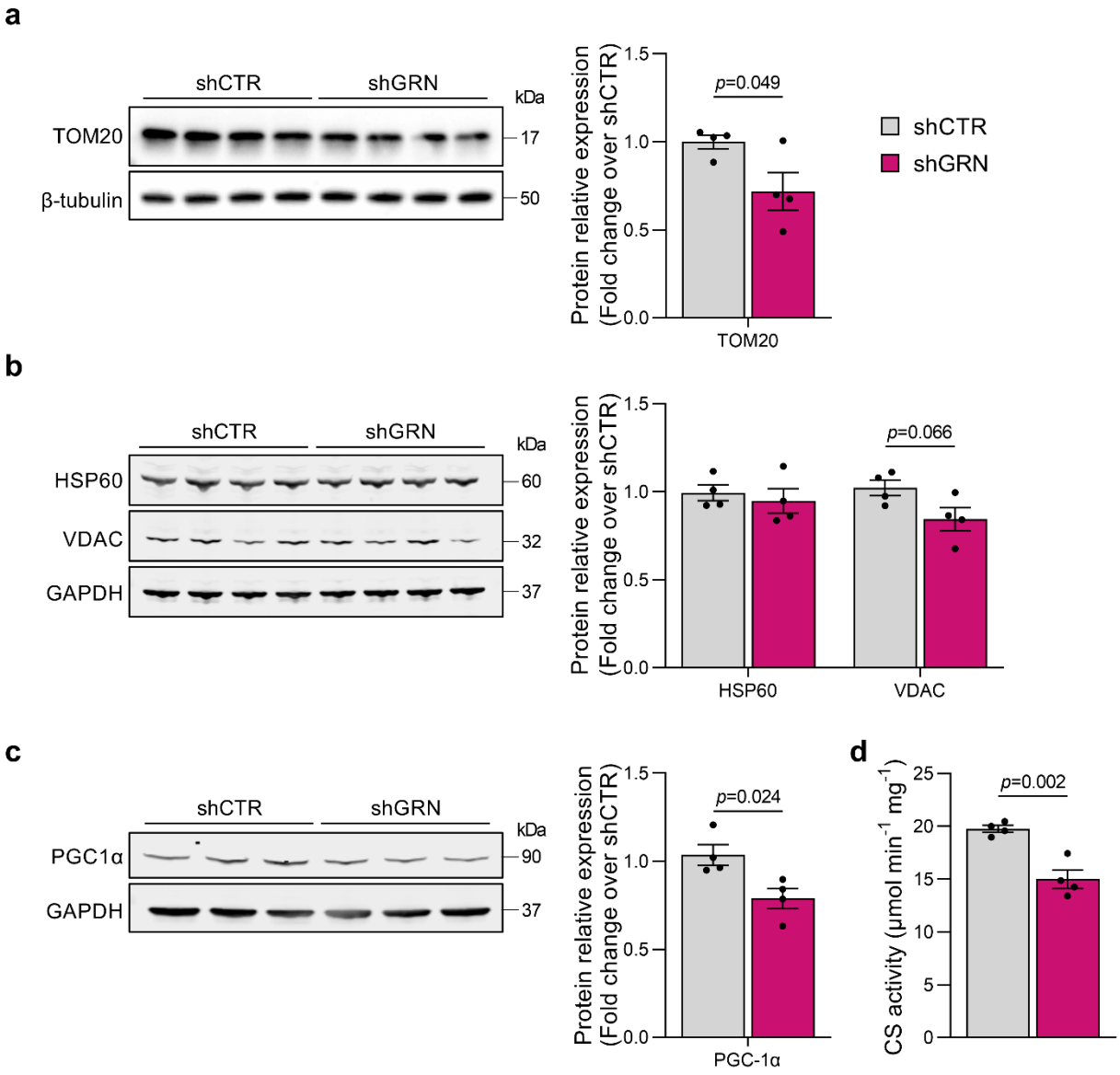

Figure 3.3 Decreased mitochondrial mass in shGRN H4 cells. a Representative western blot and summary bar graph showing the relative protein expression of TOM20 (*n*=4). **b** Representative western blot and summary bar graph showing the relative protein expression of HSP60 and VDAC (*n*=4). **c** Representative western blot and summary bar graph showing the relative protein expression of PGC-1α (*n*=4). **d** Citrate synthase (CS) activity assay measurement in shGRN H4 cells (*n*=4). Data are expressed as mean±SEM, where each data point represents an independent passage, and it is the average of at least three technical replicates; unpaired *t*-test.

Normalising mitochondrial dysfunction read-outs to the mitochondrial content

While the previous read-outs of mitochondrial parameters were normalised to a housekeeping protein or to the total protein concentration, there remained an outstanding question regarding whether the observed decrease in mitochondrial complexes assembly or activity was due to an impairment in mitochondrial respiration, a decrease in mitochondrial content, or both. To address this question, I normalised the complex assembly results obtained by BN-PAGE and CN-PAGE (Fig. 3.2c), as well as COX activity (Fig. 3.2e), by the mitochondrial content according to the citrate synthase activity assay (Fig. 3.3d). Notably, neither the signal of the native complexes nor the COX activity were significantly reduced anymore (Fig. 3.4a, 3.4b), although they still presented a trend towards a decrease. This suggested that the decrease in complexes assembly and the COX activity were partly attributed to the decrease in mitochondrial content in PGRN-deficient H4 cells, although other factors may also be involved.

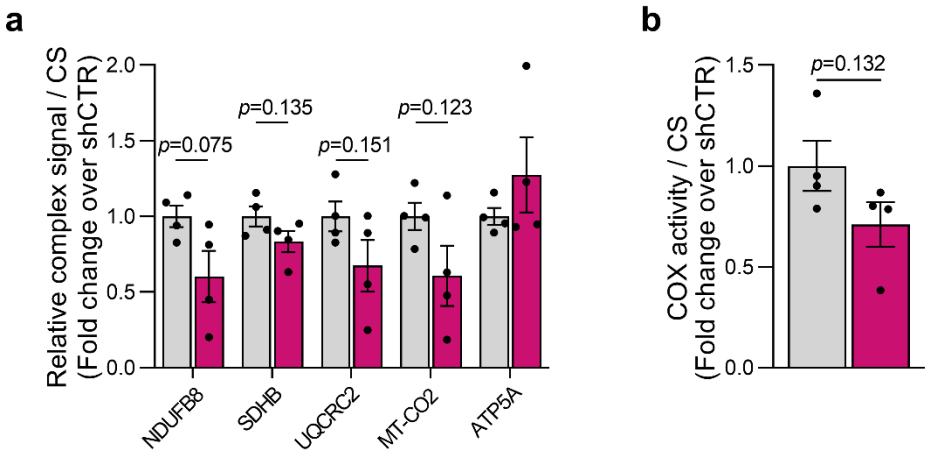

Figure 3.4 Normalising complexes assembly signal and COX activity by citrate synthase in shGRN H4 cells. a Summary bar graph showing the signal of the native complexes, normalised to citrate synthase (CS) (*n*=4). **b** Summary bar graph showing the COX activity, relative to citrate synthase (*n*=4). Data are expressed as mean±SEM, where each data point represents an independent passage, and it is the average of at least three technical replicates; unpaired *t*-test.

PGRN deficiency reduces the expression of the mitochondrial-encoded genome in shGRN H4 cells

The recognition of mtDNA damage and dysfunction in neurodegenerative disorders underscores the heightened vulnerability of neurons to mitochondrial metabolic alterations[231]. In investigating the repercussions of PGRN deficiency on the mitochondrial genome, mtDNA was assessed in shGRN H4 cells, revealing a significant decrease (Fig. 3.5a). Strikingly, the protein level of the mitochondrial transcription factor A (TFAM), crucial for mtDNA maintenance, exhibited a concurrent decrease (Fig. 3.5b), inferring an impairment in mtDNA integrity.

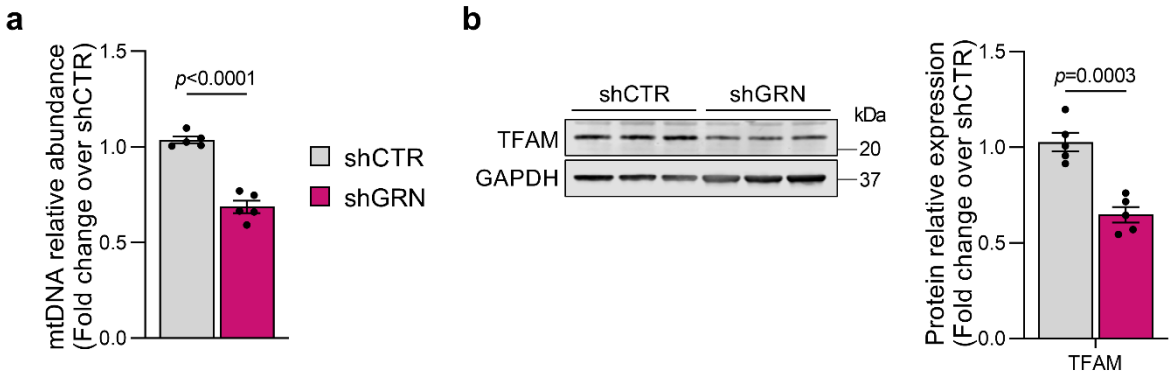

Figure 3.5 Decreased mtDNA in shGRN H4 cells. a Relative abundance of mtDNAcn in shGRN H4 cells (*n*=5). **b** Representative western blot and summary bar graph showing the relative protein expression of TFAM (*n*=5). Data are expressed as mean±SEM, where each data point represents an independent passage, and it is the average of at least three technical replicates; unpaired *t*-test.

At the transcriptional expression level, there was a significant decrease in five out of seven mitochondrial-encoded transcripts (*MT-ND1*, *MT-ATP6*, *MT-COX3*, *MT-CYTB* and *MT-ND6*) (Fig. 3.6a). However, there was no change in nuclear-encoded transcripts (Fig. 3.6b).

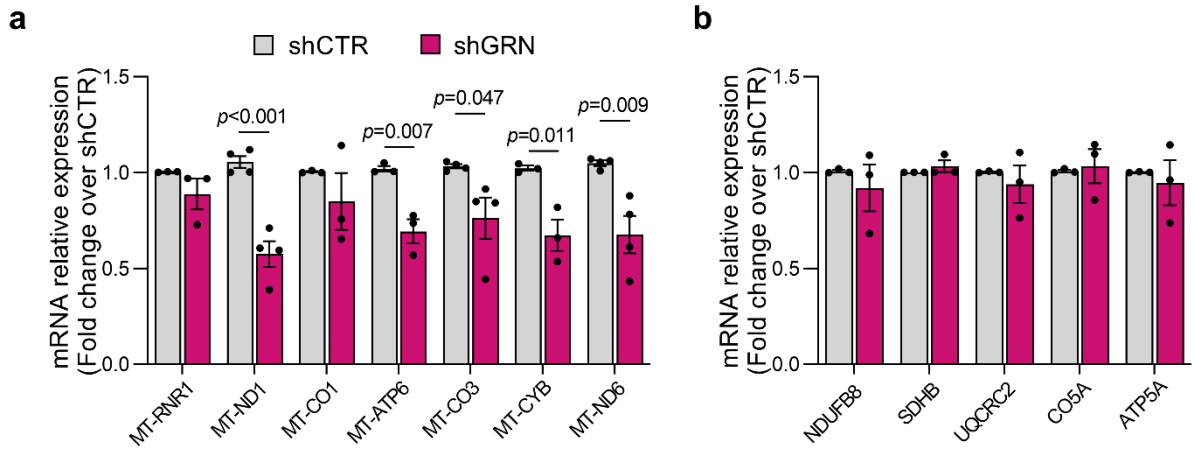

Figure 3.6 Decreased mitochondrial-encoded RNA transcripts in shGRN H4 cells. a Relative expression of mitochondrial-encoded transcripts (*n*=3-4). **b** Relative expression of nuclear-encoded transcripts (*n*=3). Data are expressed as mean±SEM, where each data point represents an independent passage, and it is the average of at least three technical replicates; unpaired *t*-test.

Similarly, the distinctive impact of PGRN deficiency on mitochondrial genomics was substantiated by a decrease in the protein level of the mitochondrial-encoded MT-ND1 (Fig. 3.7a). No significant alterations were observed in nuclear-encoded OXPHOS proteins (Fig. 3.7b) Noteworthy is the absence of change in the expression of the mitochondrial-encoded MT-CO2 protein, hinting at the possibility that mitochondrial dysfunction could selectively impact specific complexes. Overall, these results suggested that mitochondrial dysfunction may constitute a specific pathological hallmark of *GRN*-related FTD, although further validation is required across diverse *in vitro* models and human tissues.

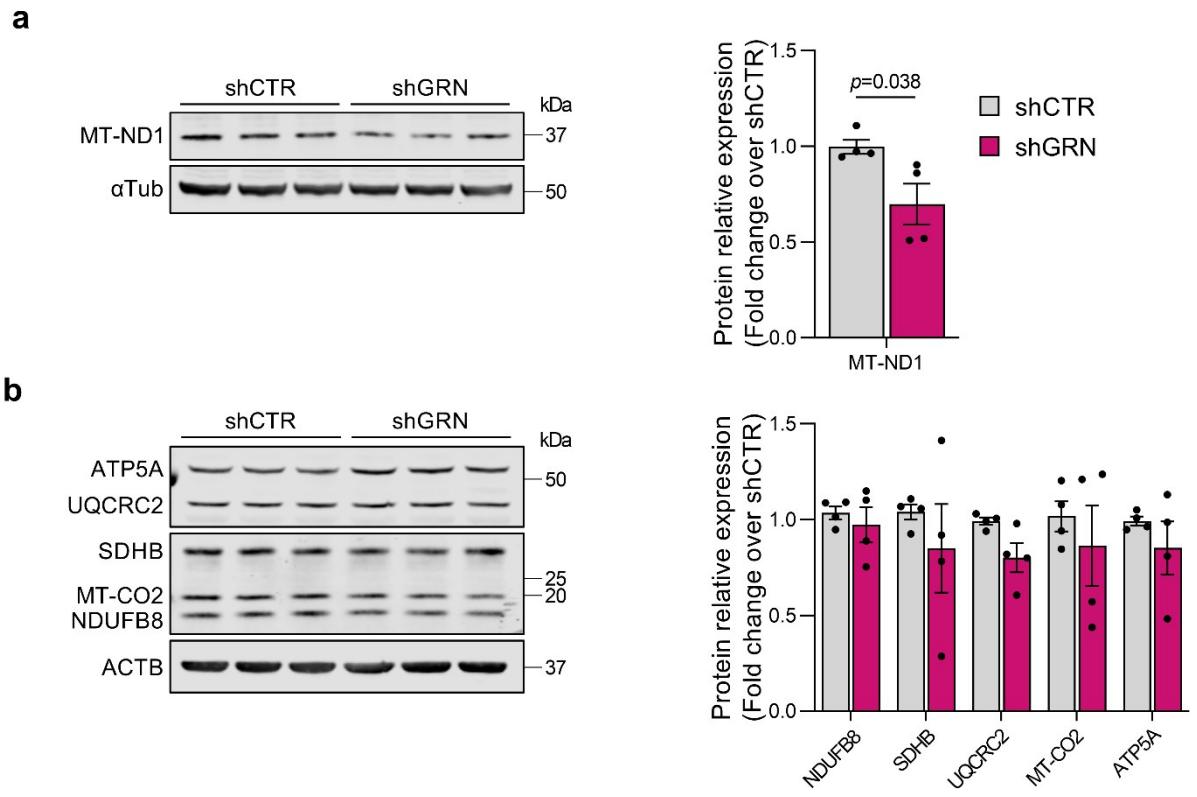

Figure 3.7 Decreased mitochondrial-encoded proteins in shGRN H4 cells. a Representative western blot and summary bar graph showing the relative protein expression of MT-ND1 (*n*=4). **b** Representative western blot and summary bar graph showing the relative protein expression of nuclear-encoded proteins (*n*=4). Data are expressed as mean±SEM, where each data point represents an independent passage, and it is the average of at least three technical replicates; unpaired *t*-test.

Preliminary investigation of CL-related genes in shGRN H4 cells

A decrease in CL total levels has been previously reported in human FTLD-*GRN* brains[203]. To interrogate the state of CL in shGRN H4 cells, I proceed to carry out a preliminary investigation of the transcription expression of genes involved in the CL *de novo* biosynthesis and remodelling pathways. This did not demonstrate any changes (Fig. 3.8), which could indicate that PGRN deficiency does not affect the transcription expression of CL-related genes. However, it is still unknown whether CL abundance or species are affected, and therefore, future research should explore CL employing HPLC-MS techniques in shGRN H4 cells as well as human tissues[104].

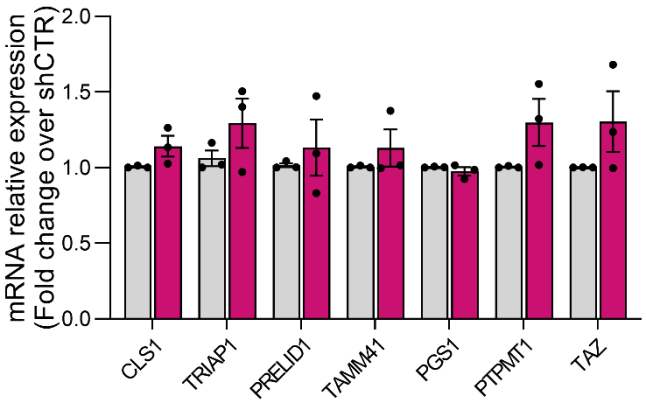

Figure 3.8 Exploring transcription expression of CL-related genes in shGRN H4 cells (*n*=3). Data are expressed as mean±SEM, where each data point represents an independent passage, and it is the average of at least three technical replicates; unpaired *t*-test.

Replicating the results in SH-SY5Y neuroblastoma cells

SH-SY5Y neuroblastoma cells were used to replicate the results obtained in H4 cells. The same transduction process than in H4 cells was employed to generate a stable *GRN* KD using a lentiviral shRNA vector. The PGRN KD was validated using RT-qPCR (Fig. 3.9a). In contrast to the H4 cells, the mtDNAcn showed no difference between shGRN SH-SY5Y cells and controls (Fig. 3.9b), presenting a large variation within the biological replicates. Although the mtDNAcn results could not be recapitulated, the expression of mitochondrial-encoded transcripts was reduced (Fig. 3.9c) and the nuclear-encoded transcripts remained mostly unchanged (Fig. 3.9d), suggesting that a specific decrease in mitochondrial-encoded mRNA was still observed.

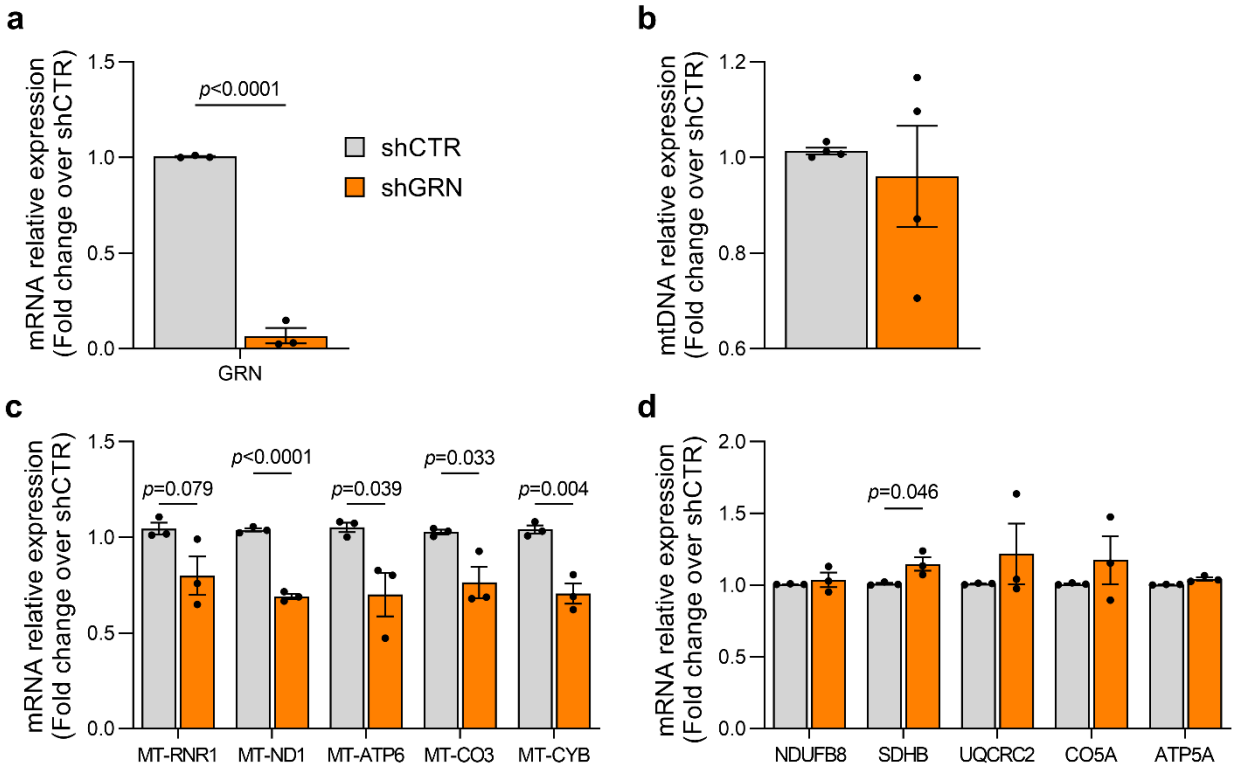

Figure 3.9 Replicating the mRNA results in shGRN SH-SY5Y neuroblastoma cells. a Relative expression of *GRN* mRNA in SH-SY5Y cells analysed by RT-qPCR (*n*=3). **b** Relative abundance of mtDNAcn in shGRN SH-SY5Y cells (*n*=4). **c** Relative expression of mitochondrial-encoded transcripts (*n*=3). **d** Relative expression of nuclear-encoded transcripts (*n*=3). Data are expressed as mean±SEM, where each data point represents an independent passage, and it is the average of at least three technical replicates; unpaired *t*-test.

Validating PGRN-deficiency in fibroblasts derived from patients with *GRN* mutations

Fibroblasts from presymptomatic patients with pathogenic *GRN* mutations, as well as from controls, were used to investigate the impact of PGRN deficiency on mitochondrial function. Mutations in *GRN* have been documented to result in comparable clinical manifestations[37]. This stands in contrast to the *MAPT* gene, where different mutations can give rise to phenotypic and neuropathological variability, involving different mechanisms[232]. To test this hypothesis, this thesis discerned between the different *GRN* mutations (C31fs, R493X and V141fs) when investigating their effects on mtDNA, mRNA and proteins levels in fibroblasts.

PGRN deficiency was validated by measuring the *GRN* transcripts using RT-qPCR and PGRN protein levels by western blotting (Fig. 3.10). The decrease in both measurements confirmed the use of the fibroblasts as a PGRN-deficient model.

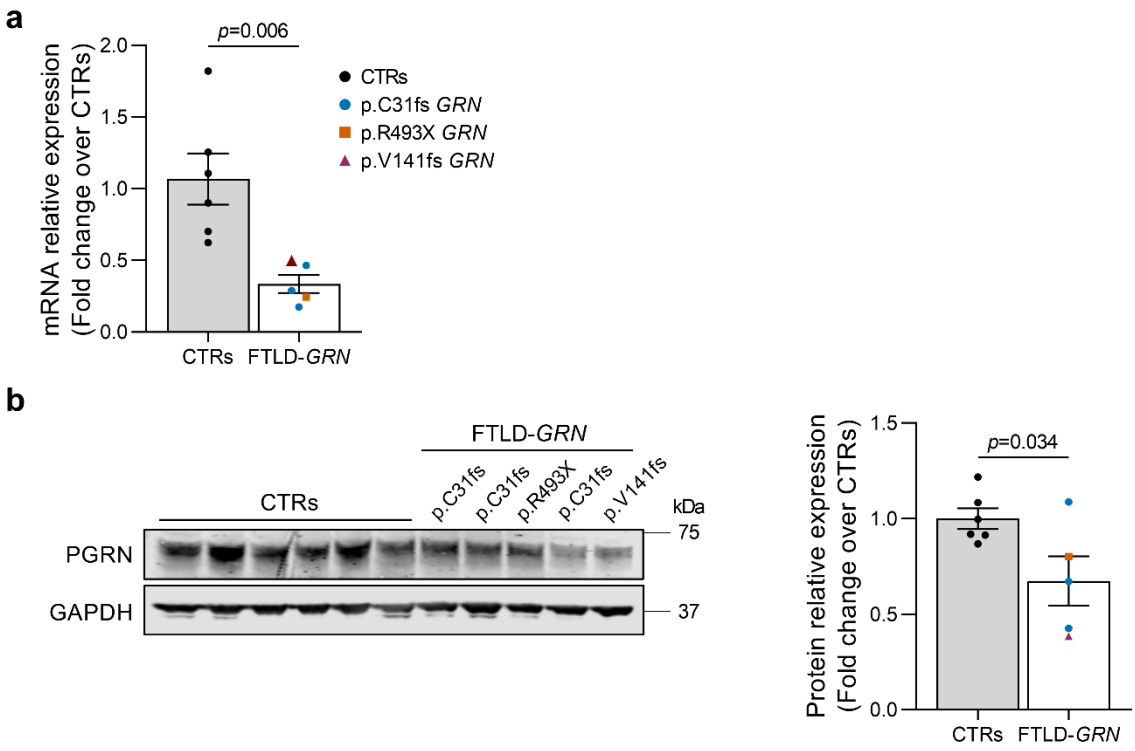

Figure 3.10 Validation of PGRN-deficient fibroblasts obtained from FTD patients with *GRN* mutations. a Relative expression of *GRN* mRNA in fibroblasts analysed by RT-qPCR (*n*=5 FTLD-*GRN*, *n*=6 controls). **b** Representative western blot and summary bar graph showing a decrease in PGRN protein (*n*=5 FTLD-*GRN*, *n*=6 controls). Data are expressed as mean±SEM, where each data point represents an independent biological sample; unpaired *t*-test.

PGRN deficiency leads to impaired mitochondrial genomics in fibroblasts

Mitochondrial genomics was assessed by extracting DNA and measuring the mtDNAcn of the PGRN-deficient fibroblasts. The mtDNAcn was assessed using both *MT-ND1*/*B2M* and *MT-CYB*/*GUSB* set of probes (Fig. 3.11a, 3.11b), which successfully replicated a reduction of the mtDNAcn in patient fibroblasts. Interestingly, PGRN protein levels were positively correlated with mtDNAcn [$r(9)=.556$, $p=.070$ for *MT-ND1*/B2M and $r(9)=.792$, $p=.011$ for *MT-CYB*/*GUSB*, Pearson's correlation, Fig. 3.11c], suggesting a relation between PGRN-deficiency and mitochondrial dysfunction in *GRN*-related FTD.

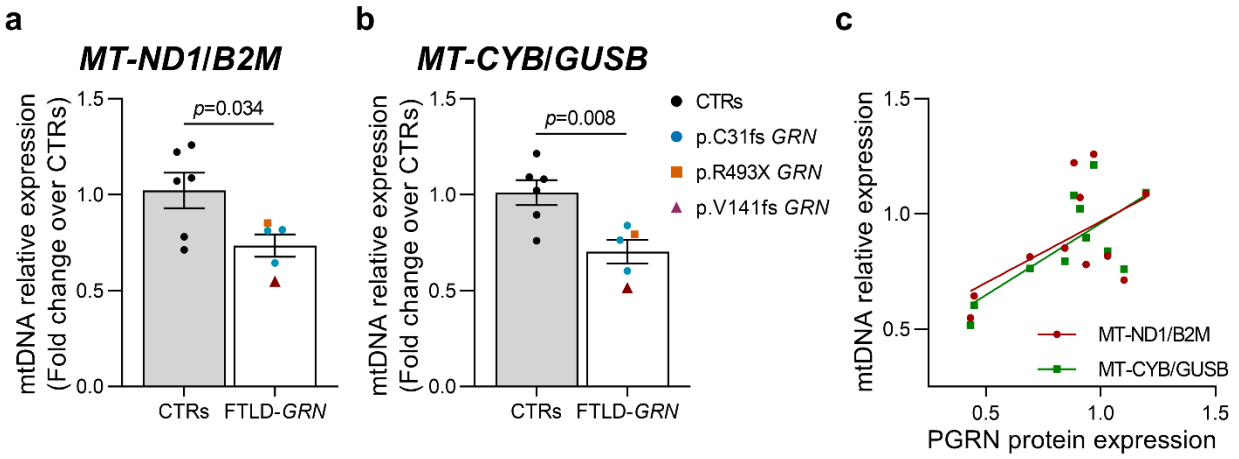

Figure 3.11 Measurement of mtDNA in PGRN-deficient fibroblasts. Relative abundance of mtDNAcn using (**a**) *MT-ND1*/*B2M* and (**b**) *MT-CYB*/*GUSB* in fibroblasts from patients with *GRN* mutations (n=5 FTLD-*GRN*, n=6 controls). **c** Pearson's correlation between PGRN protein expression and mtDNA relative expression (n=5 FTLD-*GRN*, n=6 controls). Data are expressed as mean±SEM, where each data point represents an independent biological sample; unpaired *t*-test, Pearson's correlation.

Mitochondrial-encoded and nuclear-encoded RNA transcripts showed no difference across samples, potentially due to the large variation between individual cases (Fig. 3.12a, 3.12b). Similarly, protein expression of the OXPHOS cocktail and mitochondrial mass markers (MIC60, HSP60 and TOM20) showed no difference (Supplementary Fig. 3.12c, 3.12d).

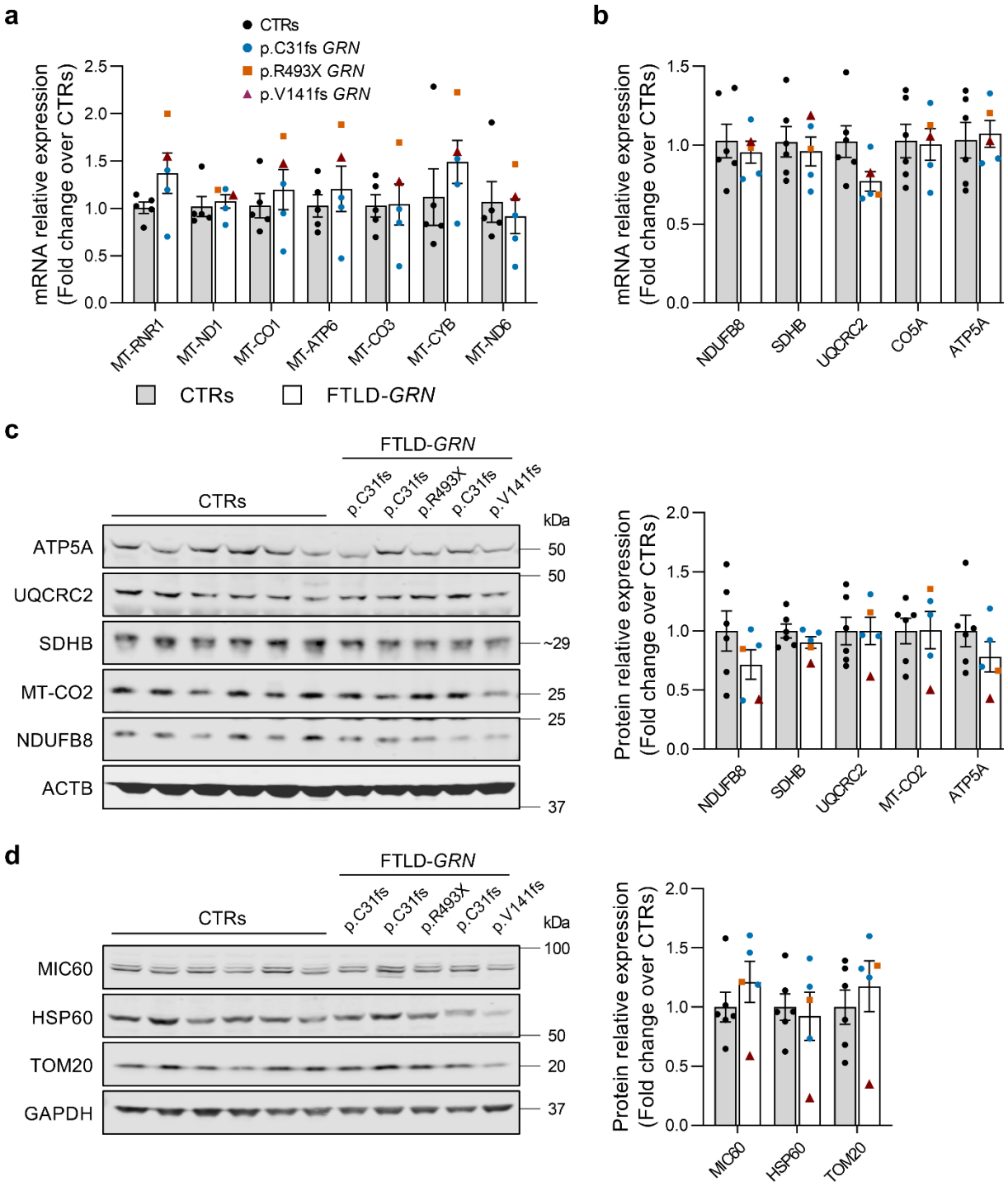

Figure 3.12 PGRN deficiency does not show any changes at the mRNA or protein levels in PGRN-deficient fibroblasts. a Relative expression of mitochondrial-encoded transcripts (*n*=5 FTLD-*GRN*, *n*=6 controls). **b** Relative expression of nuclear-encoded transcripts (*n*=5 FTLD-*GRN*, *n*=6 controls). **c** Representative western blot and summary bar graph showing the relative expression of OXPHOS-encoding proteins (*n*=5 FTLD-*GRN*, *n*=6 controls). **d** Representative western blot and summary bar graph showing the relative protein expression of mitochondrial markers (*n*=5 FTLD-*GRN*, *n*=6 controls). Data are expressed as mean±SEM, where each data point represents an independent biological sample; unpaired *t*-test.

To ascertain whether different *GRN* mutations have specific effects on mitochondrial function, Grubbs' test was performed to identify any outliers in the dataset. Overall, the mutations C31fs and R493X did not exhibit significant differences. However, the mutation V141fs had a lower mtDNAcn and protein level compared to the other mutations (Fig. 3.11, 3.12c, 3.12d). Although the Grubbs' test confirmed that the results for the mutation V141fs deviated the furthest from the rest, the difference reached statistical significance ($p<0.05$) only for TOM20 at the protein level. This value was kept to maintain consistency in the number of biological replicates in the statistical analysis. Moreover, given the limited representation of the mutation V141fs with only one patient, out of a small cohort of 5 patients, it posed a challenge to discern whether the decrease in mtDNAcn and protein levels was mutation-specific or merely patient-specific.

Exploring a correlation between mRNA and proteins

Due to the high variability in mRNA across the different patients' fibroblasts, mostly at the mitochondrial-encoded transcripts, Pearson's correlation was carried out to explore a potential relationship between the transcriptional expression of *GRN* and the other explored genes. The aim was to determine whether there was any existing correlation between *GRN* and mitochondrial- or nuclear-encoded transcripts according to the results obtained from RT-qPCR in both human FTLD-*GRN* and controls fibroblasts. As seen in Table 3.1, *GRN* mRNA expression was statistically, positively correlated to the *NDUFB8* and *UQCRC2* transcripts, as well as positively, but not significantly, correlated to the *MT-ND6*, *SDHB* and *CO5A* transcripts. These results suggested that *GRN* transcripts expression had a weak/moderate correlation with nuclear-encoded transcripts, but not with mitochondrial-encoded transcripts.

		Pearson's correlation											
		mitochondrial-encoded transcripts							nuclear-encoded transcripts				
		MT-RNR1	MT-ND1	MT-CO1	MT-ATP6	MT-CO3	MT-CYB	MT-ND6	NDUFB8	SDHB	UQCRC2	COX5A	ATP5A
GRN	*p*-value	0.3393	0.3703	0.8280	0.9929	0.7863	0.5963	0.0788	0.0270	0.1195	0.0185	0.0791	0.2248
	r-value	-0.3381	0.3181	0.0791	0.0032	0.0987	0.1914	0.5800	0.6602	0.4974	0.6912	0.5507	0.3985

Table 3.1 Pearson's correlation between *GRN* transcripts expression and mitochondrial- and nuclear-encoded transcripts in controls and PGRN-deficient fibroblasts. The colour of each box represents the degree of statistical significance, with red indicating a highly significant difference, blue a non-significant difference and white a borderline/trend difference.

As with the mRNA RT-qPCR results, there was a high variability in protein levels between the different samples based on the western blot SDS-PAGE results. Pearson's correlation was carried out to explore a potential relationship between PGRN and the other protein levels. As seen in Table 3.2, PGRN expression was statistically, positively correlated only to HSP60 protein expression in fibroblasts, with a low correlation with the other investigated proteins.

		Pearson's correlation							
		OXPHOS proteins					mitochondrial mass markers		
		NDUFB8	SDHB	UQCRC2	MT-CO2	ATP5A	MIC60	HSP60	TOM20
PGRN	*p*-value	0.2306	0.2455	0.8673	0.6549	0.4854	0.8725	0.0477	0.4900
	r-value	0.3940	0.3826	0.0572	0.1523	0.2357	0.0550	0.6069	0.2333

Table 3.2 Pearson's correlation between PGRN protein expression and OXPHOS proteins or mitochondrial mass markers protein expression in controls and PGRN-deficient fibroblasts. The colour of each box represents the degree of statistical significance, with red indicating a highly significant difference, blue a non-significant difference and white a borderline/trend difference.

Characterising transcription expression in iPSC-derived neurons and astrocytes

From Wray's lab, RNA was extracted from *GRN*-mutated iPSC-derived neurons and astrocytes. From this material, cDNA synthesis and RT-qPCR were carried out. The transcripts expression was then assessed, exploring whether mitochondrial-encoded transcripts were reduced as in shGRN H4 cells (Fig. 3.6a) or whether they were unaltered as observed in fibroblasts from patients with *GRN* mutations (Fig. 3.12a). Both iPSC-derived neurons and astrocytes from FTLD-*GRN* patients showed a decrease towards a trend in *GRN* transcription levels (Fig. 3.13a, 3.13b). Although neurons showed a decrease in *MT-ND1* transcripts, the transcripts *MT-CYB* in neurons and *MT-ND1* in astrocytes were not changed. The lack of a change in mitochondrial-encoded transcripts in comparison to the shGRN H4 model may be due a milder decrease in *GRN* transcripts, suggesting that the level of *GRN* KD may influence the variability in the expression of transcripts.

Isogenic controls for both neurons and astrocytes were additionally derived with heterozygous and homozygous *GRN* R493X mutations. Interestingly, heterozygous mutations did not show any change, whereas the homozygous mutation showed a strong trend towards a decrease in transcripts expression (Fig. 3.13c, 3.13d). In the neurons, this extended to all the tested mitochondria-related transcripts, including mitochondrial- and nuclear-encoded transcripts. This suggests a *GRN* expression-dependent threshold after which mitochondrial dysfunction may arise, and that both neurons and astrocytes behave similarly.

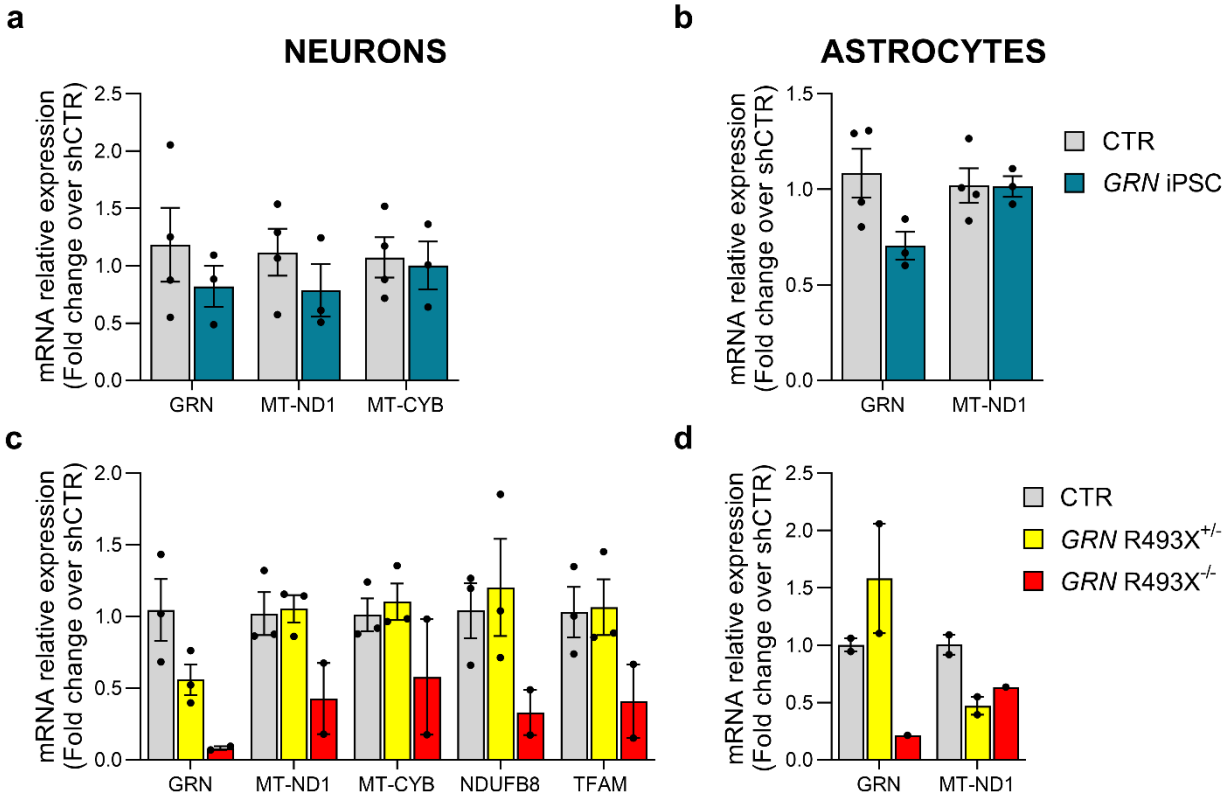

Figure 3.13 Transcripts expression in iPSC-derived neurons and astrocytes. mRNA expression of iPSC-derived (**a**) neurons and (**b**) astrocytes from individuals with *GRN* mutations (*n*=3). mRNA expression of isogenic iPSC-derived (**c**) neurons and (**d**) astrocytes with heterozygous and homozygous *GRN* R493X mutations (*n*=1-3). Data are expressed as mean±SEM, where each data point represents an independent induction, and it is the average of three technical replicates; unpaired *t*-test.

3.5 Discussion

In this chapter, the state of mitochondria was assessed across three *in vitro* PGRN-deficient models, including shGRN immortalised cell lines, fibroblasts from patients with *GRN* pathogenic mutations and iPSC-derived cells. This investigation revealed that PGRN deficiency led to a mitochondrial bioenergetic deficit, decreased mitochondrial mass and biogenesis, and affected the mitochondrial genome.

Mitochondrial dysfunction is involved in the shGRN H4 cell line

The use of immortalised cell models to explore *GRN*-related FTD may be considered useful for an initial characterisation of the effect of PGRN deficiency on mitochondrial function[233]. The validation and characterization of the shGRN H4 cell model confirmed its suitability as a PGRN-deficient model, revealing a decrease in cell proliferation and viability, consistent with prior research findings[234,235].

The assessment of mitochondrial bioenergetics in shGRN H4 cells provided valuable insights into the impact of PGRN deficiency on cellular respiration. The observed reductions in basal respiration, proton leak, ATP-linked respiration, and maximal respiration indicated a bioenergetic deficit, potentially related to an alteration of the ETC. Spare capacity was not calculated due to the observed high variability in the Seahorse results associated with this parameter. Further investigation into the assembly and activity of mitochondrial complexes revealed notable findings, such as impaired assembly of CI-IV that suggested a disruption in the structural integrity of the ETC. In addition, the activity of all the complexes was decreased, with a significant difference in CI and CIV, reinforcing the notion of impaired mitochondrial activity and bioenergetics in shGRN H4 cells. These findings collectively indicated mitochondrial dysfunction as a pathological manifestation in *GRN*-related FTD.

Given the importance of mitochondrial bioenergetics, it is thus important to better understand the impact of PGRN haploinsufficiency in other factors of mitochondria that may drive the phenotype into a pathological state. In the present study, a decrease in mitochondrial mass was detected in the shGRN H4 cells. These results contradicted the findings observed in Rodríguez-Periñán and colleagues' study who reported increased mitochondrial mass[206]. Their results may be a response to a compensatory mechanism due to their PGRN-deficient model being a transient *GRN* KD in SH-SY5Y neuroblastoma cells since their model did not

account for life-long adaptations to germline *GRN* mutations observed in human post-mortem brains or even in a stable shGRN model. This raises important discussions on the choice of the best *in vitro* models for neurodegenerative disease studies and the importance of validation in human samples[236].

A repeating component of mitochondrial dysfunction in neurodegenerative diseases is the decrease in mitochondrial biogenesis[237,238], which disruption has been reported in *C9orf72*-related FTD[239]. Exploring the role of the master regulator PGC-1α by western blotting demonstrated a decrease in biogenesis in shGRN H4 cells. Some of the effects of a reduction in mitochondrial biogenesis include a reduction in mitochondrial mass, impaired energy production and cellular metabolism, increased oxidative stress and overall mitochondrial dysfunction[230]. Strikingly, these established effects on mitochondrial function closely resemble the mitochondrial phenotype characterised in the shGRN H4 cells.

Based on these findings, it could be proposed that PGRN deficiency induces mitochondrial dysfunction by reducing PGC-1α through an unidentified mechanism. To validate this hypothesis, a rescue experiment could be conducted to elevate PGC-1α and evaluate whether it restores a normal mitochondrial phenotype. A similar experiment was performed in human *C9orf72* iPSC-derived motor neurons in which the overexpression of a PGC-1α lentivirus rescued the bioenergetic deficit and axonal length phenotype[175]. Curiously, while gene therapy has demonstrated promising results in *in vitro* and *in vivo* mice AD models, its clinical translation has shown limited benefits in clinical trials[240,241]. This underscores the need for cautious interpretation of results from pre-clinical models and emphasises the importance of further research to delineate the underlying mechanisms and assess translational potential.

The decrease in mitochondrial biogenesis was confirmed by a decrease in citrate synthase activity, indicating a decrease in mitochondrial content. This prompted the hypothesis that the impairment in mitochondrial complexes assembly and activity may be due to a reduction in content. By normalising the mitochondrial complexes assembly and COX activity read outs by citrate synthase, the mitochondrial parameters were still reduced, but not significantly. This suggested that the mitochondrial bioenergetic deficit was partially due to a reduction in mitochondrial content, but other factors such as dysfunctional ETC may also be playing a role.

The mtDNA in shGRN H4 cells was compromised, as evidenced by a decrease in both mtDNAcn and TFAM protein levels. The specific decrease in mitochondrial-encoded transcripts and the protein MT-ND1 additionally demonstrated that PGRN deficiency induced mitochondrial dysfunction. However, it is still unknown whether the decrease in mtDNAcn was due to a specific mechanism targeting mtDNA or due to an overall decrease in mitochondrial content. A decrease in mtDNAcn and quality has been observed across different neurodegenerative diseases[242,243], making further experimental work in other PGRN-deficient models essential to better validate the pathological relevance of impaired mtDNA in *GRN*-related FTD.

The findings in shGRN H4 cells contribute to a better understanding of the pathophysiological phenotype underlying PGRN deficiency and highlight the potential for targeted therapeutic interventions in the future. Future research is warranted to validate these observations in additional *in vitro* models and human tissues, ultimately advancing our comprehension of the role of mitochondria in *GRN*-related FTD.

Interpreting mitochondrial dysfunction in the shGRN SH-SY5Y cell model

In contrast to the results observed in H4 cells, the shGRN SH-SY5Y cells did not show a change in mtDNA, with a large variation between biological replicates. However, the specific decrease in mitochondrial-encoded transcripts expression, but not nuclear-encoded ones, was still present.

The differences in nature between the two human immortalised cell lines may partly explain the variation in results, with H4 cells being considered more glial-like whereas SH-SY5Y cells are more neuron-like. This could suggest that the effect of PGRN haploinsufficiency on mitochondrial dysfunction may depend on the cell type. Therefore, H4 cells could be considered a model more closely related to microglia in which PGRN may play a more physiologically relevant role. In addition, a study reported that the levels of total PGRN levels were higher in H4 cells that in SH-SY5Y cells[224]. Thus, a reduction in PGRN in H4 cells may induce a more strenuous impact on the cellular physiology, leading to mitochondrial dysfunction, in comparison to PGRN-deficient SH-SY5Y cells.

Decreased mtDNAcn in fibroblasts could be explored as a diagnostic biomarker

Fibroblasts from presymptomatic patients with familial *GRN* mutations were consecutively used to characterise mitochondria and compare the results to those obtained from shGRN immortalised cell lines.

The PGRN-deficient fibroblasts presented a significant decrease in the mtDNAcn confirming the previous results obtained from shGRN H4 cells. Previous studies have shown that neurodegenerative diseases can affect mtDNAcn[244], exploring changes in the mitochondrial genome as a potential diagnostic biomarker for PD and Huntington's disease[245,246]. The fact that the fibroblasts in this thesis were obtained from presymptomatic patients makes the decrease in mtDNAcn even more exciting as a marker for systemic mitochondrial dysfunction before the onset of FTLD symptoms. This would provide a unique window of opportunity for early intervention and treatment, potentially slowing down the progression of the disease before irreversible damage occurs. Considering that peripheral blood and CSF are routinely used to assess mtDNAcn due to their accessibility and correlation with clinical symptoms, it would be interesting to replicate these experiments using clinical fluids. This would be especially relevant since pathological manifestations in peripheral blood and fibroblasts represent the overall systemic condition of an individual and can provide insights into general health and specific disease-related changes.

In contrast to the H4 cells, bioenergetic assays were not conducted in fibroblasts due to the high variability observed in the Seahorse assay, and the different growth rates among fibroblast cell lines, particularly the slower growth rates in the fibroblasts from FTLD-*GRN* cases. Despite these limitations, this experimental work could be attempted in fibroblasts in the future to further enhance our understanding of the decrease in mitochondrial bioenergetics across different PGRN-deficient models.

No changes were observed at the mRNA transcripts level nor at the protein level, mostly due to the large variation in expression across PGRN-deficient fibroblasts. To certain extent, this variation was also observed in another study exploring mitophagy mRNA and protein levels in fibroblasts from six carriers with *GRN* pathogenic variants[202]. They reported significant decreases in parkin (PRKN) and PGRN protein levels, but a non-significant, large variation in MFN2 and VDAC proteins, which are downstream targets of parkin. Interestingly, when they created a transient *GRN* KD in fibroblasts, they then observed a decrease in MFN2 and VDAC proteins which was significant and relatively more consistent than the fibroblasts from patients. This suggested that life-long adaptations to germline *GRN* mutations in fibroblasts can show a great variability between individuals, which could also explain the wide range of results in this thesis. Another possibility is that the genetic heterogeneity between the tested fibroblast cell lines could have masked the differences. These two interpretations could explain the variability and discrepancy in results in contrast to the shGRN H4 results.

Based on the RT-qPCR and western blotting results in human fibroblasts, potential correlations were explored between *GRN* mRNA expression and mitochondrial- and nuclear-encoded transcripts expression, and between PGRN levels and other proteins expression. Overall, no strong evidence of correlations was observed when carrying out Pearson's correlation. Peculiarly, the most striking positive, significant correlations occurred between *GRN* and the nuclear-encoded *NDUFB8* and *UQCRC2* transcripts. However, when exploring the correlations between PGRN, NDUFB8 and UQCRC2 protein levels, these correlations did not replicate. The contradicting results may be due to the aforementioned limitations in using fibroblasts to characterise mitochondria, as well as the differences in nature between mRNA and protein, with each having a half-life of 9 h and 46 h median, respectively[247]. In conclusion, it is challenging to determine any correlations between the mRNA and proteins of human fibroblasts, as well as their physiological relevance.

The extent of *GRN* KD in iPSCs may influence the effect on mitochondrial dysfunction

Gene transcription was measured in iPSC-derived cortical neurons and astrocytes from controls and patients with *GRN* mutations, and from an isogenic CRISPR series containing control, heterozygous and homozygous R493X *GRN* mutations.

No difference in transcription expression was detected between controls and patient iPSC-derived neurons and astrocytes, nor in the heterozygous line in comparison to the controls. Notably, there was a strong trend towards a decrease in mitochondria-related transcription expression in the homozygous neurons and astrocytes. The unaltered transcription expression in the heterozygous line may be due to a compensatory upregulation of PGRN protein levels from the wild type allele which is absent in the homozygous line.

These results resemble those of a study from 2012 when they derived iPSC neurons with PGRN deficiency and did not observe mitochondrial dysfunction under different doses of mitochondrial stressors[200], implying that mitochondrial dysfunction was not present in *GRN*-related FTD. However, another explanation was that iPSCs may not accurately capture the age-related aspects of FTD, and mitochondrial dysfunction may develop at a later stage of disease progression in these brain cells. If this limitation was to extend to the PGRN-deficient iPSC model used in this thesis, this would highlight the need of other models, such as human brain tissue, to characterise the pathology of mitochondria at a late stage of the pathology progression.

Because there were fewer than three biological replicates for the isogenic iPSCs, thereby limiting the statistical power, these results did not provide confirmation whether a homozygous *GRN* mutation significantly impacts the mitochondria-related transcripts.

Overall, neurons and astrocytes presented a similar mRNA transcription expression profile, with no clear cell-type specific contributions of PGRN to mitochondria-related transcripts. Future work should aim at expanding the iPSC models, especially deriving microglia due to its relevance to PGRN[248]. Acknowledging the time-demand and high costs associated with the generation of iPSCs, it would be interesting to employ iPSCs to carry out a more comprehensive characterisation of mitochondria, including mtDNA and bioenergetics.

Conclusion and future directions

In conclusion, the findings in this chapter revealed that PGRN deficiency induces mitochondrial dysfunction across *in vitro* models. This extends the roles of PGRN as a regulator of mitochondrial function and homeostasis in *GRN*-related FTD. Since the *in vitro* models are relatively easy to genetically manipulate, future experimental work should aim at identifying the pathological mechanisms by rescuing potential targets, such as boosting mitochondrial biogenesis.

Beyond the *in vitro* models used to characterise mitochondria in this chapter, it would be interesting to employ more sophisticated models, such as the use 3D human cerebral organoids to characterise mitochondria in *GRN*-related FTD. Whilst brain organoids have been previously developed to characterise pathological hallmarks in FTLD-*GRN*, this model has not been used to investigate mitochondrial function[225]. In a similar way, the role of PGRN has been extensively studied in rodent models[249–251], but there is no work investigating the mitochondrial phenotype in mice with *GRN* mutations. These two established models present a physiology more closely related to humans and would enable a better understanding of changes in the mitochondrial phenotype in specific organs across time as well as facilitate the use of therapeutic drugs.

Finally, the extensive work in *in vitro* models needs to be replicated and validated in samples with greater clinical relevance, thus enhancing the translational significance of the research. Therefore, human post-mortem brains from FTLD-*GRN* and sporadic FTLD-TDP patients will be employed in the following chapter to investigate the presence of mitochondrial function.

4 Characterising mitochondria in human FTLD-*GRN* brains

Cocoon in retrograde (charcoal) – by Dr Emily Y. Wang

4.1 Introduction

The brain is an exceptionally energy-demanding organ, accounting for a consumption of 20% of the total body energy[252]. The extensive energy requirement is met through the efficient functioning of mitochondria through the process of OXPHOS needed for neuronal processes. Mitochondria are indeed crucial for maintaining the synaptic transmission, ion channel regulation, and axonal transport that underpin brain function.

It is crucial to note that neurons are post-mitotic and have a lifespan that closely matches that of the entire organism[253], unlike many other cell types in the body that are replaced during an individual's lifetime. Therefore, post-mitotic cells like neurons are more prone to accumulating dysfunctional mitochondria during ageing and neurodegenerative diseases[254]. Understanding whether mitochondrial dysfunction is involved in *GRN*-related FTD is essential for the development of targeted therapeutic interventions and strategies aimed at preserving or restoring mitochondrial function. By elucidating the intricate connections between the brain, mitochondria and PGRN, researchers can uncover new avenues for potential treatments, offering hope for patients and families affected by this devastating condition.

A wide range of pathological hallmarks have been identified using human brain samples from FTLD-*GRN* patients. However, the characterisation of the mitochondrial phenotype remains unexplored in this organ, with only a few studies delving into the metabolic enigma in an indirect way by utilising multi-omics techniques. As an illustration, a study utilised lipidomics to investigate gangliosides, which are glycosphingolipids that are highly abundant in the nervous system. In their supplementary data, they reported a reduction in the mitochondrial lipids PE and CL in the frontal lobe of FTLD-*GRN* patients[203]. Considering the crucial roles of CL, a reduction of the lipid may lead to disassembled mitochondrial structure,

bioenergetic deficit and impaired dynamics, although this was not addressed by the authors. In a similar fashion, another study carried out transcriptomics in the frontal-cortex tissue of FTLD-*GRN* patients in comparison to other forms of sporadic FTLD-TDP. They reported a significant enrichment in mitochondrial dysfunction terms in differentially expressed genes in the astrocytes[255], but further analysis of the transcriptomic dataset is required to assess the downregulated genes and hypothesise a potential mechanism. Therefore, a more mitochondria-centric approach is required to better understand the phenotype and mechanism, and the use of post-mortem brain tissue can provide a unique length through which to understand the disease's aetiology, the final stage of pathology and therapeutic interventions.

Due to the brain's particular sensitivity to mitochondrial dysfunction, this chapter focused on exploring the *GRN*-related FTD brain processes from a mitochondrial perspective by asking: 1) What happens to brain mitochondrial bioenergetics, biogenesis and genomics during *GRN*-related FTD?, and 2) How do the results in this post-mortem brain tissue relate to the prior findings in H4 cells, SH-SY5Y cells, fibroblasts and iPSCs?

4.2 Aims

The overall aim of this chapter was to investigate the role of mitochondria in human FTLD post-mortem brains, comparing FTLD-*GRN* cases and controls.

The specific aims were:

- To interrogate the mitochondrial bioenergetics in the grey matter of human post-mortem brains from FTLD-*GRN* patients, assessing mitochondrial complexes activity and assembly;

- To explore the mitochondrial content and biogenesis in the grey matter of human post-mortem brains from FTLD-*GRN* and sporadic FTLD-TDP cases;

- To analyse the mitochondrial genome in human post-mortem brains from FTLD-*GRN* and sporadic FTLD-TDP cases, assessing mtDNAcn and integrity across both white and grey matter in the frontal lobe, temporal lobe and cerebellum.

4.3 Materials and methods

Snap-frozen brains from all twenty-seven human post-mortem brain cases (17 FTLD and 10 controls) were employed in this chapter to characterise mitochondria. A summary of the demographics is presented in Table 2.2. These included seven with *GRN* mutations (FTLD-*GRN*; three C31fs, two R493X, one Q130fs and one IVS3-7T>G; all FTLD-TDPA) and ten with sporadic FTLD-TDP cases without *GRN* mutations (sporadic FTLD-TDP; three FTLD-TDPA, three FTLD-TDPB and four FTLD-TDPC).

Comparisons of age at onset, age at death, disease duration, post-mortem delay, sex and Braak stage across groups are shown in Fig. 4.1. Age at onset, disease duration and sex were similar between cases and controls. FTLD-*GRN* and sporadic FTLD-TDP had a younger age at death compared with controls (p=0.0487 and p=0.0150, respectively). Sporadic FTLD-TDP cases had a non-significant reduction in post-mortem delay, which could suggest that sporadic cases' tissue integrity may have been maintained slightly better. Braak stage showed some variability, with one sporadic case with Braak stage V.

Detailed methods to characterise mitochondria in the post-mortem brains can be found in Chapter 2. Overall, mitochondrial bioenergetics were measured by BN-PAGE, CN-PAGE and COX activity assay, whilst comparing the frontal grey matter of controls and FTLD-*GRN* brains. Mitochondrial mass, biogenesis and content were assessed by western blotting and citrate synthase activity assay in the frontal grey matter of controls, FTLD-*GRN* and sporadic FTLD-TDP cases. Mitochondrial genomics were quantified by qPCR and western blotting across all brain regions and cases, and by preliminary NGS in the frontal grey matter of controls and FTLD-*GRN* cases. Finally, the levels of mitochondrial- and nuclear- encoded proteins were assessed by western blotting in the frontal grey matter of controls, FTLD-*GRN* and sporadic FTLD-TDP cases.

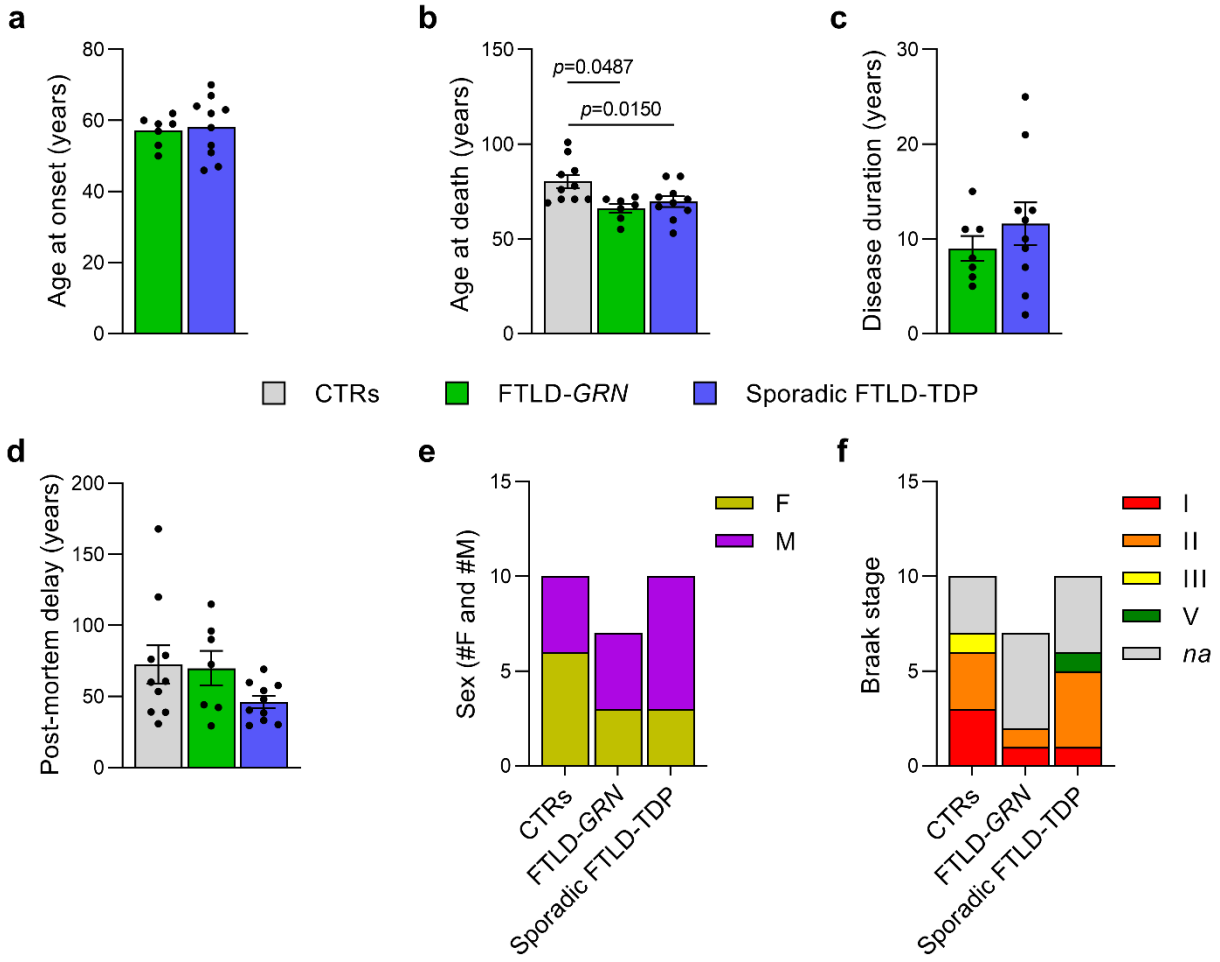

Figure 4.1 Comparison of demographics between groups. Graphs show comparison of (**a**) age at onset, (**b**) age at death, (**c**) disease duration and (**d**) post-mortem delay, (**e**) sex and Braak stage (range I to V) across groups (*n*=7 FTLD-*GRN*, *n*=10 sporadic FTLD-TDP, *n*=10 controls). Data are expressed as mean±SEM, where each data point represents an independent biological sample; unpaired *t*-test, one-way ANOVA with Tukey's multiple comparison test.

4.4 Results

Mitochondrial bioenergetic deficit is present in human FTLD-GRN brains

The brain's high metabolic demand consumes 20% of the oxygen in our body, making the role of mitochondrial bioenergetics essential in maintaining neuronal function within the organ. The frontal grey matter was used to assess the mitochondrial bioenergetics state in FTLD-*GRN* patients compared to controls.

The in-gel activity of mitochondrial CI, CII and CV was quantified in FTLD-*GRN* patients using BN-PAGE (CI) and CN-PAGE (CII and CV) (Fig. 4.2a). In addition, COX activity was spectrophotometrically measured as a read-out of CIV activity (Fig. 4.2b). Strikingly, the activity of CI, CIV and CV were significantly reduced in FTLD-*GRN* brain tissues in comparison to controls, confirming an impairment in mitochondrial bioenergetics in human FTLD-*GRN* post-mortem brains similar to the bioenergetic deficit previously observed in shGRN H4 cells.

The assembly of the mitochondrial complexes was consequently interrogated to assess whether mitochondrial bioenergetic dysfunction was due to a reduced assembly of the complexes (Fig. 4.2c). BN-PAGE measured CI-IV assembly and CN-PAGE measured CV assembly. The assembly of the CV was significantly decreased in FTLD-*GRN* cases in comparison to controls, which may account for the decrease in CV activity. Assembly of the CI-IV were reduced, but not significantly. Overall, these results confirmed that mitochondrial bioenergetics dysfunction through defective mitochondrial respiration is present in human FTLD-*GRN* brains.

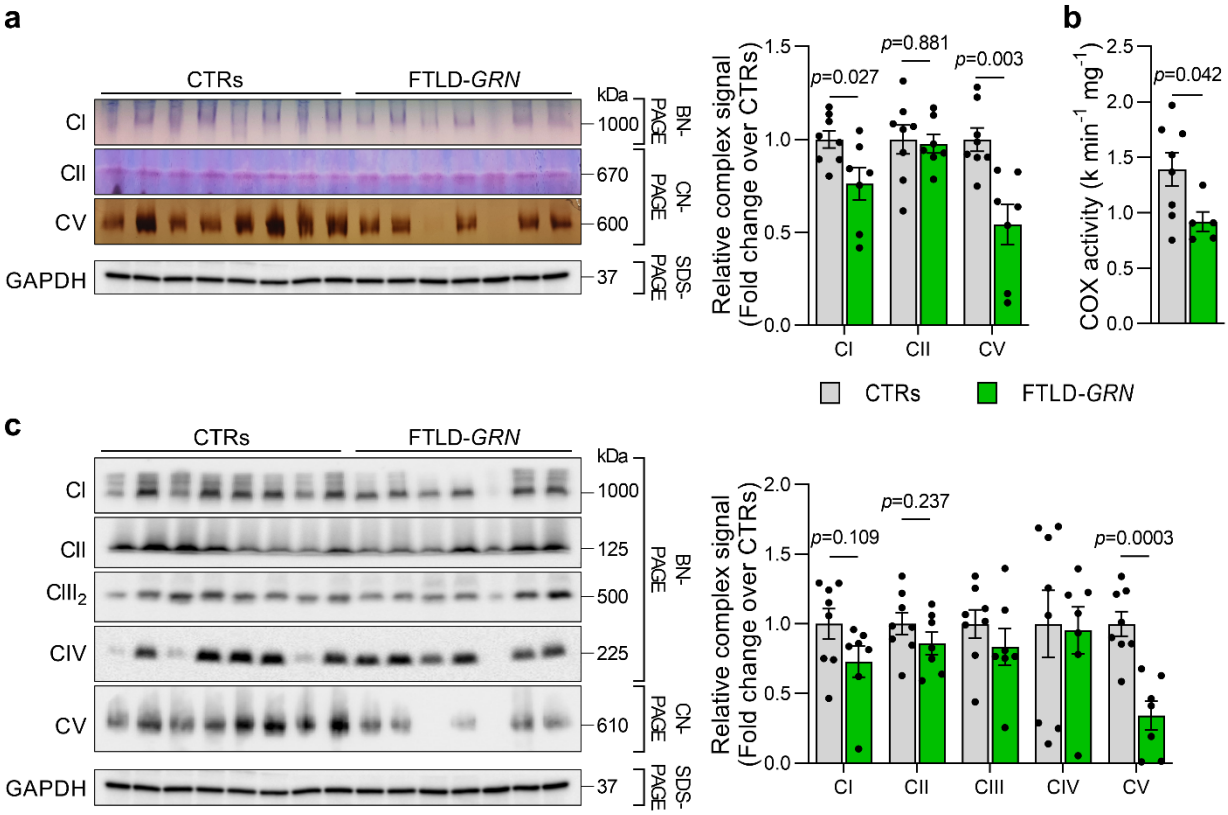

Figure 4.2 PGRN deficiency causes impaired mitochondrial bioenergetics in human FTLD-*GRN* post-mortem brains. a BN-PAGE (CI) and CN-PAGE (CII and CV) and summary bar graph showing the complexes in-gel activity, relative to the SDS-PAGE membrane (*n*=7 FTLD-*GRN*, *n*=8 controls). **b** COX activity measurements (*n*=5 FTLD-*GRN*, *n*=8 controls). **c** BN-PAGE (CI to CIV) and CN-PAGE (CV) and summary bar graph showing the signal of the native complexes, relative to the SDS-PAGE membrane (*n*=7 FTLD-*GRN*, *n*=8 controls). Data are expressed as mean±SEM, where each data point represents an independent biological sample; unpaired *t*-test.

Mitochondrial mass and biogenesis are decreased in human FTLD-*GRN* brains

To further interrogate whether the impairment in mitochondrial bioenergetics was due to changes in mitochondrial mass, the abundance of different mitochondrial protein markers was quantified in the frontal grey matter of FTLD-*GRN* brains compared to controls and sporadic FTLD-TDP (Fig. 4.3a, 4.3b). VDAC and TOM20 were significant reduced in FTLD-*GRN* samples, whilst MIC60 and HSP60 presented a trend towards a decrease. Interestingly, sporadic FTLD-TDP cases did not show a change in MIC60, HSP60 nor VDAC in comparison to controls, but had a decrease in TOM20 mitochondrial mass, although not as striking as in the FTLD-*GRN* cases.

The PGC-1*α* master regulator of mitochondrial biogenesis was consequently measured, which was shown to be decreased in FTLD-*GRN* brains (Fig. 4.3c). The decrease in citrate synthase activity in FTLD-*GRN* patients confirmed the decrease in mitochondrial content (Fig. 4.3d). The mitochondrial mass and the PGC-1*α* protein levels were unaltered in sporadic FTLD-TDP cases in comparison to controls. Overall, these observations replicated the results previously identified in shGRN H4 cells, suggesting that PGRN deficiency is related to an impairment in mitochondrial mass and biogenesis.

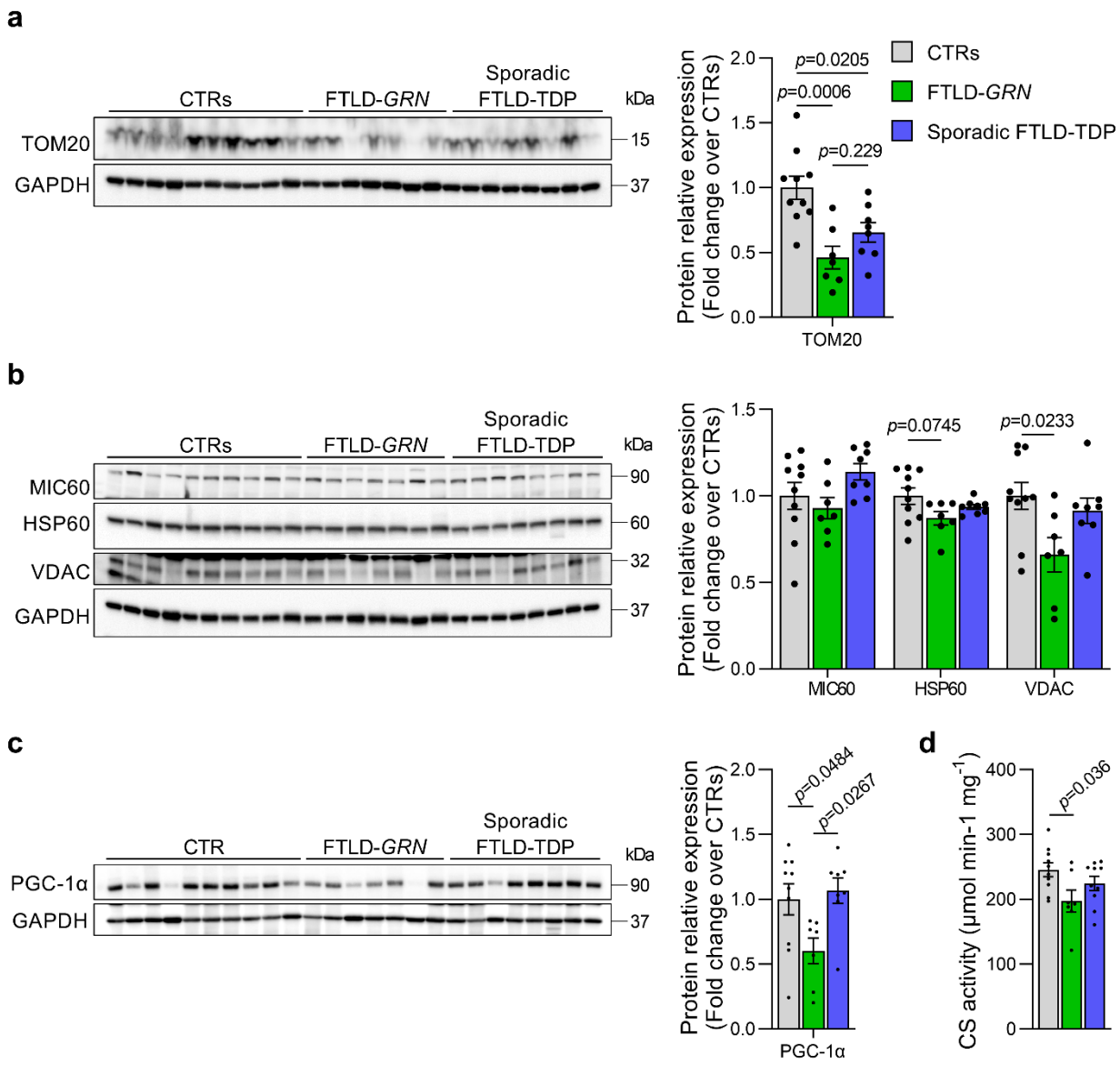

Figure 4.3 Decreased mitochondrial mass and biogenesis in human FTLD-*GRN* post-mortem brains. a Representative western blot and summary bar graph showing the relative protein expression of TOM20 (*n*=7 FTLD-*GRN*, *n*=8 sporadic FTLD-TDP, *n*=10 controls). **b** Representative western blot and summary bar graph showing the relative protein expression of MIC60, HSP60 and VDAC (*n*=7 FTLD-*GRN*, *n*=8 sporadic FTLD-TDP, *n*=10 controls). **c** Representative western blot and summary bar graph showing the relative protein expression of PGC-1α (*n*=7 FTLD-*GRN*, *n*=8 sporadic FTLD-TDP, *n*=10 controls). **d** Citrate synthase (CS) activity measurements (*n*=7 FTLD-*GRN*, *n*=10 sporadic FTLD-TDP, *n*=10 controls). Data are expressed as mean±SEM, where each data point represents an independent biological sample; one-way ANOVA with Tukey's multiple comparison test.

Unaltered quantity and reduced quality of mtDNA in human FTLD-*GRN* brains

The integrity of mtDNA was explored in FTLD-*GRN* brains taking into consideration the previous findings of reduced mtDNAcn in the *in vitro* PGRN-deficient models. Firstly, the mtDNAcn was measured across the different brain regions, comparing FTLD-*GRN* individuals, sporadic FTLD-TDP cases and controls. Two different sets of probes, *MT-CYB*/*GUSB* (Fig. 4.4a-e) and *MT-ND1*/*B2M* (Fig. 4.4f-j), were used. In contrast to the previous results, the mtDNAcn did not show any changes in FTLD-*GRN* cases compared to controls and sporadic FTLD-TDP cases, largely due to a high variability between individuals. Only FG showed an increase in mtDNAcn in sporadic FTLD-TDP cases (Fig. 4.4a).

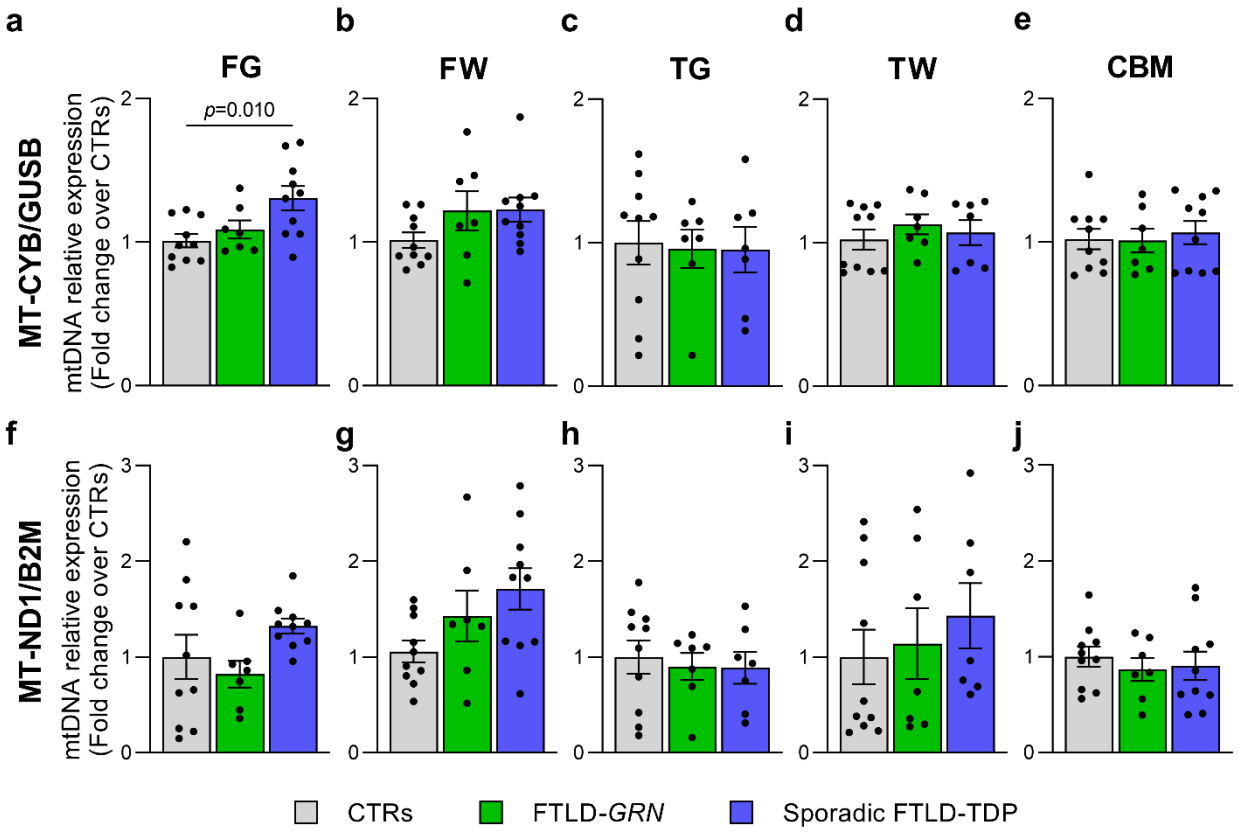

Figure 4.4 FTLD-*GRN* brains show unaltered mtDNAcn. Relative abundance of mtDNAcn in (**a**) FG, (**b**) FW, (**c**) TG, (**d**) TW and (**e**) CBM using MT-CYB/GUSB probes (*n*=7 FTLD-GRN, *n*=10 sporadic FTLD-TDP, *n*=10 controls). Relative abundance of mtDNAcn in (**f**) FG, (**g**) FW, (**h**) TG, (**i**) TW and (**j**) CBM using MT-ND1/B2M probes (*n*=7 FTLD-GRN, *n*=10 sporadic FTLD-TDP, *n*=10 controls). Data are expressed as mean±SEM, where each data point represents an independent biological sample; one-way ANOVA with Tukey's multiple comparison test.

Since mtDNAcn was not affected, mtDNA quality was assessed in the frontal grey matter by quantifying TFAM, a mtDNA binding protein regulating packaging, stability and replication[256]. Strikingly, TFAM was significantly decreased in FTLD-*GRN* samples (Fig. 4.5a), suggesting that mtDNA integrity may be affected. To further assess the mtDNA, NGS data of the mitochondrial genome was processed through eKLIPse to identify deletions that contributed to mitochondrial dysfunction[257]. As preliminary work, NGS was carried out in the frontal grey matter to explore mtDNA deletions in FTLD-*GRN* cases and controls (Fig. 4.5b, 4.5c). This evidence suggested an increase in the number of deletions in FTLD-*GRN* patients compared to controls.

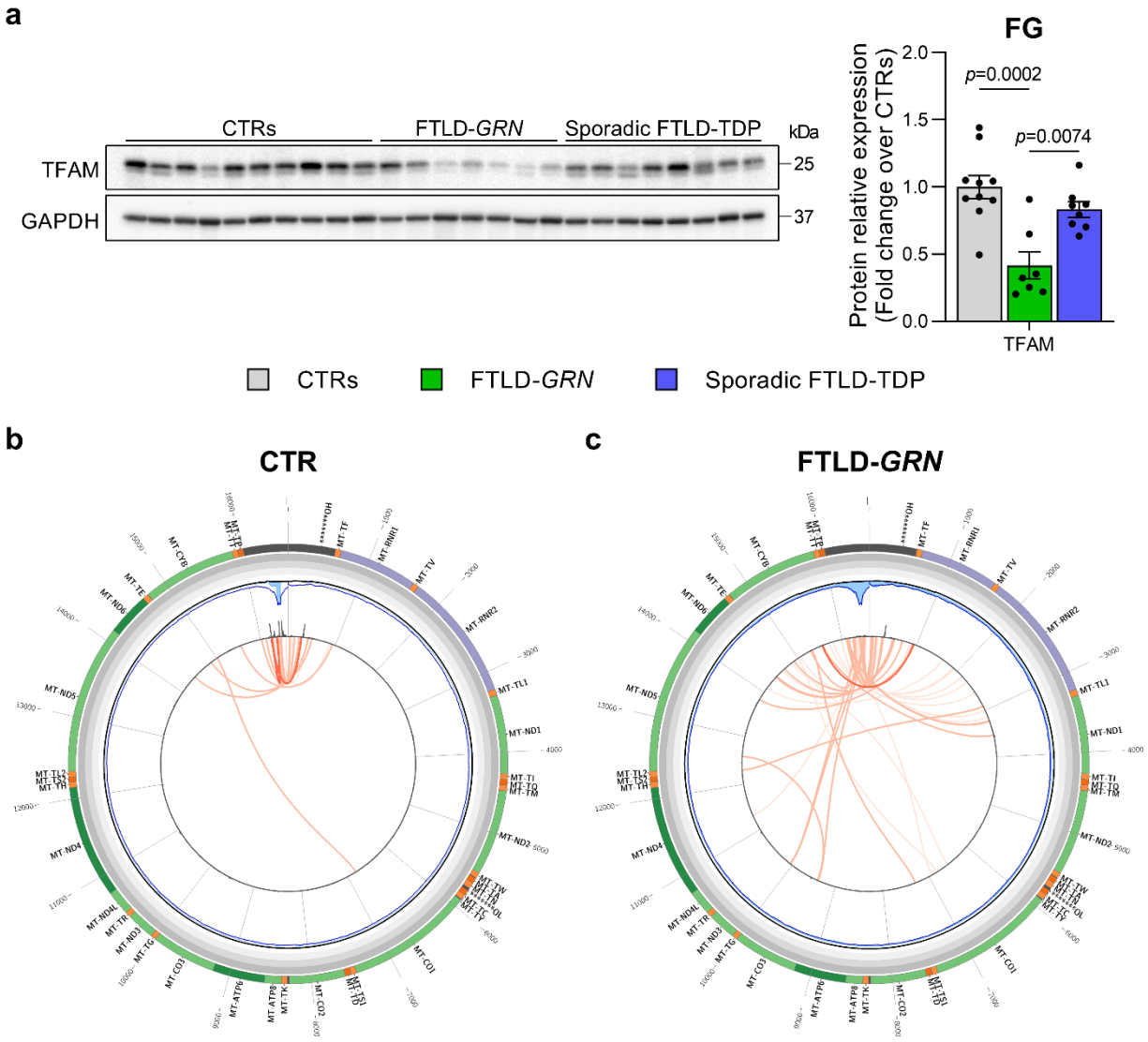

Figure 4.5 Decreased TFAM expression and increased mtDNA deletions in FTLD-*GRN* post-mortem brains. a Representative western blot and summary bar graph showing the relative protein expression of TFAM (*n*=7 FTLD-*GRN*, *n*=8 sporadic FTLD-TDP, *n*=10 controls). **b** Representative mtDNA deletion profile generated using eKLIPse in a control. **c** Representative mtDNA deletion profile generated using eKLIPse in a FTLD-*GRN* case. The outer circle represents the mtDNA genome. Deletions are visualised as red arcs in the centre. Data are expressed as mean±SEM, where each data point represents an independent biological sample; one-way ANOVA with Tukey's multiple comparison test.

The levels of mitochondrial- and nuclear-encoded proteins remain largely unaffected

Following the unaltered levels of mtDNAcn in post-mortem brains, mitochondrial- and nuclear-encoded proteins were assessed in the frontal grey matter. The levels of the mitochondrial-encoded proteins MT-CYB, MT-CO1 and MT-ATP8 remained mostly unaffected across cases (Fig. 4.6a, 4.6b) in alignment with the unchanged levels of mtDNAcn.

The OXPHOS proteins were assessed to explore any changes in nuclear-encoded proteins. The protein levels were unchanged across group cases (Fig. 4.6c). The lack of a significant change was mostly due to the large variation in protein levels within each group.

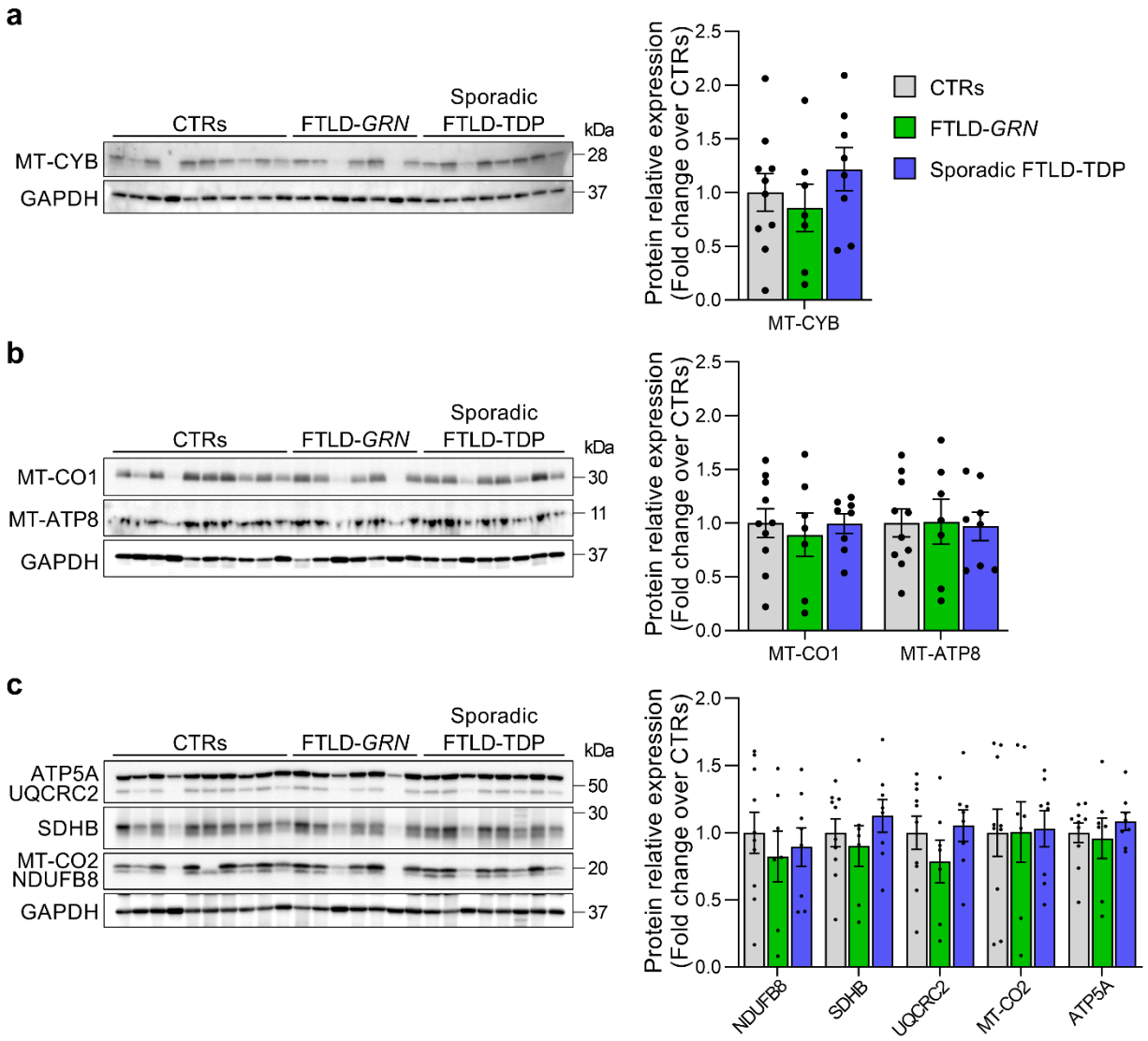

Figure 4.6 FTLD-*GRN* brains show unaltered mitochondrial- and nuclear-encoded protein levels. a Representative western blot and summary bar graph showing the relative protein expression of MT-CYB (*n*=7 FTLD-GRN, *n*=8 sporadic FTLD-TDP, *n*=10 controls). **b** Representative western blot and summary bar graph showing the relative protein expression of MT-CO1 and MT-ATP8 (*n*=7 FTLD-GRN, *n*=8 sporadic FTLD-TDP, *n*=10 controls). **c** Representative western blot and summary bar graph showing the relative protein expression of OXPHOS proteins (*n*=7 FTLD-GRN, *n*=8 sporadic FTLD-TDP, *n*=10 controls). Data are expressed as mean±SEM, where each data point represents an independent biological sample; one-way ANOVA with Tukey's multiple comparison test.

Exploring the effect of different *GRN* mutations in human post-mortem brains

Following the identification of mitochondrial dysfunction in FTLD-*GRN* brains, a *GRN* mutation-specific effect on mitochondrial function was explored. The analysis of three different mitochondrial parameters (mtDNAcn in the FG region, in-gel activity by BN-PAGE (CI and CII) and CN-PAGE (CV), and relative protein expression of PGC-1α by western blotting) were plotted again whilst differentiating between the four *GRN* mutations (C31fs, R493X, Q130fs and IVS3-7T>G) found in the FTLD-*GRN* cases (Fig. 4.7).

The mutations C31fs and Q130fs did not exhibit any remarkable variance from the average. Notably, the mutation IVS3-7T>G presented higher mtDNAcn, complexes activity and PGC-1α protein level. In an opposite direction, the mutation Q130fs displayed the lowest mtDNAcn and enzymes activity, but not PGC-1α protein level. Although no outliers were determined by Grubbs' test, it is noteworthy that the mutations IVS3-7T>G and Q130fs showed contrasting trends to the average of the FTLD-*GRN* cases. Since there was only one patient with a IVS3-7T>G mutation and one with a Q130fs mutation, distinguishing between mutation-specific and patient-specific factors proved to be a complex task. Therefore, the discovery of mitochondrial dysfunction across the FLTD-*GRN* brain tissues was assumed as a shared pathological hallmark across the different *GRN* mutations.

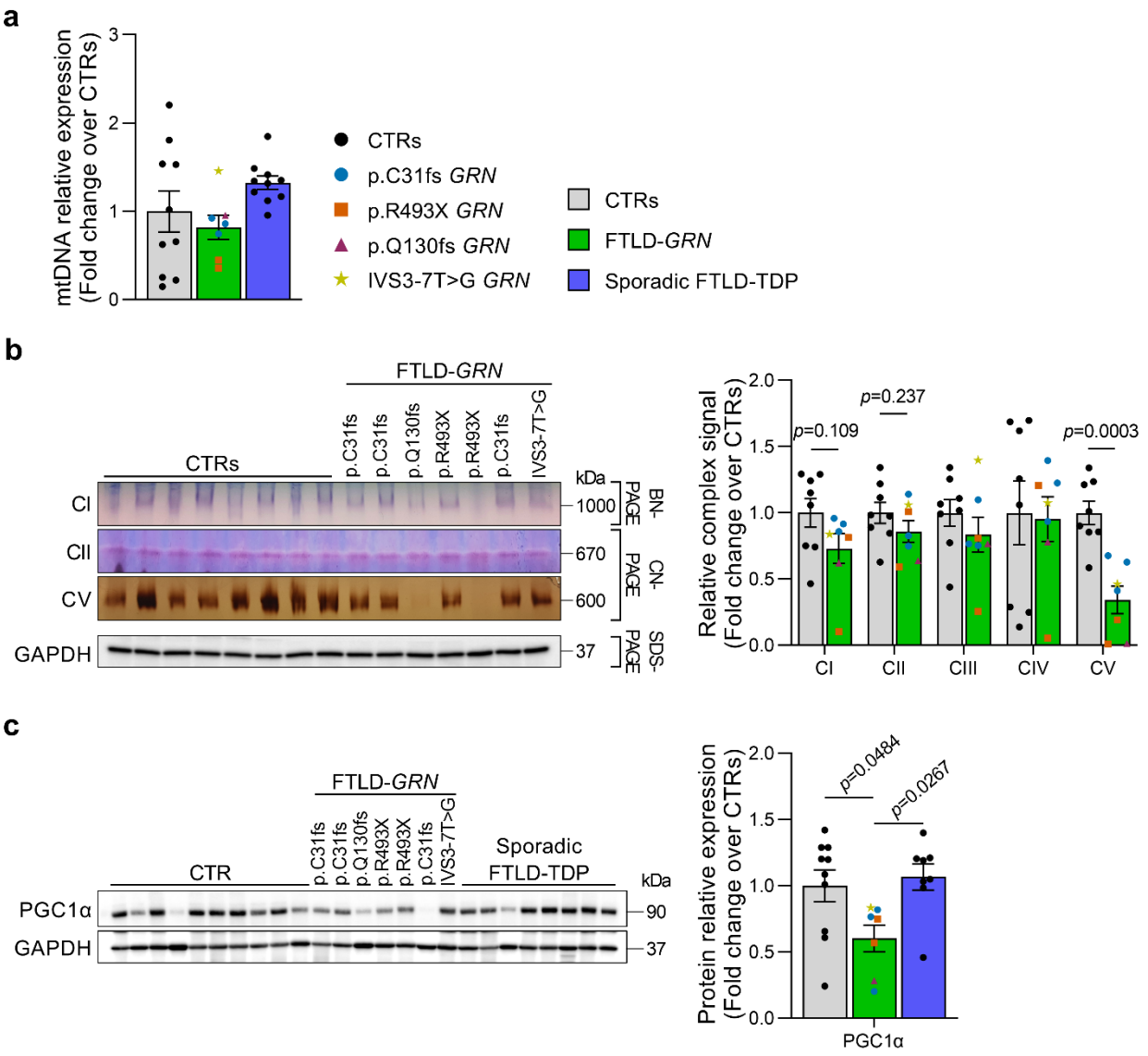

Figure 4.7 Distinguishing between *GRN* mutations when interpreting the mitochondrial phenotype in post-mortem brains. a Relative abundance of mtDNAcn in FG using the *MT-ND1*/*B2M* probe (n=7 FTLD-GRN, n=10 sporadic FTLD-TDP, n=10 controls). **b** BN-PAGE (CI) and CN-PAGE (CII and CV) and summary bar graph showing the complexes in-gel activity, relative to the SDS-PAGE membrane (*n*=7 FTLD-*GRN*, *n*=8 controls). **c** Representative western blot and summary bar graph showing the relative protein expression of PGC-1α (*n*=7 FTLD-*GRN*, *n*=8 sporadic FTLD-TDP, *n*=10 controls). Data are expressed as mean±SEM, where each data point represents an independent biological sample; unpaired *t*-test, one-way ANOVA with Tukey's multiple comparison test.

4.5 Discussion

This chapter conducted a comprehensive and quantitative assessment of mitochondrial phenotypes, evaluating bioenergetics, mitochondrial mass, biogenesis and genotype in post-mortem brain tissue from individuals with FTLD-*GRN*, sporadic FTLD-TDP and controls. The neuropathological post-mortem findings revealed the presence of metabolic deficits in FTLD-*GRN* brains, but not in sporadic FTLD-TDP cases or controls. Given the brain's susceptibility to metabolic stress[258], these results strongly suggested that PGRN haploinsufficiency induces mitochondrial dysfunction, potentially playing a pivotal role in the development of the neurodegenerative disease.

Revealed mitochondrial bioenergetic deficit in human brain samples

Due to the brain's substantial energy requirements relying on OXPHOS, a disruption in mitochondrial metabolism can lead to oxidative stress and neuronal cell death. By using BN-PAGE, CN-PAGE and spectrophotometric measurements, the activity of the CI, CII, CIV and CV in the FG brain region from FTLD-*GRN* patients was found to be decreased. These findings validated the previous results in shGRN H4 cells and confirmed that mitochondrial bioenergetic deficit is involved in *GRN*-related FTD. The specific decrease in CI and CIV observed in FTLD-*GRN* brains is indeed a common pathological hallmark that underlies numerous neurodegenerative diseases, including AD, PD and ALS[237,259].

Disrupted mitochondrial bioenergetics can give rise to changes in neurometabolic coupling, energy processing and neuronal function. In neurons in particular, any disruption of the OXPHOS process could affect the synaptic function and neurotransmitter synthesis, release, and uptake. Unlike other brain cell types, neurons lack the essential enzymes required to switch to glycolytic or non-aerobic ATP production[260]. Consequently, neurons depend on astrocytes to boost their glycolytic production of lactate to aid neurons[261]. However, this can lead to an imbalance in lactate and glucose levels, modifying mitochondrial function and further contribute to mitochondrial impairment, glutamate toxicity and neurodegeneration[262,263].

One of the limitations in the assessment of mitochondrial bioenergetics was the lack of a comparison of FTLD-*GRN* and control brains with the sporadic FTLD-TDP cases. Therefore, the bioenergetic deficit observed in FTLD-*GRN* may not be exclusively associated with PGRN deficiency, but also with a potential overarching mitochondrial phenotype in other FTLD-TDP types. Although this was due to a technical limitation in the gel size available for in-gel activity, future work will attempt to compare controls with sporadic FTLD-TDP cases.

PGRN haploinsufficiency induces a decrease in mitochondrial mass and biogenesis

A decrease in mitochondrial bioenergetics and the crucial components of the ETC can indicate decreased mitochondrial mass, impaired mitochondrial biogenesis or increased mitochondrial clearance. In this chapter, mitochondrial mass markers TOM20 and VDAC were found to be significantly decreased in FTLD-*GRN* brains in comparison to controls, suggesting that mitochondrial mass was reduced in PGRN-deficient brains. The mitochondrial content was also decreased based on the measurement of citrate synthase activity.

Both mitochondrial mass and content are influenced by mitochondrial biogenesis. Impaired PGC-1α levels have been reported in human and mice models of neurodegenerative disorders, including PD, Huntington's disease and AD[264–266]. In the FTLD-*GRN* brains, the downregulation of PGC-1α indicated that the biogenesis master may play a role in the decrease in bioenergetics, mass and content. This biogenesis impairment was not observed in sporadic FTLD-TDP patients, revealing a specific response by which PGRN deficiency leads to mitochondrial dysfunction.

Accumulating evidence has suggested the presence of a strong correlation between glucose metabolism, mitochondrial function and neurodegenerative disorders[267]. The impairment in mitochondrial respiration and biogenesis in FTLD-*GRN* brain in comparison to control brains could partly explain the glucose hypometabolic phenotype previously reported in FTLD-*GRN* patients[201]. Interestingly, brain glucose hypometabolism began on average 7 years before disease onset, indicating that this reduced metabolic activity, and by extension mitochondrial dysfunction, may play a role in the phenotypic disease onset and progression of *GRN*-related FTD pathogenesis.

PGRN deficiency affects mtDNA maintenance in brains

The mtDNAcn in human post-mortem brains has previously been reported to be unchanged in FTD cases compared to controls[243]. Our findings similarly showed no difference in mtDNAcn across brain regions of FTLD-*GRN* and sporadic FTLD-TDP patients. In contrast, a decrease in mtDNAcn was observed in shGRN H4 cells (Fig. 3.5) and in the PGRN-deficient fibroblasts (Fig. 3.11). The difference in mtDNAcn findings may be due to the intrinsic physiological differences across the models, indicating variability in the systemic effect beyond the CNS by which PGRN haploinsufficiency affects the mitochondrial phenotype.

It is curious to note that the levels of mtDNAcn remained unchanged across the brain regions despite the decrease in mitochondrial content in the frontal grey matter. The separation of these two variables may be explained by the presence of different mechanisms regulating the levels of mtDNAcn and mitochondrial content, which have been effectively modified in model systems to control one of the read-outs without impacting the other one[244].

The employed experimental qPCR method to quantify mtDNAcn required the homogenisation of the brain tissue which removed any possibility to distinguish different types of brain cells (i.e., neurons, microglia and astrocytes). However, in age-associated forms of neurodegeneration, reactive gliosis has been related to the loss of certain neuronal populations which would be underrepresented in brain homogenates[268]. Therefore, the application of single-cell techniques to post-mortem brain tissue could facilitate the understanding of the variations across different cell populations in *GRN*-related FTD and uncover cell-specific mtDNA responses.

Despite the lack of a change in mtDNAcn, the decrease in TFAM protein expression in brains suggested altered mtDNA integrity. As part of preliminary work analysing NGS data using

eKLIPse, an increase in mtDNA deletions was observed in the frontal grey matter of the FTLD-*GRN* brains. Therefore in this thesis, PGRN deficiency has been demonstrated to affect mtDNA maintenance in post-mortem brains, which can consequently accelerate the process of metabolic defect and mitochondrial dysfunction.

These results are in alignment with previous studies that have reported an increase in mtDNA deletions in ageing and other neurodegenerative disorders, including other forms of FTD, which indicate an increased burden of mitochondrial pathology[192,243,269,270]. Results vary across research studies when reporting specific brain region alterations in mtDNAcn and deletions in neurodegenerative diseases[244]. The use of complementary quantitative methods, such as whole exome sequencing and digital droplet PCR, could provide additional validation for the reported results in the post-mortem brains. Future experiments will build upon the preliminary NGS work presented in this thesis. This will encompass a thorough amplification, sequencing, and analysis processed through eKLIPse for all post-mortem brains across different brain regions, which will offer a more comprehensive exploration of the mtDNA deletion profile specific to FTD.

Limitations in the study of post-mortem brains

The results in this chapter uncovered that PGRN dysfunction induces mitochondrial dysfunction in *GRN*-related FTD. Careful consideration of the limitations is essential for a comprehensive understanding of research findings.

While controls were requested to be age- and sex-matched with FLTD cases, there was a lower number of FTLD-*GRN* cases than of controls or sporadic FTLD-TDP, and the controls were older than the FTLD cases. Consequently, all controls were not strictly “age- and sex-matched”. Although this may have affected comparisons between groups, it is important to note that there was a limited availability of controls at the brain bank centre with a similar age- and sex-match to the FTLD groups. In addition, ageing has been associated with a decrease in mitochondrial activity and higher mtDNA mutations[271–273]. According to this statement, brains from older controls would likely display a lower mitochondrial activity and higher mtDNA mutations, potentially strengthening the results from this study since FTLD-*GRN* patients demonstrated increased mitochondrial dysfunction compared to older controls.

Conclusion and future directions

To conclude, the study of mitochondria in the context of *GRN*-related FTD is indispensable for unravelling the complex web of molecular events underlying this devastating neurodegenerative disorder. Following the research carried out in this chapter, mitochondrial dysfunction is now associated with the pathogenesis of FTLD-*GRN* brain tissues, affecting mitochondrial bioenergetics, biogenesis, content and mtDNA integrity. Future work identifying the mechanistic links between mitochondrial dysfunction and *GRN*-related FTD will shed light on the development of novel biomarkers and therapeutic strategies to treat FTD and other neurodegenerative diseases.

In the current chapter, mitochondrial bioenergetics, mass and biogenesis were characterised only in the FG matter of FTLD-*GRN* brains, whereas the mtDNA was assessed in all FG, FW, TG, TW and CBM of FTLD-*GRN* brains. Although this was due to either technical limitations or time-constrains, the characterisation of these mitochondrial parameters across the different brain regions for both grey and white matter could provide further insight into brain region-specific mitochondrial changes.

The investigation of the role of mitochondria in FTLD-*GRN* patients would be complemented by studying the mitochondrial phenotype in other human tissues, such as serum and CSF, which can be considered more widely accessible and less invasive for patients. These could offer an opportunity to explore circulating cell-free mtDNA in health and disease, and potentially identify mitochondrial markers that correlate to the disease onset and progression. While mitochondria hold promise as biomarkers for neurodegeneration, challenges remain, including the need for standardized diagnostic criteria and assays. Future research is needed to validate these biomarkers and establish their clinical utility.

The findings in this chapter highlight for the first time an impairment in mitochondrial function in post-mortem brains from patients with *GRN*-related FTD. This supports the evidence of a link between PGRN haploinsufficiency and mitochondrial dysfunction in *in vitro* models. However, whether mitochondrial dysfunction arises due to a specific PGRN deficiency mechanism or a mechanism overarching all FTLD-TDP types remains unknown. As a future step, the use of multi-omics techniques to characterise cell-specific mitochondrial phenotypes will help address and further investigate this crucial issue.

5 Employing histopathology techniques to explore FTD brains

Dotted science (pen and markers) – by Javier S. Bautista

5.1. Introduction

The use of neuropathology techniques for FTLD diagnosis

Definitive diagnosis of human neurodegenerative disorders requires neuropathological examination of the patients. The use of IHC, morphological, biochemical and molecular genetic tests is considered crucial for experienced pathologists to identify a disease and its specific subtypes. Therefore, the development and optimisation of histopathology techniques to characterise the healthy and pathological state of human tissues can provide a better understanding of the disease, improving the process of diagnosis and guiding the selection of the most optimal therapeutic strategies.

Due to the large complexity of FTD subtypes, a combination of clinical, molecular and genetic diagnosis is required to quickly identify and treat FTD cases. This thesis chapter primarily focused on characterising neuropathological changes in FFPE human post-mortem brains of FTLD-*GRN* cases in comparison to controls and sporadic FTLD-TDP. Since the identification of autosomal-dominant *GRN* mutations as a cause of FTD in 2006[16], several studies have widely reported the pathology of FTLD patients, emphasising on the pTDP-43 burden in cases with *GRN* mutations, an aspect further explored in this chapter. Other well characterised pathological features include a ubiquitin-positive, tau-negative profile[274,275], and microglial dystrophy[49]. In addition, given the overall aim of this PhD project investigating the role of mitochondria in *GRN*-related FTD, there was an interest in characterising the state of mitochondria in FTD brains employing histopathology techniques.

Over the last decade, the quantification of histopathology techniques relying on image analysis has rapidly advanced with the development of open-source, user-friendly software. Therefore, semi-automatic quantitative methods were developed to characterise FTD histopathology. The overall purpose of developing semi-automatic quantitative method was

not only to expedite the diagnostic process but also to standardise the measurements with a deeper level of insight, particularly in terms of stained area, thereby mitigating any accidental biases from a pathologist's perspective.

Finally, I wanted to highlight that the work in this chapter was carried out within the Department of Neuropathology, Queen Square, and I am grateful for the guidance provided by Darren Chambers, Dr Juliane Mueller, Dr Francesco Catapano and Dr Rahul Phadke.

Investigating the expression of pTDP-43 across FTLD brain regions

Before the discovery of *GRN*-mutations, IHC assays showed that many FTLD cases had ubiquitin inclusions, which led to the denomination of the subtype as FTLDU (FTLD with ubiquitin inclusions)[276]. In 2006, Neumann et al.[277] demonstrated that abnormal, ubiquitinated pTDP-43 was the main protein constituent linked to ubiquitin in FTLDU cases which led to the eventual renaming of the subtype into FTLD-TDP. TDP-43 is a nuclear-encoded 414-amino-acid protein that is involved in gene transcription, exon splicing regulation and nuclear body functions[278,279]. However, in pathological conditions, TDP-43 can aggregate in both the cytoplasm and the nuclei of affected neurons and glia[280]. TDP-43 aggregates have also been associated with hyperphosphorylation, ubiquitination and C-terminal cleavage[281–283]. Notably, pTDP-43 aggregation was also observed in ALS cases[277], highlighting the clinicopathological spectrum shared between FTD and ALS[284].

As the field of TDP-43 proteinopathy started to blossom, two independent groups reported mutations of the gene *GRN* leading to FTLD which were tau-negative, ubiquitin-positive and with moderate numbers of lentiform neuronal intranuclear inclusions[16,33]. FTLD-*GRN* also presented pTDP-43 proteinopathy, which placed them within the FTLD-TDP subtype, more specifically FTLD-TDP type A. Therefore, the accumulation of pTDP-43 aggregates has been hypothesised to be linked to the process of neurodegeneration.

As part of the investigation of pTDP-43 burden, there were two main unanswered questions regarding the neuropathology of pTDP-43 in FTLD-*GRN* cases: 1) Can a standardised, quantitative method be developed to assess pTDP-43 burden using histopathology techniques, and 2) Are there any differences in pTDP-43 across different brain regions of FTD patients? To explore these two questions, I attempted to devise a semi-automatic quantitative method to assess the pTDP-43 burden. The results were then compared among

controls, FTLD-*GRN* and sporadic FTLD-TDP cases, all whilst differentiating between grey and white matter, as well as among the frontal lobe, temporal lobe and cerebellum.

Characterising the state of mitochondria in FFPE human brains

Immunohistochemical staining techniques have been crucial for spatially visualising mitochondria and respiratory chain dysfunction in tissues. Despite the use of state-of-the-art techniques and advanced genetic testing that are improving the diagnosing of mitochondrial diseases, the unknown effect of genetic abnormalities essentially requires tissue and morphological characterisation assays to further investigate the pathology.

Some of the most traditional histochemical techniques to investigate mitochondria involve measuring the activity of the enzymes succinate dehydrogenase (SDH) and COX[285]. However, these two enzymes cannot be explored in formalin-fixed paraffin-embedded tissues as formalin fixation results in loss of enzymatic activity[286]. IHC techniques are also regularly employed to visualise mitochondria and specific subunits of the OXPHOS complex. These include the use of methods based upon enzyme-substrate reactions giving rise to coloured precipitates. For instance, at the Department of Neuropathology, Queen Square, DAB staining is routinely used to study the expression of proteins. The use of enzyme-substrate reactions enables the visualisation and potential quantification of mitochondria, whereas fluorescent techniques on FFPE tissues tend to display autofluorescence from accumulated lipofuscin granules or fixatives in the green fluorescent range[287]. Based on this technique, in parallel to the biochemical characterisation in the previous chapters, I proceeded to optimise and investigate the expression of the MT-CO1 protein, which is part of the mitochondrial CIV, using DAB staining on FFPE human FTLD post-mortem brains.

Developing an RNAscope mtDNA assay in FFPE human brains

Currently, NGS is considered the "gold standard" technique in pathology labs to investigate mtDNA deletions and depletions. NGS, in addition to qPCR, was carried out on the snap-frozen FTD brains as demonstrated in Chapter 4 (Fig. 4.5). However, the need for homogenised tissues brings up several limitations, such as the loss of cell type discrimination (e.g., microglia vs astrocytes) and the lack of fibre distinction in skeletal muscles (e.g., slow vs fast fibres with different mtDNAcn)[288]. Another emerging technique is single-cell qPCR, which has similar results, but it is more expensive, requires arduous microdissections and yields a lesser number of fibres for analysis[289]. To tackle the challenges faced by NGS and (single-cell) qPCR, RNAscope ISH enables the target of single DNA and/or RNA molecules, providing spatial mitochondrial gene expression results under the microscope.

To date, only a few studies explored the mitochondrial state by RNAscope. Most works initially focused on using the technique to explore the transcription expression of mitochondria-related genes, including *AIFM1* (involved in apoptosis), *PINK1* and *mcPGK1* (mitochondrial circRNA for translocating phosphoglycerate kinase 1)[290–292]. Recent studies have started used RNAscope probes to visualise mtDNA. For example, one of the first articles was published in 2020, when Chen et al. used RNAscope CISH to map mtDNA across different mammalian tissues, including mouse cerebellum[293]. This study was based on the principle that although transcription of the circular mtDNA is bidirectional, most light strand transcription is rapidly degraded, including the anti-sense strand of mtDNA genes[294]. Then, in 2021, Mehta et al. employed BaseScope CISH to map mtDNA in post-mortem spinal cord neurons and attempted signal quantification[175]. BaseScope works in a similar way but it targets shorter RNA sequences between 50-300nt, whereas RNAscope targets lncRNA and mRNA sequences greater than 300nt[295]. Finally, in 2022, a study used

RNAscope ISH to detect *MT-ND1* and *MT-ND4* mtDNA transcripts in skeletal muscle biopsies, which enabled the differentiation between common deletions (*MT-ND1*) and depletions (*MT-ND4*) at a single fibre level. Whilst these studies set the foundations for RNAscope ISH mtDNA exploration, there were still outstanding questions about the translation of this technique to human FFPE post-mortem brains and the viability of a quantitative approach.

Therefore, the aim of this subsection was to determine the feasibility of a CISH assay to detect and quantify mtDNA in human post-mortem brains. This assay was part of an ongoing, unpublished work which has largely focused on developing a multiplex mtDNA assay to explore mtDNA deletions and depletions in skeletal muscle at a single-cell level. Before heading into this project, some of the results so far included an optimised fluorescence singleplex RNAscope assay probing for the major arc, the minor arc and the D-loop of mtDNA in skeletal muscle. Multiplexing of the probes however led to decreased specificity and quenched signal, potentially due to steric hindrance between the probes.

In the diagnostic process for mitochondrial diseases, skeletal muscle is sampled due to the relevance of the tissue to neuromuscular disorders, the susceptibility to mitochondrial dysfunction and how the biopsy in patients is less invasive compared to brain biopsies. New and existing mitochondria-investigating techniques tend to be optimised first in fresh-frozen skeletal muscle before being employed in other regions. Following this pattern, the optimisation of this new RNAscope assay was first explored in the skeletal muscle and then in human FFPE post-mortem brain.

In an effort to characterise the mitochondrial genome in human brains diagnosed with FTD, an RNAscope CISH method was developed to spatially map mtDNA in tissue brain sections. The probe *MT-ND5* was employed to target the major arc of the mtDNA since most of the

common mtDNA deletions take place there. In addition, a quantitative method was devised to quantify the *MT-ND5* RNAscope signal in human brains.

5.2. Aims

The overall aim of this chapter was to optimise histopathology techniques and develop semi-automatic quantitative techniques to identify and measure neuropathological changes in FTLD-*GRN* cases.

The specific aims of this chapter were:

- To develop a semi-automatic quantitative method to investigate pTDP-43 burden in FTLD-*GRN* cases, sporadic FTLD-TDP cases and controls across brain regions;

- To explore the levels of MT-CO1 using IHC DAB staining across FTD cases and different brain regions;

- To optimise an RNAscope CISH assay for spatial mapping of mtDNA in human brains, whilst developing a quantitative method to compare *MT-ND5* signal across FTD cases and brain regions.

5.3. Materials and methods

FFPE histological sections were acquired from the QSBB. Eighteen cases (14 FTLD and 4 controls) were employed for histopathology studies, and a summary of the demographics for these cases are presented in Table 2.2. These cases constituted a smaller subset compared to the complete cohort used in the previous chapter, as the histopathology experiments were treated as a pilot research project.

The 14 FTLD different cases included four with *GRN* mutations (FTLD-*GRN*; two C31fs mutation, one R493X mutation, and one Q130fs mutation; all FTLD-TDPA) and ten with sporadic FTLD-TDP cases without *GRN* mutations (sporadic FTLD-TDP; three FTLD-TDPA, three FTLD-TDPB and four FTLD-TDPC). Parameters were compared between FTLD-*GRN*, sporadic FTLD-TDP and controls, as well as between grey and white matter of the frontal and temporal lobes and the cerebellum.

Comparisons of age of onset, age at death, disease duration, post-mortem delay, sex and braak stage across groups are shown in Fig. 5.1. Age at onset, disease duration and sex were generally similar between cases and controls. FTLD-*GRN* and sporadic FTLD-TDP had a younger age at death compared with controls (p = 0.0070 and p = 0.0145, respectively). Sporadic FTLD-TDP cases had a shorter post-mortem delay than controls (p = 0.0458), suggesting that sporadic cases may have maintained tissue integrity to a slightly superior degree. Braak stage showed some variability, with one sporadic case with Braak stage V.

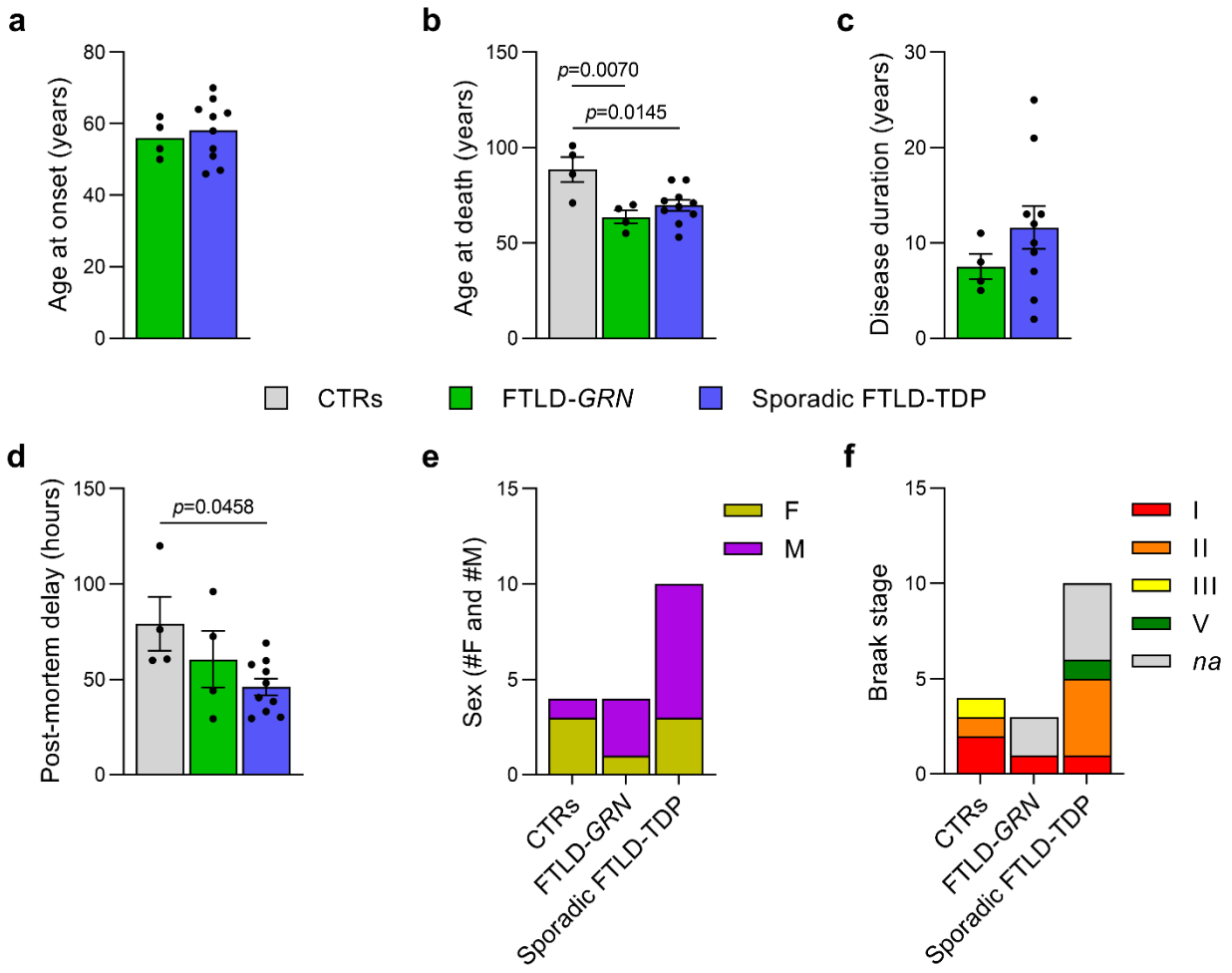

Figure 5.1 Comparison of demographics between the human FFPE post-mortem brains. Graphs show comparison of (**a**) age at onset, (**b**) age at death, (**c**) disease duration, (**d**) post-mortem delay, (**e**) sex and (**f**) Braak stage (range I to V) across groups (*n*=4 FTLD-*GRN*, *n*=10 sporadic FTLD-TDP, *n*=4 controls). Data are expressed as mean±SEM, where each data point represents an independent biological sample; unpaired *t*-test, one-way ANOVA with Tukey's multiple comparison test.

The first aim in this chapter involved the assessment of pTDP-43 burden in FTLD-*GRN* cases. A wide range of methods have been previously employed to investigate pTDP-43 burden, including western blotting on human brains[296], immunofluorescence in a cell-based system with brain-derived pathological TDP-43 from FTD[297], and semi-quantitative methods with a severity grading system[298]. The novelty in this work was the attempt to quantify pTDP-43 burden by staining the sections and developing a semi-automatic method as described

in Chapter 2. This was executed using QuPath, a software designed at Queen's University Belfast that supports a wide range of additional image analysis applications[299].

Another technique employed in this chapter included IHC staining of MT-CO1 in the human FFPE brain samples in order to investigate the expression of the mitochondrial protein. Finally, the use of the probe *MT-ND5* in the CISH RNAscope assay was optimised in skeletal muscles and brain samples, and a semi-automatic method was designed on QuPath for the quantification of mtDNA abundance. Detailed methods can be found in Chapter 2.

5.4. Results

Increased pTDP-43 burden in human FTLD post-mortem brains

The staining for pTDP-43 aggregation was carried out in every brain histological section, and representative stains can be found in Figure 5.2 for the different pathological cases (controls, FTLD-*GRN* and sporadic FTLD-TDP) and each brain region (frontal lobe, temporal lobe and cerebellum). Additionally, differentiation between grey and white matter was discernible in each tissue, facilitated by Haematoxylin staining.

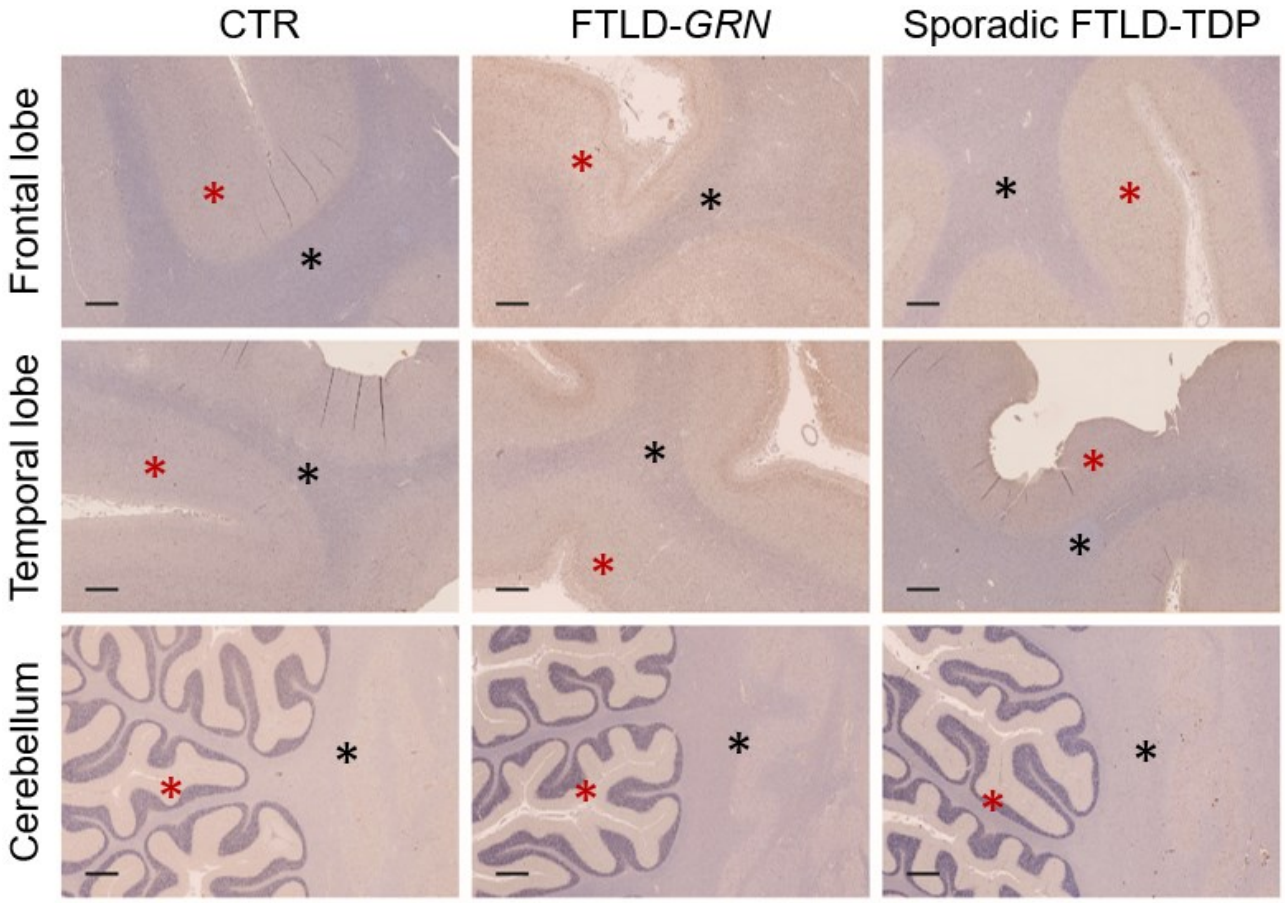

Figure 5.2 pTDP-43 DAB staining of human post-mortem brains. Black asterisks denote the white matter and the red asterisks denote the grey matter. Scale bar = 1 mm.

As previously described, scripts were developed and ran on QuPath software, enabling the semi-automatic quantification of pTDP-43 burden. Three approaches were employed to measure pTDP-43 burden based on the percentage of pTDP-43-stained area (Fig. 5.3a), number of pTDP-43 clusters (Fig. 5.3b) and total number of pTDP-43 spots (Fig. 5.3c).

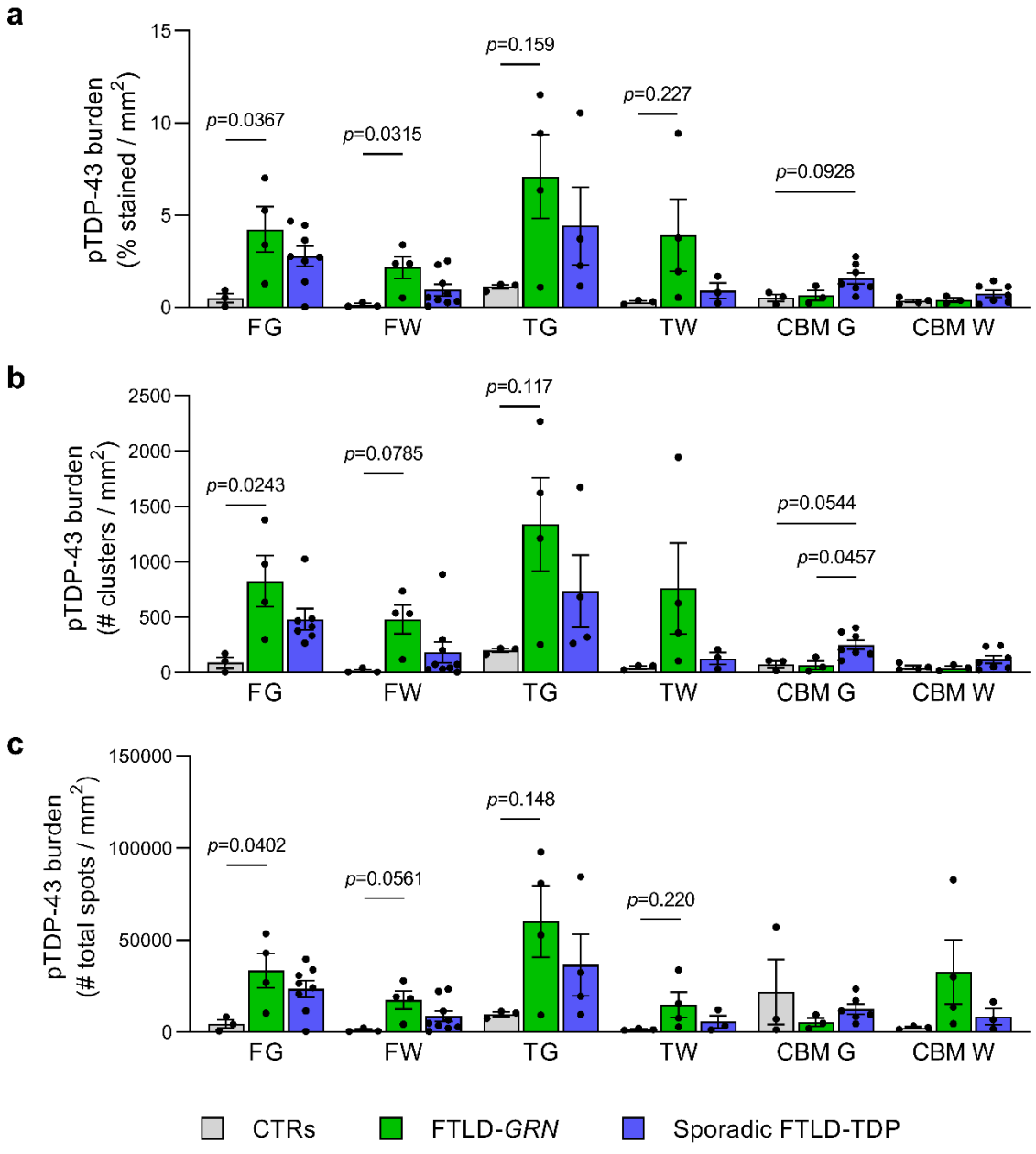

Figure 5.3 pTDP-43 burden in human post-mortem brains. The pTDP-43 burden was measured according to the (**a**) % stained / mm^2, (**b**) number of pTDP-43 clusters / mm^2 and (**c**) number of total pTDP-43 counts (*n*=3-4 FTLD-*GRN*, *n*=4-9 sporadic FTLD-TDP, *n*=3-4 controls). Data are expressed as mean±SEM, where each data point represents an independent biological sample; one-way ANOVA with Tukey's multiple comparison test. Abbreviations: FG, frontal grey; FW, frontal white; TG, temporal grey; TW, temporal white; CBM G, cerebellum grey; CBM W, cerebellum white.

A similar pattern in pTDP-43 burden could be observed across the three different quantitative approaches, presenting similar results and degrees of variability across cases. However, pTDP-43 staining was detected and quantified in controls and in the cerebellum across patients. Taking into consideration that there should not be pTDP-43 signal in these areas, I proceeded to manually inspect the specific micrographs which indeed presented pTDP-43 staining and clusters. This indicated that the pTDP-43 signal may not be specific, potentially due to the antibody reacting with non-pathological TDP-43, and/or inaccuracies in the QuPath parameters used to quantify the pTDP-43 signal. As a results of these limitations, no further analysis was pursued, and the preliminary findings and constraints will be covered in the discussion.

High variability of MT-CO1 protein in human post-mortem brains

MT-CO1 IHC staining was carried out in the frontal lobe, temporal lobe and cerebellum of each case (Fig. 5.4). There was a high variability of MT-CO1 signal across cases, making it challenging to visually identify any differences in signal intensity. Across regions, more MT-CO1 signal can be observed in the frontal lobe and the cerebellum than in the temporal lobe. The high variability between cases made any attempts of quantification redundant.

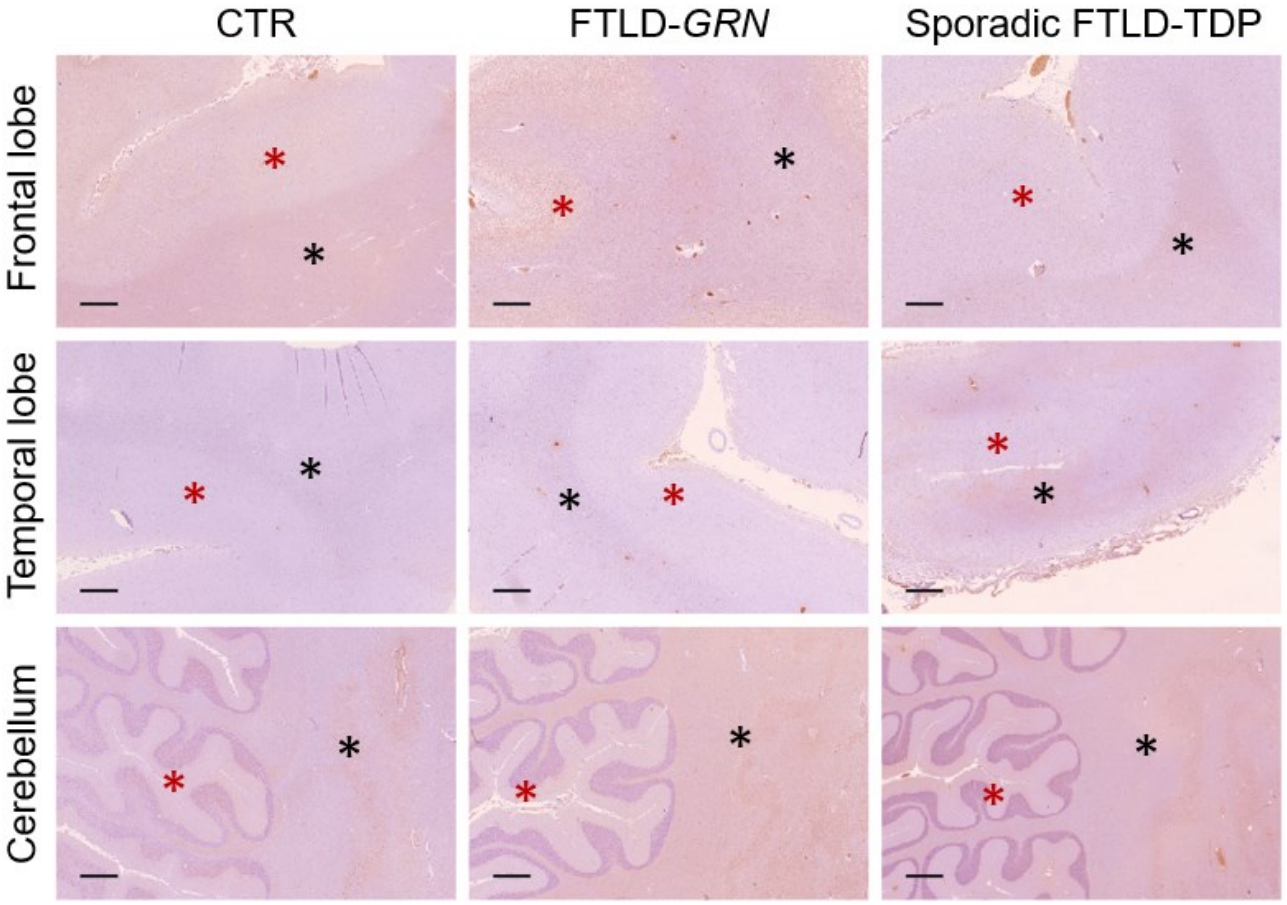

Figure 5.4 MT-CO1 DAB staining of human post-mortem brains. Black asterisks denote the white matter and the red asterisks denote the grey matter. Scale bar = 1 mm.

Notably, the dentate nucleus, the largest deep cerebellar cluster of neurons in the cerebellum, exhibited a higher level of MT-CO1 expression compared to the surrounding white matter.

Using RNAscope CISH to interrogate mtDNA in human brains

The RNAscope assay using the sense strand *MT-ND5* probe was carried out in the frontal lobe of the brain histological sections, facilitating the comparison between controls, FTLD-*GRN* cases and sporadic FTLD-TDP cases in both grey and white matter (Fig. 5.5).

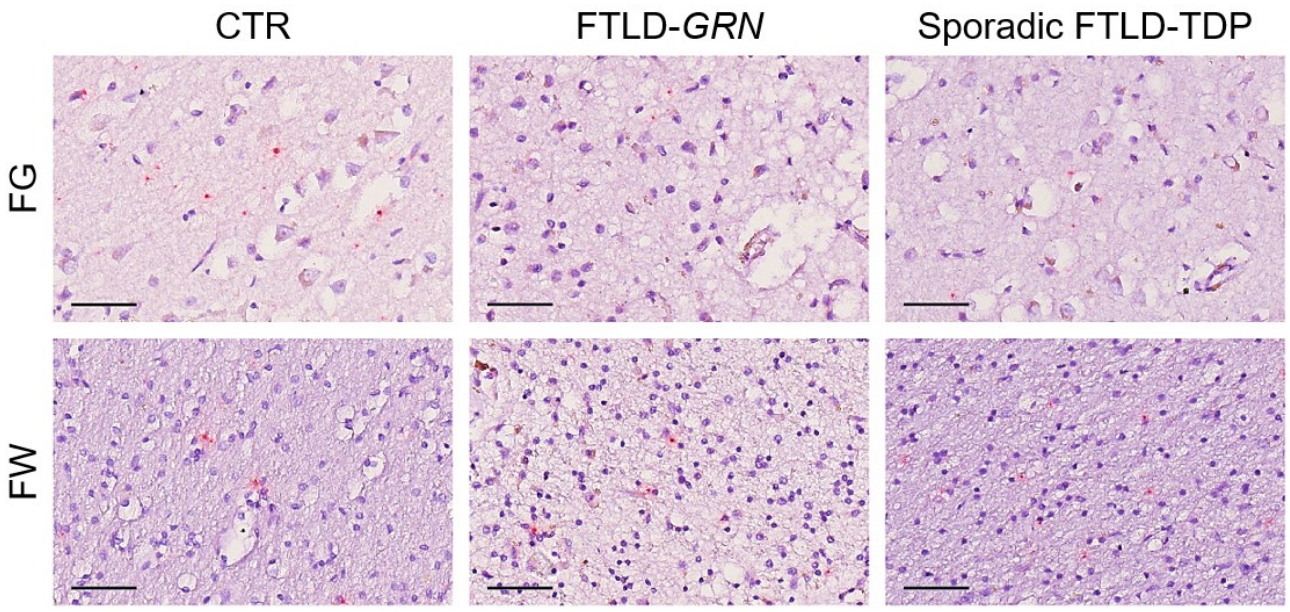

Figure 5.5 RNAscope CISH *MT-ND5* staining of human FTLD post-mortem brains. Abbreviations: FG, frontal grey; FW, frontal white. Graph bar = 50 μm.

No clear differences in *MT-ND5* signal were visually discernible among the various cases and regions, primarily due to high variability across patients. Consequently, a semi-automatic quantitative method was developed to assess the RNAscope assay, and QuPath software along with the scripts were used to measure the mtDNA signal in the RNAscope CISH-stained brain sections (Fig. 5.20). This quantitative method revealed a decrease in *MT-ND5* spots in FG of both FTLD-*GRN* and sporadic FTLD-TDP (Fig. 5.6a), and a decrease in *MT-ND5* spots in FW of sporadic FTLD-TDP only (Fig. 5.6b). However, these findings contradicted the qPCR results previously obtained from snap-frozen brains of the same cases (Fig. 4.4), which showed no changes in mtDNAcn. Considering how qPCR is a more specific and reliable quantitative technique, this discrepancy raised concerns about

the accuracy of quantifying RNAscope signal. Considering the conflicting results between RNAscope and qPCR, coupled with the high costs of RNAscope and the limited availability of tissue sections, staining and quantification were omitted for the temporal lobe and cerebellum. The controversies and limitations in quantifying RNAscope will be further discussed in the following subsection.

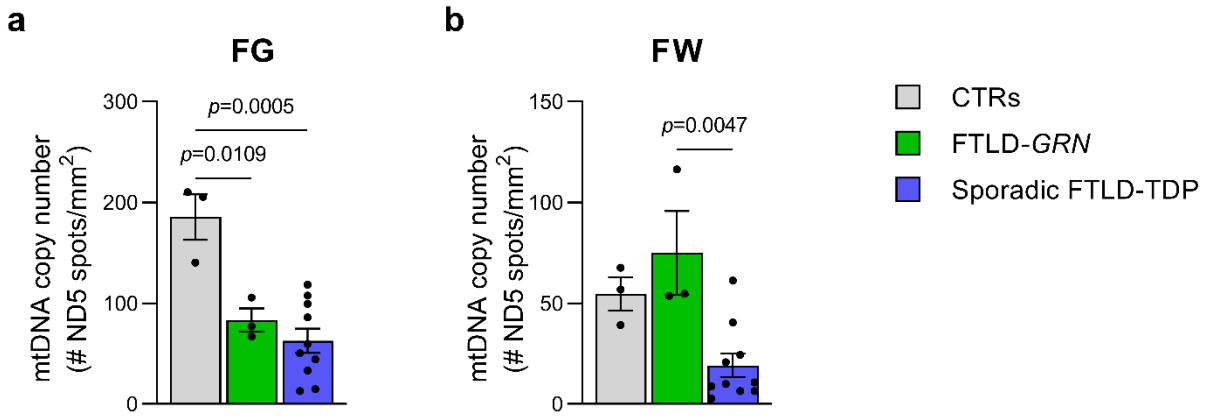

Figure 5.6 Quantification of *MT-ND5* spots in FG and FW of human FTLD brains. *MT-ND5* spots were quantified in (**a**) FG and (**b**) FW using RNAscope assay (*n*=3 FTLD-*GRN*, *n*=10 sporadic FTLD-TDP, *n*=3 controls). Data are expressed as mean±SEM, where each data point represents an independent biological sample; one-way ANOVA with Tukey's multiple comparison test. Abbreviations: FG, frontal grey; FW, frontal white.

Before making a final decision on the reliability of this quantification method for assessing RNAscope CISH staining, I interrogated the assumption related to whether cell density in the brain impacted the *MT-ND5* signal. This exploration aimed to discern whether the observed decrease in *MT-ND5* signal in FTLD-*GRN* cases resulted from lower cell density or other factors, such as *GRN*-specific mechanistic differences or an unreliable quantification method. To test this assumption, the number of nuclei was quantified in ten random squares, each measuring 500x500 µm, for the cases in FG. The *MT-ND5* signal was then either normalised or not normalised to the nuclei (Fig. 5.7a,b). Pearson's correlation test was used to compare the *MT-ND5* results between both normalisation methods (Fig. 5.7c), and the analysis revealed a very high correlation (R^2 = 0.975, p <

0.0001), suggesting that not accounting for cell density does not significantly impact the results.

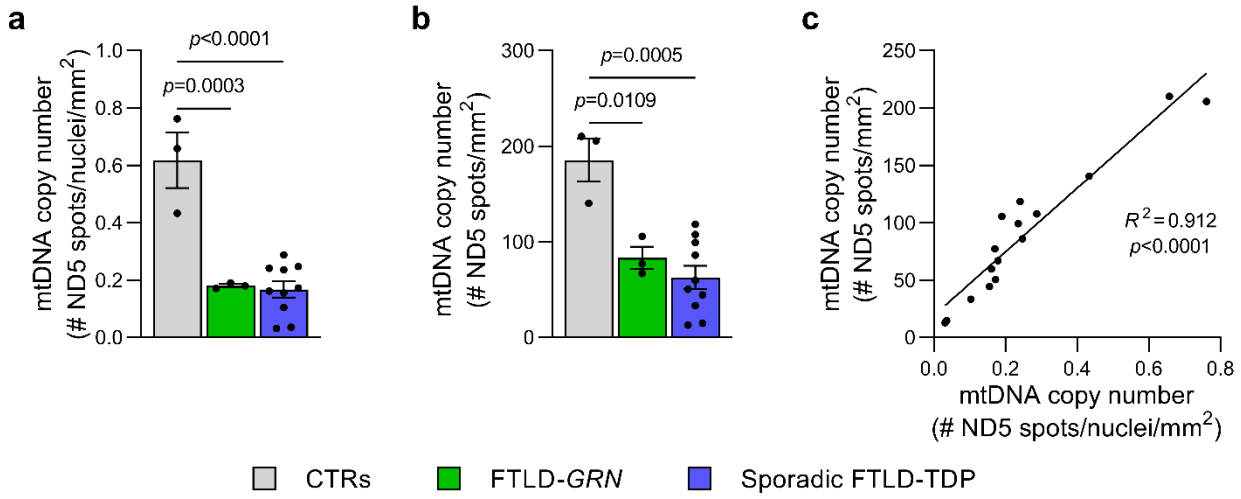

Figure 5.7 Comparison of *MT-ND5* quantification normalised by number of nuclei or not. *MT-ND5* quantification with (**a**) nuclei normalisation and (**b**) without nuclei normalisation (*n*=3 FTLD-*GRN*, *n*=10 sporadic FTLD-TDP, *n*=3 controls). **c** Pearson's correlation of the methods. Data are expressed as mean±SEM, where each data point represents an independent biological sample; one-way ANOVA with Tukey's multiple comparison test, Pearson's correlation test.

5.5. Discussion

Overall, histopathology techniques were optimised to investigate pTDP-43 burden, MT-CO1 protein expression and RNAscope *MT-ND5* expression in human FFPE post-mortem brain across the frontal lobe, temporal lobe and cerebellum. Additionally, preliminary semi-automatic quantitative methods were developed to quantify and compare pTDP-43 burden and RNAscope CISH among FTLD cases, although not successfully. A comprehensive discussion on the results, relevant literature, encountered limitations and avenues for future research is provided in the current section.

Increased pTDP-43 burden across regions in FTLD-*GRN* brains

In this subsection, a preliminary semi-automatic quantitative method was developed to quantify qTDP-43 staining with the purpose of assessing the pTDP-43 burden in FTLD-*GRN* in comparison to sporadic FTLD-TDP and controls. However, inconsistencies in the results based on the expected results suggest that either the staining or the quantification method, or both, were not optimal.

In FTLD-*GRN* patients, all FG, FW, TG and TW regions presented increased pTDP-43 staining. However, when interpreting the different results, it must be noted that low levels of pTDP-43 burden were measured in the control cases across the different brain regions. Similarly, cerebellum across all the cases also showed low pTDP-43 burden levels. Bearing in mind that controls should not present any pTDP-43 burden, and the cerebellum should be free from proteinaceous inclusions, the detection of pTDP-43 burden implies that the technical design was not accurate. In addition, since the pTDP-43 burden analysis could not be considered accurate, the three different approaches could not be compared to select the most suitable one.

A potential explanation is that the antibody may be binding to non-pathological TDP-43, which limits the interpretation of the signal. In addition, the semi-automatic quantitative scripts may not have been precisely optimised to distinguish the pTDP-43 staining from non-specific signal. In this specific piece work, the validation of the technique would greatly benefit from the collaboration with an experienced neuropathologist familiarised with pTDP-43 staining in order to carefully identify the correct parameters.

An experimental design oversight in the histopathological analysis was the combination of the different sporadic FTLD-TDP subtypes A, B and C when interpreting the pTDP-43 burden. As demonstrated by Lashley and colleagues, each FTLD-TDP subtype features different TDP-43-positive inclusion types under microscopic observation[280]. Future work should aim to specifically compare FTLD-*GRN* to sporadic FTLD-TDPA subtype as the pathology in the B and C subtypes may be deemed completely different.

Other limitations to be considered include the relatively small subgroup sizes of human FFPE post-mortem brains and the variable interhemispheric asymmetry of cortical atrophy, a characteristic feature of FTLD-TDP cases[300]. These underscore the need for future studies with larger cohorts to validate the findings presented in this chapter.

Over the last two decades, several studies have shown that FTLD-*GRN* and sporadic FTLD-TDP cases have higher levels of pTDP-43 aggregation than non-pathological controls[297,297]. Considering the broader context of this PhD project, these reported findings prompt a fundamental question: Does pTDP-43 pathology modulate mitochondrial function in individuals with *GRN* mutations? TDP-43 toxicity has been shown to enter mitochondria and preferentially bind mitochondria-encoded ND3 and ND6 subunits, which leads to disassembly of CI[184]. The entrance of TDP-43 has also been demonstrated to trigger mtDNA release via the mitochondrial permeability transition pore (mtPTP), activating the neuroinflammatory cGAS/STING pathway in ALS[183]. Interestingly, the treatment of *GRN* KD SH-SY5Y with pTDP-43 inhibitors showed a restoration of the mitochondrial membrane potential[206]. Future studies are required to better elucidate a potential mechanism relating *GRN* mutations to the increase in pTDP-43 burden and consequent mitochondrial dysfunction, which could provide a potential therapeutic target for FTLD-*GRN* and other pTDP-43 proteinopathy-related neurological diseases.

In summary, although this preliminary attempt to quantify pTDP-43 demonstrated an increased pTDP-43 burden in FTLD-*GRN* brains, further work is required to optimise and validate the DAB IHC staining and the semi-automatic quantitative method. The elevation in pTDP-43 burden in FTLD-*GRN* could provide additional support for the hypothesis that PGRN haploinsufficiency contributes to a distinctive mechanism that further promotes pTDP-43 aggregation. If pTDP-43 proteinopathy indeed plays a role in the pathogenesis of FTLD, future studies should explore a causal link between pPTDP-43 aggregations and the dysfunction of other cellular processes, particularly mitochondrial dysfunction, in the presence of *GRN* mutations.

High variability of MT-CO1 signal across brain regions

In an effort to characterise the mitochondrial state using IHC staining, the antibody MT-CO1 was optimised in FFPE brains. However, the MT-CO1 signal exhibited a wide range of variability across the FTD cases, with no differences observed by visual inspection.

The distribution of MT-CO1 signal displayed considerable variation across different brain regions, with a stronger signal intensity observed in the frontal lobe and the cerebellum than at temporal lobe. This variability highlights differences in energy demand across brain regions, and consequently distinct roles for mitochondria. In addition, no visual differences were observed between FTLD-*GRN* cases, sporadic FTLD-TDP cases and controls. This observed high variability across cases aligns with the results from a western blot performed in the previous chapter when MT-CO2, another subunit of the mitochondrial CIV, also showed a lot of variation (Fig. 4.7).

One of the main limitations was the ubiquitous signal of mitochondria across the brain, which hinders any attempts to quantify the signal using scripts as previously done with pTDP-43 burden. Mitochondria can be found everywhere around the nucleus and across the cytoplasm. In fact, the number of mitochondria vary greatly across different tissues, with each human cell containing hundreds to thousands of mitochondria, and each mitochondrion has 2 to 10 mtDNA copies[301] . Based on these numbers, the quantification of mitochondrial protein levels is deemed practically impossible, leaving us only with a qualitative analysis to spatially map mitochondria.

RNAscope is useful for spatial mapping of mtDNA, but not for quantification

The work on this chapter has shown a successful optimisation of the singleplex RNAscope CISH assay to stain for mtDNA in human FFPE post-mortem brains, which has not been previously reported. This facilitated the spatial mapping of mtDNA expression across the brain tissue. An attempt to quantify RNAscope mtDNA signal was carried out by developing a quantitative method on QuPath, which did not recapitulate the results previously obtained from qPCR.

Based on the RNAscope results, the *MT-ND5* signal was significantly decreased in the FG region of FTLD-*GRN* and sporadic FTLD-TDP cases, and significantly decreased in the FW region of sporadic FTLD-TDP cases (Fig. 5.20). However, these results contradicted the previous qPCR results in snap-frozen brain in which mtDNAcn showed no change (Fig. 4.5). Although RNAscope IHC staining can be useful for a qualitative visualisation and analysis of mtDNA distribution, the qPCR technique is widely considered more reliable and sensitive in terms of quantification[302]. Despite the thorough validation of the semi-automatic quantitative method of mtDNA in RNAscope staining, the contrasting results suggested that RNAscope may not be a reliable or accurate technique for quantifying mtDNA.

Several limitations can be drawn to explain the substantial variation observed between RNAscope and qPCR results in the quantification of mtDNA.

1) One of the main limitations in *MT-ND5* RNAscope CISH staining was the ubiquitous presence of mitochondria across the brain tissue, as it was also observed using MT-CO1 IHC protein staining (Fig. 5.18). Based on this, an accurate quantification of mtDNA is each cell can be deemed practically impossible using RNAscope CISH techniques.

2) Another notorious limitation of RNAscope CISH staining was the lack of normalisation to nuclear DNA, RNA or protein; whereas in the qPCR method, the DNA probes *MT-CYB* and *MT-ND1* are normalised to nuclear *GUSB* and *B2M*, respectively.

3) The QuPath scripts quantified the *MT-ND5* spots based on a threshold and their size. However, the scripts do not differentiate between different spot sizes, which may ignore multiple individual spots that cluster as one big spot. In addition, due to the ubiquitous signal previously mentioned, the threshold may ignore *MT-ND5* spots that can be found across the cell but have a signal intensity lower than the threshold.

4) A final drawback was the reduced number of biological cases used for RNAscope (*n*=4 FTLD-*GRN*, *n*=10 sporadic FTLD-TDP, *n*=4 controls) in contrast to qPCR (*n*=7 FTLD-*GRN*, *n*=10 sporadic FTLD-TDP, *n*=10 controls). This further highlights the intrinsic variation across human brains (i.e., formalin fixation, post-mortem delay, age or histopathological manipulation), which could lead to non-real results and potentially be minimised with a larger pool of cases.

Exploring the compendium of literature, only one attempt has been made to visually quantify mtDNA using BaseScope CISH in post-mortem spinal cord neurons by Mehta and colleagues[175]. In fact, their study served as inspiration for the development of the quantification method detailed in this section. However, upon closer scrutiny, the results from their staining quantification exhibited significant flaws. Two main issues undermine the reliability of their results included: 1) mtDNA expression was not ubiquitous which does not reflect a real spatial mapping of mitochondria, and 2) a lack of validation using qPCR. This thesis further confirmed the challenges associated with quantifying mtDNA expression, emphasising that, for now, mtDNA may be more suited for qualitative rather than quantitative analyses when employing histopathology techniques.

Overall, the use of RNAscope should not be deemed useless for the study of mtDNA. In the brain, RNAscope CISH could be used for qualitative read-outs of the spatial distribution of mtDNA expression. In addition, the optimisation of fluorescence RNAscope could be useful to qualitatively explore cell-specific mtDNA changes. For example, the staining of the FTD brain with mtDNA and cell-specific antibodies (e.g., IBA1 for microglia) could provide with insights into the spatial distribution across specific cells relevant for FTD.

Finally, it is possible to use RNAscope in combination with other techniques such as immunofluorescence[303] and imaging mass cytometry[304]. This could enable the assessment of both mtDNA, RNA transcripts and proteins in the same brain tissue. However, it requires further optimisation in the human FFPE brains to ensure that there is no degradation of any of the targets.

Conclusion and future directions

To conclude, this chapter attempted to optimise histopathology techniques and develop semi-automatic quantitative methods that characterise pTDP-43 burden in FTLD-*GRN* cases and sporadic FTLD-TDP cases across brain regions, despite the unsuccessful outcome. In addition, MT-CO1 IHC and *MT-ND5* RNAscope CISH staining were also optimised in human FFPE post-mortem brains of FTD cases, although quantification of the staining was not viable.

One of the main outstanding questions in this study involves unravelling the mechanistic interplay between the identified neuropathological features and FTLD pathology itself, along with understanding when or how these factors might contribute to the development of the disease. Bearing in mind that post-mortem tissue is a window to the end stage of a disease, it would be interesting to investigate pTDP-43 changes using the quantification method developed in this thesis at earlier stages of disease progression, including the presymptomatic stage. It is also important to consider that variations across human tissues due to post-mortem delay or fixation time could influence histopathology results.

Future efforts should focus on validating the results in this chapter with a larger pool of controls and FTLD-*GRN* patients, as well as other neurological diseases, to further characterise the neuropathological changes. Additionally, due to the limited access to human tissue with rare neurological disorders such as FTD, leveraging experimental work on mice could serve as a crucial avenue. This approach would facilitate the acquisition of diseased brain samples, allowing for the exploration of histopathological phenotypes over time and the investigation of potential mechanisms through pathology rescue efforts.

6 Discussion and future directions

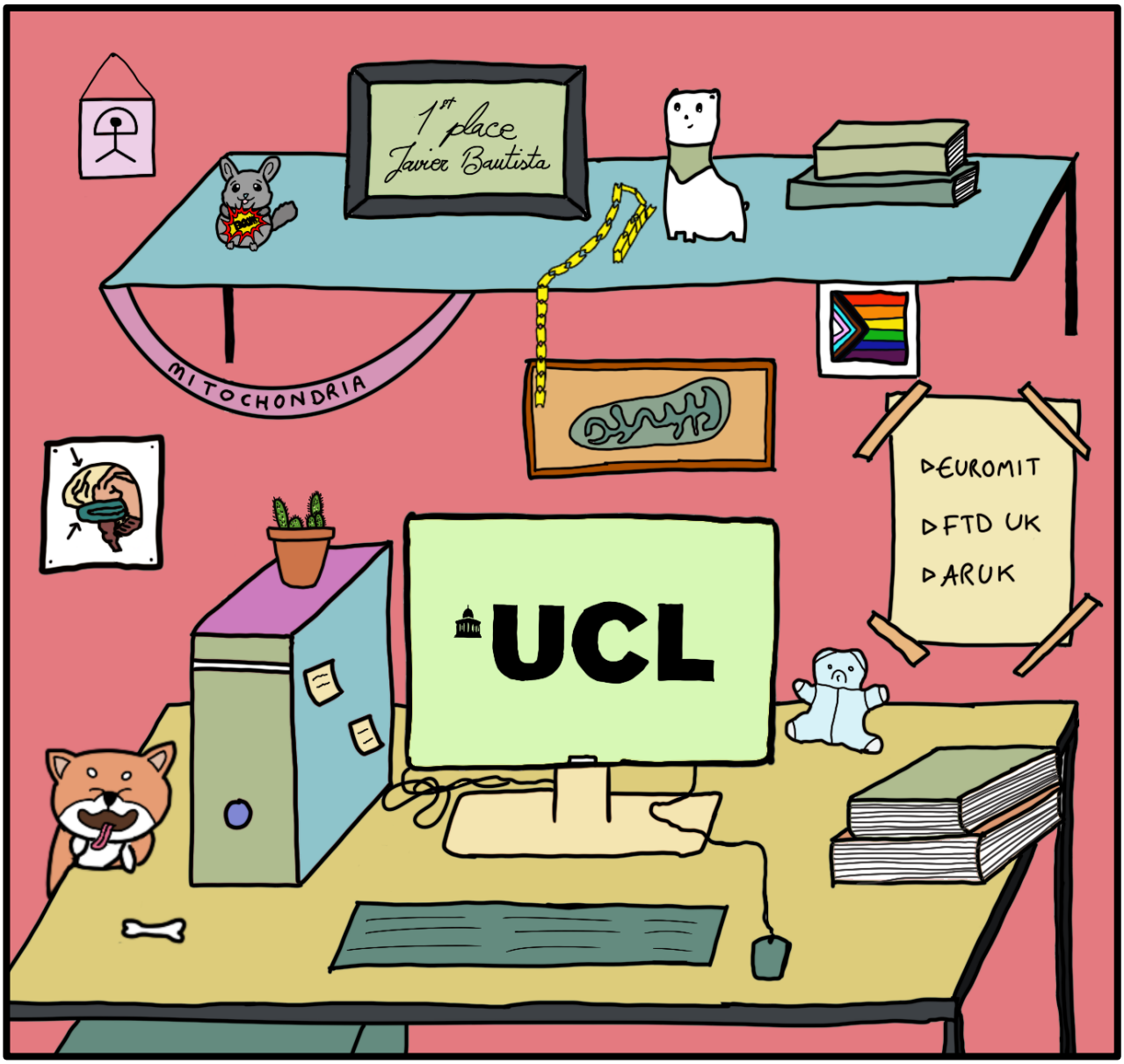

A desk at Queen Square House IoN (digital art) – by Christopher J Dobson

6.1 General discussion

The findings derived from both PGRN-deficient *in vitro* models and human post-mortem brains consistently establish the presence of mitochondrial dysfunction in *GRN*-related FTD. The mitochondrial phenotype was characterised using stable *GRN* KD immortalised cell lines, fibroblasts from patients with *GRN* pathogenic mutations, iPSC-derived neurons and astrocytes, and post-mortem brains from FTLD-*GRN* patients compared with controls and sporadic FTLD-TDP cases. This comprehensive analysis revealed mitochondrial bioenergetic deficits, decreased mitochondrial mass, and mtDNA maintenance defects, strongly implicating the mitochondrion as an organelle affected by PGRN deficiency. The data strongly support the initial hypothesis that mitochondrial dysfunction plays a role in the pathogenesis of *GRN*-related FTD.

The solid foundations in this thesis were built through the utilisation of three *in vitro* PGRN-deficient models which have not been previously employed for an extensive characterisation of the impact of PGRN deficiency in mitochondria. The use of cellular models to investigate neurodegenerative diseases was considered valuable for the initial characterisation of the effect of a gene on mitochondrial function[233].

However, the major strength in the experimental design lied in the use of human post-mortem brains, providing insights into the mitochondrial phenotype at the final stage of FTLD patients. Despite the multisystem expression of PGRN across tissues, PGRN haploinsufficiency primarily manifests in the pathology of the CNS. The observed mitochondrial dysfunction in the brain suggests that the specific target of the organ may be due to its high energy-demand and its susceptibility to metabolic impairment[305], which may initiate the generation of ROS, subsequently leading to neuroinflammation and neuronal death[306]. Furthermore, at a single cell level, considering that FTD is characterised by

neuronal loss and neurons are highly metabolically active cells requiring substantial amounts of energy, the decline in mitochondrial function may be more attributable to the decrease in neuronal number than to other cell types.

Hence, future work will delve deeper into the potential links between PGRN and mitochondrial function, exploring how these findings can be translated into a clinical environment, all whilst characterising brain- and cell-specific mitochondrial phenotypes employing multi-omics techniques[307].

6.2 Potential mechanisms linking PGRN and mitochondria

This PhD thesis has successfully demonstrated that mitochondrial dysfunction is associated with *GRN*-related FTD. However, the main limitation in this project is the absence of a clear causal mechanism linking the gene *GRN* or the protein PGRN and mitochondrial dysfunction. This gap has given rise to opposing hypotheses as to whether 1) mitochondrial dysfunction leads to the pathological hallmarks and clinical manifestations found in *GRN*-related FTD, making the rescue of mitochondria a promising therapeutic target; or whether 2) mitochondrial dysfunction is an undesired downstream-effect of a plethora of cellular malfunctions during the disease progression. Therefore, forthcoming research endeavours will focus on unravelling this link, aiming to understand how PGRN deficiency can lead to mitochondrial dysfunction. Building on the results of this PhD project and the existing literature, I would like to propose four potential mechanisms: 1) a TDP-43 dependent mechanism, 2) an inflammatory mechanism, 3) a mitochondrial biogenesis pathway, and 4) an inter-organellar interaction mechanism.

1) TDP-43-dependent mechanism

As reiterated throughout the thesis, one of the hallmarks of FTLD-TDP cases is the aggregation of pTDP-43. Chapter 5, in particular, revealed an increased pTDP-43 burden in histopathological FTLD-*GRN* cases compared to controls, with a more moderate increase in sporadic FTLD-TDP cases. This pathological feature is shared with other FTD-related genes including *C9orf72* and *MAPT*, which have been previously linked to mitochondrial dysfunction. Despite this association, there is not a clear understanding as to how *GRN* mutations, along with the other implicated genes, accelerate aggregation and increase toxicity.

Setting aside the unknown mechanism behind the increase in pTDP-43 burden, several studies have proposed different theories on how the accumulation of this protein may lead to mitochondrial dysfunction. Mitochondrial OXPHOS defects have been widely reported in TDP-43-related experimental models. For instance, in motor neuron-like NSC-34 cells, the overexpression of wild-type or mutant TDP-43 decreased CI activity, mitochondrial transmembrane potential and ATP synthesis[308]. It also decreased mitochondrial uncoupling protein 2, activating the UPR^{mt} [182]. This mitochondrial response was also confirmed in cellular and animal models with increased TDP-43 expression[182].

In ALS, TDP-43 toxicity has been shown to enter mitochondria and trigger mtDNA release via the mtPTP. This induced cytosolic mtDNA accumulation that activated the neuroinflammatory cGAS/STING pathway, leading to neuron loss and decreased motor function[183]. Pharmaceutically blocking STING prevented neuroinflammation and neurodegeneration *in vitro* and *in vivo*, confirming the TDP-43-mitochondria interaction[183]. The entrance of full-length TDP-43 has also been demonstrated to disassemble CI by preferentially binding mitochondria-encoded ND3 and ND6 subunits, whereas truncated

TDP-43 without the M1 mitochondrial location sequence had no effect on the mitochondrial subunits[184]. Finally, lymphoblast cell lines derived from TDP-43-mutant ALS patients showed mitochondrial dysfunction, displaying decreased spare respiratory capacity, which suggests impaired mitochondrial energy production[309]. Considering the interaction between TDP-43 and mitochondria, the clearance or removal of TDP-43 could lead to an amelioration of mitochondrial function and improve the clinical phenotype of the patient. Notably, mitochondria also have a regulatory role on TDP-43 toxicity. In yeasts, it was reported that respiration-related hydrogen peroxide enhanced TDP-43 toxicity[310], suggesting mitochondria as a therapeutic target to treat TDP-43-related diseases.

While the accumulation of pTDP-43 proteins in *GRN*-mutation carriers, as evidenced in this thesis, has been documented, the underlying mechanism remains unclear. Two previously proposed links involve caspases and cell stress[311]. However, only one study has shown that the inhibition of pTDP-43 in *GRN* KD SH-SY5Y cells lead to the recovery of the mitochondrial phenotype, as evidenced by an increase in mitochondrial membrane potential. Further research is imperative to elucidate how PGRN haploinsufficiency leads to pTDP-43 accumulation, and whether PGRN-related pTDP-43 toxicity is responsible for mitochondrial dysfunction that could be salvaged. Rescue experiments, such as increasing *GRN* expression, inhibiting TDP-43 or boosting mitochondrial function, could prove invaluable in characterising the pathological mechanism between PGRN haploinsufficiency, pTDP-43 and mitochondrial dysfunction.

2) Inflammatory mechanism

PGRN haploinsufficiency has also been reported to trigger regulatory, pro-inflammatory cytokines including interleukin 1 beta (IL- 1β), IL-8, and TNF-α[312]. Although I previously explained a TDP-43-depedent mechanism leading to inflammation, a TDP-43-independent inflammatory mechanism should also be explored. PGRN haploinsufficiency leads to microglial activation, which consequently releases pro-inflammatory cytokines release (e.g., IL-1β, IL-18 and TNFα) and mitochondrial ROS. This in turn alters neuronal functions and induces inflammatory cell death, also known as necroptosis[313]. Subsequently, damage-associated molecular patterns (DAMPs), specifically mtDNA, are released in the extracellular environment, eliciting local inflammation by increasing NLP3 inflammasome activation[314]. This exacerbates microglial activation releasing more pro-inflammatory cytokines and mitochondrial damage releasing ROS, eventually reaching a continuous cycle of neuronal cell death. Prolonged inflammation over years due to microglial inflammasome activation, mitochondrial ROS and pro-inflammatory cytokines combined with defective neuronal metabolism could be hypothesised to trigger FTLD pathogenesis.

It is well-established that PGRN can act as an antagonist of the pro-inflammatory cytokine TNF receptors, and PGRN haploinsufficiency leads to an increase in inflammation[66]. Interestingly, TNFα has been reported to reduce PGC-1α expression through nuclear factor-κB and p38 mitogen-activated protein kinase pathways, decreasing mitochondrial biogenesis[315]. The inflammatory cytokine also increased mitochondrial fragmentation by affecting OPA1 isoform balance[316]. Although the effect of TNFα on PGC-1α has not been investigated in neuronal tissue, in this PhD project, I have reported a decrease in PGC-1α in human post-mortem brains. In addition, IL-1β has been shown to impair mitochondrial bioenergetics and to induce mitochondrial fragmentation in astrocytes, interlinking the role of proinflammatory cytokines with mitochondrial dynamics[317]. These inflammatory

mechanisms affecting OXPHOS and mitochondrial dynamics could also explain why there is an increase in mtDNA deletions in human FTLD-*GRN* brains as reported in chapter 4. Therefore, since therapies targeting the inflammatory process can lead to a reduction in disease progression, this treatment could also prevent mitochondrial toxicity in patients.

3) A mitochondrial biogenesis mechanism

The pathway of mitochondrial biogenesis is coordinated by PGC-1α, which activates NRF1 and NRF2, and consequently TFAM. This leads to the synthesis of mtDNA and proteins, and the generation of new mitochondria. PGC-1α is upstream regulated by AMPK, SIRT1 and CREB. The alteration of any of these pathways or proteins has been reported to cause other pathologies, including a study that demonstrated that PGRN is involved in mitochondrial homeostasis via PGRN-Sirt1-PGC-1α/FoxO1 signalling, where FoxO1 is involved in transcription factor[194]. As reported in this thesis, human post-mortem brains from *GRN*-mutation carriers exhibited a decrease in PGC-1α, TFAM and mitochondrial content, along with an increase in mtDNA deletions. From these findings, it could be proposed that the biogenesis pathway becomes impaired at some stage during FTLD-*GRN* pathogenesis.

The use of transcriptomics and proteomics would provide insights into alterations in genes and proteins expression resulting from PGRN haploinsufficiency. Then, the rescue of the mitochondrial biogenesis pathway could confirm the pathological mechanism and provide potential therapeutic strategies. For instance, a study investigating how *C9orf72* mutations lead to mitochondrial dysfunction in human iPSC-derived motor neurons rescued the mitochondrial “normal” phenotype by lentiviral-mediated overexpression of PGC-1α[175]. This demonstrates that the restoration of the PGC-1α-NRF1-TFAM pathway could be considered a potential therapeutic strategy to be explored in FTLD-*GRN* patients.

4) An inter-organellar interaction mechanism

Mitochondria are in constant contact with other organelles in the cell and disruptions in this comprehensive networking can lead to disease. The discovery that PGRN may affect the formation and function of intracellular organelles suggests a fourth mechanism exploring how the dysfunction of another organelle due to PGRN haploinsufficiency may lead to mitochondrial dysfunction.

The interplay between the endoplasmic reticulum (ER) and mitochondria is highly regulated, and aberrations of this interaction have been implicated in several neurological disorders, including AD, Charcot-Marie-Tooth disease, PD, and ALS. Since PGRN is synthesised in the ER and regulated in the ER-Golgi apparatus secretory pathway, it may be relevant to assess a potential disruption between the organelles that could provide with new evidence into the FTD mechanism.

In addition to the ER, the most important organelles to explore are the lysosomes due to the relevant functions of PGRN in the organelle. Lysosomes play an important role in later stages of mitophagy, and lysosomal dysfunction in lysosomal storage disorders has been associated with an increase in the balance of dysfunctional mitochondria[318]. The lysosomal-mitochondrial interaction has been more extensively investigated in other lysosomal storage disorders as illustrated in Gaucher's disease, caused by a defective glucocerebrosidase (GCase) enzyme. A study using a mouse model of neuronopathic Gaucher's disease showed mitochondria and quality control defects, including impaired respiration and decreased mitochondrial membrane potential due to altered autophagy and dysfunctional proteasomal pathways[319]. In addition, the inhibition of autophagy with bafilomycin and chloroquine was also reported to decrease mitochondrial quality control and TCA cycle intermediates in primary cortical rat neurons[320].

Homozygous mutations in *GRN* result in neuronal ceroid lipofuscinosis characterised by defective lysosomal function. Notably, animal models with neuronal ceroid lipofuscinosis have shown an accumulation of mitochondrial dysfunction [321]. The presence of both lysosomal and mitochondrial dysfunction raises questions about which pathological process is a downstream consequence of the other. For instance, respiratory chain deficiency has been reported to inhibit lysosomal hydrolysis and induce lysosomal dysfunction by various pathways[322,323]. Therefore, it is important to consider a potential two-way interaction when referring to inter-organellar dysfunction.

It is becoming clearer that organelles are continuously interacting with each other, and this should be explored in future studies by employing imaging techniques, such as fluorescence microscopy and super-resolution techniques, which enable a high-throughput analysis of membrane contact sites. Targeted co-immunoprecipitation may also be useful to identify novel protein-protein interactions between the different organelles.

When exploring potential mechanisms, it is necessary to consider that due to the pleiotropic function of PGRN, there is a possibility that not just one isolated mechanism may be leading to FTD, but rather the interplay between different mechanisms – both mitochondrial and non-mitochondrial. Another outstanding question is whether the undiscovered, pathological mechanism(s) leading to mitochondrial dysfunction is specific to the gene *GRN* or shared across the FTLD-TDP pathologies, and therefore potentially be due to other hallmarks such as TDP-43 toxicity. Addressing this query is crucial to carefully distinguishing the effect of different FTD-causing genes on mitochondrial function and should be considered during the experimental design of future projects.

6.3 Future directions towards therapeutic strategies

The long-term goal behind the experimental work in this thesis was to develop therapeutic strategies to ameliorate and prevent the development of clinical syndromes in patients with *GRN*-related FTD and other neurodegenerative disorders.

At the moment, there are no disease-modifying treatments that halt or reverse the progression of FTLD, let alone specific drugs for *GRN*-related FTD, and the clinical management focuses on alleviating the symptoms. The glutamate blocker riluzole is the only approved disease-modifying drug to treat ALS, which has been shown to slow the progression and increase survival for some patients[324]. Several clinical trials have focused on repurposing anti-dementia drugs to treat FTD with little or no success, or even worsening the condition. For instance, the AD drug memantine was observed to accelerate cognitive decline in FTD patients[325].

Since PGRN haploinsufficiency represents one of the major pathological hallmarks of FLTD-*GRN* patients, many studies have focused on increasing PGRN levels as a therapeutic strategy. These treatments included gene therapy using AAV-mediated *GRN* gene delivery to the CNS; downregulating sortilin (SORT1), a clearance receptor of PGRN with anti-SORT1 antibodies; antisense oligonucleotides to stabilise the *GRN* mRNA with nonsense mutations; aminoglycosides to promote ribosomal readthrough of nonsense *GRN* mutations; lysosomal activity-enhancing drugs; and anti-inflammatory drugs[325–327].

Following the identification of mitochondrial dysfunction in *GRN*-related FTD, the use of mitochondria targeting drugs emerges as a promising avenue to ameliorate clinical manifestations in patients. Pending the results that will arise from uncovering the pathological mechanisms, the exploration of various established drugs may become

conceivable. These could include compounds increasing mitochondrial function, and therapies targeting mitochondrial biogenesis[328].

For instance, studies in mice, worms and iPSCs have demonstrated that NAD^+ augmentation using different precursors can lead to rescued mitochondrial function (e.g., increase in mitochondrial biogenesis and bioenergetics), decreased oxidative damage, decreased inflammation and increased neurogenesis[329,330]. Interestingly, a recent clinical trial compared the effect of a combination of nicotinamide riboside and the antioxidant pterostilbene to bolster NAD^+ levels against placebo control in ALS patients. Compared to placebo, NAD^+-increased ALS patients displayed significant improvements in the ALS functional rating scale, pulmonary function, muscular strength, and in skeletal muscle/fat weight ratio[331]. Although still at an early stage, this suggests mitochondria-targeting drugs could be explored as a disease-modifying therapy for FTD patients.

Finally, the use of drugs to target mitochondria mostly relies on the assumption that mitochondria are an upstream effect of PGRN deficiency, although it is unclear whether an impairment in the mitochondrial phenotype is an upstream or downstream effect. At an initial glance, a downstream effect may seem clinically irrelevant as a therapeutic approach. However, the identification of mitochondrial dysfunction in PGRN-deficient cases can still be used as a biomarker to validate the efficiency of therapeutic strategies to increase the levels of PGRN or other approaches improving upstream mechanisms. Future studies characterising disease mechanisms and biomarkers will be essential for the development of therapeutics for *GRN*-related FTD.

6.4 Overall conclusion

In conclusion, this PhD project has unveiled the association between mitochondrial dysfunction and *GRN*-related FTD. This prompted the hypothesis that various mechanisms may contribute to PGRN-dependent mitochondrial dysfunction, potentially serving as a pathological driver of FTD. Bridging the gap between genetics and biological mechanisms poses a major challenge in neurodegenerative disorders. This emphasises the need for a better understanding of the pathological mechanism, with the goal of enhancing treatments and identifying potential biomarkers. As the understanding of the relationship between PGRN and mitochondria deepens, the potential for developing novel therapeutic strategies increases. This, in turn, may ultimately lead to improved treatments and a better life quality for individuals affected by *GRN*-related FTD and other neurodegenerative diseases; thereby expanding our knowledge of the role of mitochondria in health and disease.

References

1. Bang, J., Spina, S., and Miller, B.L. (2015). Frontotemporal dementia. The Lancet *386*, 1672–1682. 10.1016/S0140-6736(15)00461-4.

2. Coyle-Gilchrist, I.T.S., Dick, K.M., Patterson, K., Vázquez Rodríquez, P., Wehmann, E., Wilcox, A., Lansdall, C.J., Dawson, K.E., Wiggins, J., Mead, S., et al. (2016). Prevalence, characteristics, and survival of frontotemporal lobar degeneration syndromes. Neurology *86*, 1736–1743. 10.1212/WNL.0000000000002638.

3. Rascovsky, K., Hodges, J.R., Knopman, D., Mendez, M.F., Kramer, J.H., Neuhaus, J., van Swieten, J.C., Seelaar, H., Dopper, E.G.P., Onyike, C.U., et al. (2011). Sensitivity of revised diagnostic criteria for the behavioural variant of frontotemporal dementia. Brain *134*, 2456–2477. 10.1093/brain/awr179.

4. Grossman, M. (2012). The non-fluent/agrammatic variant of primary progressive aphasia. Lancet Neurol. *11*, 545–555. 10.1016/S1474-4422(12)70099-6.

5. Renton, A.E., Majounie, E., Waite, A., Simón-Sánchez, J., Rollinson, S., Gibbs, J.R., Schymick, J.C., Laaksovirta, H., van Swieten, J.C., Myllykangas, L., et al. (2011). A Hexanucleotide Repeat Expansion in C9ORF72 Is the Cause of Chromosome 9p21-Linked ALS-FTD. Neuron *72*, 257–268. 10.1016/j.neuron.2011.09.010.

6. Dickson, D.W., Kouri, N., Murray, M.E., and Josephs, K.A. (2011). Neuropathology of Frontotemporal Lobar Degeneration-Tau (FTLD-Tau). J. Mol. Neurosci. *45*, 384–389. 10.1007/s12031-011-9589-0.

7. Mackenzie, I.R.A., Neumann, M., Baborie, A., Sampathu, D.M., Du Plessis, D., Jaros, E., Perry, R.H., Trojanowski, J.Q., Mann, D.M.A., and Lee, V.M.Y. (2011). A harmonized classification system for FTLD-TDP pathology. Acta Neuropathol. (Berl.) *122*, 111–113. 10.1007/s00401-011-0845-8.

8. Neumann, M., Bentmann, E., Dormann, D., Jawaid, A., DeJesus-Hernandez, M., Ansorge, O., Roeber, S., Kretzschmar, H.A., Munoz, D.G., Kusaka, H., et al. (2011). FET proteins TAF15 and EWS are selective markers that distinguish FTLD with FUS pathology from amyotrophic lateral sclerosis with FUS mutations. Brain *134*, 2595–2609. 10.1093/brain/awr201.

9. Panza, F., Lozupone, M., Seripa, D., Daniele, A., Watling, M., Giannelli, G., and Imbimbo, B.P. (2020). Development of disease-modifying drugs for frontotemporal dementia spectrum disorders. Nat. Rev. Neurol. *16*, 213–228. 10.1038/s41582-020-0330-x.

10. Buée, L., and Delacourte, A. (1999). Comparative Biochemistry of Tau in Progressive Supranuclear Palsy, Corticobasal Degeneration, FTDP-17 and Pick's Disease. Brain Pathol. *9*, 681–693. 10.1111/j.1750-3639.1999.tb00550.x.

11. Delacourte, A., Robitaille, Y., Sergeant, N., Buée, L., Hof, P.R., Wattez, A., Laroche-Cholette, A., Mathieu, J., Chagnon, P., and Gauvreau, D. (1996). Specific Pathological Tau Protein Variants Characterize Pick's Disease. J. Neuropathol. Exp. Neurol. *55*, 159–168. 10.1097/00005072-199602000-00004.

12. Sergeant, N., Wattez, A., and Delacourte, A. (1999). Neurofibrillary Degeneration in Progressive Supranuclear Palsy and Corticobasal Degeneration. J. Neurochem. *72*, 1243–1249. 10.1046/j.1471-4159.1999.0721243.x.

13. Kovacs, G.G., Majtenyi, K., Spina, S., Murrell, J.R., Gelpi, E., Hoftberger, R., Fraser, G., Crowther, R.A., Goedert, M., Budka, H., et al. (2008). White Matter Tauopathy With Globular Glial Inclusions: A Distinct Sporadic Frontotemporal Lobar Degeneration. J. Neuropathol. Exp. Neurol. *67*, 963–975. 10.1097/NEN.0b013e318187a80f.

14. Ferrer, I., Santpere, G., and van Leeuwen, F.W. (2008). Argyrophilic grain disease. Brain *131*, 1416–1432. 10.1093/brain/awm305.

15. Mackenzie, I.R., and Neumann, M. (2017). Reappraisal of TDP-43 pathology in FTLD-U subtypes. Acta Neuropathol. (Berl.) *134*, 79–96. 10.1007/s00401-017-1716-8.

16. Baker, M., Mackenzie, I.R., Pickering-Brown, S.M., Gass, J., Rademakers, R., Lindholm, C., Snowden, J., Adamson, J., Sadovnick, A.D., Rollinson, S., et al. (2006). Mutations in progranulin cause tau-negative frontotemporal dementia linked to chromosome 17. Nature *442*, 916–919. 10.1038/nature05016.

17. Kimonis, V.E., Fulchiero, E., Vesa, J., and Watts, G. (2008). VCP disease associated with myopathy, Paget disease of bone and frontotemporal dementia: Review of a unique disorder. Biochim. Biophys. Acta BBA - Mol. Basis Dis. *1782*, 744–748. 10.1016/j.bbadis.2008.09.003.

18. Skibinski, G., Parkinson, N.J., Brown, J.M., Chakrabarti, L., Lloyd, S.L., Hummerich, H., Nielsen, J.E., Hodges, J.R., Spillantini, M.G., Thusgaard, T., et al. (2005). Mutations in the endosomal ESCRTIII-complex subunit CHMP2B in frontotemporal dementia. Nat. Genet. *37*, 806–808. 10.1038/ng1609.

19. Wood, E.M., Falcone, D., Suh, E., Irwin, D.J., Chen-Plotkin, A.S., Lee, E.B., Xie, S.X., Van Deerlin, V.M., and Grossman, M. (2013). Development and Validation of Pedigree Classification Criteria for Frontotemporal Lobar Degeneration. JAMA Neurol. *70*, 1411–1417. 10.1001/jamaneurol.2013.3956.

20. Rohrer, J.D., Isaacs, A.M., Mizielinska, S., Mead, S., Lashley, T., Wray, S., Sidle, K., Fratta, P., Orrell, R.W., Hardy, J., et al. (2015). C9orf72 expansions in frontotemporal dementia and amyotrophic lateral sclerosis. Lancet Neurol. *14*, 291–301. 10.1016/S1474-4422(14)70233-9.

21. Murphy, N.A., Arthur, K.C., Tienari, P.J., Houlden, H., Chiò, A., and Traynor, B.J. (2017). Age-related penetrance of the C9orf72 repeat expansion. Sci. Rep. *7*, 2116. 10.1038/s41598-017-02364-1.

22. DeJesus-Hernandez, M., Mackenzie, I.R., Boeve, B.F., Boxer, A.L., Baker, M., Rutherford, N.J., Nicholson, A.M., Finch, N.A., Flynn, H., Adamson, J., et al. (2011). Expanded GGGGCC Hexanucleotide Repeat in Noncoding Region of C9ORF72 Causes Chromosome 9p-Linked FTD and ALS. Neuron *72*, 245–256. 10.1016/j.neuron.2011.09.011.

23. Gijselinck, I., Langenhove, T.V., Zee, J. van der, Sleegers, K., Philtjens, S., Kleinberger, G., Janssens, J., Bettens, K., Cauwenberghe, C.V., Pereson, S., et al. (2012). A C9orf72 promoter repeat expansion in a Flanders-Belgian cohort with

disorders of the frontotemporal lobar degeneration-amyotrophic lateral sclerosis spectrum: a gene identification study. Lancet Neurol. *11*, 54–65. 10.1016/S1474-4422(11)70261-7.

24. Fournier, C., Barbier, M., Camuzat, A., Anquetil, V., Lattante, S., Clot, F., Cazeneuve, C., Rinaldi, D., Couratier, P., Deramecourt, V., et al. (2019). Relations between C9orf72 expansion size in blood, age at onset, age at collection and transmission across generations in patients and presymptomatic carriers. Neurobiol. Aging *74*, 234.e1-234.e8. 10.1016/j.neurobiolaging.2018.09.010.

25. Zhang, M., Ferrari, R., Tartaglia, M.C., Keith, J., Surace, E.I., Wolf, U., Sato, C., Grinberg, M., Liang, Y., Xi, Z., et al. (2018). A C6orf10/LOC101929163 locus is associated with age of onset in C9orf72 carriers. Brain *141*, 2895–2907. 10.1093/brain/awy238.

26. Illán-Gala, I., Casaletto, K.B., Borrego-Écija, S., Arenaza-Urquijo, E.M., Wolf, A., Cobigo, Y., Goh, S.Y.M., Staffaroni, A.M., Alcolea, D., Fortea, J., et al. (2021). Sex differences in the behavioral variant of frontotemporal dementia: A new window to executive and behavioral reserve. Alzheimers Dement. *17*, 1329–1341. 10.1002/alz.12299.

27. Barandiaran, M., Estanga, A., Moreno, F., Indakoetxea, B., Alzualde, A., Balluerka, N., Massó, J.F.M., and Munain, A.L. de (2012). Neuropsychological Features of Asymptomatic c.709-1G>A Progranulin Mutation Carriers*. J. Int. Neuropsychol. Soc. *18*, 1086–1090. 10.1017/S1355617712000823.

28. Borroni, B., Bonvicini, C., Galimberti, D., Tremolizzo, L., Papetti, A., Archetti, S., Turla, M., Alberici, A., Agosti, C., Premi, E., et al. (2011). Founder effect and estimation of the age of the Progranulin Thr272fs mutation in 14 Italian pedigrees with frontotemporal lobar degeneration. Neurobiol. Aging *32*, 555.e1-555.e8. 10.1016/j.neurobiolaging.2010.08.009.

29. Floris, G., Borghero, G., Cannas, A., Di Stefano, F., Murru, M.R., Corongiu, D., Cuccu, S., Tranquilli, S., Cherchi, M.V., Serra, A., et al. (2015). Clinical phenotypes and radiological findings in frontotemporal dementia related to TARDBP mutations. J. Neurol. *262*, 375–384. 10.1007/s00415-014-7575-5.

30. Rohrer, J.D., Nicholas, J.M., Cash, D.M., van Swieten, J., Dopper, E., Jiskoot, L., van Minkelen, R., Rombouts, S.A., Jorge Cardoso, M., Clegg, S., et al. (2015). Presymptomatic cognitive and neuroanatomical changes in genetic frontotemporal dementia in the Genetic Frontotemporal dementia Initiative (GENFI) study: a cross-sectional analysis. Lancet Neurol. *14*, 253–262. 10.1016/S1474-4422(14)70324-2.

31. Bhandari, V., and Bateman, A. (1992). Structure and chromosomal location of the human granulin gene. Biochem. Biophys. Res. Commun. *188*, 57–63. 10.1016/0006-291X(92)92349-3.

32. Hrabal, R., Chen, Z., James, S., Bennett, H.P., and Ni, F. (1996). The hairpin stack fold, a novel protein architecture for a new family of protein growth factors. Nat. Struct. Biol. *3*, 747–752. 10.1038/nsb0996-747.

33. Cruts, M., Gijselinck, I., van der Zee, J., Engelborghs, S., Wils, H., Pirici, D., Rademakers, R., Vandenberghe, R., Dermaut, B., Martin, J.-J., et al. (2006). Null

mutations in progranulin cause ubiquitin-positive frontotemporal dementia linked to chromosome 17q21. Nature *442*, 920–924. 10.1038/nature05017.

34. Yu, C.-E., Bird, T.D., Bekris, L.M., Montine, T.J., Leverenz, J.B., Steinbart, E., Galloway, N.M., Feldman, H., Woltjer, R., Miller, C.A., et al. (2010). The Spectrum of Mutations in Progranulin: A Collaborative Study Screening 545 Cases of Neurodegeneration. Arch. Neurol. *67*, 161–170. 10.1001/archneurol.2009.328.

35. Terryn, J., Verfaillie, C.M., and Van Damme, P. (2021). Tweaking Progranulin Expression: Therapeutic Avenues and Opportunities. Front. Mol. Neurosci. *14*, 713031. 10.3389/fnmol.2021.713031.

36. Gijselinck, I., van der Zee, J., Engelborghs, S., Goossens, D., Peeters, K., Mattheijssens, M., Corsmit, E., Del-Favero, J., De Deyn, P. p., Van Broeckhoven, C., et al. (2008). Progranulin locus deletion in frontotemporal dementia. Hum. Mutat. *29*, 53–58. 10.1002/humu.20651.

37. Le Ber, I., Camuzat, A., Hannequin, D., Pasquier, F., Guedj, E., Rovelet-Lecrux, A., Hahn-Barma, V., van der Zee, J., Clot, F., Bakchine, S., et al. (2008). Phenotype variability in progranulin mutation carriers: a clinical, neuropsychological, imaging and genetic study. Brain *131*, 732–746. 10.1093/brain/awn012.

38. Shankaran, S.S., Capell, A., Hruscha, A.T., Fellerer, K., Neumann, M., Schmid, B., and Haass, C. (2008). Missense Mutations in the Progranulin Gene Linked to Frontotemporal Lobar Degeneration with Ubiquitin-immunoreactive Inclusions Reduce Progranulin Production and Secretion *. J. Biol. Chem. *283*, 1744–1753. 10.1074/jbc.M705115200.

39. Meeter, L.H., Patzke, H., Loewen, G., Dopper, E.G.P., Pijnenburg, Y.A.L., Minkelen, R. van, and Swieten, J.C. van (2016). Progranulin Levels in Plasma and Cerebrospinal Fluid in Granulin Mutation Carriers. Dement. Geriatr. Cogn. Disord. Extra *6*, 330–340. 10.1159/000447738.

40. Galimberti, D., Fumagalli, G.G., Fenoglio, C., Cioffi, S.M.G., Arighi, A., Serpente, M., Borroni, B., Padovani, A., Tagliavini, F., Masellis, M., et al. (2018). Progranulin plasma levels predict the presence of GRN mutations in asymptomatic subjects and do not correlate with brain atrophy: results from the GENFI study. Neurobiol. Aging *62*, 245.e9-245.e12. 10.1016/j.neurobiolaging.2017.10.016.

41. Smith, K.R., Damiano, J., Franceschetti, S., Carpenter, S., Canafoglia, L., Morbin, M., Rossi, G., Pareyson, D., Mole, S.E., Staropoli, J.F., et al. (2012). Strikingly Different Clinicopathological Phenotypes Determined by Progranulin-Mutation Dosage. Am. J. Hum. Genet. *90*, 1102–1107. 10.1016/j.ajhg.2012.04.021.

42. Rohrer, J.D., Woollacott, I.O.C., Dick, K.M., Brotherhood, E., Gordon, E., Fellows, A., Toombs, J., Druyeh, R., Cardoso, M.J., Ourselin, S., et al. (2016). Serum neurofilament light chain protein is a measure of disease intensity in frontotemporal dementia. Neurology *87*, 1329–1336. 10.1212/WNL.0000000000003154.

43. Meeter, L.H., Dopper, E.G., Jiskoot, L.C., Sanchez-Valle, R., Graff, C., Benussi, L., Ghidoni, R., Pijnenburg, Y.A., Borroni, B., Galimberti, D., et al. (2016). Neurofilament light chain: a biomarker for genetic frontotemporal dementia. Ann. Clin. Transl. Neurol. *3*, 623–636. 10.1002/acn3.325.

44. Woollacott, I.O.C., Nicholas, J.M., Heslegrave, A., Heller, C., Foiani, M.S., Dick, K.M., Russell, L.L., Paterson, R.W., Keshavan, A., Fox, N.C., et al. (2018). Cerebrospinal fluid soluble TREM2 levels in frontotemporal dementia differ by genetic and pathological subgroup. Alzheimers Res. Ther. *10*, 79. 10.1186/s13195-018-0405-8.

45. Cash, D.M., Bocchetta, M., Thomas, D.L., Dick, K.M., van Swieten, J.C., Borroni, B., Galimberti, D., Masellis, M., Tartaglia, M.C., Rowe, J.B., et al. (2018). Patterns of gray matter atrophy in genetic frontotemporal dementia: results from the GENFI study. Neurobiol. Aging *62*, 191–196. 10.1016/j.neurobiolaging.2017.10.008.

46. Jiskoot, L.C., Panman, J.L., Meeter, L.H., Dopper, E.G.P., Donker Kaat, L., Franzen, S., van der Ende, E.L., van Minkelen, R., Rombouts, S.A.R.B., Papma, J.M., et al. (2019). Longitudinal multimodal MRI as prognostic and diagnostic biomarker in presymptomatic familial frontotemporal dementia. Brain *142*, 193–208. 10.1093/brain/awy288.

47. Bocchetta, M., Iglesias, J.E., Scelsi, M.A., Cash, D.M., Cardoso, M.J., Modat, M., Altmann, A., Ourselin, S., Warren, J.D., and Rohrer, J.D. (2018). Hippocampal Subfield Volumetry: Differential Pattern of Atrophy in Different Forms of Genetic Frontotemporal Dementia. J. Alzheimers Dis. *64*, 497–504. 10.3233/JAD-180195.

48. Sudre, C.H., Bocchetta, M., Cash, D., Thomas, D.L., Woollacott, I., Dick, K.M., van Swieten, J., Borroni, B., Galimberti, D., Masellis, M., et al. (2017). White matter hyperintensities are seen only in GRN mutation carriers in the GENFI cohort. NeuroImage Clin. *15*, 171–180. 10.1016/j.nicl.2017.04.015.

49. Woollacott, I.O.C., Toomey, C.E., Strand, C., Courtney, R., Benson, B.C., Rohrer, J.D., and Lashley, T. (2020). Microglial burden, activation and dystrophy patterns in frontotemporal lobar degeneration. J. Neuroinflammation *17*, 234. 10.1186/s12974-020-01907-0.

50. Van Deerlin, V.M., Sleiman, P.M.A., Martinez-Lage, M., Chen-Plotkin, A., Wang, L.-S., Graff-Radford, N.R., Dickson, D.W., Rademakers, R., Boeve, B.F., Grossman, M., et al. (2010). Common variants at 7p21 are associated with frontotemporal lobar degeneration with TDP-43 inclusions. Nat. Genet. *42*, 234–239. 10.1038/ng.536.

51. Pottier, C., Zhou, X., Perkerson, R.B., Baker, M., Jenkins, G.D., Serie, D.J., Ghidoni, R., Benussi, L., Binetti, G., de Munain, A.L., et al. (2018). Potential genetic modifiers of disease risk and age at onset in patients with frontotemporal dementia and GRN mutations: a genome-wide association study. Lancet Neurol. *17*, 548–558. 10.1016/S1474-4422(18)30126-1.

52. Carrasquillo, M.M., Nicholson, A.M., Finch, N., Gibbs, J.R., Baker, M., Rutherford, N.J., Hunter, T.A., DeJesus-Hernandez, M., Bisceglio, G.D., Mackenzie, I.R., et al. (2010). Genome-wide Screen Identifies rs646776 near Sortilin as a Regulator of Progranulin Levels in Human Plasma. Am. J. Hum. Genet. *87*, 890–897. 10.1016/j.ajhg.2010.11.002.

53. Nicholson, A.M., Finch, N.A., Almeida, M., Perkerson, R.B., van Blitterswijk, M., Wojtas, A., Cenik, B., Rotondo, S., Inskeep, V., Almasy, L., et al. (2016). Prosaposin is a regulator of progranulin levels and oligomerization. Nat. Commun. *7*, 11992. 10.1038/ncomms11992.

54. Jiao, J., Herl, L.D., Jr, R.V.F., and Gao, F.-B. (2010). MicroRNA-29b Regulates the Expression Level of Human Progranulin, a Secreted Glycoprotein Implicated in Frontotemporal Dementia. PLOS ONE *5*, e10551. 10.1371/journal.pone.0010551.

55. Rademakers, R., Eriksen, J.L., Baker, M., Robinson, T., Ahmed, Z., Lincoln, S.J., Finch, N., Rutherford, N.J., Crook, R.J., Josephs, K.A., et al. (2008). Common variation in the miR-659 binding-site of GRN is a major risk factor for TDP43-positive frontotemporal dementia. Hum. Mol. Genet. *17*, 3631–3642. 10.1093/hmg/ddn257.

56. Wang, W.-X., Wilfred, B.R., Madathil, S.K., Tang, G., Hu, Y., Dimayuga, J., Stromberg, A.J., Huang, Q., Saatman, K.E., and Nelson, P.T. (2010). miR-107 Regulates Granulin/Progranulin with Implications for Traumatic Brain Injury and Neurodegenerative Disease. Am. J. Pathol. *177*, 334–345. 10.2353/ajpath.2010.091202.

57. Galimberti, D., D'Addario, C., Dell'Osso, B., Fenoglio, C., Marcone, A., Cerami, C., Cappa, S.F., Palazzo, M.C., Arosio, B., Mari, D., et al. (2013). Progranulin gene (GRN) promoter methylation is increased in patients with sporadic frontotemporal lobar degeneration. Neurol. Sci. *34*, 899–903. 10.1007/s10072-012-1151-5.

58. Banzhaf-Strathmann, J., Claus, R., Mücke, O., Rentzsch, K., van der Zee, J., Engelborghs, S., De Deyn, P.P., Cruts, M., van Broeckhoven, C., Plass, C., et al. (2013). Promoter DNA methylation regulates progranulin expression and is altered in FTLD. Acta Neuropathol. Commun. *1*, 16. 10.1186/2051-5960-1-16.

59. Baba, T., Hoff III, H.B., Nemoto, H., Lee, H., Orth, J., Arai, Y., and Gerton, G.L. (1993). Acrogranin, an acrosomal cysteine-rich glycoprotein, is the precursor of the growth-modulating peptides, granulins, and epithelins, and is expressed in somatic as well as male germ cells. Mol. Reprod. Dev. *34*, 233–243. 10.1002/mrd.1080340302.

60. Parnell, P.G., Wunderlich, J., Carter, B., and Halper, J. (1992). Transforming Growth Factor e: Amino Acid Analysis and Partial Amino Acid Sequence. Growth Factors *7*, 65–72. 10.3109/08977199209023938.

61. Zhou, J., Gao, G., Crabb, J.W., and Serrero, G. (1993). Purification of an autocrine growth factor homologous with mouse epithelin precursor from a highly tumorigenic cell line. J. Biol. Chem. *268*, 10863–10869. 10.1016/S0021-9258(18)82064-6.

62. Plowman, G.D., Green, J.M., Neubauer, M.G., Buckley, S.D., McDonald, V.L., Todaro, G.J., and Shoyab, M. (1992). The epithelin precursor encodes two proteins with opposing activities on epithelial cell growth. J. Biol. Chem. *267*, 13073–13078. 10.1016/S0021-9258(18)42382-4.

63. Sardiello, M., Palmieri, M., di Ronza, A., Medina, D.L., Valenza, M., Gennarino, V.A., Di Malta, C., Donaudy, F., Embrione, V., Polishchuk, R.S., et al. (2009). A gene network regulating lysosomal biogenesis and function. Science *325*, 473–477. 10.1126/science.1174447.

64. Huang, M., Modeste, E., Dammer, E., Merino, P., Taylor, G., Duong, D.M., Deng, Q., Holler, C.J., Gearing, M., Dickson, D., et al. (2020). Network analysis of the progranulin-deficient mouse brain proteome reveals pathogenic mechanisms shared in human frontotemporal dementia caused by GRN mutations. Acta Neuropathol. Commun. *8*, 163. 10.1186/s40478-020-01037-x.

65. He, Z., Ong, C.H.P., Halper, J., and Bateman, A. (2003). Progranulin is a mediator of the wound response. Nat. Med. *9*, 225–229. 10.1038/nm816.

66. Tang, W., Lu, Y., Tian, Q.-Y., Zhang, Y., Guo, F.-J., Liu, G.-Y., Syed, N.M., Lai, Y., Lin, E.A., Kong, L., et al. (2011). The Growth Factor Progranulin Binds to TNF Receptors and Is Therapeutic Against Inflammatory Arthritis in Mice. Science *332*, 478–484. 10.1126/science.1199214.

67. Zhu, J., Nathan, C., Jin, W., Sim, D., Ashcroft, G.S., Wahl, S.M., Lacomis, L., Erdjument-Bromage, H., Tempst, P., Wright, C.D., et al. (2002). Conversion of Proepithelin to Epithelins: Roles of SLPI and Elastase in Host Defense and Wound Repair. Cell *111*, 867–878. 10.1016/S0092-8674(02)01141-8.

68. Kao, A.W., McKay, A., Singh, P.P., Brunet, A., and Huang, E.J. (2017). Progranulin, lysosomal regulation and neurodegenerative disease. Nat. Rev. Neurosci. *18*, 325–333. 10.1038/nrn.2017.36.

69. Matsuwaki, T., Asakura, R., Suzuki, M., Yamanouchi, K., and Nishihara, M. (2011). Age-Dependent Changes in Progranulin Expression in the Mouse Brain. J. Reprod. Dev. *57*, 113–119. 10.1262/jrd.10-116S.

70. Daniel, R., He, Z., Carmichael, K.P., Halper, J., and Bateman, A. (2000). Cellular Localization of Gene Expression for Progranulin. J. Histochem. Cytochem. *48*, 999–1009. 10.1177/002215540004800713.

71. Suzuki, M., Yonezawa, T., Fujioka, H., Matuamuro, M., and Nishihara, M. (2001). Induction of granulin precursor gene expression by estrogen treatment in neonatal rat hypothalamus. Neurosci. Lett. *297*, 199–202. 10.1016/S0304-3940(00)01699-2.

72. Van Damme, P., Van Hoecke, A., Lambrechts, D., Vanacker, P., Bogaert, E., van Swieten, J., Carmeliet, P., Van Den Bosch, L., and Robberecht, W. (2008). Progranulin functions as a neurotrophic factor to regulate neurite outgrowth and enhance neuronal survival. J. Cell Biol. *181*, 37–41. 10.1083/jcb.200712039.

73. Ryan, C.L., Baranowski, D.C., Chitramuthu, B.P., Malik, S., Li, Z., Cao, M., Minotti, S., Durham, H.D., Kay, D.G., Shaw, C.A., et al. (2009). Progranulin is expressed within motor neurons and promotes neuronal cell survival. BMC Neurosci. *10*, 130. 10.1186/1471-2202-10-130.

74. Gass, J., Lee, W.C., Cook, C., Finch, N., Stetler, C., Jansen-West, K., Lewis, J., Link, C.D., Rademakers, R., Nykjær, A., et al. (2012). Progranulin regulates neuronal outgrowth independent of Sortilin. Mol. Neurodegener. *7*, 33. 10.1186/1750-1326-7-33.

75. Rhinn, H., Tatton, N., McCaughey, S., Kurnellas, M., and Rosenthal, A. (2022). Progranulin as a therapeutic target in neurodegenerative diseases. Trends Pharmacol. Sci. *43*, 641–652. 10.1016/j.tips.2021.11.015.

76. Zhang, Y., Chen, K., Sloan, S.A., Bennett, M.L., Scholze, A.R., O'Keeffe, S., Phatnani, H.P., Guarnieri, P., Caneda, C., Ruderisch, N., et al. (2014). An RNA-Sequencing Transcriptome and Splicing Database of Glia, Neurons, and Vascular Cells of the Cerebral Cortex. J. Neurosci. *34*, 11929–11947. 10.1523/JNEUROSCI.1860-14.2014.

77. Nelson, D.L., Lehninger, A.L., and Cox, M.M. (2008). Lehninger principles of biochemistry (Macmillan).

78. Osellame, L.D., Blacker, T.S., and Duchen, M.R. (2012). Cellular and molecular mechanisms of mitochondrial function. Best Pract. Res. Clin. Endocrinol. Metab. *26*, 711–723. 10.1016/j.beem.2012.05.003.

79. Duchen, M.R. (2004). Roles of Mitochondria in Health and Disease. Diabetes *53*, S96–S102. 10.2337/diabetes.53.2007.S96.

80. Seo, A.Y., Joseph, A.-M., Dutta, D., Hwang, J.C.Y., Aris, J.P., and Leeuwenburgh, C. (2010). New insights into the role of mitochondria in aging: mitochondrial dynamics and more. J. Cell Sci. *123*, 2533–2542. 10.1242/jcs.070490.

81. Ernster, L., and Schatz, G. (1981). Mitochondria: a historical review. J. Cell Biol. *91*, 227s–255s. 10.1083/jcb.91.3.227s.

82. Altmann, R. (1894). Die Elementarorganismen und ihre Beziehungen zu den Zellen (Veit).

83. Benda, C. (1898). Ueber die Spermatogenese der Vertebraten und höherer Evertebraten. 393–398.

84. Warburg, O. (1926). The effect of carbonoxide on substance exchange of yeast. Biochem. Z., 471–486.

85. Chance, B., and Williams, G.R. (1956). The respiratory chain and oxidative phosphorylation. Adv. Enzymol. Relat. Subj. Biochem. *17*, 65–134. 10.1002/9780470122624.ch2.

86. Lipmann, F. (1941). Metabolic Generation and Utilization of Phosphate Bond Energy. In Advances in Enzymology and Related Areas of Molecular Biology (John Wiley & Sons, Ltd), pp. 99–162. 10.1002/9780470122464.ch4.

87. Mitchell, P., and Moyle, J. (1967). Chemiosmotic Hypothesis of Oxidative Phosphorylation. Nature *213*, 137–139. 10.1038/213137a0.

88. Abrahams, J.P., Leslie, A.G.W., Lutter, R., and Walker, J.E. (1994). Structure at 2.8 Â resolution of F1-ATPase from bovine heart mitochondria. Nature *370*, 621–628. 10.1038/370621a0.

89. Boyer, P.D. (1997). The Atp Synthase—a Splendid Molecular Machine. Annu. Rev. Biochem. *66*, 717–749. 10.1146/annurev.biochem.66.1.717.

90. Siekevitz, P. (1957). Powerhouse of the Cell. Sci. Am. *197*, 131–140. 10.1038/scientificamerican0757-131.

91. Kingsbury, B.F. (1912). Cytoplasmic fixation. Anat. Rec. *6*, 39–52. 10.1002/ar.1090060202.

92. Meves, F. (1908). Chondriosome as a carrier hereditary system - Cytologic studies in fowls embryos. Arch Mikro Anat Entw, 816–865.

93. Nass, M.M. (1966). The circularity of mitochondrial DNA. Proc. Natl. Acad. Sci. U. S. A. *56*, 1215–1222.

94. Martin, W.F., Garg, S., and Zimorski, V. (2015). Endosymbiotic theories for eukaryote origin. Philos. Trans. R. Soc. B Biol. Sci. *370*, 20140330. 10.1098/rstb.2014.0330.

95. Gray, M.W., Burger, G., and Lang, B.F. (1999). Mitochondrial evolution. Science *283*, 1476–1481. 10.1126/science.283.5407.1476.

96. Miyazono, Y., Hirashima, S., Ishihara, N., Kusukawa, J., Nakamura, K., and Ohta, K. (2018). Uncoupled mitochondria quickly shorten along their long axis to form indented spheroids, instead of rings, in a fission-independent manner. Sci. Rep. *8*, 350. 10.1038/s41598-017-18582-6.

97. Llopis, J., McCaffery, J.M., Miyawaki, A., Farquhar, M.G., and Tsien, R.Y. (1998). Measurement of cytosolic, mitochondrial, and Golgi pH in single living cells with green fluorescent proteins. Proc. Natl. Acad. Sci. U. S. A. *95*, 6803–6808.

98. Wiedemann, N., Kozjak, V., Chacinska, A., Schönfisch, B., Rospert, S., Ryan, M.T., Pfanner, N., and Meisinger, C. (2003). Machinery for protein sorting and assembly in the mitochondrial outer membrane. Nature *424*, 565–571. 10.1038/nature01753.

99. Schmidt, O., Pfanner, N., and Meisinger, C. (2010). Mitochondrial protein import: from proteomics to functional mechanisms. Nat. Rev. Mol. Cell Biol. *11*, 655–667. 10.1038/nrm2959.

100. Dekker, P.J., Martin, F., Maarse, A.C., Bömer, U., Müller, H., Guiard, B., Meijer, M., Rassow, J., and Pfanner, N. (1997). The Tim core complex defines the number of mitochondrial translocation contact sites and can hold arrested preproteins in the absence of matrix Hsp70-Tim44. EMBO J. *16*, 5408–5419. 10.1093/emboj/16.17.5408.

101. Kovermann, P., Truscott, K.N., Guiard, B., Rehling, P., Sepuri, N.B., Müller, H., Jensen, R.E., Wagner, R., and Pfanner, N. (2002). Tim22, the Essential Core of the Mitochondrial Protein Insertion Complex, Forms a Voltage-Activated and Signal-Gated Channel. Mol. Cell *9*, 363–373. 10.1016/S1097-2765(02)00446-X.

102. Houtkooper, R.H., and Vaz, F.M. (2008). Cardiolipin, the heart of mitochondrial metabolism. Cell. Mol. Life Sci. *65*, 2493–2506. 10.1007/s00018-008-8030-5.

103. Hovius, R., Lambrechts, H., Nicolay, K., and de Kruijff, B. (1990). Improved methods to isolate and subfractionate rat liver mitochondria. Lipid composition of the inner and outer membrane. Biochim. Biophys. Acta BBA - Biomembr. *1021*, 217–226. 10.1016/0005-2736(90)90036-N.

104. Bautista, J.S., Falabella, M., Flannery, P.J., Hanna, M.G., Heales, S.J.R., Pope, S.A.S., and Pitceathly, R.D.S. (2022). Advances in methods to analyse cardiolipin and their clinical applications. Trends Anal. Chem. TRAC *157*, 116808. 10.1016/j.trac.2022.116808.

105. Oemer, G., Lackner, K., Muigg, K., Krumschnabel, G., Watschinger, K., Sailer, S., Lindner, H., Gnaiger, E., Wortmann, S.B., Werner, E.R., et al. (2018). Molecular

structural diversity of mitochondrial cardiolipins. Proc. Natl. Acad. Sci. *115*, 4158–4163. 10.1073/pnas.1719407115.

106. Falabella, M., Vernon, H.J., Hanna, M.G., Claypool, S.M., and Pitceathly, R.D.S. (2021). Cardiolipin, Mitochondria, and Neurological Disease. Trends Endocrinol. Metab. *32*, 224–237. 10.1016/j.tem.2021.01.006.

107. Ahmadpour, S.T., Mahéo, K., Servais, S., Brisson, L., and Dumas, J.-F. (2020). Cardiolipin, the Mitochondrial Signature Lipid: Implication in Cancer. Int. J. Mol. Sci. *21*, 8031. 10.3390/ijms21218031.

108. Dudek, J., Hartmann, M., and Rehling, P. (2019). The role of mitochondrial cardiolipin in heart function and its implication in cardiac disease. Biochim. Biophys. Acta BBA - Mol. Basis Dis. *1865*, 810–821. 10.1016/j.bbadis.2018.08.025.

109. Taanman, J.-W. (1999). The mitochondrial genome: structure, transcription, translation and replication. Biochim. Biophys. Acta BBA - Bioenerg. *1410*, 103–123. 10.1016/S0005-2728(98)00161-3.

110. Barshad, G., Marom, S., Cohen, T., and Mishmar, D. (2018). Mitochondrial DNA Transcription and Its Regulation: An Evolutionary Perspective. Trends Genet. *34*, 682–692. 10.1016/j.tig.2018.05.009.

111. Montoya, J., Christianson, T., Levens, D., Rabinowitz, M., and Attardi, G. (1982). Identification of initiation sites for heavy-strand and light-strand transcription in human mitochondrial DNA. Proc. Natl. Acad. Sci. *79*, 7195–7199. 10.1073/pnas.79.23.7195.

112. Bitner-Glindzicz, M., Pembrey, M., Duncan, A., Heron, J., Ring, S.M., Hall, A., and Rahman, S. (2009). Prevalence of Mitochondrial 1555A→G Mutation in European Children. N. Engl. J. Med. *360*, 640–642. 10.1056/NEJMc0806396.

113. Payne, B.A.I., Gardner, K., and Chinnery, P.F. (2015). Mitochondrial DNA mutations in ageing and disease: implications for HIV? Antivir. Ther. *20*, 109–120. 10.3851/IMP2824.

114. Rath, S., Sharma, R., Gupta, R., Ast, T., Chan, C., Durham, T.J., Goodman, R.P., Grabarek, Z., Haas, M.E., Hung, W.H.W., et al. (2021). MitoCarta3.0: an updated mitochondrial proteome now with sub-organelle localization and pathway annotations. Nucleic Acids Res. *49*, D1541–D1547. 10.1093/nar/gkaa1011.

115. Kanki, T., Nakayama, H., Sasaki, N., Takio, K., Alam, T.I., Hamasaki, N., and Kang, D. (2004). Mitochondrial Nucleoid and Transcription Factor A. Ann. N. Y. Acad. Sci. *1011*, 61–68. 10.1196/annals.1293.007.

116. Kukat, C., Wurm, C.A., Spåhr, H., Falkenberg, M., Larsson, N.-G., and Jakobs, S. (2011). Super-resolution microscopy reveals that mammalian mitochondrial nucleoids have a uniform size and frequently contain a single copy of mtDNA. Proc. Natl. Acad. Sci. *108*, 13534–13539. 10.1073/pnas.1109263108.

117. Kukat, C., Davies, K.M., Wurm, C.A., Spåhr, H., Bonekamp, N.A., Kühl, I., Joos, F., Polosa, P.L., Park, C.B., Posse, V., et al. (2015). Cross-strand binding of TFAM to a single mtDNA molecule forms the mitochondrial nucleoid. Proc. Natl. Acad. Sci. *112*, 11288–11293. 10.1073/pnas.1512131112.

118. D'Souza, A.R., and Minczuk, M. (2018). Mitochondrial transcription and translation: overview. Essays Biochem. *62*, 309–320. 10.1042/EBC20170102.

119. Baradaran, R., Berrisford, J.M., Minhas, G.S., and Sazanov, L.A. (2013). Crystal structure of the entire respiratory complex I. Nature *494*, 443–448. 10.1038/nature11871.

120. Stroud, D.A., Surgenor, E.E., Formosa, L.E., Reljic, B., Frazier, A.E., Dibley, M.G., Osellame, L.D., Stait, T., Beilharz, T.H., Thorburn, D.R., et al. (2016). Accessory subunits are integral for assembly and function of human mitochondrial complex I. Nature *538*, 123–126. 10.1038/nature19754.

121. Sazanov, L.A. (2015). A giant molecular proton pump: structure and mechanism of respiratory complex I. Nat. Rev. Mol. Cell Biol. *16*, 375–388. 10.1038/nrm3997.

122. Wikström, M. (1984). Two protons are pumped from the mitochondrial matrix per electron transferred between NADH and ubiquinone. FEBS Lett. *169*, 300–304. 10.1016/0014-5793(84)80338-5.

123. Schapira, A.H.V., Cooper, J.M., Dexter, D., Jenner, P., Clark, J.B., and Marsden, C.D. (1989). MITOCHONDRIAL COMPLEX I DEFICIENCY IN PARKINSON'S DISEASE. The Lancet *333*, 1269. 10.1016/S0140-6736(89)92366-0.

124. Chouchani, E.T., Pell, V.R., Gaude, E., Aksentijević, D., Sundier, S.Y., Robb, E.L., Logan, A., Nadtochiy, S.M., Ord, E.N.J., Smith, A.C., et al. (2014). Ischaemic accumulation of succinate controls reperfusion injury through mitochondrial ROS. Nature *515*, 431–435. 10.1038/nature13909.

125. Leyane, T.S., Jere, S.W., and Houreld, N.N. (2022). Oxidative Stress in Ageing and Chronic Degenerative Pathologies: Molecular Mechanisms Involved in Counteracting Oxidative Stress and Chronic Inflammation. Int. J. Mol. Sci. *23*, 7273. 10.3390/ijms23137273.

126. Hadrava Vanova, K., Kraus, M., Neuzil, J., and Rohlena, J. (2020). Mitochondrial complex II and reactive oxygen species in disease and therapy. Redox Rep. *25*, 26–32. 10.1080/13510002.2020.1752002.

127. Skillings, E.A., and Morton, A.J. (2016). Delayed Onset and Reduced Cognitive Deficits through Pre-Conditioning with 3-Nitropropionic Acid is Dependent on Sex and CAG Repeat Length in the R6/2 Mouse Model of Huntington's Disease. J. Huntingt. Dis. *5*, 19–32. 10.3233/JHD-160189.

128. Barletta, J.A., and Hornick, J.L. (2012). Succinate Dehydrogenase-deficient Tumors: Diagnostic Advances and Clinical Implications. Adv. Anat. Pathol. *19*, 193. 10.1097/PAP.0b013e31825c6bc6.

129. Luo, K., Yu, J.H., Quan, Y., Shin, Y.J., Lee, K.E., Kim, H.L., Ko, E.J., Chung, B.H., Lim, S.W., and Yang, C.W. (2019). Therapeutic potential of coenzyme Q10 in mitochondrial dysfunction during tacrolimus-induced beta cell injury. Sci. Rep. *9*, 7995. 10.1038/s41598-019-44475-x.

130. Muller, F.L., Lustgarten, M.S., Jang, Y., Richardson, A., and Van Remmen, H. (2007). Trends in oxidative aging theories. Free Radic. Biol. Med. *43*, 477–503. 10.1016/j.freeradbiomed.2007.03.034.

131. DiMauro, S. (2006). Mitochondrial myopathies. Curr. Opin. Rheumatol. *18*, 636. 10.1097/01.bor.0000245729.17759.f2.

132. Schuelke, M., Krude, H., Finckh, B., Mayatepek, E., Janssen, A., Schmelz, M., Trefz, F., Trijbels, F., and Smeitink, J. (2002). Septo-optic dysplasia associated with a new mitochondrial cytochrome b mutation. Ann. Neurol. *51*, 388–392. 10.1002/ana.10151.

133. Wibrand, F., Ravn, K., Schwartz, M., Rosenberg, T., Horn, N., and Vissing, J. (2001). Multisystem disorder associated with a missense mutation in the mitochondrial cytochrome b gene. Ann. Neurol. *50*, 540–543. 10.1002/ana.1224.

134. Bowman, S.E.J., and Bren, K.L. (2008). The Chemistry and Biochemistry of Heme c: Functional Bases for Covalent Attachment. Nat. Prod. Rep. *25*, 1118–1130. 10.1039/b717196j.

135. Garrido, C., Galluzzi, L., Brunet, M., Puig, P.E., Didelot, C., and Kroemer, G. (2006). Mechanisms of cytochrome c release from mitochondria. Cell Death Differ. *13*, 1423–1433. 10.1038/sj.cdd.4401950.

136. Tsukihara, T., Aoyama, H., Yamashita, E., Tomizaki, T., Yamaguchi, H., Shinzawa-Itoh, K., Nakashima, R., Yaono, R., and Yoshikawa, S. (1995). Structures of Metal Sites of Oxidized Bovine Heart Cytochrome c Oxidase at 2.8 Å. Science *269*, 1069–1074. 10.1126/science.7652554.

137. Pecina, P., Houstková, H., Hansíková, H., Zeman, J., and Houstek, J. (2004). Genetic defects of cytochrome c oxidase assembly. Physiol. Res. *53 Suppl 1*, S213-223.

138. Di Filippo, M., Chiasserini, D., Tozzi, A., Picconi, B., and Calabresi, P. (2010). Mitochondria and the Link Between Neuroinflammation and Neurodegeneration. J. Alzheimers Dis. *20*, S369–S379. 10.3233/JAD-2010-100543.

139. Itoh, K., Weis, S., Mehraein, P., and Müller-Höcker, J. (1996). Cytochrome c oxidase defects of the human substantia nigra in normal aging. Neurobiol. Aging *17*, 843–848. 10.1016/S0197-4580(96)00168-6.

140. Solaini, G., and Harris, D.A. (2005). Biochemical dysfunction in heart mitochondria exposed to ischaemia and reperfusion. Biochem. J. *390*, 377–394. 10.1042/BJ20042006.

141. Schägger, H., and Ohm, T.G. (1995). Human Diseases with Defects in Oxidative Phosphorylation. Eur. J. Biochem. *227*, 916–921. 10.1111/j.1432-1033.1995.0916p.x.

142. Choi, S.Y., Lopez-Gonzalez, R., Krishnan, G., Phillips, H.L., Li, A.N., Seeley, W.W., Yao, W.-D., Almeida, S., and Gao, F.-B. (2019). C9ORF72-ALS/FTD-associated poly(GR) binds Atp5a1 and compromises mitochondrial function in vivo. Nat. Neurosci. *22*, 851–862. 10.1038/s41593-019-0397-0.

143. D'Antoni, S., Bari, L. de, Valenti, D., Borro, M., Bonaccorso, C.M., Simmaco, M., Vacca, R.A., and Catania, M.V. (2020). Aberrant mitochondrial bioenergetics in the

cerebral cortex of the Fmr1 knockout mouse model of fragile X syndrome. Biol. Chem. *401*, 497–503. 10.1515/hsz-2019-0221.

144. Chance, B., and Williams, G.R. (1955). A Method for the Localization of Sites for Oxidative Phosphorylation. Nature *176*, 250–254. 10.1038/176250a0.

145. Boumans, H., Grivell, L.A., and Berden, J.A. (1998). The Respiratory Chain in Yeast Behaves as a Single Functional Unit *. J. Biol. Chem. *273*, 4872–4877. 10.1074/jbc.273.9.4872.

146. Schägger, H., and Pfeiffer, K. (2000). Supercomplexes in the respiratory chains of yeast and mammalian mitochondria. EMBO J. *19*, 1777–1783. 10.1093/emboj/19.8.1777.

147. Zhang, M., Mileykovskaya, E., and Dowhan, W. (2002). Gluing the Respiratory Chain Together: CARDIOLIPIN IS REQUIRED FOR SUPERCOMPLEX FORMATION IN THE INNER MITOCHONDRIAL MEMBRANE *. J. Biol. Chem. *277*, 43553–43556. 10.1074/jbc.C200551200.

148. Lenaz, G., and Genova, M.L. (2012). Supramolecular Organisation of the Mitochondrial Respiratory Chain: A New Challenge for the Mechanism and Control of Oxidative Phosphorylation. In Mitochondrial Oxidative Phosphorylation: Nuclear-Encoded Genes, Enzyme Regulation, and Pathophysiology Advances in Experimental Medicine and Biology., B. Kadenbach, ed. (Springer), pp. 107–144. 10.1007/978-1-4614-3573-0_5.

149. Schäfer, E., Seelert, H., Reifschneider, N.H., Krause, F., Dencher, N.A., and Vonck, J. (2006). Architecture of Active Mammalian Respiratory Chain Supercomplexes *. J. Biol. Chem. *281*, 15370–15375. 10.1074/jbc.M513525200.

150. Ispada, J., da Fonseca Junior, A.M., de Lima, C.B., dos Santos, E.C., Fontes, P.K., Nogueira, M.F.G., da Silva, V.L., Almeida, F.N., Leite, S. de C., Chitwood, J.L., et al. (2020). Tricarboxylic Acid Cycle Metabolites as Mediators of DNA Methylation Reprogramming in Bovine Preimplantation Embryos. Int. J. Mol. Sci. *21*, 6868. 10.3390/ijms21186868.

151. Cardaci, S., and Ciriolo, M.R. (2012). TCA Cycle Defects and Cancer: When Metabolism Tunes Redox State. Int. J. Cell Biol. *2012*, 161837. 10.1155/2012/161837.

152. Lai, L., Wang, M., Martin, O.J., Leone, T.C., Vega, R.B., Han, X., and Kelly, D.P. (2014). A Role for Peroxisome Proliferator-activated Receptor γ Coactivator 1 (PGC-1) in the Regulation of Cardiac Mitochondrial Phospholipid Biosynthesis. J. Biol. Chem. *289*, 2250–2259. 10.1074/jbc.M113.523654.

153. Virbasius, J.V., and Scarpulla, R.C. (1994). Activation of the human mitochondrial transcription factor A gene by nuclear respiratory factors: a potential regulatory link between nuclear and mitochondrial gene expression in organelle biogenesis. Proc. Natl. Acad. Sci. *91*, 1309–1313. 10.1073/pnas.91.4.1309.

154. Lagouge, M., Argmann, C., Gerhart-Hines, Z., Meziane, H., Lerin, C., Daussin, F., Messadeq, N., Milne, J., Lambert, P., Elliott, P., et al. (2006). Resveratrol Improves Mitochondrial Function and Protects against Metabolic Disease by Activating SIRT1 and PGC-1α. Cell *127*, 1109–1122. 10.1016/j.cell.2006.11.013.

155. Jäger, S., Handschin, C., St.-Pierre, J., and Spiegelman, B.M. (2007). AMP-activated protein kinase (AMPK) action in skeletal muscle via direct phosphorylation of PGC-1α. Proc. Natl. Acad. Sci. *104*, 12017–12022. 10.1073/pnas.0705070104.

156. Finck, B.N., and Kelly, D.P. (2006). PGC-1 coactivators: inducible regulators of energy metabolism in health and disease. J. Clin. Invest. *116*, 615–622. 10.1172/JCI27794.

157. Cantó, C., Gerhart-Hines, Z., Feige, J.N., Lagouge, M., Noriega, L., Milne, J.C., Elliott, P.J., Puigserver, P., and Auwerx, J. (2009). AMPK regulates energy expenditure by modulating NAD+ metabolism and SIRT1 activity. Nature *458*, 1056–1060. 10.1038/nature07813.

158. Jovaisaite, V., and Auwerx, J. (2015). The mitochondrial unfolded protein response—synchronizing genomes. Curr. Opin. Cell Biol. *33*, 74–81. 10.1016/j.ceb.2014.12.003.

159. Lebeau, J., Rainbolt, T.K., and Wiseman, R.L. (2018). Chapter Three - Coordinating Mitochondrial Biology Through the Stress-Responsive Regulation of Mitochondrial Proteases. In International Review of Cell and Molecular Biology Mitochondria and Longevity., C. López-Otín and L. Galluzzi, eds. (Academic Press), pp. 79–128. 10.1016/bs.ircmb.2018.05.003.

160. Vanstone, J.R., Smith, A.M., McBride, S., Naas, T., Holcik, M., Antoun, G., Harper, M.-E., Michaud, J., Sell, E., Chakraborty, P., et al. (2016). DNM1L-related mitochondrial fission defect presenting as refractory epilepsy. Eur. J. Hum. Genet. *24*, 1084–1088. 10.1038/ejhg.2015.243.

161. Sheng, Z.-H., and Cai, Q. (2012). Mitochondrial transport in neurons: impact on synaptic homeostasis and neurodegeneration. Nat. Rev. Neurosci. *13*, 77–93. 10.1038/nrn3156.

162. McLelland, G.-L., Soubannier, V., Chen, C.X., McBride, H.M., and Fon, E.A. (2014). Parkin and PINK1 function in a vesicular trafficking pathway regulating mitochondrial quality control. EMBO J. *33*, 282–295. 10.1002/embj.201385902.

163. Rahman, J., and Rahman, S. (2019). The utility of phenomics in diagnosis of inherited metabolic disorders. Clin. Med. *19*, 30–36. 10.7861/clinmedicine.19-1-30.

164. Niyazov, D.M., Kahler, S.G., and Frye, R.E. (2016). Primary Mitochondrial Disease and Secondary Mitochondrial Dysfunction: Importance of Distinction for Diagnosis and Treatment. Mol. Syndromol. *7*, 122–137. 10.1159/000446586.

165. Rahman, S. (2023). Chapter 4 - Leigh syndrome. In Handbook of Clinical Neurology Mitochondrial Diseases., R. Horvath, M. Hirano, and P. F. Chinnery, eds. (Elsevier), pp. 43–63. 10.1016/B978-0-12-821751-1.00015-4.

166. Orsucci, D., Siciliano, G., and Mancuso, M. (2018). Revealing the Complexity of Mitochondrial DNA-Related Disorders. eBioMedicine *30*, 3–4. 10.1016/j.ebiom.2018.03.007.

167. Krishnan, K.J., Reeve, A.K., Samuels, D.C., Chinnery, P.F., Blackwood, J.K., Taylor, R.W., Wanrooij, S., Spelbrink, J.N., Lightowlers, R.N., and Turnbull, D.M. (2008). What causes mitochondrial DNA deletions in human cells? Nat. Genet. *40*, 275–279. 10.1038/ng.f.94.

168. Alberio, S., Mineri, R., Tiranti, V., and Zeviani, M. (2007). Depletion of mtDNA: Syndromes and genes. Mitochondrion *7*, 6–12. 10.1016/j.mito.2006.11.010.

169. Taylor, R.W., and Turnbull, D.M. (2005). Mitochondrial DNA mutations in human disease. Nat. Rev. Genet. *6*, 389–402. 10.1038/nrg1606.

170. McLaughlin, K.L., Hagen, J.T., Coalson, H.S., Nelson, M.A.M., Kew, K.A., Wooten, A.R., and Fisher-Wellman, K.H. (2020). Novel approach to quantify mitochondrial content and intrinsic bioenergetic efficiency across organs. Sci. Rep. *10*, 17599. 10.1038/s41598-020-74718-1.

171. Lowell, B.B., and Shulman, G.I. (2005). Mitochondrial Dysfunction and Type 2 Diabetes. Science *307*, 384–387. 10.1126/science.1104343.

172. Porporato, P.E., Filigheddu, N., Pedro, J.M.B.-S., Kroemer, G., and Galluzzi, L. (2018). Mitochondrial metabolism and cancer. Cell Res. *28*, 265–280. 10.1038/cr.2017.155.

173. Ballinger, S.W. (2005). Mitochondrial dysfunction in cardiovascular disease. Free Radic. Biol. Med. *38*, 1278–1295. 10.1016/j.freeradbiomed.2005.02.014.

174. Johri, A., and Beal, M.F. (2012). Mitochondrial Dysfunction in Neurodegenerative Diseases. J. Pharmacol. Exp. Ther. *342*, 619–630. 10.1124/jpet.112.192138.

175. Mehta, A.R., Gregory, J.M., Dando, O., Carter, R.N., Burr, K., Nanda, J., Story, D., McDade, K., Smith, C., Morton, N.M., et al. (2021). Mitochondrial bioenergetic deficits in C9orf72 amyotrophic lateral sclerosis motor neurons cause dysfunctional axonal homeostasis. Acta Neuropathol. (Berl.) *141*, 257–279. 10.1007/s00401-020-02252-5.

176. Esteras, N., Rohrer, J.D., Hardy, J., Wray, S., and Abramov, A.Y. (2017). Mitochondrial hyperpolarization in iPSC-derived neurons from patients of FTDP-17 with 10+16 MAPT mutation leads to oxidative stress and neurodegeneration. Redox Biol. *12*, 410–422. 10.1016/j.redox.2017.03.008.

177. Bannwarth, S., Ait-El-Mkadem, S., Chaussenot, A., Genin, E.C., Lacas-Gervais, S., Fragaki, K., Berg-Alonso, L., Kageyama, Y., Serre, V., Moore, D.G., et al. (2014). A mitochondrial origin for frontotemporal dementia and amyotrophic lateral sclerosis through CHCHD10 involvement. Brain *137*, 2329–2345. 10.1093/brain/awu138.

178. Wang, T., Liu, H., Itoh, K., Oh, S., Zhao, L., Murata, D., Sesaki, H., Hartung, T., Na, C.H., and Wang, J. (2021). C9orf72 regulates energy homeostasis by stabilizing mitochondrial complex I assembly. Cell Metab. *33*, 531-546.e9. 10.1016/j.cmet.2021.01.005.

179. Gomez-Suaga, P., Mórotz, G.M., Markovinovic, A., Martín-Guerrero, S.M., Preza, E., Arias, N., Mayl, K., Aabdien, A., Gesheva, V., Nishimura, A., et al. (2022). Disruption of ER-mitochondria tethering and signalling in C9orf72-associated amyotrophic lateral sclerosis and frontotemporal dementia. Aging Cell *21*, e13549. 10.1111/acel.13549.

180. Prudencio, M., Belzil, V.V., Batra, R., Ross, C.A., Gendron, T.F., Pregent, L.J., Murray, M.E., Overstreet, K.K., Piazza-Johnston, A.E., Desaro, P., et al. (2015). Distinct brain transcriptome profiles in C9orf72-associated and sporadic ALS. Nat. Neurosci. *18*, 1175–1182. 10.1038/nn.4065.

181. Wang, W., Arakawa, H., Wang, L., Okolo, O., Siedlak, S.L., Jiang, Y., Gao, J., Xie, F., Petersen, R.B., and Wang, X. (2017). Motor-Coordinative and Cognitive Dysfunction Caused by Mutant TDP-43 Could Be Reversed by Inhibiting Its Mitochondrial Localization. Mol. Ther. *25*, 127–139. 10.1016/j.ymthe.2016.10.013.

182. Wang, P., Deng, J., Dong, J., Liu, J., Bigio, E.H., Mesulam, M., Wang, T., Sun, L., Wang, L., Lee, A.Y.-L., et al. (2019). TDP-43 induces mitochondrial damage and activates the mitochondrial unfolded protein response. PLoS Genet. *15*, e1007947. 10.1371/journal.pgen.1007947.

183. Yu, C.-H., Davidson, S., Harapas, C.R., Hilton, J.B., Mlodzianoski, M.J., Laohamonthonkul, P., Louis, C., Low, R.R.J., Moecking, J., De Nardo, D., et al. (2020). TDP-43 Triggers Mitochondrial DNA Release via mPTP to Activate cGAS/STING in ALS. Cell *183*, 636-649.e18. 10.1016/j.cell.2020.09.020.

184. Wang, W., Wang, L., Lu, J., Siedlak, S.L., Fujioka, H., Liang, J., Jiang, S., Ma, X., Jiang, Z., da Rocha, E.L., et al. (2016). The inhibition of TDP-43 mitochondrial localization blocks its neuronal toxicity. Nat. Med. *22*, 869–878. 10.1038/nm.4130.

185. Dafinca, R., Barbagallo, P., Farrimond, L., Candalija, A., Scaber, J., Ababneh, N.A., Sathyaprakash, C., Vowles, J., Cowley, S.A., and Talbot, K. (2020). Impairment of Mitochondrial Calcium Buffering Links Mutations in C9ORF72 and TARDBP in iPS-Derived Motor Neurons from Patients with ALS/FTD. Stem Cell Rep. *14*, 892–908. 10.1016/j.stemcr.2020.03.023.

186. Davis, S.A., Itaman, S., Khalid-Janney, C.M., Sherard, J.A., Dowell, J.A., Cairns, N.J., and Gitcho, M.A. (2018). TDP-43 interacts with mitochondrial proteins critical for mitophagy and mitochondrial dynamics. Neurosci. Lett. *678*, 8–15. 10.1016/j.neulet.2018.04.053.

187. Hayes, L.R., and Kalab, P. (2022). Emerging Therapies and Novel Targets for TDP-43 Proteinopathy in ALS/FTD. Neurotherapeutics *19*, 1061–1084. 10.1007/s13311-022-01260-5.

188. Tracy, T.E., Madero-Pérez, J., Swaney, D.L., Chang, T.S., Moritz, M., Konrad, C., Ward, M.E., Stevenson, E., Hüttenhain, R., Kauwe, G., et al. (2022). Tau interactome maps synaptic and mitochondrial processes associated with neurodegeneration. Cell *185*, 712-728.e14. 10.1016/j.cell.2021.12.041.

189. Esteras, N., Kopach, O., Maiolino, M., Lariccia, V., Amoroso, S., Qamar, S., Wray, S., Rusakov, D.A., Jaganjac, M., and Abramov, A.Y. (2022). Mitochondrial ROS control neuronal excitability and cell fate in frontotemporal dementia. Alzheimers Dement. *18*, 318–338. 10.1002/alz.12394.

190. Genin, E.C., Plutino, M., Bannwarth, S., Villa, E., Cisneros-Barroso, E., Roy, M., Ortega-Vila, B., Fragaki, K., Lespinasse, F., Pinero-Martos, E., et al. (2016). CHCHD10 mutations promote loss of mitochondrial cristae junctions with impaired mitochondrial genome maintenance and inhibition of apoptosis. EMBO Mol. Med. *8*, 58–72. 10.15252/emmm.201505496.

191. Ruan, Y., Hu, J., Che, Y., Liu, Y., Luo, Z., Cheng, J., Han, Q., He, H., and Zhou, Q. (2022). CHCHD2 and CHCHD10 regulate mitochondrial dynamics and integrated stress response. Cell Death Dis. *13*, 1–12. 10.1038/s41419-022-04602-5.

192. Nie, Y., Murley, A., Golder, Z., Rowe, J.B., Allinson, K., and Chinnery, P.F. (2022). Heteroplasmic mitochondrial DNA mutations in frontotemporal lobar degeneration. Acta Neuropathol. (Berl.) *143*, 687–695. 10.1007/s00401-022-02423-6.

193. Phan, K., He, Y., Pickford, R., Bhatia, S., Katzeff, J.S., Hodges, J.R., Piguet, O., Halliday, G.M., and Kim, W.S. (2020). Uncovering pathophysiological changes in frontotemporal dementia using serum lipids. Sci. Rep. *10*, 3640. 10.1038/s41598-020-60457-w.

194. Zhou, D., Zhou, M., Wang, Z., Fu, Y., Jia, M., Wang, X., Liu, M., Zhang, Y., Sun, Y., Lu, Y., et al. (2019). PGRN acts as a novel regulator of mitochondrial homeostasis by facilitating mitophagy and mitochondrial biogenesis to prevent podocyte injury in diabetic nephropathy. Cell Death Dis. *10*, 1–16. 10.1038/s41419-019-1754-3.

195. Chen, S., Bie, M., Wang, X., Fan, M., Chen, B., Shi, Q., and Jiang, Y. (2021). PGRN exacerbates the progression of non-small cell lung cancer via PI3K/AKT/Bcl-2 antiapoptotic signaling. Genes Dis. 10.1016/j.gendis.2021.05.005.

196. Daya, M., Loilome, W., Techasen, A., Thanee, M., Sa-Ngiamwibool, P., Titapun, A., Yongvanit, P., and Namwat, N. (2018). Progranulin modulates cholangiocarcinoma cell proliferation, apoptosis, and motility via the PI3K/pAkt pathway. OncoTargets Ther. *11*, 395–408. 10.2147/OTT.S155511.

197. Liu, F., Zhang, W., Yang, F., Feng, T., Zhou, M., Yu, Y., Yu, X., Zhao, W., Yi, F., Tang, W., et al. (2016). Interleukin-6-stimulated progranulin expression contributes to the malignancy of hepatocellular carcinoma cells by activating mTOR signaling. Sci. Rep. *6*, 21260. 10.1038/srep21260.

198. Dong, Y., Tan, H., Wang, L., and Liu, Z. (2023). Progranulin promoted the proliferation, metastasis, and suppressed apoptosis via JAK2-STAT3/4 signaling pathway in papillary thyroid carcinoma. Cancer Cell Int. *23*, 191. 10.1186/s12935-023-03033-2.

199. Tao, J., Ji, F., Wang, F., Liu, B., and Zhu, Y. (2012). Neuroprotective effects of progranulin in ischemic mice. Brain Res. *1436*, 130–136. 10.1016/j.brainres.2011.11.063.

200. Almeida, S., Zhang, Z., Coppola, G., Mao, W., Futai, K., Karydas, A., Geschwind, M.D., Tartaglia, M.C., Gao, F., Gianni, D., et al. (2012). Induced Pluripotent Stem Cell Models of Progranulin-Deficient Frontotemporal Dementia Uncover Specific Reversible Neuronal Defects. Cell Rep. *2*, 789–798. 10.1016/j.celrep.2012.09.007.

201. Jacova, C., Hsiung, G.-Y.R., Tawankanjanachot, I., Dinelle, K., McCormick, S., Gonzalez, M., Lee, H., Sengdy, P., Bouchard-Kerr, P., Baker, M., et al. (2013). Anterior brain glucose hypometabolism predates dementia in progranulin mutation carriers. Neurology *81*, 1322–1331. 10.1212/WNL.0b013e3182a8237e.

202. Gaweda-Walerych, K., Walerych, D., Berdyński, M., Buratti, E., and Zekanowski, C. (2021). Parkin Levels Decrease in Fibroblasts With Progranulin (PGRN) Pathogenic Variants and in a Cellular Model of PGRN Deficiency. Front. Mol. Neurosci. *14*.

203. Boland, S., Swarup, S., Ambaw, Y.A., Malia, P.C., Richards, R.C., Fischer, A.W., Singh, S., Aggarwal, G., Spina, S., Nana, A.L., et al. (2022). Deficiency of the

frontotemporal dementia gene GRN results in gangliosidosis. Nat. Commun. *13*, 5924. 10.1038/s41467-022-33500-9.

204. Marian, O.C., Teo, J.D., Lee, J.Y., Song, H., Kwok, J.B., Landin-Romero, R., Halliday, G., and Don, A.S. (2023). Disrupted myelin lipid metabolism differentiates frontotemporal dementia caused by GRN and C9orf72 gene mutations. Acta Neuropathol. Commun. *11*, 52. 10.1186/s40478-023-01544-7.

205. Rinaldo, P., Matern, D., and Bennett, M.J. (2002). Fatty acid oxidation disorders. Annu. Rev. Physiol. *64*, 477–502. 10.1146/annurev.physiol.64.082201.154705.

206. Rodríguez-Periñán, G., de la Encarnación, A., Moreno, F., López de Munain, A., Martínez, A., Martín-Requero, Á., Alquézar, C., and Bartolomé, F. (2023). Progranulin Deficiency Induces Mitochondrial Dysfunction in Frontotemporal Lobar Degeneration with TDP-43 Inclusions. Antioxidants *12*, 581. 10.3390/antiox12030581.

207. Ramos, D.M., Skarnes, W.C., Singleton, A.B., Cookson, M.R., and Ward, M.E. (2021). Tackling neurodegenerative diseases with genomic engineering: A new stem cell initiative from the NIH. Neuron *109*, 1080–1083. 10.1016/j.neuron.2021.03.022.

208. Marttinen, M., Paananen, J., Neme, A., Mitra, V., Takalo, M., Natunen, T., Paldanius, K.M.A., Mäkinen, P., Bremang, M., Kurki, M.I., et al. (2019). A multiomic approach to characterize the temporal sequence in Alzheimer's disease-related pathology. Neurobiol. Dis. *124*, 454–468. 10.1016/j.nbd.2018.12.009.

209. Rolfe, D.F., and Brown, G.C. (1997). Cellular energy utilization and molecular origin of standard metabolic rate in mammals. Physiol. Rev. *77*, 731–758. 10.1152/physrev.1997.77.3.731.

210. Attwell, D., and Laughlin, S.B. (2001). An Energy Budget for Signaling in the Grey Matter of the Brain. J. Cereb. Blood Flow Metab. *21*, 1133–1145. 10.1097/00004647-200110000-00001.

211. Livak, K.J., and Schmittgen, T.D. (2001). Analysis of Relative Gene Expression Data Using Real-Time Quantitative PCR and the 2−ΔΔCT Method. Methods *25*, 402–408. 10.1006/meth.2001.1262.

212. Belmonte, F.R., Martin, J.L., Frescura, K., Damas, J., Pereira, F., Tarnopolsky, M.A., and Kaufman, B.A. (2016). Digital PCR methods improve detection sensitivity and measurement precision of low abundance mtDNA deletions. Sci. Rep. *6*, 25186. 10.1038/srep25186.

213. Arnold, I., Pfeiffer, K., Neupert, W., Stuart, R.A., and Schägger, H. (1998). Yeast mitochondrial F1F0-ATP synthase exists as a dimer: identification of three dimer-specific subunits. EMBO J. *17*, 7170–7178. 10.1093/emboj/17.24.7170.

214. Wittig, I., Karas, M., and Schägger, H. (2007). High Resolution Clear Native Electrophoresis for In-gel Functional Assays and Fluorescence Studies of Membrane Protein Complexes*. Mol. Cell. Proteomics *6*, 1215–1225. 10.1074/mcp.M700076-MCP200.

215. Srere, P.A. (1969). Citrate synthase: [EC 4.1.3.7. Citrate oxaloacetate-lyase (CoA-acetylating)]. In Methods in Enzymology Citric Acid Cycle. (Academic Press), pp. 3–11. 10.1016/0076-6879(69)13005-0.

216. Wharton, D.C., and Tzagoloff, A. (1967). Cytochrome oxidase from beef heart mitochondria. In Methods in Enzymology Oxidation and Phosphorylation. (Academic Press), pp. 245–250. 10.1016/0076-6879(67)10048-7.

217. Wang, H., Su, N., Wang, L.-C., Wu, X., Bui, S., Chang, K.-J., Nielsen, A., Vo, H.-T., Luo, Y., and Ma, X.-J. (2015). Multiplex Fluorescent RNA In Situ Hybridization Via RNAscope. In In Situ Hybridization Methods Neuromethods., G. Hauptmann, ed. (Springer), pp. 405–414. 10.1007/978-1-4939-2303-8_21.

218. Anderson, R.M., Hadjichrysanthou, C., Evans, S., and Wong, M.M. (2017). Why do so many clinical trials of therapies for Alzheimer's disease fail? The Lancet *390*, 2327–2329. 10.1016/S0140-6736(17)32399-1.

219. Pfeuffer, S., Ruck, T., Kleinschnitz, C., Wiendl, H., and Meuth, S.G. (2016). Failed, interrupted and inconclusive trials on relapsing multiple sclerosis treatment: update 2010–2015. Expert Rev. Neurother. *16*, 689–700. 10.1080/14737175.2016.1176531.

220. Gordon, K., Clouaire, T., Bao, X.X., Kemp, S.E., Xenophontos, M., de Las Heras, J.I., and Stancheva, I. (2014). Immortality, but not oncogenic transformation, of primary human cells leads to epigenetic reprogramming of DNA methylation and gene expression. Nucleic Acids Res. *42*, 3529–3541. 10.1093/nar/gkt1351.

221. Renner, M., Lancaster, M.A., Bian, S., Choi, H., Ku, T., Peer, A., Chung, K., and Knoblich, J.A. (2017). Self-organized developmental patterning and differentiation in cerebral organoids. EMBO J. *36*, 1316–1329. 10.15252/embj.201694700.

222. Deus, C.M., Pereira, S.P., Cunha-Oliveira, T., Pereira, F.B., Raimundo, N., and Oliveira, P.J. (2020). Mitochondrial remodeling in human skin fibroblasts from sporadic male Parkinson's disease patients uncovers metabolic and mitochondrial bioenergetic defects. Biochim. Biophys. Acta BBA - Mol. Basis Dis. *1866*, 165615. 10.1016/j.bbadis.2019.165615.

223. Pereira, S.P., Deus, C.M., Serafim, T.L., Cunha-Oliveira, T., and Oliveira, P.J. (2018). Metabolic and Phenotypic Characterization of Human Skin Fibroblasts After Forcing Oxidative Capacity. Toxicol. Sci. *164*, 191–204. 10.1093/toxsci/kfy068.

224. Holler, C.J., Taylor, G., Deng, Q., and Kukar, T. (2017). Intracellular Proteolysis of Progranulin Generates Stable, Lysosomal Granulins that Are Haploinsufficient in Patients with Frontotemporal Dementia Caused by GRN Mutations. eNeuro *4*, ENEURO.0100-17.2017. 10.1523/ENEURO.0100-17.2017.

225. de Majo, M., Koontz, M., Marsan, E., Salinas, N., Ramsey, A., Kuo, Y.-M., Seo, K., Li, H., Dräger, N., Leng, K., et al. (2023). Granulin loss of function in human mature brain organoids implicates astrocytes in TDP-43 pathology. Stem Cell Rep. *18*, 706–719. 10.1016/j.stemcr.2023.01.012.

226. Pinarbasi, E.S., and Barmada, S.J. Glia in FTLD-GRN: from supporting cast to leading role. J. Clin. Invest. *133*, e168215. 10.1172/JCI168215.

227. Marsan, E., Velmeshev, D., Ramsey, A., Patel, R.K., Zhang, J., Koontz, M., Andrews, M.G., Majo, M. de, Mora, C., Blumenfeld, J., et al. (2023). Astroglial toxicity promotes synaptic degeneration in the thalamocortical circuit in frontotemporal dementia with *GRN* mutations. J. Clin. Invest. *133*. 10.1172/JCI164919.

228. He, Z., Ismail, A., Kriazhev, L., Sadvakassova, G., and Bateman, A. (2002). Progranulin (PC-cell-derived growth factor/acrogranin) regulates invasion and cell survival. Cancer Res. *62*, 5590–5596.

229. Austin, S., and St-Pierre, J. (2012). PGC1α and mitochondrial metabolism – emerging concepts and relevance in ageing and neurodegenerative disorders. J. Cell Sci. *125*, 4963–4971. 10.1242/jcs.113662.

230. Fernandez-Marcos, P.J., and Auwerx, J. (2011). Regulation of PGC-1α, a nodal regulator of mitochondrial biogenesis. Am. J. Clin. Nutr. *93*, 884S-890S. 10.3945/ajcn.110.001917.

231. Yang, J.-L., Weissman, L., Bohr, V.A., and Mattson, M.P. (2008). Mitochondrial DNA damage and repair in neurodegenerative disorders. DNA Repair *7*, 1110–1120. 10.1016/j.dnarep.2008.03.012.

232. Strang, K.H., Golde, T.E., and Giasson, B.I. (2019). MAPT mutations, tauopathy, and mechanisms of neurodegeneration. Lab. Invest. *99*, 912–928. 10.1038/s41374-019-0197-x.

233. Alcaide, D., Cacheux, J., Bancaud, A., Muramatsu, R., and T. Matsunaga, Y. (2023). Solute transport in the brain tissue: what are the key biophysical parameters tying in vivo and in vitro studies together? Biomater. Sci. *11*, 3450–3460. 10.1039/D3BM00027C.

234. Yabe, K., Yamamoto, Y., Takemura, M., Hara, T., Tsurumi, H., Serrero, G., Nabeshima, T., and Saito, K. (2021). Progranulin depletion inhibits proliferation via the transforming growth factor beta/SMAD family member 2 signaling axis in Kasumi-1 cells. Heliyon *7*, e05849. 10.1016/j.heliyon.2020.e05849.

235. Liu, C., and Bosch, X. (2012). Progranulin: A growth factor, a novel TNFR ligand and a drug target. Pharmacol. Ther. *133*, 124–132. 10.1016/j.pharmthera.2011.10.003.

236. Slanzi, A., Iannoto, G., Rossi, B., Zenaro, E., and Constantin, G. (2020). In vitro Models of Neurodegenerative Diseases. Front. Cell Dev. Biol. *8*.

237. Golpich, M., Amini, E., Mohamed, Z., Azman Ali, R., Mohamed Ibrahim, N., and Ahmadiani, A. (2016). Mitochondrial Dysfunction and Biogenesis in Neurodegenerative diseases: Pathogenesis and Treatment. CNS Neurosci. Ther. *23*, 5–22. 10.1111/cns.12655.

238. Jamwal, S., Blackburn, J.K., and Elsworth, J.D. (2021). PPARγ/PGC1α signaling as a potential therapeutic target for mitochondrial biogenesis in neurodegenerative disorders. Pharmacol. Ther. *219*, 107705. 10.1016/j.pharmthera.2020.107705.

239. Onesto, E., Colombrita, C., Gumina, V., Borghi, M.O., Dusi, S., Doretti, A., Fagiolari, G., Invernizzi, F., Moggio, M., Tiranti, V., et al. (2016). Gene-specific mitochondria

dysfunctions in human TARDBP and C9ORF72 fibroblasts. Acta Neuropathol. Commun. *4*. 10.1186/s40478-016-0316-5.

240. Mota, B.C., and Sastre, M. (2021). The Role of PGC1α in Alzheimer's Disease and Therapeutic Interventions. Int. J. Mol. Sci. *22*, 5769. 10.3390/ijms22115769.

241. Katsouri, L., Lim, Y.M., Blondrath, K., Eleftheriadou, I., Lombardero, L., Birch, A.M., Mirzaei, N., Irvine, E.E., Mazarakis, N.D., and Sastre, M. (2016). PPARγ-coactivator-1α gene transfer reduces neuronal loss and amyloid-β generation by reducing β-secretase in an Alzheimer's disease model. Proc. Natl. Acad. Sci. U. S. A. *113*, 12292–12297. 10.1073/pnas.1606171113.

242. Dölle, C., Flønes, I., Nido, G.S., Miletic, H., Osuagwu, N., Kristoffersen, S., Lilleng, P.K., Larsen, J.P., Tysnes, O.-B., Haugarvoll, K., et al. (2016). Defective mitochondrial DNA homeostasis in the substantia nigra in Parkinson disease. Nat. Commun. *7*, 13548. 10.1038/ncomms13548.

243. Wei, W., Keogh, M.J., Wilson, I., Coxhead, J., Ryan, S., Rollinson, S., Griffin, H., Kurzawa-Akinibi, M., Santibanez-Koref, M., Talbot, K., et al. (2017). Mitochondrial DNA point mutations and relative copy number in 1363 disease and control human brains. Acta Neuropathol. Commun. *5*, 13. 10.1186/s40478-016-0404-6.

244. Filograna, R., Mennuni, M., Alsina, D., and Larsson, N.-G. (2021). Mitochondrial DNA copy number in human disease: the more the better? FEBS Lett. *595*, 976–1002. 10.1002/1873-3468.14021.

245. Petersen, M.H., Budtz-Jørgensen, E., Sørensen, S.A., Nielsen, J.E., Hjermind, L.E., Vinther-Jensen, T., Nielsen, S.M.B., and Nørremølle, A. (2014). Reduction in mitochondrial DNA copy number in peripheral leukocytes after onset of Huntington's disease. Mitochondrion *17*, 14–21. 10.1016/j.mito.2014.05.001.

246. Pyle, A., Brennan, R., Kurzawa-Akanbi, M., Yarnall, A., Thouin, A., Mollenhauer, B., Burn, D., Chinnery, P.F., and Hudson, G. (2015). Reduced cerebrospinal fluid mitochondrial DNA is a biomarker for early-stage Parkinson's disease. Ann. Neurol. *78*, 1000–1004. 10.1002/ana.24515.

247. Schwanhäusser, B., Busse, D., Li, N., Dittmar, G., Schuchhardt, J., Wolf, J., Chen, W., and Selbach, M. (2011). Global quantification of mammalian gene expression control. Nature *473*, 337–342. 10.1038/nature10098.

248. Sakae, N., Roemer, S.F., Bieniek, K.F., Murray, M.E., Baker, M.C., Kasanuki, K., Graff-Radford, N.R., Petrucelli, L., Van Blitterswijk, M., Rademakers, R., et al. (2019). Microglia in frontotemporal lobar degeneration with progranulin or C9ORF72 mutations. Ann. Clin. Transl. Neurol. *6*, 1782–1796. 10.1002/acn3.50875.

249. Lui, H., Zhang, J., Makinson, S.R., Cahill, M.K., Kelley, K.W., Huang, H.-Y., Shang, Y., Oldham, M.C., Martens, L.H., Gao, F., et al. (2016). Progranulin Deficiency Promotes Circuit-Specific Synaptic Pruning by Microglia via Complement Activation. Cell *165*, 921–935. 10.1016/j.cell.2016.04.001.

250. Zhang, J., Velmeshev, D., Hashimoto, K., Huang, Y.-H., Hofmann, J.W., Shi, X., Chen, J., Leidal, A.M., Dishart, J.G., Cahill, M.K., et al. (2020). Neurotoxic microglia promote

TDP-43 proteinopathy in progranulin deficiency. Nature *588*, 459–465. 10.1038/s41586-020-2709-7.

251. Filiano, A.J., Martens, L.H., Young, A.H., Warmus, B.A., Zhou, P., Diaz-Ramirez, G., Jiao, J., Zhang, Z., Huang, E.J., Gao, F.-B., et al. (2013). Dissociation of Frontotemporal Dementia–Related Deficits and Neuroinflammation in Progranulin Haploinsufficient Mice. J. Neurosci. *33*, 5352–5361. 10.1523/JNEUROSCI.6103-11.2013.

252. Magistretti, P.J., and Allaman, I. (2015). A Cellular Perspective on Brain Energy Metabolism and Functional Imaging. Neuron *86*, 883–901. 10.1016/j.neuron.2015.03.035.

253. Terman, A., Kurz, T., Navratil, M., Arriaga, E.A., and Brunk, U.T. (2010). Mitochondrial Turnover and Aging of Long-Lived Postmitotic Cells: The Mitochondrial–Lysosomal Axis Theory of Aging. Antioxid. Redox Signal. *12*, 503–535. 10.1089/ars.2009.2598.

254. Kowald, A., and Kirkwood, T.B.L. (2000). Accumulation of Defective Mitochondria through Delayed Degradation of Damaged Organelles and Its Possible Role in the Ageing of Post-mitotic and Dividing Cells. J. Theor. Biol. *202*, 145–160. 10.1006/jtbi.1999.1046.

255. Pottier, C., Mateiu, L., Baker, M.C., DeJesus-Hernandez, M., Teixeira Vicente, C., Finch, N.A., Tian, S., van Blitterswijk, M., Murray, M.E., Ren, Y., et al. (2022). Shared brain transcriptomic signature in TDP-43 type A FTLD patients with or without GRN mutations. Brain *145*, 2472–2485. 10.1093/brain/awab437.

256. Kang, I., Chu, C.T., and Kaufman, B.A. (2018). The mitochondrial transcription factor TFAM in neurodegeneration: Emerging evidence and mechanisms. FEBS Lett. *592*, 793–811. 10.1002/1873-3468.12989.

257. Macken, W.L., Vandrovcova, J., Hanna, M.G., and Pitceathly, R.D.S. (2021). Applying genomic and transcriptomic advances to mitochondrial medicine. Nat. Rev. Neurol. *17*, 215–230. 10.1038/s41582-021-00455-2.

258. Fantini, J., and Yahi, N. (2015). Brain Lipids in Synaptic Function and Neurological Disease: Clues to Innovative Therapeutic Strategies for Brain Disorders (Academic Press).

259. Bhatti, G.K., Gupta, A., Pahwa, P., Khullar, N., Singh, S., Navik, U., Kumar, S., Mastana, S.S., Reddy, A.P., Reddy, P.H., et al. (2022). Targeting mitochondrial bioenergetics as a promising therapeutic strategy in metabolic and neurodegenerative diseases. Biomed. J. *45*, 733–748. 10.1016/j.bj.2022.05.002.

260. Herrero-Mendez, A., Almeida, A., Fernández, E., Maestre, C., Moncada, S., and Bolaños, J.P. (2009). The bioenergetic and antioxidant status of neurons is controlled by continuous degradation of a key glycolytic enzyme by APC/C–Cdh1. Nat. Cell Biol. *11*, 747–752. 10.1038/ncb1881.

261. Bélanger, M., Allaman, I., and Magistretti, P.J. (2011). Brain Energy Metabolism: Focus on Astrocyte-Neuron Metabolic Cooperation. Cell Metab. *14*, 724–738. 10.1016/j.cmet.2011.08.016.

262. Plotegher, N., Perocheau, D., Ferrazza, R., Massaro, G., Bhosale, G., Zambon, F., Rahim, A.A., Guella, G., Waddington, S.N., Szabadkai, G., et al. (2020). Correction: Impaired cellular bioenergetics caused by GBA1 depletion sensitizes neurons to calcium overload. Cell Death Differ. *27*, 2534. 10.1038/s41418-020-0525-0.

263. Strope, T.A., Birky, C.J., and Wilkins, H.M. (2022). The Role of Bioenergetics in Neurodegeneration. Int. J. Mol. Sci. *23*, 9212. 10.3390/ijms23169212.

264. Zheng, B., Liao, Z., Locascio, J.J., Lesniak, K.A., Roderick, S.S., Watt, M.L., Eklund, A.C., Zhang-James, Y., Kim, P.D., Hauser, M.A., et al. (2010). PGC-1α, A Potential Therapeutic Target for Early Intervention in Parkinson's Disease. Sci. Transl. Med. *2*, 52ra73-52ra73. 10.1126/scitranslmed.3001059.

265. Cui, L., Jeong, H., Borovecki, F., Parkhurst, C.N., Tanese, N., and Krainc, D. (2006). Transcriptional Repression of PGC-1α by Mutant Huntingtin Leads to Mitochondrial Dysfunction and Neurodegeneration. Cell *127*, 59–69. 10.1016/j.cell.2006.09.015.

266. Qin, W., Haroutunian, V., Katsel, P., Cardozo, C.P., Ho, L., Buxbaum, J.D., and Pasinetti, G.M. (2009). PGC-1α Expression Decreases in the Alzheimer Disease Brain as a Function of Dementia. Arch. Neurol. *66*, 352–361. 10.1001/archneurol.2008.588.

267. Han, R., Liang, J., and Zhou, B. (2021). Glucose Metabolic Dysfunction in Neurodegenerative Diseases—New Mechanistic Insights and the Potential of Hypoxia as a Prospective Therapy Targeting Metabolic Reprogramming. Int. J. Mol. Sci. *22*, 5887. 10.3390/ijms22115887.

268. Buffo, A., Rite, I., Tripathi, P., Lepier, A., Colak, D., Horn, A.-P., Mori, T., and Götz, M. (2008). Origin and progeny of reactive gliosis: A source of multipotent cells in the injured brain. Proc. Natl. Acad. Sci. *105*, 3581–3586. 10.1073/pnas.0709002105.

269. Macken, W.L., Falabella, M., McKittrick, C., Pizzamiglio, C., Ellmers, R., Eggleton, K., Woodward, C.E., Patel, Y., Labrum, R., Phadke, R., et al. (2022). Specialist multidisciplinary input maximises rare disease diagnoses from whole genome sequencing. Nat. Commun. *13*, 6324. 10.1038/s41467-022-32908-7.

270. Phillips, N.R., Simpkins, J.W., and Roby, R.K. (2014). Mitochondrial DNA deletions in Alzheimer's brains: A review. Alzheimers Dement. *10*, 393–400. 10.1016/j.jalz.2013.04.508.

271. Boveris, A., and Navarro, A. (2008). Brain mitochondrial dysfunction in aging. IUBMB Life *60*, 308–314. 10.1002/iub.46.

272. Lagouge, M., and Larsson, N.-G. (2013). The role of mitochondrial DNA mutations and free radicals in disease and ageing. J. Intern. Med. *273*, 529–543. 10.1111/joim.12055.

273. Linnane, A., Ozawa, T., Marzuki, S., and Tanaka, M. (1989). MITOCHONDRIAL DNA MUTATIONS AS AN IMPORTANT CONTRIBUTOR TO AGEING AND DEGENERATIVE DISEASES. The Lancet *333*, 642–645. 10.1016/S0140-6736(89)92145-4.

274. Gass, J., Cannon, A., Mackenzie, I.R., Boeve, B., Baker, M., Adamson, J., Crook, R., Melquist, S., Kuntz, K., Petersen, R., et al. (2006). Mutations in progranulin are a major

cause of ubiquitin-positive frontotemporal lobar degeneration. Hum. Mol. Genet. *15*, 2988–3001. 10.1093/hmg/ddl241.

275. Morris, H.R., Khan, M.N., Janssen, J.C., Brown, J.M., Perez-Tur, J., Baker, M., Ozansoy, M., Hardy, J., Hutton, M., Wood, N.W., et al. (2001). The Genetic and Pathological Classification of Familial Frontotemporal Dementia. Arch. Neurol. *58*, 1813–1816. 10.1001/archneur.58.11.1813.

276. Josephs, K.A., Holton, J.L., Rossor, M.N., Godbolt, A.K., Ozawa, T., Strand, K., Khan, N., Al-Sarraj, S., and Revesz, T. (2004). Frontotemporal lobar degeneration and ubiquitin immunohistochemistry. Neuropathol. Appl. Neurobiol. *30*, 369–373. 10.1111/j.1365-2990.2003.00545.x.

277. Neumann, M., Sampathu, D.M., Kwong, L.K., Truax, A.C., Micsenyi, M.C., Chou, T.T., Bruce, J., Schuck, T., Grossman, M., Clark, C.M., et al. (2006). Ubiquitinated TDP-43 in Frontotemporal Lobar Degeneration and Amyotrophic Lateral Sclerosis. Science *314*, 130–133. 10.1126/science.1134108.

278. Buratti, E., Dörk, T., Zuccato, E., Pagani, F., Romano, M., and Baralle, F.E. (2001). Nuclear factor TDP-43 and SR proteins promote in vitro and in vivo CFTR exon 9 skipping. EMBO J. *20*, 1774–1784. 10.1093/emboj/20.7.1774.

279. Buratti, E., and Baralle, F.E. (2009). Chapter 1 The Molecular Links Between TDP-43 Dysfunction and Neurodegeneration. In Advances in Genetics Advances in Genetics. (Academic Press), pp. 1–34. 10.1016/S0065-2660(09)66001-6.

280. Lashley, T., Rohrer, J.D., Mead, S., and Revesz, T. (2015). Review: An update on clinical, genetic and pathological aspects of frontotemporal lobar degenerations. Neuropathol. Appl. Neurobiol. *41*, 858–881. 10.1111/nan.12250.

281. Bigio, E.H. (2011). TDP-43 Variants of Frontotemporal Lobar Degeneration. J. Mol. Neurosci. *45*, 390–401. 10.1007/s12031-011-9545-z.

282. Bahia, V.S., Takada, L.T., and Deramecourt, V. (2013). Neuropathology of frontotemporal lobar degeneration: a review. Dement. Neuropsychol. *7*, 19–26. 10.1590/S1980-57642013DN70100004.

283. Hasegawa, M., Arai, T., Nonaka, T., Kametani, F., Yoshida, M., Hashizume, Y., Beach, T.G., Buratti, E., Baralle, F., Morita, M., et al. (2008). Phosphorylated TDP-43 in frontotemporal lobar degeneration and amyotrophic lateral sclerosis. Ann. Neurol. *64*, 60–70. 10.1002/ana.21425.

284. Mackenzie, I.R.A., and H. Feldman, H. (2005). Ubiquitin Immunohistochemistry Suggests Classic Motor Neuron Disease, Motor Neuron Disease With Dementia, and Frontotemporal Dementia of the Motor Neuron Disease Type Represent a Clinicopathologic Spectrum. J. Neuropathol. Exp. Neurol. *64*, 730–739. 10.1097/01.jnen.0000174335.27708.0a.

285. Franco-Iborra, S., and Tanji, K. (2020). Chapter 10 - Histochemical and immunohistochemical staining methods to visualize mitochondrial proteins and activity. In Methods in Cell Biology Mitochondria, 3rd Edition., L. A. Pon and E. A. Schon, eds. (Academic Press), pp. 247–270. 10.1016/bs.mcb.2019.11.024.

286. Phadke, R. (2017). Myopathology of Adult and Paediatric Mitochondrial Diseases. J. Clin. Med. *6*, 64. 10.3390/jcm6070064.

287. Erben, L., and Buonanno, A. (2019). Detection and Quantification of Multiple RNA Sequences Using Emerging Ultrasensitive Fluorescent in situ Hybridization Techniques. Curr. Protoc. Neurosci. *87*, e63. 10.1002/cpns.63.

288. Herbst, A., Widjaja, K., Nguy, B., Lushaj, E.B., Moore, T.M., Hevener, A.L., McKenzie, D., Aiken, J.M., and Wanagat, J. (2017). Digital PCR Quantitation of Muscle Mitochondrial DNA: Age, Fiber Type, and Mutation-Induced Changes. J. Gerontol. A. Biol. Sci. Med. Sci. *72*, 1327–1333. 10.1093/gerona/glx058.

289. Rygiel, K.A., Grady, J.P., Taylor, R.W., Tuppen, H.A.L., and Turnbull, D.M. (2015). Triplex real-time PCR–an improved method to detect a wide spectrum of mitochondrial DNA deletions in single cells. Sci. Rep. *5*, 9906. 10.1038/srep09906.

290. Harbauer, A.B., Hees, J.T., Wanderoy, S., Segura, I., Gibbs, W., Cheng, Y., Ordonez, M., Cai, Z., Cartoni, R., Ashrafi, G., et al. (2022). Neuronal mitochondria transport Pink1 mRNA via synaptojanin 2 to support local mitophagy. Neuron *110*, 1516-1531.e9. 10.1016/j.neuron.2022.01.035.

291. Timper, K., Paeger, L., Sánchez-Lasheras, C., Varela, L., Jais, A., Nolte, H., Vogt, M.C., Hausen, A.C., Heilinger, C., Evers, N., et al. (2018). Mild Impairment of Mitochondrial OXPHOS Promotes Fatty Acid Utilization in POMC Neurons and Improves Glucose Homeostasis in Obesity. Cell Rep. *25*, 383-397.e10. 10.1016/j.celrep.2018.09.034.

292. Chen, Z., He, Q., Lu, T., Wu, J., Shi, G., He, L., Zong, H., Liu, B., and Zhu, P. (2023). mcPGK1-dependent mitochondrial import of PGK1 promotes metabolic reprogramming and self-renewal of liver TICs. Nat. Commun. *14*, 1121. 10.1038/s41467-023-36651-5.

293. Chen, J., Zheng, Q., Peiffer, L.B., Hicks, J.L., Haffner, M.C., Rosenberg, A.Z., Levi, M., Wang, X.X., Ozbek, B., Baena-Del Valle, J., et al. (2020). An in Situ Atlas of Mitochondrial DNA in Mammalian Tissues Reveals High Content in Stem and Proliferative Compartments. Am. J. Pathol. *190*, 1565–1579. 10.1016/j.ajpath.2020.03.018.

294. Mercer, T.R., Neph, S., Dinger, M.E., Crawford, J., Smith, M.A., Shearwood, A.-M.J., Haugen, E., Bracken, C.P., Rackham, O., Stamatoyannopoulos, J.A., et al. (2011). The Human Mitochondrial Transcriptome. Cell *146*, 645–658. 10.1016/j.cell.2011.06.051.

295. Selvaraj, S., Mezzano, V., Loomis, C., and Hanniford, D. (2020). RNAscope® and BaseScope™: In-situ RNA analysis for formalin-fixed paraffin-embedded tissues and beyond. J. Biomol. Tech. JBT *31*, S31.

296. Cairns, N.J., Neumann, M., Bigio, E.H., Holm, I.E., Troost, D., Hatanpaa, K.J., Foong, C., White, C.L., Schneider, J.A., Kretzschmar, H.A., et al. (2007). TDP-43 in Familial and Sporadic Frontotemporal Lobar Degeneration with Ubiquitin Inclusions. Am. J. Pathol. *171*, 227–240. 10.2353/ajpath.2007.070182.

297. Porta, S., Xu, Y., Restrepo, C.R., Kwong, L.K., Zhang, B., Brown, H.J., Lee, E.B., Trojanowski, J.Q., and Lee, V.M.-Y. (2018). Patient-derived frontotemporal lobar degeneration brain extracts induce formation and spreading of TDP-43 pathology in vivo. Nat. Commun. *9*, 4220. 10.1038/s41467-018-06548-9.

298. Tan, R.H., Kril, J.J., Fatima, M., McGeachie, A., McCann, H., Shepherd, C., Forrest, S.L., Affleck, A., Kwok, J.B.J., Hodges, J.R., et al. (2015). TDP-43 proteinopathies: pathological identification of brain regions differentiating clinical phenotypes. Brain *138*, 3110–3122. 10.1093/brain/awv220.

299. Bankhead, P., Loughrey, M.B., Fernández, J.A., Dombrowski, Y., McArt, D.G., Dunne, P.D., McQuaid, S., Gray, R.T., Murray, L.J., Coleman, H.G., et al. (2017). QuPath: Open source software for digital pathology image analysis. Sci. Rep. *7*, 16878. 10.1038/s41598-017-17204-5.

300. Irwin, D.J., McMillan, C.T., Xie, S.X., Rascovsky, K., Van Deerlin, V.M., Coslett, H.B., Hamilton, R., Aguirre, G.K., Lee, E.B., Lee, V.M.Y., et al. (2018). Asymmetry of post-mortem neuropathology in behavioural-variant frontotemporal dementia. Brain *141*, 288–301. 10.1093/brain/awx319.

301. Zhang, Y., Qu, Y., Gao, K., Yang, Q., Shi, B., Hou, P., and Ji, M. (2015). High copy number of mitochondrial DNA (mtDNA) predicts good prognosis in glioma patients. Am. J. Cancer Res. *5*, 1207–1216.

302. Atout, S., Shurrab, S., and Loveridge, C. (2022). Evaluation of the Suitability of RNAscope as a Technique to Measure Gene Expression in Clinical Diagnostics: A Systematic Review. Mol. Diagn. Ther. *26*, 19–37. 10.1007/s40291-021-00570-2.

303. Kersigo, J., Pan, N., Lederman, J.D., Chatterjee, S., Abel, T., Pavlinkova, G., Silos-Santiago, I., and Fritzsch, B. (2018). A RNAscope whole mount approach that can be combined with immunofluorescence to quantify differential distribution of mRNA. Cell Tissue Res. *374*, 251–262. 10.1007/s00441-018-2864-4.

304. Schulz, D., Zanotelli, V.R.T., Fischer, J.R., Schapiro, D., Engler, S., Lun, X.-K., Jackson, H.W., and Bodenmiller, B. (2018). Simultaneous Multiplexed Imaging of mRNA and Proteins with Subcellular Resolution in Breast Cancer Tissue Samples by Mass Cytometry. Cell Syst. *6*, 25-36.e5. 10.1016/j.cels.2017.12.001.

305. Wallace, D.C. (2013). A mitochondrial bioenergetic etiology of disease. J. Clin. Invest. *123*, 1405–1412. 10.1172/JCI61398.

306. Islam, Md.T. (2017). Oxidative stress and mitochondrial dysfunction-linked neurodegenerative disorders. Neurol. Res. *39*, 73–82. 10.1080/01616412.2016.1251711.

307. Labory, J., Fierville, M., Ait-El-Mkadem, S., Bannwarth, S., Paquis-Flucklinger, V., and Bottini, S. (2020). Multi-Omics Approaches to Improve Mitochondrial Disease Diagnosis: Challenges, Advances, and Perspectives. Front. Mol. Biosci. *7*.

308. Lu, J., Duan, W., Guo, Y., Jiang, H., Li, Z., Huang, J., Hong, K., and Li, C. (2012). Mitochondrial dysfunction in human TDP-43 transfected NSC34 cell lines and the protective effect of dimethoxy curcumin. Brain Res. Bull. *89*, 185–190. 10.1016/j.brainresbull.2012.09.005.

309. Pansarasa, O., Bordoni, M., Drufuca, L., Diamanti, L., Sproviero, D., Trotti, R., Bernuzzi, S., La Salvia, S., Gagliardi, S., Ceroni, M., et al. (2018). Lymphoblastoid cell lines as a model to understand amyotrophic lateral sclerosis disease mechanisms. Dis. Model. Mech. *11*, dmm031625. 10.1242/dmm.031625.

310. Park, S.-K., Park, S., and Liebman, S.W. (2019). Respiration enhances TDP-43 toxicity, but TDP-43 retains some toxicity in the absence of respiration. J. Mol. Biol. *431*, 2050–2059. 10.1016/j.jmb.2019.03.014.

311. Kumar-Singh, S. (2011). Progranulin and TDP-43: Mechanistic Links and Future Directions. J. Mol. Neurosci. *45*, 561–573. 10.1007/s12031-011-9625-0.

312. Jian, J., Konopka, J., and Liu, C. (2013). Insights into the role of progranulin in immunity, infection, and inflammation. J. Leukoc. Biol. *93*, 199–208. 10.1189/jlb.0812429.

313. Missiroli, S., Genovese, I., Perrone, M., Vezzani, B., Vitto, V.A.M., and Giorgi, C. (2020). The Role of Mitochondria in Inflammation: From Cancer to Neurodegenerative Disorders. J. Clin. Med. *9*, 740. 10.3390/jcm9030740.

314. Nakahira, K., Haspel, J.A., Rathinam, V.A.K., Lee, S.-J., Dolinay, T., Lam, H.C., Englert, J.A., Rabinovitch, M., Cernadas, M., Kim, H.P., et al. (2011). Autophagy proteins regulate innate immune responses by inhibiting the release of mitochondrial DNA mediated by the NALP3 inflammasome. Nat. Immunol. *12*, 222–230. 10.1038/ni.1980.

315. Palomer, X., Álvarez-Guardia, D., Rodríguez-Calvo, R., Coll, T., Laguna, J.C., Davidson, M.M., Chan, T.O., Feldman, A.M., and Vázquez-Carrera, M. (2009). TNF-α reduces PGC-1α expression through NF-κB and p38 MAPK leading to increased glucose oxidation in a human cardiac cell model. Cardiovasc. Res. *81*, 703–712. 10.1093/cvr/cvn327.

316. Hahn, W.S., Kuzmicic, J., Burrill, J.S., Donoghue, M.A., Foncea, R., Jensen, M.D., Lavandero, S., Arriaga, E.A., and Bernlohr, D.A. (2014). Proinflammatory cytokines differentially regulate adipocyte mitochondrial metabolism, oxidative stress, and dynamics. Am. J. Physiol.-Endocrinol. Metab. *306*, E1033–E1045. 10.1152/ajpendo.00422.2013.

317. Motori, E., Puyal, J., Toni, N., Ghanem, A., Angeloni, C., Malaguti, M., Cantelli-Forti, G., Berninger, B., Conzelmann, K.-K., Götz, M., et al. (2013). Inflammation-Induced Alteration of Astrocyte Mitochondrial Dynamics Requires Autophagy for Mitochondrial Network Maintenance. Cell Metab. *18*, 844–859. 10.1016/j.cmet.2013.11.005.

318. Wong, Y.C., Ysselstein, D., and Krainc, D. (2018). Mitochondria–lysosome contacts regulate mitochondrial fission via RAB7 GTP hydrolysis. Nature *554*, 382–386. 10.1038/nature25486.

319. Osellame, L.D., Rahim, A.A., Hargreaves, I.P., Gegg, M.E., Richard-Londt, A., Brandner, S., Waddington, S.N., Schapira, A.H.V., and Duchen, M.R. (2013). Mitochondria and Quality Control Defects in a Mouse Model of Gaucher Disease—Links to Parkinson's Disease. Cell Metab. *17*, 941–953. 10.1016/j.cmet.2013.04.014.

320. Redmann, M., Benavides, G.A., Berryhill, T.F., Wani, W.Y., Ouyang, X., Johnson, M.S., Ravi, S., Barnes, S., Darley-Usmar, V.M., and Zhang, J. (2017). Inhibition of autophagy with bafilomycin and chloroquine decreases mitochondrial quality and bioenergetic function in primary neurons. Redox Biol. *11*, 73–81. 10.1016/j.redox.2016.11.004.

321. Jolly, R.D., Brown, S., Das, A.M., and Walkley, S.U. (2002). Mitochondrial dysfunction in the neuronal ceroid-lipofuscinoses (Batten disease). Neurochem. Int. *40*, 565–571. 10.1016/S0197-0186(01)00128-0.

322. Fernandez-Mosquera, L., Yambire, K.F., Couto, R., Pereyra, L., Pabis, K., Ponsford, A.H., Diogo, C.V., Stagi, M., Milosevic, I., and Raimundo, N. (2019). Mitochondrial respiratory chain deficiency inhibits lysosomal hydrolysis. Autophagy *15*, 1572–1591. 10.1080/15548627.2019.1586256.

323. Demers-Lamarche, J., Guillebaud, G., Tlili, M., Todkar, K., Bélanger, N., Grondin, M., Nguyen, A.P., Michel, J., and Germain, M. (2016). Loss of Mitochondrial Function Impairs Lysosomes *. J. Biol. Chem. *291*, 10263–10276. 10.1074/jbc.M115.695825.

324. Tsai, R.M., and Boxer, A.L. (2014). Treatment of Frontotemporal Dementia. Curr. Treat. Options Neurol. *16*, 319. 10.1007/s11940-014-0319-0.

325. Boxer, A.L., Knopman, D.S., Kaufer, D.I., Grossman, M., Onyike, C., Graf-Radford, N., Mendez, M., Kerwin, D., Lerner, A., Wu, C.-K., et al. (2013). Memantine in patients with frontotemporal lobar degeneration: a multicentre, randomised, double-blind, placebo-controlled trial. Lancet Neurol. *12*, 149–156. 10.1016/S1474-4422(12)70320-4.

326. Amin, S., Carling, G., and Gan, L. (2022). New insights and therapeutic opportunities for progranulin-deficient frontotemporal dementia. Curr. Opin. Neurobiol. *72*, 131–139. 10.1016/j.conb.2021.10.001.

327. Kurnellas, M., Mitra, A., Schwabe, T., Paul, R., Arrant, A.E., Roberson, E.D., Ward, M., Yeh, F., Long, H., and Rosenthal, A. (2023). Latozinemab, a novel progranulin-elevating therapy for frontotemporal dementia. J. Transl. Med. *21*, 387. 10.1186/s12967-023-04251-y.

328. Singh, A., Faccenda, D., and Campanella, M. (2021). Pharmacological advances in mitochondrial therapy. eBioMedicine *65*. 10.1016/j.ebiom.2021.103244.

329. Mehmel, M., Jovanović, N., and Spitz, U. (2020). Nicotinamide Riboside—The Current State of Research and Therapeutic Uses. Nutrients *12*, 1616. 10.3390/nu12061616.

330. Lautrup, S., Sinclair, D.A., Mattson, M.P., and Fang, E.F. (2019). NAD+ in Brain Aging and Neurodegenerative Disorders. Cell Metab. *30*, 630–655. 10.1016/j.cmet.2019.09.001.

331. de la Rubia, J.E., Drehmer, E., Platero, J.L., Benlloch, M., Caplliure-Llopis, J., Villaron-Casales, C., de Bernardo, N., AlarcÓn, J., Fuente, C., Carrera, S., et al. (2019). Efficacy and tolerability of EH301 for amyotrophic lateral sclerosis: a randomized, double-blind, placebo-controlled human pilot study. Amyotroph. Lateral Scler. Front. Degener. *20*, 115–122. 10.1080/21678421.2018.1536152.